pennsylvania
DEPARTMENT OF TRANSPORTATION

Continuation of Joint and Full Waveform Inversion to Improve Evaluation of Sinkholes and Karst Features

FINAL REPORT

11/10/23

By Joseph Coe (PI), Bechara Abboud (co-PI), Ahmed Faheem (co-PI), Jonathan Nyquist (co-PI), and Pourya Alidoust Golroudbari

Temple University

COMMONWEALTH OF PENNSYLVANIA
DEPARTMENT OF TRANSPORTATION

CONTRACT # 4400017651 / 511802
WORK ORDER # TEM 015

Technical Report Documentation Page

1. Report No.	2. Government Accession No.	3. Recipient's Catalog No.
FHWA-PA-2023-010-TEM WO 015		

4. Title and Subtitle	5. Report Date
Continuation of Joint and Full Waveform Inversion to Improve Evaluation of Sinkholes and Karst Features	November 10, 2023
	6. Performing Organization Code

7. Author(s)	8. Performing Organization Report No.
Joseph Coe, Bechara Abboud, Ahmed Faheem, Jonathan Nyquist, and Pourya Alidoust Golroudbari	

9. Performing Organization Name and Address	10. Work Unit No. (TRAIS)
Temple University College of Engineering 1947 N. 12th St. Philadelphia, PA 19122	**11. Contract or Grant No.** **4400017651**

12. Sponsoring Agency Name and Address	13. Type of Report and Period Covered
The Pennsylvania Department of Transportation Bureau of Planning and Research Commonwealth Keystone Building 400 North Street, 6th Floor Harrisburg, PA 17120-0064	Final Report: 12/12/2022 – 11/10/2023
	14. Sponsoring Agency Code:

15. Supplementary Notes

Technical Advisors: Sarah McInnes, P.E. – Principal Assistant Construction Engineer - Services; smcinnes@pa.gov; (610)205-6544

16. Abstract

Geophysical methods can provide fast and reliable information regarding sinkholes and karst features over a broad area of coverage. Often, these geophysical methods involve the solution to an inversion problem to deduce subsurface details based on surface measurements. Solution of the inversion problem is a non-trivial issue that has warranted significant study. A number of advanced methods have been examined in the recent past that focus on jointly inverting multiple datasets or using full waveform approaches that numerically model the subsurface. The purpose of this report is to summarize research efforts regarding the capabilities of advanced geophysical techniques when applied specifically to evaluate the severity and extent of sinkhole/karst hazards and quality control of mitigation efforts. The objective of this research project was to provide the Pennsylvania Department of Transportation (PennDOT) recommendations regarding the use of such advanced geophysical techniques in their efforts to manage sinkhole risk across the Commonwealth of Pennsylvania. The focus of this project was full waveform inversion (FWI) and its implementation at a site with active sinkholes.

17. Key Words	18. Distribution Statement
Karst, Sinkholes, Geophysics, Full Waveform Inversion, Joint Inversion	No restrictions. This document is available from the National Technical Information Service, Springfield, VA 22161

19. Security Classif. (of this report)	20. Security Classif. (of this page)	21. No. of Pages	22. Price
Unclassified	Unclassified	185	

Statement of Credit
This work was sponsored by the Pennsylvania Department of Transportation and the U.S. Department of Transportation, Federal Highway Administration.

Joint and Full Waveform Inversion to Improve Evaluation of Sinkholes and Karst Features

TEM Work Order (WO) 015

Contract No. 4400017651

Task 6 - Deliverable 6.2 Report:
Final Report

By:
Temple University Research Team

Principal Investigator: Joseph Thomas Coe, Jr., Ph.D.
Associate Professor

Co-Principal Investigator: Bechara E. Abboud, Ph.D., P.E.
Associate Professor

Co-Principal Investigator: Ahmed Faheem, Ph.D.
Associate Professor

Co-Principal Investigator: Jonathan Nyquist, Ph.D.
Professor

Graduate Research Assistant: Pourya Alidoust Golroudbari

November 10, 2023

TABLE OF CONTENTS

LIST OF FIGURES

LIST OF TABLES

1. INTRODUCTION

Karst conditions in soluble bedrock are present across a significant portion of the United States. Central and eastern Pennsylvania (including parts of District 6-0) have several well-developed areas of karst that require special attention before any construction and during long-term maintenance of highway infrastructure. Such infrastructure can face various problems such as sudden subsidence or ground surface instability due to the occurrence of cavities or other karst-related collapses. Given the limited advanced warning of many karstic collapses, it remains critical to employ comprehensive site characterization methods to detect karst-related features in the areas surrounding a project site. Effective site characterization and any associated mitigation techniques are crucial to improve project designs, reduce uncertainties, and minimize long-term project costs. Quality control of karst projects and learning from case histories are also part of these efforts to minimize risk and enhance the reliability of highway infrastructure. Due to the heterogeneity of the underlying soil, site-specific conditions, type of karst features and their dimensions, differences in project budgets, and even the amount of tolerable risk, the management plan for karst-related issues should not be considered identical for two sites. A unique approach must be tailored to each site to better characterize problematic features and efficiently mitigate any anomalies. Knowledge of successful characterization and mitigation techniques can improve our ability to make better decisions in response to karst-related problems in highway infrastructure projects. To that effect, geophysical methods can provide fast and reliable information regarding sinkholes and karst features over a broad area of coverage that can supplement existing geotechnical site characterization techniques. Several advanced analytical and processing methods have been developed in recent years to better utilize geophysical datasets and more accurately resolve subsurface conditions.

1.1. Objectives and Scope

The purpose of this report is to summarize research efforts regarding the capabilities of advanced geophysical techniques when applied specifically to evaluate the severity and extent of sinkhole/karst hazards and quality control of mitigation efforts. The objective of this research project was to provide the Pennsylvania Department of Transportation (PennDOT) recommendations regarding the use of such advanced geophysical techniques in their efforts to manage sinkhole risk across the Commonwealth of Pennsylvania. The focus of this project was full waveform inversion (FWI) and its implementation at a site with active sinkholes. Several tasks were identified as part of these research efforts, including:

1. Review exiting literature related to sinkholes and advanced geophysical methods
2. Review PennDOT sinkhole case histories
3. Review PennDOT experiences with sinkholes and identify needs
4. Identify a PennDOT sinkhole test site to apply advanced geophysical testing
5. Develop a comprehensive field and numerical simulation work plan
6. Perform field testing at the selected site and numerical simulations of geophysical tests
7. Process the acquired data and analyze results
8. Develop recommendations regarding the implementation of full waveform inversion for sinkhole characterization

This report summarizes the execution of these tasks and the implications of their findings.

1.2. Organization of the Report

This report is organized into multiple chapters, that each roughly correspond to the tasks identified during the development of the research project:

- Chapter 2 provides background regarding the current standard of practice and the current state of the art with respect to evaluating sinkholes and karst with geophysical methods. This is accomplished by summarizing the existing literature regarding subsurface investigation for sinkhole evaluation and quality control of mitigation efforts.

- Chapter 3 discusses the detailed investigation performed on PennDOT District 6-0 projects related to sinkhole hazards to establish their experiences with sinkholes and karst. It details the efforts to locate suitable case histories that highlight the ways in which PennDOT has evaluated, mitigated, and provided for quality control of these kinds of hazards as well as the implementation of geophysics in their investigation.

- Chapter 4 summarizes efforts to identify a suitable test site to apply the advanced geophysical testing proposed in this project. Details regarding the selected field site are provided, including a discussion of the sinkholes at the site and previous investigation efforts. Finally, a summary is provided of the field geophysical testing efforts.

- Chapter 5 details the data pre- and post-processing efforts on the collected field data. Background information is provided regarding choice of parameters and algorithms. Also summarized are the analyses of the subsequent results from data pre- and post-processing.

- Chapter 6 summarizes efforts related to numerical and theoretical modeling of the proposed geophysical inversion techniques in this study. Such efforts allow for more generalized recommendations to be made regarding the suitability of FWI and joint inversion of geophysical datasets beyond the field site selected for this study.

- Chapter 7 provides an overall summary of the research efforts. Recommendations regarding the use of full waveform tomography and joint inversion for sinkhole characterization are provided.

2. LITERATURE REVIEW

This chapter provides a literature review with background related to sinkholes as well as the advanced geophysical testing implemented in this study. A thorough review is initially provided of how karst and sinkholes form, followed by a discussion of the extent of karst rock formations across the United States and the Commonwealth of Pennsylvania, and finishing with a review of the various geophysical and non-geophysical methods for evaluating sinkholes. The discussion of geophysical techniques provides an in-depth discussion of recent advancements in the analysis and post-processing of geophysical data, including joint inversion approaches and full waveform tomography.

2.1. Karst and Sinkhole Formation

To gain a better understanding of karst and sinkhole formation, this initial section focuses on the formation of sedimentary rocks and the factors that lead to the development of conditions fostering karst and sinkhole formation. Additionally, the spatial distribution of karst conditions is discussed within the greater United States and within the Commonwealth of Pennsylvania specifically.

2.1.1. Sedimentary Rocks

The rock cycle describes the resulting transitions caused by plate tectonics and the water cycle for rocks located at the near surface (Figure 2.1). These transitions lead to a constant state among the three main rock types: igneous, metamorphic, and sedimentary. Igneous rocks result from the solidification of magma as it cools near the surface. Metamorphic rocks result from the physical and chemical changes caused by exposure to high temperatures and pressures. However, mechanical disintegration of particles or the chemical decomposition of rocks can lead to production of soil, unconsolidated rock detritus, and components dissolved in groundwater and runoff. Various transport processes such as moving bodies of water, wind, and glaciers can subsequently deposit the unconsolidated geologic material. Sedimentary rocks form as a result of the accumulation, lithification, and solidification process of these weathered by-products. These kinds of rocks are the most common rocks exposed on the Earth's surface (more than 66% of the surface area and over 90% on ocean basins) but only extended down to an insignificant depth of the entire crust (less than 5%), which is dominated by igneous and metamorphic rocks (Blatt and Jones 1975). Nevertheless, easy access of sedimentary rocks on the surface layers of earth alongside an accurate understanding and interpretation of sedimentary rocks provides us with invaluable information on the history, geography, and depositional settings of the planet. Fossil records of sedimentary rocks enable the documentation of the evolutionary advancement of life cycle in the earth history (Ojakangas 1982; Holman 1995).

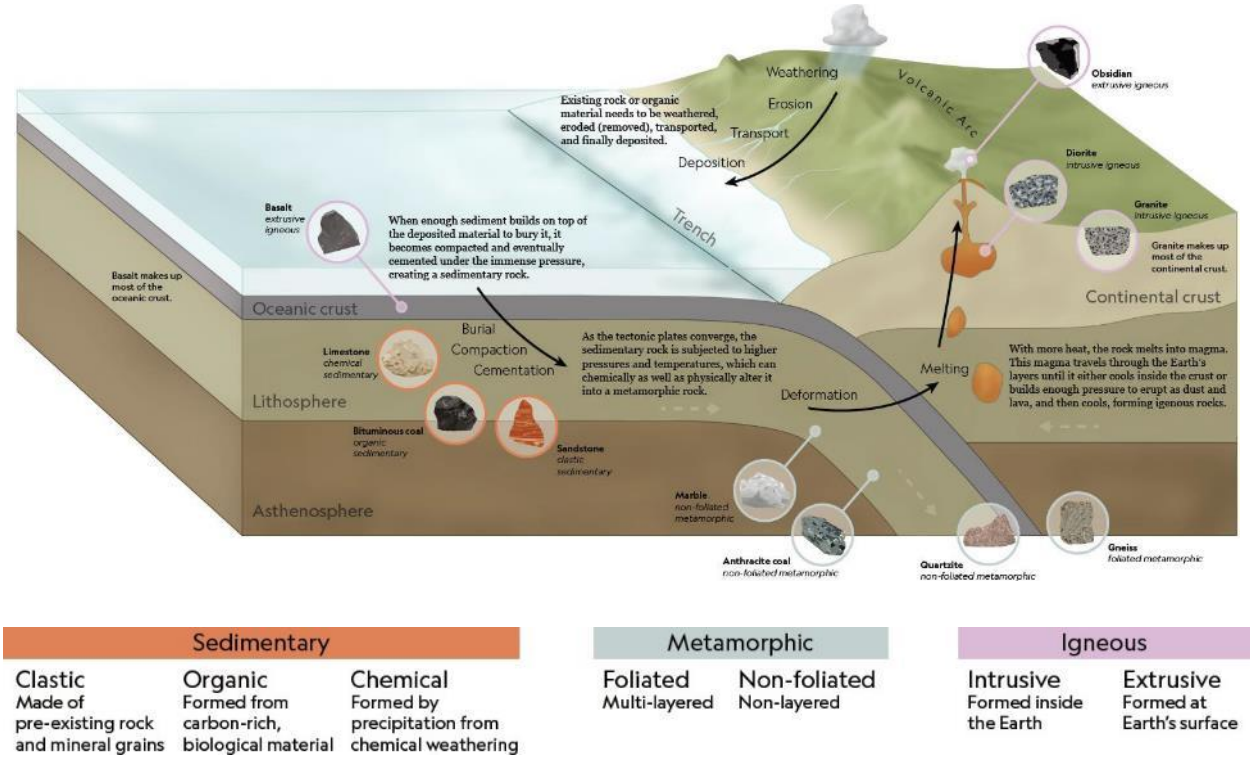

Figure 2.1. The rock cycle and associated rock types.

Sedimentary rocks, based on the type of weathering they experience, are classified into two (2) main groups:

- Clastic sedimentary rocks
- Chemical sedimentary rocks (including bio-chemical and organic sedimentary rocks)

Clastic sedimentary rocks consist of pieces (clasts) of pre-existing rocks and mineral grains of varying sizes that have been loosened by weathering and subsequently deposited in various geologic settings. The particle size in these kinds of rocks may vary from clays to pebbles (grains larger than 2 mm) and boulder-sized materials. Under lithification, different particle types form into the various clastic sedimentary rock types. For example, sand particles can become sandstone, clay particles can form into shale, and pebble and boulder-sized material turn into conglomerate and breccia. Chemical and mineral precipitation of dissolved rock material leads to the formation of chemical sedimentary rocks. Commonly, inorganic chemical sedimentary rock formation occurs when changes occur in water temperature, acidity, ion concentration, dissolved gasses, temperatures, or pressures, which all cause minerals to crystallize. For example, gypsum forms as a result of evaporation in water while limestone is produced by changes in water temperature. Bio-chemical sedimentary rocks are formed from shells and bodies of underwater organisms that contain aragonite, a mineral similar to and commonly replaced by calcite, and silica. Organic sedimentary rocks are typically formed underwater by organic material (e.g., plant and animal remains) that has been deposited and lithified.

2.1.2. Carbonate and Evaporite Rocks

Carbonate rocks are a particular class of sedimentary rocks that are composed primarily of carbonate ions, including calcite, aragonite, and dolomite. Existing data shows that about one-fifth of all sedimentary rocks contain such carbonate ions (Stow 2005). The two (2) major kinds of carbonate rocks include limestones and dolostones. Limestone consists of 50% or more of calcite and/or aragonite (both different crystal forms of $CaCO_3$) and can be formed both by chemical and mechanical processes of sediments. Limestone is often used for many industrial purposes, including in the manufacture of Portland cement, quicklime, and other raw building materials, as well as for commercial drugs (e.g., antacids and calcium supplements) (Neese 2011). Dolomite is mainly produced by the secondary modification or replacement of limestone where the mineral dolomite [$CaMg(CO_3)_2$] replaces the calcite and aragonite minerals in limestone during diagenesis (Klein and Philpotts 2013). Carbonate rocks and other clastic sedimentary rocks (e.g., sandstones) can form a favorable setting for petroleum and gas. For example, it has been estimated that up to 50%-60% of the worldwide "conventional" petroleum resources are in carbonate rocks reservoirs (Burchette 2012).

Evaporite rocks are another major class of sedimentary rocks that form from chemical sediments. Evaporite refers to the concentration and subsequent crystallization of mineral sediments after they have been evaporated from an aqueous solution in either a marine or nonmarine setting. For example, such minerals may form from brines where the amount of evaporated water exceeds the total incoming water (e.g., from rainfall, rivers, etc.). Most evaporite rocks develop in arid coastal environments on evaporitic mudflats or in shallow evaporitic seas/lakes (Cooper 2018). Evaporite minerals include carbonates (e.g., calcite, dolomite, magnesite, and aragonite), sulfates (anhydrite and gypsum), chlorides (particularly halite, sylvite, and carnallite), borates, silicates, nitrates, and sulfocarbonates. The main evaporite rocks include gypsum and salt. These kinds of rocks have the highest solubility of common rocks. Hence, water that is unsaturated with respect to gypsum or salt rapidly dissolves them and carries them in solution (Martinez et al. 1998). Evaporites are present in 32 of the 48 contiguous states of the United States (Johnson 2005).

2.1.3. Formation of Karst

Karst refers to a particular topography that results from the dissolution of soluble carbonate or evaporite rocks (Figure 2.2). Over a period of time, ground water containing dissolved carbon dioxide forms a mild acid, which can slowly dissolve alkaline materials. Alkaline carbonate and evaporite bedrock units are affected by this process when the slightly acidic ground water moves through the units and is neutralized by the carbonate which increases the size of the fracture in which the water is flowing. As this process continues, larger openings form in the rock allowing for increased ground-water flow and rate of rock dissolution. Karst is typically characterized by surficial features of various scales including sinkholes, valleys, disappearing (losing) streams, and clints/grikes. Complex underground drainage systems (e.g., aquifers) and extensive caverns also form in the subsurface. In geologic settings where the soluble rock is covered by unconsolidated sediments or other non-soluble strata, the surficial features may not be visible and only the subsurface features may be distinguished. All 50 states in the US have areas with karst

potential, although some states like Florida and Missouri have extensive amounts compared to others (Weary and Doctor 2014). The principal difference between karst in carbonate rock and in evaporite rock is that evaporite karst and its subsidence features can form rapidly, in a matter of days, weeks, or years, whereas in carbonate rocks this typically takes years, decades, or centuries to form (Johnson 2005).

Generally, the design and construction of engineering structures in karst regions must address challenges associated with difficulty of excavating and grading the ground over pinnacled rockheads, instability of the ground surface, and unpredictable groundwater flow conditions (Zhou and Beck 2011). In karst environments, sinkholes and underground conduits are the primary sources of problems for engineers and land use planners (Galve et al. 2011). Hence, the occurrence of cavities in the rock and the soil requires special engineering considerations to provide stable foundations for the construction of roads and structures.

Figure 2.2. Karst topography south of Mammoth Cave National Park in Kentucky, United States (U.S. Department of the Interior, National Park Service Mammoth Cave National Park, Karst Geology Brochure).

2.1.4. Sinkhole Collapse Types

Sinkholes are commonly funnel-shaped subsidence features present in karst environments with generally subterranean drainage (Bates and Jackson 1984) (Figure 2.3). They display a wide range of morphologies

(cylindrical, conical, bowl or pan-shaped) and can range from several meters to hundreds of meters in diameter and tens of meters in depth (Williams 2003). Even small sinkhole collapses can pose a serious threat to public safety and the integrity of infrastructure and transportation networks, particularly in populated areas (Newton 1987). Moreover, sinkholes threaten water and environmental resources by creating pathways that allow the transmission of surface contaminants into underlying aquifers causing the degradation of groundwater resources (Tihansky 1999).

Sinkhole collapses occur naturally through the processes of erosion or gradual removal of soluble bedrock. There are many processes that can initiate and/or accelerate the development and collapse of sinkholes, including:

- Decline of water levels (e.g., drought, ground water pumping)
- Disturbance of soil (e.g., drilling, excavations, digging, underground mining)
- Point-sources of concentrated water flow (e.g., leaking water pipe, sewer drains, waterways)
- Heavy surficial loads (e.g., equipment, new structures)

Though some of these processes may occur naturally, many damaging sinkholes are induced by human activities. Natural sinkholes and induced sinkholes can generally be separated based on physical characteristics, frequency and density of occurrence, and environmental setting. Induced sinkholes generally develop much faster than natural sinkholes, although all collapsed sinkholes require some dissolution of the underlying bedrock.

(a) **(b)**

Figure 2.3. Sinkholes in Pennsylvania (Kochanov 2015): (a) sinkhole in Dauphin County exposing a utility line; (b) multiple sinkholes in the Saucon Valley of Lehigh County.

There are two (2) main types of sinkholes (Gunn 2004; Waltham et al. 2005a,b; Guerrero et al. 2008): 1) solution sinkholes; and 2) subsidence sinkholes. Dissolution is the ultimate cause of all sinkholes, but the type of sinkhole is also controlled by the thickness and type of overburden materials and the local hydrology (Figure 2.4). Solution sinkholes form in areas where the exposed karst rocks at the surface are dissolved in water and carried away from the surface. Soil settles down into the enlarged openings forming a small depression at the ground surface. The dissolution enlarges natural openings in the rock such as

joints, fractures, and bedding planes. Subsidence sinkholes result from both subsurface dissolution and downward gravitational movement (internal erosion or deformation) of the undermined overlying material. These sinkholes are the most important from a hazard and engineering perspective (Gutiérrez et al. 2014).

Figure 2.4 describes the types of subsidence sinkholes using two (2) terms. The first descriptor refers to the material affected by internal erosion and/or deformation processes (cover, bedrock or caprock), and the second descriptor indicates the main subsidence process (collapse, suffusion, or sagging). The term "Cover" in Figure 2.4 refers to unconsolidated allogenic deposits or residual soil material. The term "Bedrock" refers to the karst rocks and the term "Caprock" refers to the non-karst rocks at a site. Collapse is the brittle deformation of soil or rock material either by the development of well-defined failure planes or brecciation. Suffosion refers to the downward migration of cover deposits through voids and their progressive settling. Finally, the sagging term refers to the ductile bending of sediments caused by the lack of basal support. Frequently, more than one material type and several processes are involved in the generation of subsidence sinkholes. These complex sinkholes can be described using combinations of the proposed terms with the dominant material and/or process followed by the secondary one (e.g., cover and bedrock collapse sinkhole).

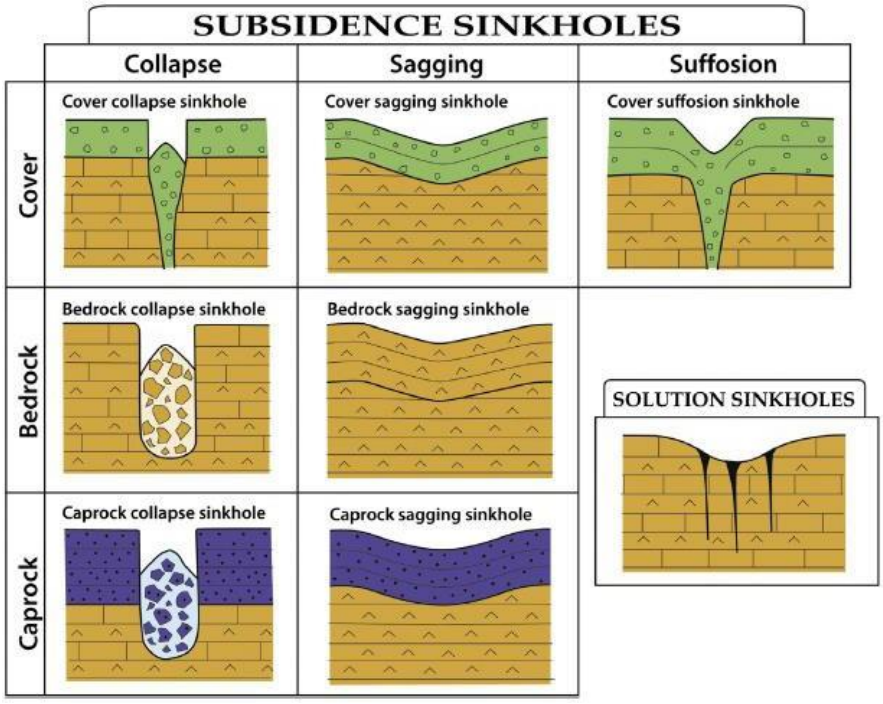

Figure 2.4. Classification of sinkholes (adapted from Gutiérrez et al. 2014).

Each collapse type in Figure 2.4 progresses through various stages of development as detailed in various sources (e.g., Culshaw and Waltham 1987, Tihansky and Knochenmus 2001, Tharp 2003, Waltham and Fookes 2003). As an example, cover-collapse sinkholes form where a clay rich covering soil settles down

into voids in the carbonate rock. The cavity subsequently migrates upward by progressive collapse of the arch formed by the cohesive sediment (Figure 2.5). The cavity continues to progress upwards until it reaches the ground surface and forms a visible sinkhole.

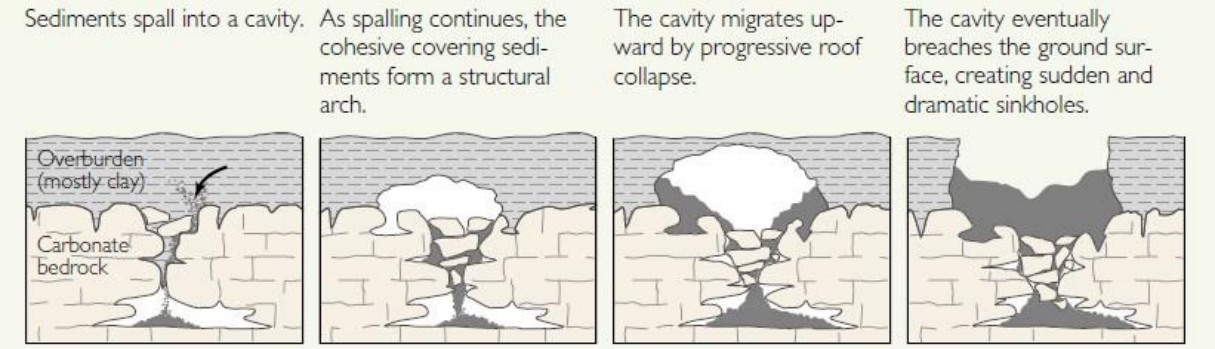

Figure 2.5. Stages in the development of cover collapse sinkholes (adapted from Culshaw and Waltham 1987).

As mentioned previously, sinkholes can be induced by human activities. Anything that may lead to the diversion of water into soluble rocks beneath the earth will accelerate the creation of sinkholes and subsequent subsidence. Stream bed diversions and water-table fluctuations caused by urban groundwater withdrawal and injection are actions that increase the risk of collapse in areas located on soluble rocks. In areas where the water table is normally above the soil-bedrock contact, soil collapses occur when the water table drops below the soil zone, either during droughts or due to high pumping rates. These collapses are caused by loss of buoyant support above the voids, or by upward propagation as saturated soil falls or washes downward. Soil collapses also occurs in situations where the water table is below the soil-bedrock contact or can be caused by water leaking from drainage wells, pipelines, septic tanks, and drainage ditches.

One (1) major source of human activity that can accelerate the sinkhole development process is construction operations. Construction at a site can create unstable or weakened conditions in carbonate/evaporite rocks due to the poor control of surface and ground water (Fischer and Fischer 2015). Construction excavations can also remove a protective layer of low permeability soils over solutioned rock, leading to the ponding of water in these compromised areas. However, strategic construction operations can also be used to minimize the effects of sinkholes on proposed infrastructure. For example, bringing the ground surface (road cut) closer to the epikarst at a site could allow sinkholes to propagate faster and avoid their effects on the final structure.

Although many sinkholes collapse with little or no advance warning, other collapses can be recognized by features at the land surface that indicate their development. Some of the more common features include (Veni et al. 2001):

- Circular and linear cracks in soil, asphalt, and concrete paving and floors

- Depressions in soil or pavement that commonly result in the ponding of water
- Downward movement of small-diameter vertical structures such as poles or posts
- Sudden muddying of water in a well that has been producing clear water
- Sudden draining of a pond or creek
- Slumping, sagging, or tilting of trees, roads, rails, fences, pipes, poles, sign boards, and other vertical or horizontal structures

Many of these features require consistent observations that are not feasible over the large spatial scale over which sinkholes may occur in a geologic setting. Consequently, given that no advance warning may be present and/or typical warning signs may not be reliably identified, management of sinkhole hazards is quite problematic.

Subsurface cavities and/or sinkholes are more prone to occur in areas covered with carbonate and evaporate rocks, which are present worldwide but concentrated in certain areas due to their geologic history. Although the potential for sinkhole occurrence (and subsequent subsidence) varies spatially across the United States, areas underlain by relatively soluble carbonate and evaporite rocks susceptible to karst exist in all 50 states and make up approximately 18% of the total area of the country (Figures 2.6 and 2.7). Such rocks are largely concentrated in Florida, Georgia, South Carolina, North Carolina, Kentucky, Tennessee, Alabama, Mississippi, Missouri, Texas, Oklahoma, Iowa, Nebraska, Illinois, Indiana, Wisconsin, Virginia, and parts of Pennsylvania (Figure 2.6). Evaporite rocks underlie about 35% - 40% of the United States, though in many areas they are buried at great depths and do not contribute to karst development (Martinez et al. 1998). This fact accounts for the discrepancy between the Martinez et al. (1998) and Weary and Doctor (2014) estimated areas for evaporite rock subject to karst.

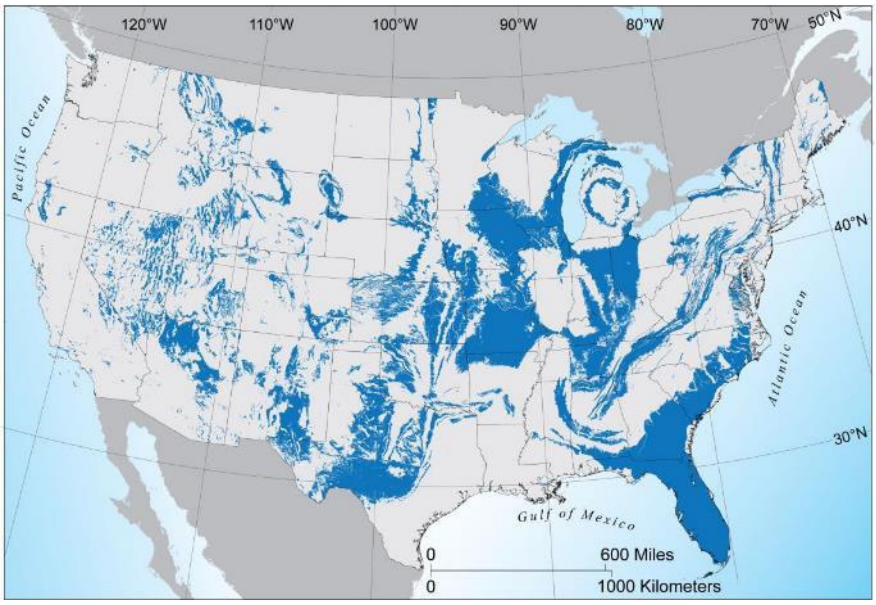

Figure 2.6. Areas in the United States underlain by carbonate and/or evaporite rock and prone to karst (adapted from Weary 2015).

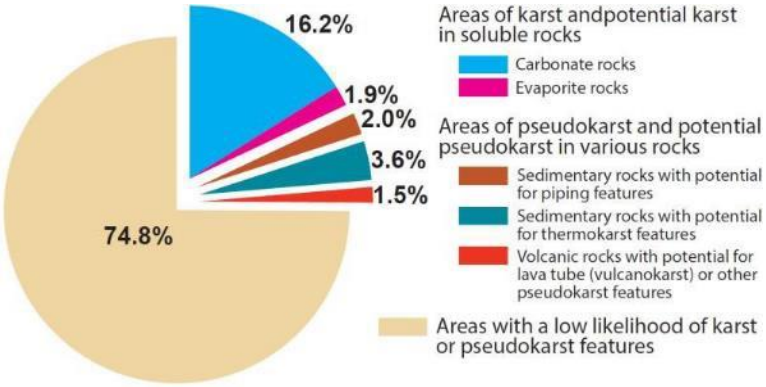

Figure 2.7. Proportion of the area of the United States underlain by rocks and sediments having karst features or the potential for them.

2.1.5. Sinkholes in Pennsylvania

Approximately 7% of the Commonwealth of Pennsylvania is underlain by carbonate bedrock susceptible to sinkhole formation (Kochanov and Reese 2003). Most of this occurs in the valleys and lowlands of south-central and southeastern Pennsylvania, where over 2 million people live (Kochanov and Reese 2003; Kochanov et al. 2015) (Figure 2.8). The major land use for the karst areas is agriculture interspersed with areas of urbanization including Cumberland, Northampton, York, and Chester counties, which have exhibited several sinkholes within the last few years (Hill 2005). In PennDOT District 6-0, the primary concentration of carbonate rock and karst conditions indicative of sinkhole activity is found within central Chester County and in the southeastern section of Montgomery County (Figure 2.9). For example, sinkhole activity in this area led to the closure and subsequent replacement of the Plymouth Road Bridge (Figure 2.10) in the winter of 2014-2015 at a cost of approximately $2.2M. Other sinkhole activity in the area includes the closure of a portion of Butler Pike from Flourtown Road to Germantown Pike in Plymouth Meeting because of another sinkhole in early August 2018, a sinkhole adjacent to Crooked Lane in the King Manor section of Upper Merion in March of 2018, and another sinkhole opening on Shaffer Road, near DeKalb Pike, in King of Prussia in September 2017. Additionally, the Route 30 (Exton) Bypass and Route 422 have also been closed for emergency sinkhole repairs in the past. It is clear from this history that this area is prone to continuous sinkhole hazards that can lead to significant damage, repair costs, and disruptions to traffic operations.

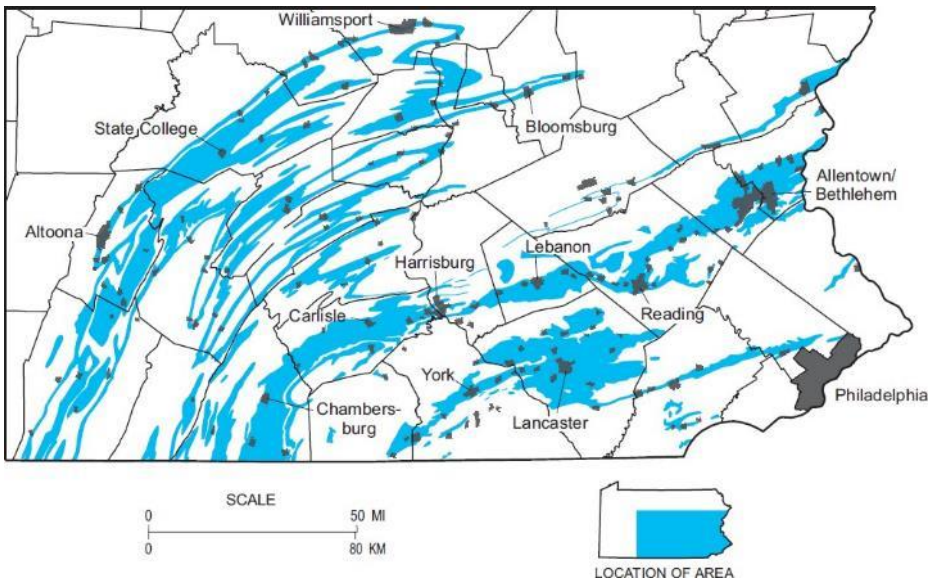

Figure 2.8. Map of carbonate bedrock and major population centers in central and eastern Pennsylvania (Kochanov 2015).

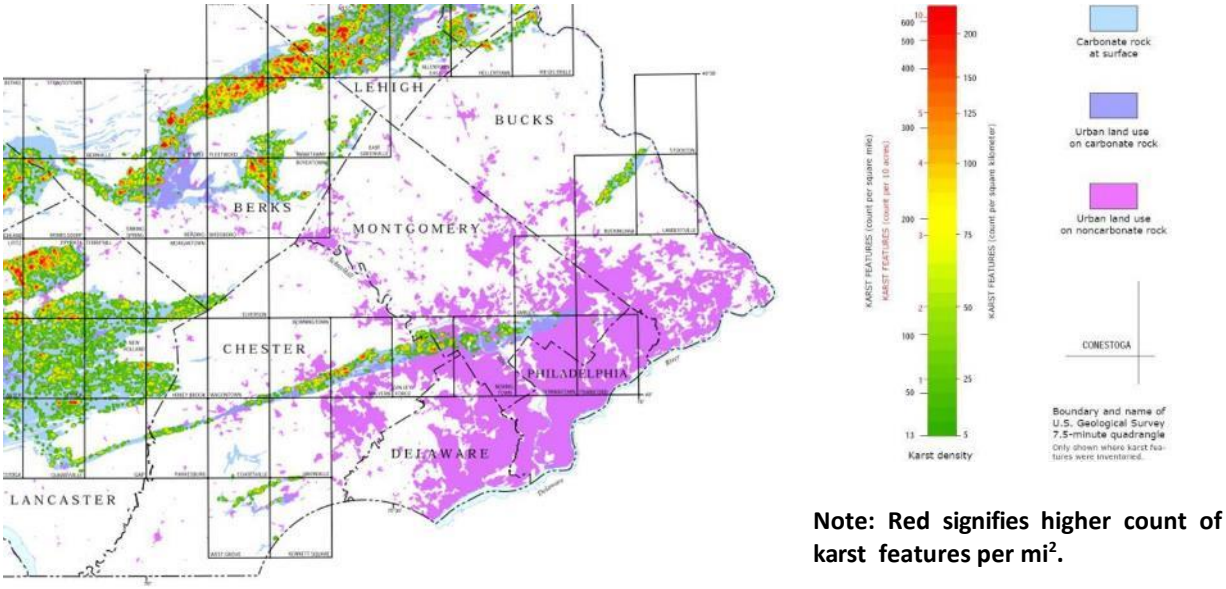

Note: Red signifies higher count of karst features per mi^2.

Figure 2.9. Density of karst features (i.e., carbonate rock, sinkholes, etc.) in southeastern Pennsylvania (Kochanov and Reese 2003).

Figure 2.10. Sinkhole damage to the Plymouth Road Bridge near Plymouth Township (August 2015).

2.2. Identification of Karst and Sinkholes

As noted previously, surficial evidence of sinkholes is not always immediately obvious depending on the nature of the overlying soil cover. Additionally, spatial variability of subsurface karst and hydrogeologic conditions complicates the evaluation of sinkhole hazards during the design, construction, and post-construction maintenance phases for highway infrastructure. The importance of mapping sinkholes as part of karst landscape management and planning efforts has increased rapidly in recent years due to human activities that accelerate the dissolution and subsidence processes. Based on the literature, two (2) broad categories of subsurface exploration techniques have been applied to identify karst features and evaluate sinkhole hazards: Traditional geotechnical techniques (e.g., drilling test borings); and near surface geophysical techniques (e.g., surface and borehole-based seismic methods, GPR, ERT, microgravity) (Kruse et al. 2006; Valois et al. 2011; Samyn 2014; Sevil et al. 2017; Pazzi et al. 2018). Additionally, other methods exist that do not specifically "sample" the subsurface, but rather deduce the presence of sinkholes from monitoring various site conditions such as ground displacements (Gutiérrez et al. 2019). These methods each have their own advantages and disadvantages and none of them can identify with absolute certainty the presence and/or extent of sinkhole features due to the heterogeneity present in karst environments and the inherent limitations of their measurements. The available budget and the acceptable level of risk for each project also affect the selection of an appropriate investigation technique. Consequently, all subsurface investigations to identify karst features and sinkholes should be tailored to each site based on the needs of the project, site conditions, and level of acceptable risk associated with sinkhole hazards (Xeidakis et al. 2004). Such investigations should be performed using an integrated approach that takes advantage of as many sources of information as possible, including desk and site reconnaissance study, aerial photos (particularly if available over long periods of time to identify changes in topography), geophysical investigation, floor elevation mapping, geotechnical investigation and geological interpretation, laboratory analysis, and structural analysis of the site (Schmidt 2005; Fischer and Fischer 2015). This particular project (TEM WO 015) focuses on the geotechnical and geophysical investigation efforts as described in the following sections.

2.2.1. Geotechnical Subsurface Exploration Techniques

Residual soils in karst terrain are often very heterogeneous with a highly irregular soil-rock interface and decreasing strength/stiffness with depth (Sowers 1996). The effects of karst are therefore evident as lateral and vertical changes in geotechnical engineering parameters. Consequently, traditional geotechnical subsurface exploration methods such as drilling test borings and disturbed/undisturbed sampling have often been implemented by engineers to evaluate stratigraphy and assess for sinkhole activity (e.g., Sowers 1996; Hudyma et al. 2005; Kiflu et al. 2013).

Subsurface drilling efforts for sinkholes are often supplemented with in-situ testing techniques such as the Standard Penetration Test (SPT) (ASTM D1586) and the Cone Penetrometer test (CPT) (ASTM D5778) (e.g., Foshee and Bixler 1994; Siegel and Belgeri 1995; Sowers 1996; Smith 1997; Bullock and Dillman 2003; Siegel and Cargill 2005; Siegel et al. 2005; Saliba et al. 2008;Shamet et al. 2017). The blow count (*N*) obtained from SPT provides an indication of the relative density of the subsurface strata as well as other geotechnical properties (e.g., friction angle) from empirical correlations. Subsequently, the variation in *N* can indicate the presence of abnormally low strength soils and raveling into a sinkhole cavity or a dissolution cavity itself, particularly when "weight- of-rod" (WOR) or "weight-of-hammer" (WOH) conditions (i.e., *N* = 0 bpf) are encountered (Shamet et al. 2017). Additionally, the loss of circulation of drilling fluid can indicate the presence of a nearby void (Kannan 1995). The drawback of SPT can be attributed to the discrete intervals typically used to acquire *N* values (Siegel and Cargill 2005). Even when "continuous" SPT testing is performed, the length of the sampler prevents *N* measurements with an interval finer than 1.5 ft (0.5 m), which may not be representative of abrupt changes in subsurface conditions as present in karst environments.

The CPT hydraulically pushes an instrumented steel cone into the soil that records tip resistance, skin friction along the cone sleeve, and pore water pressure. The cone can also be equipped with other instrumentation to best suit the scope of the exploration, including inclinometers to help identify karst anomalies that may deflect the cone tip (e.g., angled rock interface along a near- vertical soil seam). The cone is advanced at a rate of 2 cm/s and the sampling rate of the data acquisition system is typically 1 sample/second, which typically results in a measurement interval of 2 cm. The CPT thus provides a near-continuous profile of information capable of identifying much more abrupt changes in soil compared to the lower resolution SPT method (Figure 2.11). The main limitation of the CPT approach is the lack of a direct sample of the geologic material and penetration refusal when the cone tip encounters very stiff strata (e.g., bedrock, rock fragments in residual soils, construction debris, etc.). Despite these limitations, CPT is a cost-effective solution to identify karst anomalies as reported by several authors (Yang and Drumm 2002; Siegel and Cargill 2005; Shamet et al. 2017a,b; Taylor et al. 2018). CPT is often more effective at identifying karst features, particularly when the high production (e.g., 150-300 lineal meters per day) is taken advantage of to perform many soundings over a grid across the site (Siegel and Cargill 2005; Shamet et al. 2017a,b). Consequently, recent research has promoted more advanced ways of quantifying sinkhole hazards with CPT data, such as the Raveling Index (RI) and Sinkhole Resistance Ratio (SRR) (Shamet et al. 2017a,b; Nam and Shamet 2020).

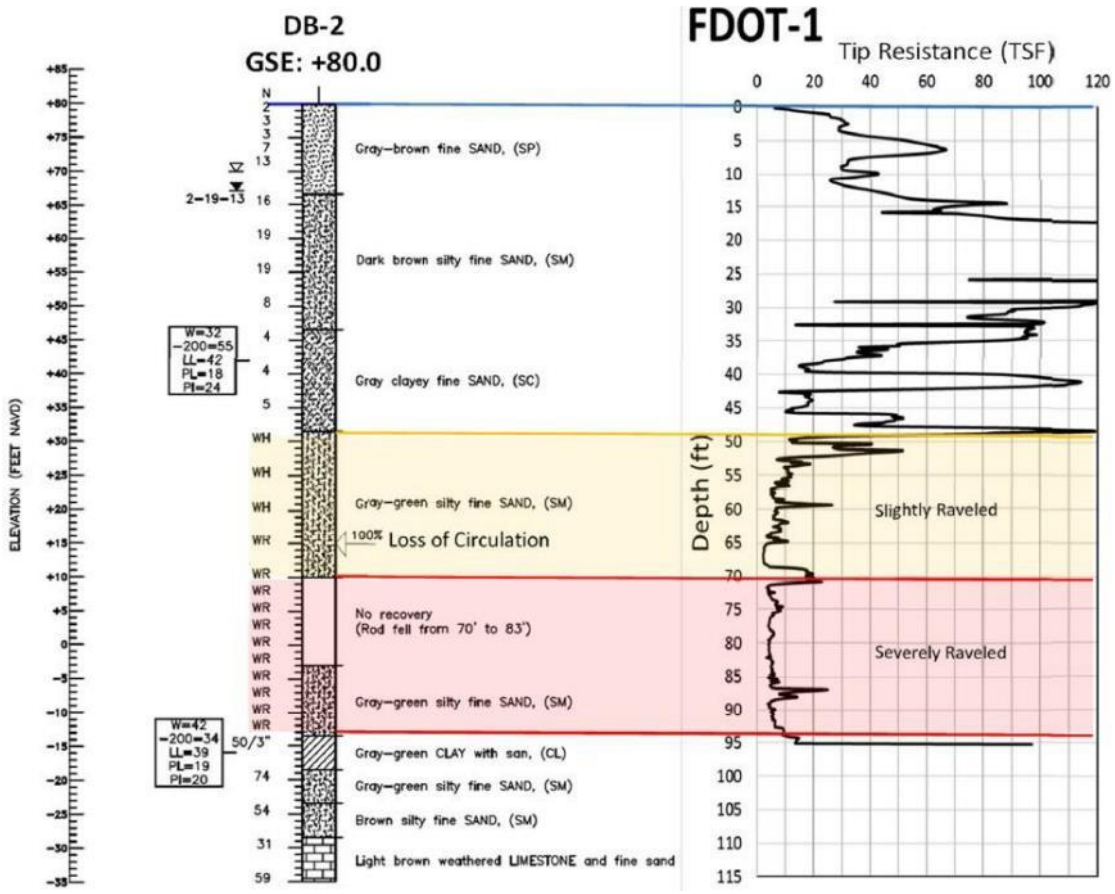

Figure 2.11. Example of CPT and SPT performed in the same location at a site in Florida showing evidence of raveling in residual soils overlying carbonate rock (Shamet et al. 2017b).

Given the large variability inherent in karst geologic settings (e.g., residual soils overlying solutioned rock), standard geotechnical subsurface exploration techniques such as drilling, SPT, and CPT can fail to adequately sample an appropriate amount of the subsurface for engineering design. For example, Bullock and Dillman (2003) illustrate this by considering a 15 m square foundation (Figure 2.12). A high standard-of-practice subsurface exploration plan may include borings and/or CPT soundings at each corner and at the center of the foundation footprint within the zone of influence, which is often considered to be a depth of twice the foundation width. Assuming a sampled diameter of approximately 0.3 m (1 ft) for each boring/sounding, only approximately 0.16% (42 m^3/27,000 m^3) of the soil beneath the foundation will be sampled in this example. This amount assumes continuous sampling within the boring/sounding. Any coarser depth interval (e.g., undisturbed sampling every 1.5 m) may further reduce the amount sampled by as much as 70%. Such limited sampling of the subsurface increases the risk of overlooking sinkhole hazards in karst settings.

2.2.2. Geophysical Techniques

Given the issues with traditional geotechnical subsurface investigations, non- destructive geophysical tests have long been implemented, tested, and validated as diagnostic and or monitoring tools in karst

areas to map and study the geology of an area (e.g., Fretwell and Stewart 1981; Doolittle and Collins 1998; Rybakov et al. 2001; Van Schoor 2002; Debeglia et al. 2006; Anchuela et al. 2009; Rodriguez et al. 2014). Geophysical methods typically measure the response of geologic materials to either an active input into the domain or some passive background source. Geophysical methods can augment drilling and in situ testing to identify "anomalous" conditions between borings or soundings for further exploration. However, it should be noted that these nondestructive methods only provide an indirect measurement of engineering properties (e.g., soil type, strength, compressibility, etc.). Thus, they are more useful as an initial check to identify potential underground cavities, raveling, and/or zones of accumulated water that can indicate sinkhole activity. Moreover, the data acquired by geophysical measurements require interpretation for engineering purposes (often necessitating extensive experience/training) and may be subject to any number of associated analytical limitations (Nam 2019).

Generally, the use of geophysical methods for sinkhole detection is clearly well established in literature and different techniques have been applied in various contexts (depending on depth target, geological setting, presence, and type of noises, etc.) at depths ranging from very surficial to 40 meters, in both urban and rural areas (Beres, Luetscher et al. 2001, Kruse, Grasmueck et al. 2006, Schrott and Sass 2008, Pepe, Martimucci et al. 2015). ASTM has published a guide that aids in the selection of an appropriate geophysical method based on application (ASTM D6429). To identify and estimate karst and subsurface voids/sinkholes, there are multiple widely accepted geophysical methods:

- Electrical Resistivity (ER)
- Ground Penetrating Radar (GPR)
- Electromagnetic Induction (EMI)
- Gravity
- Seismic (i.e., Seismic Reflection/Refraction and/or surface wave methods)

A brief discussion of each procedure is provided in the following sections to describe the uses and benefits of each method. Several examples of case histories where the geophysical method has been applied to evaluate karst are provided. However, as these geophysical methods are widely accepted, development of a list of every published article where each method is used for evaluating karst would be prohibitively long. Consequently, these references represent a comprehensive (but not exhaustive) review of the available literature for each geophysical method. Additionally, more advanced analytical approaches [e.g., Full Waveform Inversion (FWI) and joint inversion techniques] will be explored in the following sections.

2.2.2.1.*Electrical Resistivity (ER)*

The direct current (DC) electrical resistivity (ER) method is frequently used in near surface geophysical investigations to determine subsurface resistivity (e.g., Papadopoulos et al. 2010; Rucker et al. 2010; Carriere et al. 2013; Chambers et al. 2014; Pazzi et al. 2018). Based on Ohm's law, when a voltage source is connected to a conductor, it applies a potential difference (V) that creates an electric field. The electric field in turn exerts force on charges, causing a current (I). The current that flows through most substances is directly proportional to V (in units of volts, which is equal to joule/coulomb), with the proportionality

being the resistance (R) of the material. Electrical resistivity (ρ) quantifies how strongly a material resists such an electric current and is therefore related to R. A low value for the resistivity denotes a material that readily allows electric current. Geologic materials exhibit a range of ρ values that allows the ER method to differentiate strata at a site (Figure 2.12). Igneous rocks tend to have the highest resistivities; sedimentary rocks tend to be most conductive, largely due to their high pore fluid content; and metamorphic rocks have intermediate but overlapping resistivities (Reynolds 2011). The presence of water in the voids of the bedrock plays a major role in the measured ρ. This fact has been exploited by researchers to develop relationships with porosity of geologic materials. For example, Archie (1942) developed an empirical relationship for the effective resistivity of a rock formation which considers the porosity (ϕ), the fraction (s) of the pores containing water, and the fluid conductivity (ρ_w):

$$\rho = a\varphi^{-m}s^{-n}\rho_w \tag{2.1}$$

where a, m, and n are constants ($0.5 \leq a \leq 2.5$, $1.3 \leq m \leq 2.5$, and $n \approx 2$).

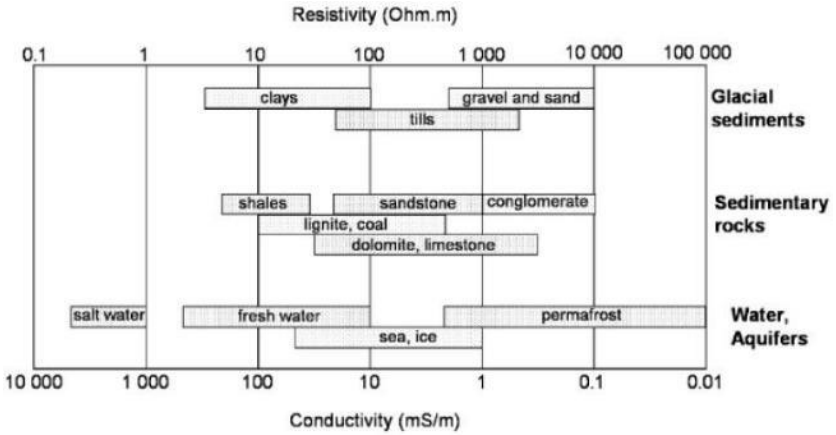

Figure 2.12. Electrical resistivity ranges for earth materials (Palacky 1987).

Electrical resistivity measurements are normally performed by injecting current into the ground through two (2) current electrodes (A and B) and measuring the resulting voltage difference at two (2) potential electrodes (M and N) (Figure 2.13a). In a homogeneous and isotropic half-space, electrical equipotentials are hemispherical when the current electrodes are located at the soil surface (Kearey et al. 2013). As can be seen in Figure 2.13(b), lines of equal voltage, equipotential, intersect the lines of equal current at right-angles. For a single current electrode implanted at the surface of a homogeneous medium, the equation for Ohm's Law in vector form is given by:

$$E = J \cdot \rho \tag{2.2}$$

where E is the voltage drop (i.e., the potential gradient $-\delta V/\delta r$) between any two (2) points on the surface separated by a distance r, J is the current density, which is the current (I) divided by the area over which

the current is distributed at the distance *r* (i.e., a hemisphere; $2\pi r^2$), and ρ is the resistivity. By integrating Equation (2) over *r* the value of potential distribution is calculated:

$$V = \int \delta V = -\int \rho \cdot \frac{I\delta r}{2\pi r^2} = \frac{\rho I}{2\pi r} \tag{2.3}$$

For a current source and sink, the potential V_P at any point P on the ground is equal to the sum of the voltages from the two (2) electrodes. This approach can be generalized by considering an electrically uniform cube of side length *L* through which the current (*I*) is passing, the material within the cube will resist the conduction of electricity through it, resulting in a potential drop (*V*) between opposite faces:

$$\rho_a = \frac{k\,V}{I} \tag{2.4}$$

where *k* is a geometric factor that accounts for the area and length of the object depending on the arrangement of the electrodes used (e.g., $k = 2\pi r$ in Equation 2.3). It should be mentioned that the calculated resistivity value is not the true resistivity of the subsurface, but an "apparent" value (hence the "*a*" subscript) which is the resistivity of a homogeneous ground which will give the same resistance value for the same electrode arrangement. To determine the true subsurface resistivity, an inversion of the measured apparent resistivity values must be performed (Loke 1999).

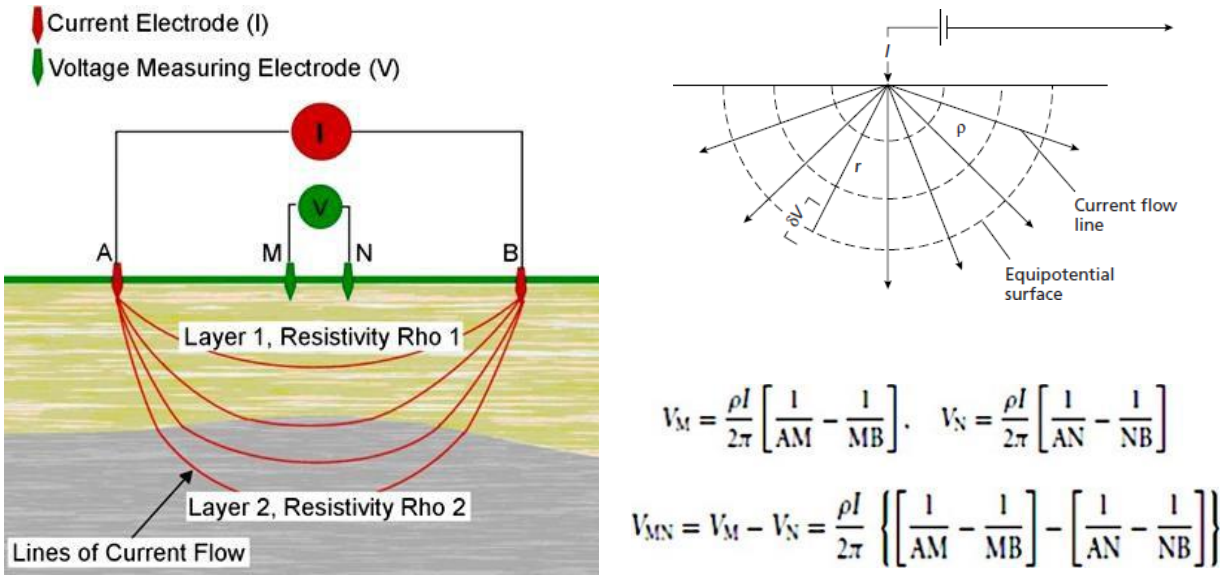

(a) **(b)**

Figure 2.13. Electrical resistivity measurements: (a) example surface electrode configuration (Wightman et al. 2003); and (b) radial current flow from a single surface electrode and subsequent voltage potential.

There are multiple possible configurations for the surface electrodes in an ER survey, each with their own *k* value and inherent strengths and limitations (Figure 2.14). Initially, ER equipment only allowed a limited number of channels for acquisition of data. Though such equipment is still available, the advent of microcomputers and advanced inversion software has promoted the use of multi-electrode or multi-node resistivity profiling to increase the mapping reliability (Kannan 2005) (Figure 2.15). The choice of surface array is therefore often a function of the user's previous familiarity with the array type, availability of cabling and data acquisition software, data processing and inversion software, as well as site-specific factors (Reynolds 2011). For example, the Schlumberger array has higher vertical resolution while the Wenner array is more sensitive to horizontal changes in ρ. The applicability of the ER method is not limited to only surface electrodes but also can be applied to between test borings or a combination of surface and test borings. This method is useful where there is a significant terrain conductivity contrast and due to this reason has been used in several karst related projects (Ahmed and Carpenter 2003; Comas et al. 2015; Kidanu et al. 2016; Prins et al. 2019). However, the presence of utilities, fences, and other metallic objects can interfere with the electrical currents generated during ER testing and render poor results. Additionally, significant clearance is required at test sites to locate the long survey lines necessary for ER to sample a suitable depth of the geologic materials at the site.

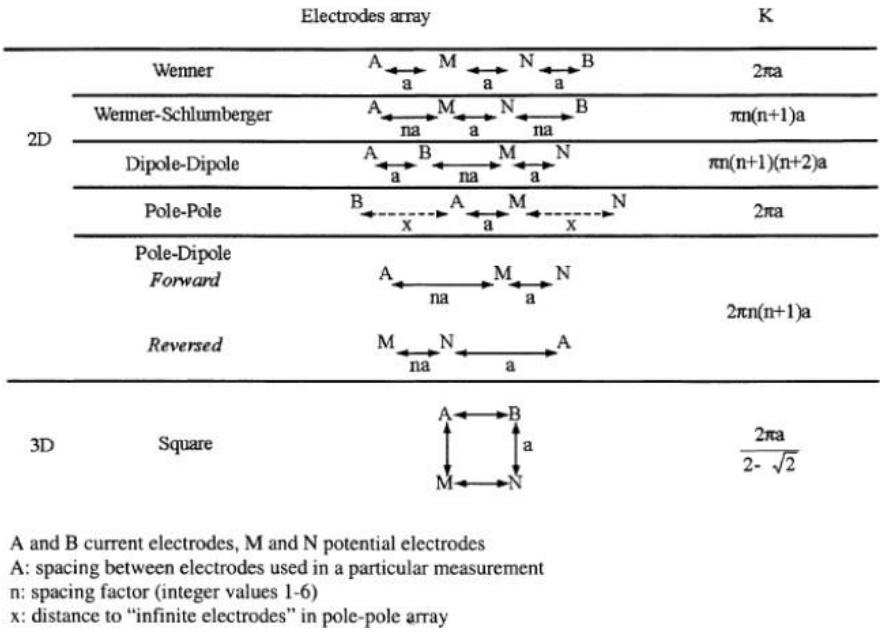

A and B current electrodes, M and N potential electrodes
A: spacing between electrodes used in a particular measurement
n: spacing factor (integer values 1-6)
x: distance to "infinite electrodes" in pole-pole array

Figure 2.14. Different electrodes array configuration (Samouëlian et al. 2005).

As noted previously, the field measurements from the electrodes represent the apparent resistivity. A plot of these values (i.e., a pseudosection) is useful as an initial guide for further quantitative interpretation but the contours depend on the type of array used as well as the true subsurface resistivity (Figure 2.16). To determine the true subsurface resistivity, an inversion algorithm must be used (Loke 1999). The inversion of ER data has been the subject of a significant amount of research since at least the 1930s (e.g., Schlichter 1933). The inversion process typically proceeds by comparing the apparent resistivity

measurements from the field to those generated by forward modeling with different numerical schemes such as finite difference or finite element methods. However, due to incompleteness and noise contamination of the observed field data, this model reconstruction process is ill posed, meaning multiple solutions produce the same apparent resistivity pseudosection (Kirsch 1996). Consequently, an optimization function must be defined to evaluate the quality of the model fit and regularization must be applied when determining the resulting changes to the model (Greenhalgh et al. 2006). A significant amount of research has been performed to find how to improve the way the inversion is performed, including using machine learning techniques, different regularization schemes, and modified data constraints (e.g., Schwarzbach et al. 2005; Papadopoulos et al. 2011; Zhou et al. 2014). Nevertheless, there remains concern regarding the uniqueness of the final inverted resistivity section and whether it truly represents the global minimum or some local minimum that solves the inversion problem.

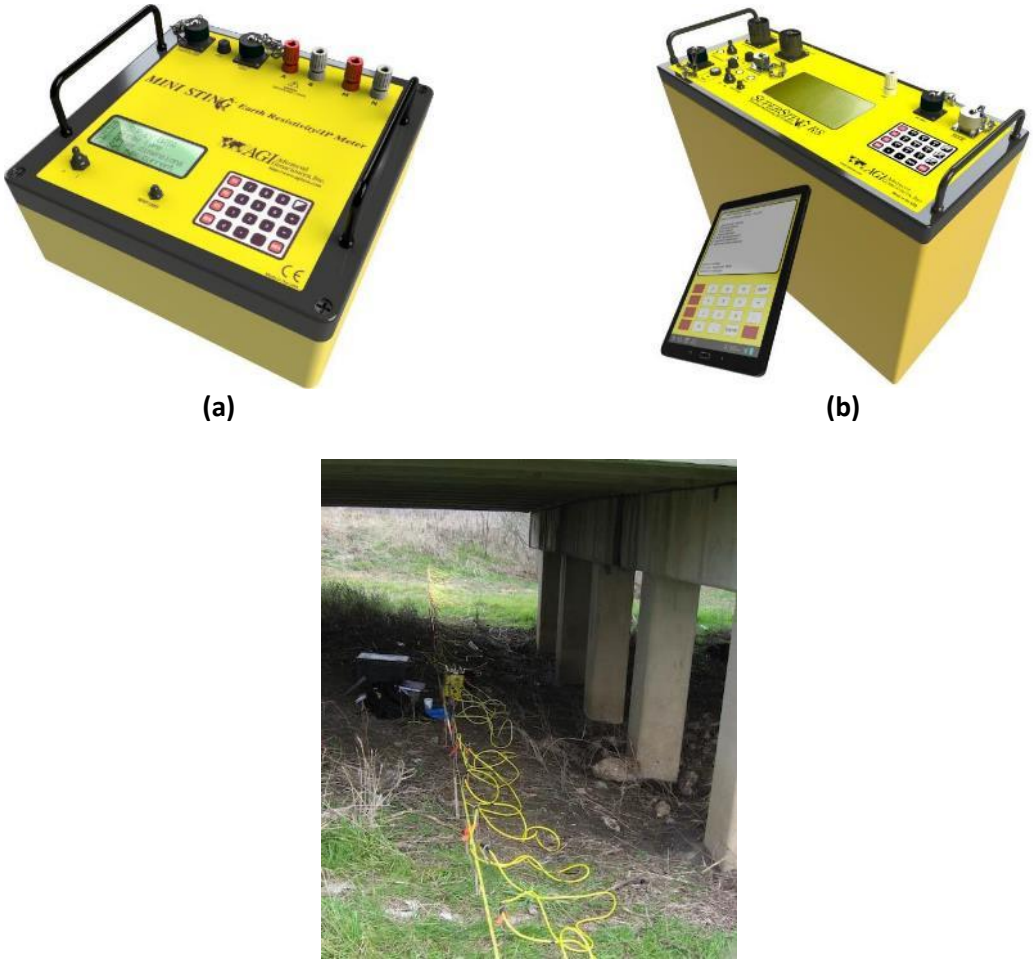

(a) **(b)**

(c)

Figure 2.15. ER equipment: (a) single channel AGI MiniSting^{TM}; (b) AGI SuperSting^{TM} (photos courtesy of AGI https://www.agiusa.com/); and (c) multi-electrode system deployed under a bridge in Texas (Briaud et al. 2012).

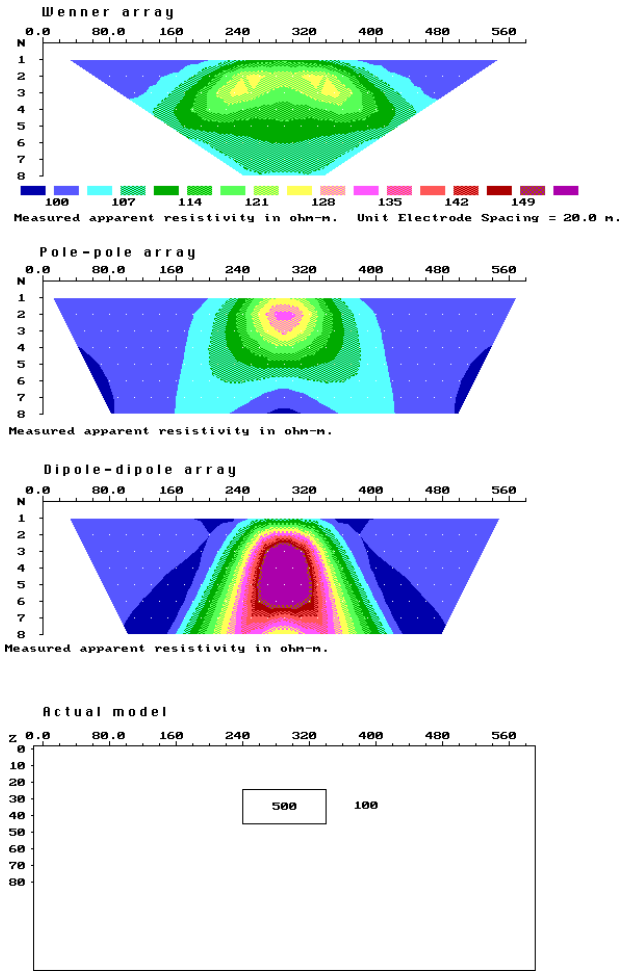

Figure 2.16. Apparent resistivity pseudosections of a rectangular block model from 2-D imaging surveys with different electrode arrays (Loke 1999).

ER testing has an extensive history for use in evaluating karst (Early and Dyer 1964; Fretwell and Stewart 1981; Zhou et al. 2000; Šumanovac and Weisser 2001; Roth et al. 2002; Van Schoor 2002; Roth and Nyquist 2003; Nyquist et al. 2007; Mitrofan et al. 2008; Park et al. 2009; Zhu et al. 2011; Ismail and Anderson 2012; Carriere et al. 2013; Park et al. 2014; Majzoub et al. 2017; Torrese 2020). Typically, use of ER to delineate potential karst features depends on the nature of the anticipated conditions at the site, which can complicate interpretation. For example, karst features can be predominantly air-filled and therefore highly resistive (e.g., >1000 Ω·m). Alternatively, if the karst feature is partially/completely water-filled or contains highly weathered soils, it may range from very conductive (e.g., 60–100 Ω·m) to relatively conductive (e.g., 100–250 Ω·m) compared to the host rock (Figure 2.17). Therefore, some basic a-priori knowledge regarding the geologic conditions can be quite useful for interpreting inverted resistivity cross sections. One (1) major limitation is the presence of conductors at the site that contact the ground. For example, buried utilities or chain-linked fences will act as current sinks due to their low resistivity. Consequently, current will preferentially flow along these structures rather than flowing through the nearby geologic material. This is particularly problematic in urbanized locations where such current sinks

may be unavoidable and/or concealed. Nevertheless, given its extensive history as a geophysical tool in karst environments, ER testing is a popular approach for evaluating sinkhole hazards.

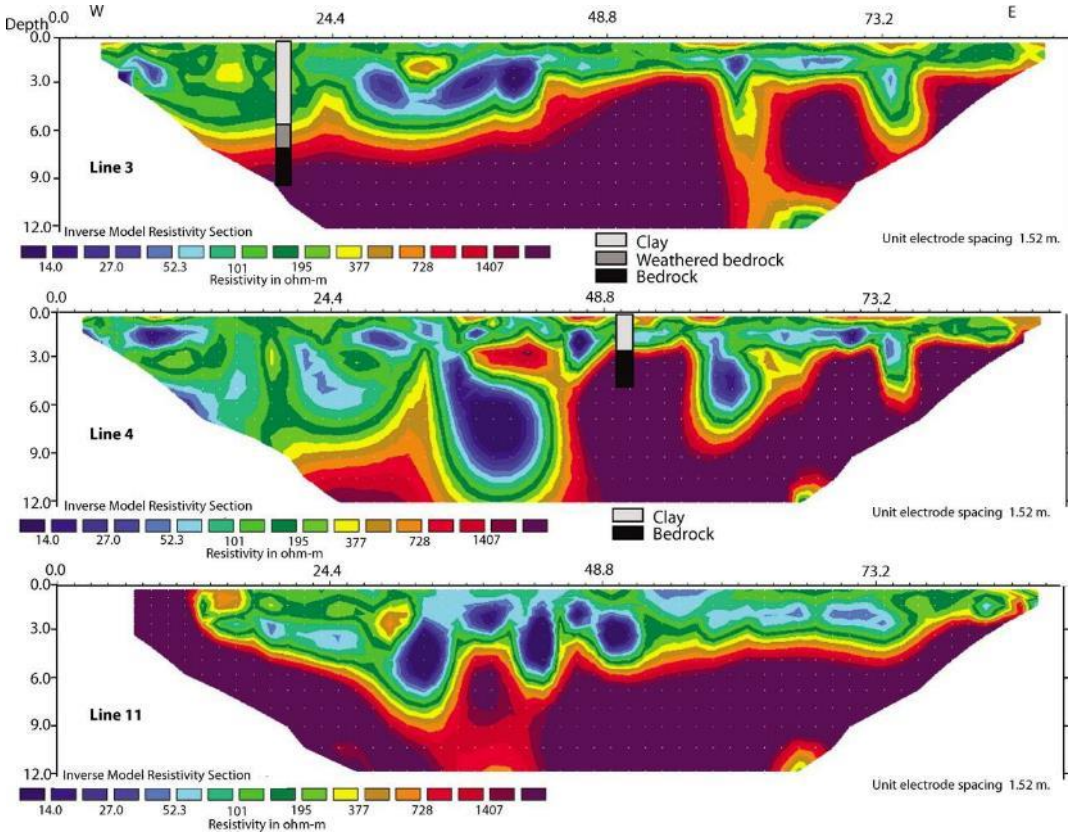

Figure 2.17. Example resistivity lines over karst (ρ < 105 Ω -m) superposed with post-ERT survey borings (Ismail and Anderson 2012).

2.2.2.2.*Ground Penetrating Radar (GPR)*

The use of Ground Penetrating Radar (GPR) technology in near surface ground investigations has increased dramatically over the last 30 years (Jol 2009; Utsi 2017). GPR has been used in a wide range of applications, examples of which include aquifer characterization and hydrogeology (Beres and Haeni 1991), agriculture (Huismann et al. 2003), archaeological investigations (Vaughan 1986), geotechnical investigations (Benedetto et al. 2012), subsurface utility mapping (Eide and Hjelmstad 2002), roadway evaluations (Saarenketo and Scullion 2000), railways (Olhoeft et al. 2004), and nondestructive testing of concrete (Maierhofer 2003). The passage of radar signals through a material is governed by the physical principles of electromagnetic (EM) wave propagation, which includes alternating electrical and magnetic fields that propagate out from an oscillating electrical charge. There are several types of EM spectrum covering different EM waves based on their frequency. Starting from lowest frequency (longest wavelength) and listing to highest frequency, the EM spectrum is as follows: radio waves, microwaves, infrared, visible light, ultraviolet, X-rays, and gamma rays. In GPR applications, EM radiation in the microwave spectrum (i.e., 300 MHz - 300 GHz) is used. The exploration depth and anticipated sizes of buried features determine the

specific antenna frequency to be selected for GPR testing. Generally, higher frequency antennas have shallower depth of penetration, but better spatial resolution (Jol 2009). A GPR system is typically comprised of a signal generator, one or more transmitting and receiving antennae, and a control unit for managing the signal generation and recording (Figure 2.18).

The response of a material to an EM wave is primarily a function of its dielectric permittivity (ε) and magnetic permeability (μ). The relative magnetic permeability (μ_r), which is the ratio of μ to the magnetic permeability of free space ($\mu_o = 4\pi \times 10^{-7}$ N·A^{-2}) is considered one for non-magnetic materials, which makes the dielectric permittivity the main physical property of interest. Dielectric permittivity is a diagnostic physical property which characterizes the degree of electrical polarization a material can store under the influence of an external EM field. It is typically defined as a dimensionless ratio with respect to the permittivity of vacuum (e.g., ε_r for water and air are 80 and 1, respectively). Despite representing a relative value, the term "permittivity" often refers directly to ε_r. Another commonly used term for ε_r is the "dielectric constant". The propagation velocity of a GPR signal is subsequently related to these factors by the relationship shown below:

$$v = \frac{c}{\sqrt{\mu_r \varepsilon_r}} \tag{2.5}$$

where v is the velocity of the GPR wave and c is the velocity of light in free space (300,000 km/s). When a transmitted GPR signal strikes an object with different ε_r, the wave is reflected and reradiated in many directions (Figure 2.19). Any reflected portion of the signal is recovered by the receiver antenna, where it is processed to determine the location of the reflector. As radar waves travel at high speeds (in air, 300,000 km/s), the travel time from the instant of transmission to any subsequent reflected signals at the receiving antenna (Rx) is on the order of a few tens to several thousand nanoseconds (10^{-9} seconds).

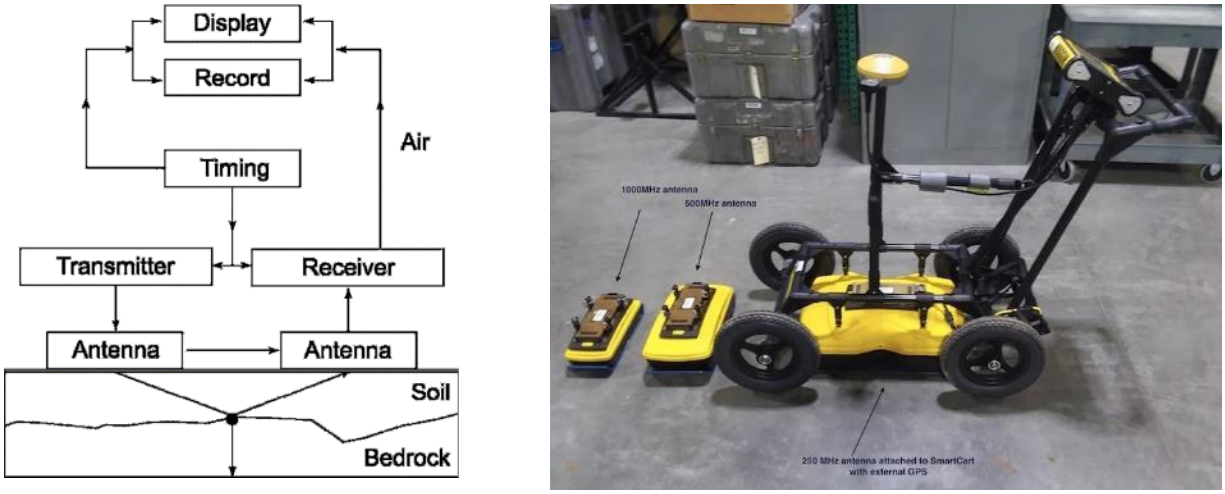

Figure 2.18. GPR systems: (a) schematic/block diagram; and (b) equipment (photo courtesy of IRIS PASSCAL Instrument Center, New Mexico Institute of Mining and Technology https://www.passcal.nmt.edu/).

The most common approach to interpret the acquired radar data is to plot the received signals as the GPR antenna is dragged along the ground surface and create what is referred to as a radargram (Figure 2.19). In this manner, reflections signals line up to form a visual representation of any anomalous conditions below the surface (e.g., shifts in layering, presence of voids, buried objects, etc.). Since GPR systems often pulse at rates between eight (8) to 100 times per second, the lateral sampling interval as the antenna is slowly dragged across the site can be on the order of cm, which is one of the highest lateral resolutions of the geophysical methods. However, when two (2) adjacent materials with similar dielectric constants are present, there may be very little reflection of the EM wave and identification of material boundaries subsequently becomes difficult (Evans 2010).

There is a significant number of published articles that demonstrate the efficient application of the GPR method to sinkhole characterization (e.g., Witten and Calvert 1999; Batayneh et al. 2002; Zisman et al. 2005; Dobecki and Upchurch 2006; Martín-Crespo and Gomez-Ortiz 2007; Carbonel et al. 2014; Rodriguez et al. 2014; Anchuela et al. 2015; Caselle et al. 2020) (Figure 2.20). However, one (1) major issue that can negatively affect the success of GPR for evaluating karst is the nature of the geologic materials present on site. Some materials, such as polar ice, are virtually "transparent" to radar waves, meaning that very little absorption takes place, and the waves can transmit significantly long distances. Other materials, such as saturated clays are highly conductive objects that can reduce the effective penetration depth of a radar wave. Carbonate rock often weathers into clayey soils, rendering the site ineffective for transmitting radar signals significant depths (Hoover 2003). This is further exacerbated by the presence of significant moisture in the clay, particularly if the water is from a saltwater source.

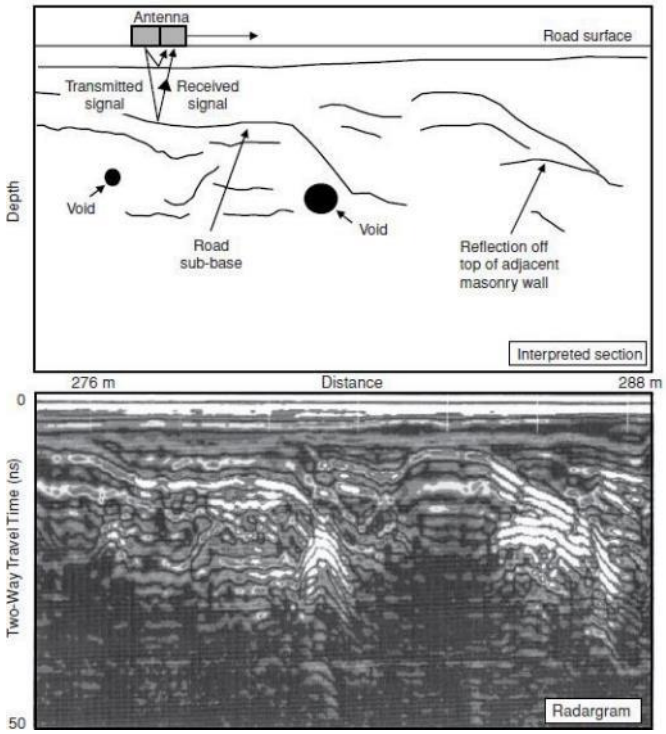

Figure 2.19. Example GPR survey: (a) schematic; and (b) radargram produced by moving the GPR antenna along a profile (Reynolds 2011).

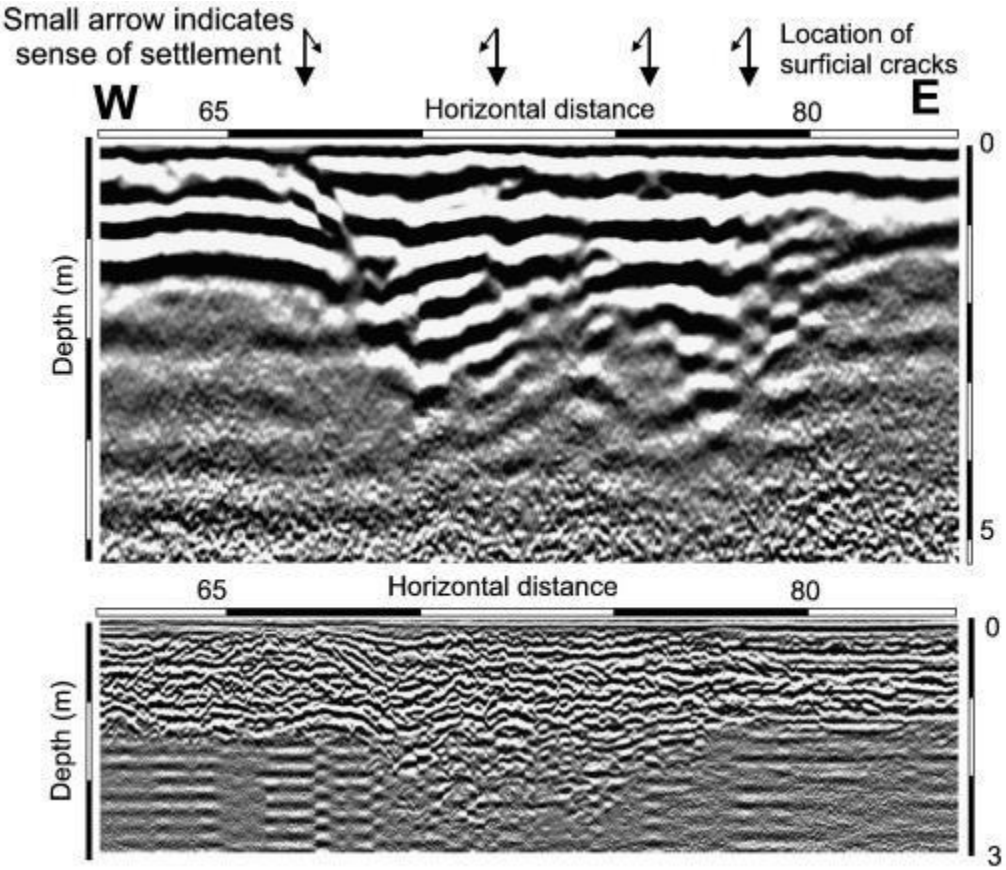

Figure 2.20. GPR radargram showing a collapse geometry (Anchuela et al. 2015).

2.2.2.3.*Electromagnetic Induction (EMI)*

Electromagnetic Induction (EMI) (also known as "terrain conductivity") instruments have had a relatively shorter history as a geophysical tool, having been developed in the 1970s (e.g., Cameron et al. 1981; Stewart 1982; McNeill 1990; Kachanoski, et al. 1998; Ahmed and Carpenter 2003; Jardani et al. 2007; Corwin 2008; Doolittle and Brevik 2014). Nevertheless, EMI applications and methods were refined and expanded in the 1980s and are quite popular, particularly given their integration with modern global positioning systems (GPS) and cost effectiveness from rapid surveying (Hoover 2003). EMI surveys measure the subsurface conductivity, which is the inverse of the resistivity measured by the ER method. Therefore, much of the fundamental background information regarding electrical theory applies to EMI testing. EMI sensors transmit a primary electromagnetic field, which induces electrical currents in the subsurface. The secondary electromagnetic field developed by these electrical currents are subsequently measured by the EMI receiver to calculate the apparent electrical conductivity (σ_a) for the volume of soil profiled.

Unlike ER methods, EM acquires data without the need to place sensors directly on the ground. Instead, the measurements are typically obtained by hand while traversing the site, though recent systems have

been integrated into a mobile EMI platform (Figure 2.21). This reduces the costs of data acquisition, both from a manpower and time perspective. For example, using a typical data collection rate of once per second, several miles of data can be collected with a hand-held EMI meter carried by an operator (Hoover 2003). Airborne EMI testing increases this efficiency in data collection by orders of magnitude (e.g., Sørensen and Auken 2004; Reninger et al. 2014). EMI meters contain both a transmitter and receiver coil with a fixed distance between them. Depth of investigation and vertical resolution are dependent on the operating frequency of the sensor, the conductivity of the underlying geologic material, the distance between the transmitter and receiver, and their orientation (i.e., horizontal versus vertical) (Hoover 2003; Corwin 2008). Depths of several tens of meters are possible (Pérez-Flores et al. 2012). Integration with GPS equipment allows highly accurate tracking of the location of EMI measurements across a site.

The results of an EMI survey are typically presented in map form, with a qualitative interpretation of the measured σ_a (Figure 2.22). Highly conductive σ_a values can be interpreted as thick soils and low σ_a values can be interpreted as shallow bedrock. However, as with ER, EMI measurements can be input into an inversion algorithm that allows a 2D or 3D image of subsurface conductivity to be estimated (e.g., Santos et al. 2010; Triantafilis and Monteiro Santos 2013) (Figure 2.22). As with ER, the presence of nearby utilities, fences, and other metallic objects can create interference with the EMI signals, limiting the use of this method in urban settings (Hoover 2003).

Figure 2.21. Examples of terrain conductivity meters: (a) hand-held units; and (b) mobile towed systems (Corwin 2008).

EMI testing has been used less often than ER for karst despite their similar theoretical basis (Pin, and Ketelle 1983; Doolittle and Collins 1998; Nyquist et al. 1999; Ahmed and Carpenter 2003; Bosch and Müller 2005; Jardani et al. 2007; Mundell and Hebert 2010; Reninger et al. 2014). This can be attributed primarily to the much more recent development of EMI equipment. As with ER, the delineation of potential karst features can be complicated by the type of feature and whether any voids contain air, water, and/or weathered residual soils. Given the rapid data acquisition, qualitative maps of σ_a as in Figure 2.23 can be

used over large spatial areas to identify potential anomalous regions in karst settings. In this context, EMI can serve as a guide to where borings/soundings and/or additional geophysical testing can be performed to further identify evidence of sinkholes.

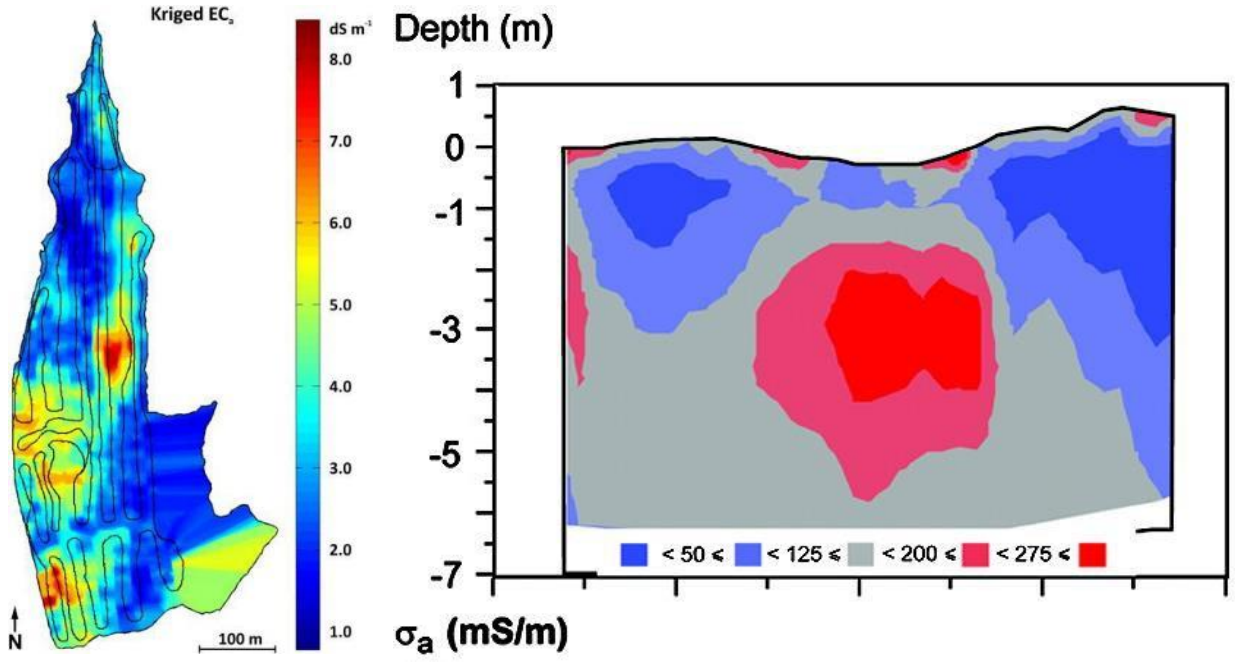

(a) (b)

Figure 2.22. Examples of EMI results: (a) qualitative mapping (Nearing et al. 2013); and (b) inverted 2D profile (Triantafilis et al. 2012).

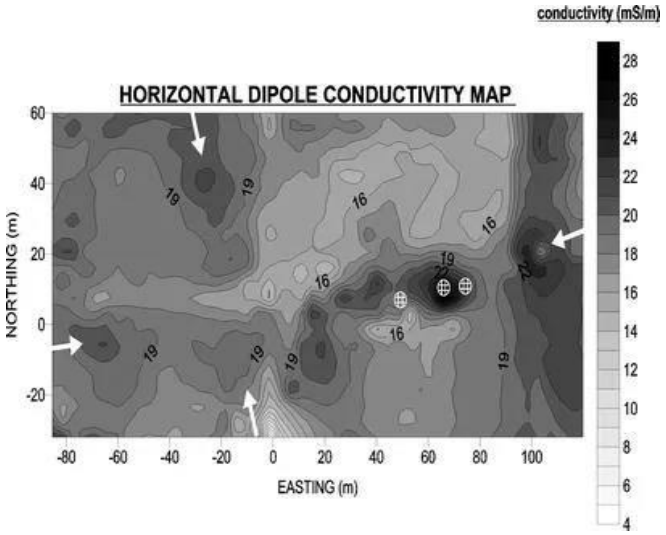

Figure 2.23. Apparent ground conductivity measurements highlighting the presence of filled sinkholes (cross-hatched white circles) (Ahmed and Carpenter 2003).

2.2.2.4.*Gravity Method*

Gravity methods measure the gravitational forces associated with an object and provide an estimate of mass density. Such methods have an extensive history within the geophysical community and have been used over a wide range of scales and purposes such as mining, oil exploration, and exploration of celestial bodies (e.g., Evjen 1936; Heiland 1943; Arzi 1975; Fountain et al. 1975; Neumann 1977; Butler 1980; Butler 1984). Nabighian et al. (2005) provides an extensive account of the historical development of gravity measurements for geophysical purposes. For engineering applications, the gravity method is typically performed at a much more localized scale (i.e., microgravity surveys) to locate subsurface features such as voids, fracture zones, changes in depth to bedrock and fill thickness, buried stream valleys, and water table levels (Hall and Hajnal 1962; Eaton et al. 1965; Domenico 1967; Wolters 1973; Arzi 1975; Fajklewicz 1976; Carmichael and Henry 1977; Butler 1984; Wang et al. 1986; Benson and Baer 1989; Pan 1989; Roberts et al. 1990; Tønnesen 1995; Benson and Floyd 2000; Hayashi et al. 2005; Davis et al. 2008; Pajot et al. 2008; Erkan et al. 2012; Mankhemthong et al. 2012).

Generally, the gravity method relies on instrumentation known as gravimeters to measure small changes in the gravitational field at the Earth's surface (Figure 2.24). For engineering applications, the typical gravity measurements range on the order of 10 - 1000 µGal (hence the use of the microgravity term), where 1 Gal is equal to 1 cm/s^2 (Butler 2007). Such small acceleration measurements were not achieved until the 1960's and 1970's, which is when microgravity surveys began to see increased usage for engineering applications (Butler 1980; Nabighian et al. 2005). Most microgravity surveys are performed with relative gravimeters that measure the difference in gravity between measurement locations. Absolute gravity instruments exist that attempt to measure the total gravitational field at a particular location, but they are more expensive, physically larger, require longer acquisition times, and are generally less user-friendly compared to relative gravity instruments (Nabighian et al. 2005).

Figure 2.24. CG-6 Autograv^{TM} relative gravimeter (courtesy of Scintrex Limited; https://scintrexltd.com/).

The gravity changes measured by gravimeters are directly dependent on five (5) factors: latitude, elevation, topography, tidal changes, and density variations (Telford et al. 1990). The density variations are of most interest in engineering applications, but they are small in relation to fluctuations that result from the other factors. Consequently, the acquired data must be post- processed to remove the effects of latitude, elevation and topographical changes, and temporal tidal fluctuations and field operations must be performed in a manner that minimizes the influence of these factors (e.g., Neumann 1977; Butler 1980; Hinze 1990; Telford et al. 1990; Mickus 2003). This results in a spatial distribution map of residual gravity measurements corresponding to any anomalous subsurface features (Figure 2.25). For example, negative residual gravity measurements typically correspond to potential cavities (Styles et al. 2005). This map can typically be used in conjunction with other subsurface investigation techniques to provide a qualitative assessment of subsurface conditions based on changes in gravity. Alternatively, more detailed analysis can be performed with inversion algorithms to better quantify the geometry of subsurface features causing the gravity variations (e.g., Li and Oldenburg 1998) (Figure 2.25).

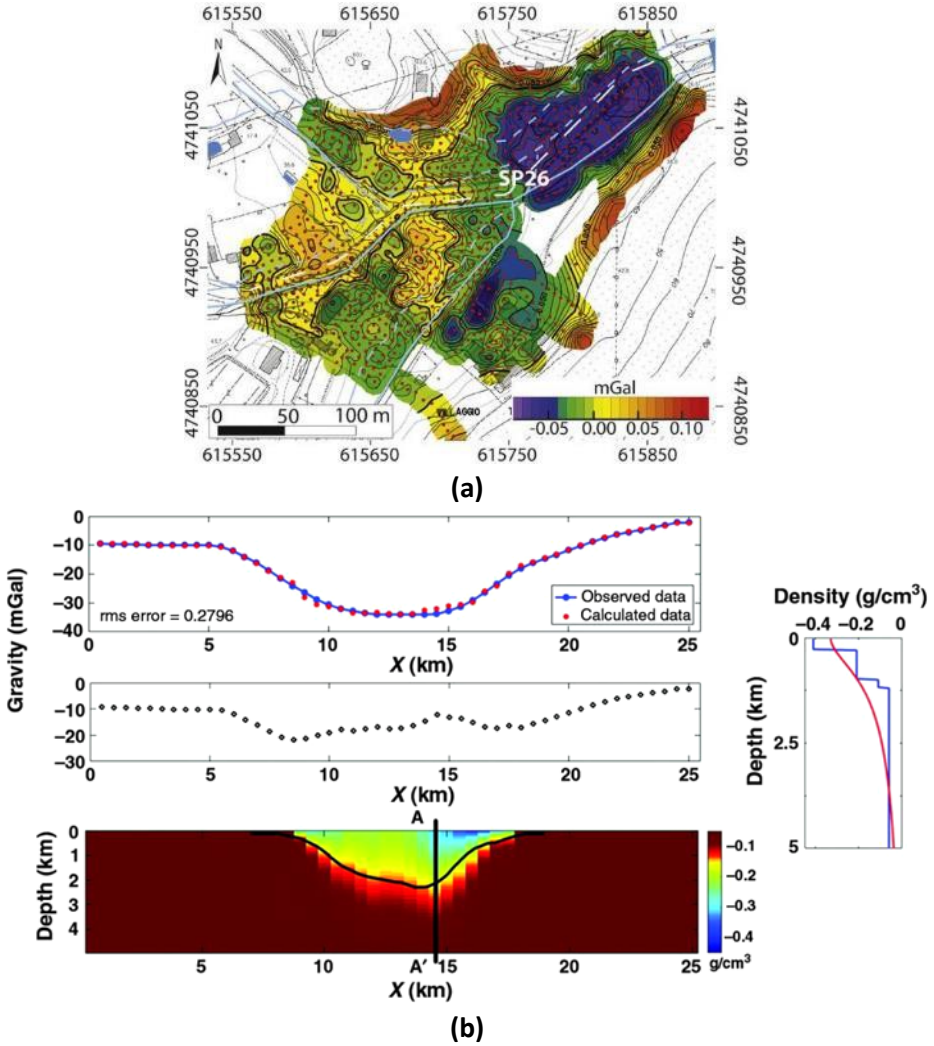

Figure 2.25. Examples of gravity survey results: (a) spatial mapping (Pazzi et al. 2018); and (b) inverted cross section (Vitale et al. 2018).

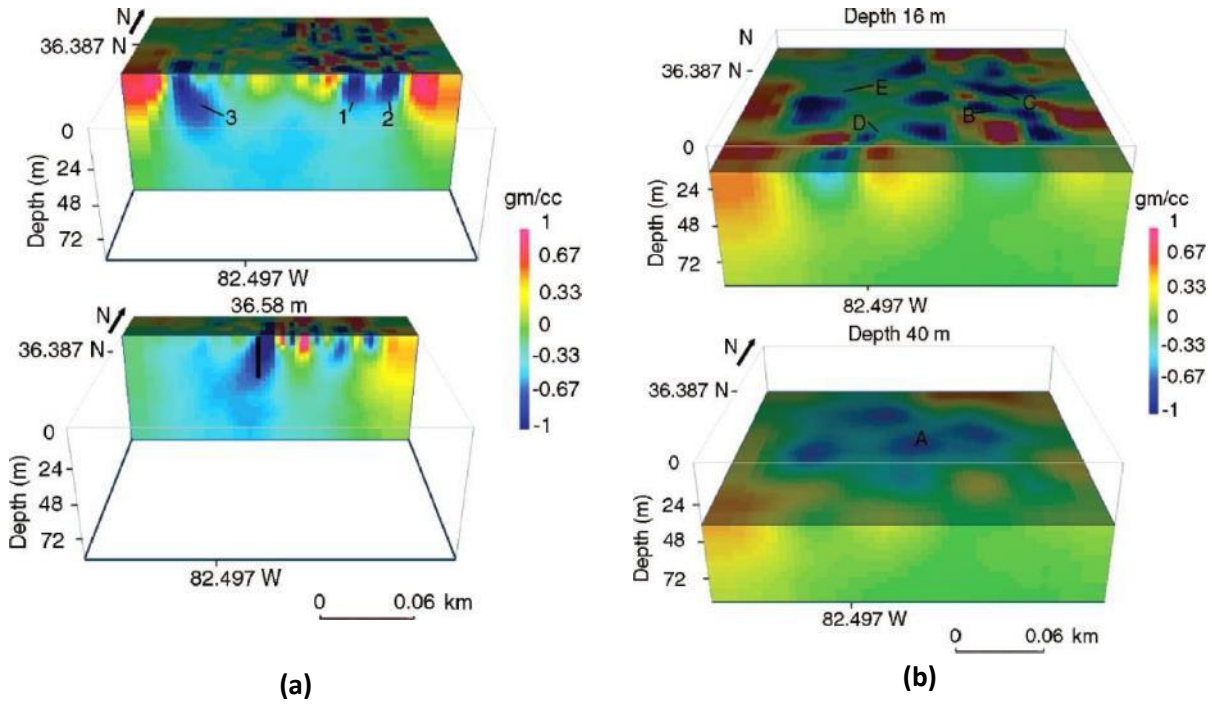

Figure 2.26. Microgravity evaluation of sinkholes at the Gray Fossil Site in Washington County, Tennessee (Whitelaw et al. 2008).

One of the most common engineering applications of microgravity surveys is to evaluate the presence of subsurface cavities such as tunnels, sinkholes, and other karst topography (Butler 1984; Wenjin and Jiajian 1990; Camacho et al. 1994; Yule et al. 1998; Beres et al. 2001; Benson et al. 2003; Styles et al. 2005; Mochales et al. 2008; Tuckwell et al. 2008; Whitelaw et al. 2008; Orfanos and Apostolopoulos 2011; Paine et al. 2012; Pazzi et al. 2018). Figure 2.26 highlights an example where microgravity surveys were used to estimate the geometry of sinkhole features at a karst site in Tennessee. Given the quality of the results highlighted in Figure 2.26, the portability of relative gravimeters, and the relative simplicity and speed of data acquisition, it is not surprising that the gravity method is often used to evaluate karst. However, there are some challenges when applying this method. Most of the data acquisition effort is spent attempting to minimize the issues associated with "noise" sources given the very small changes in gravity being measured. For example, the gravimeter registers different readings over time due to mechanical, thermal, and electrical changes in the instrument itself. This is referred to as equipment drift and it can be of sufficient magnitude as to conceal the changes in gravity caused by subsurface geologic features. Tidal variations in gravity over the course of the survey can also be larger than the changes in gravity caused by the subsurface. Additionally, a high precision survey is necessary at the site to accurately determining gravimeter station locations and elevations. High spatial density is required for the gravimeter stations as are repeated measurements to account for tidal changes and equipment drift. The gravity method is less affected by highly conductive clay-rich soils often present in solutioned carbonate rock environments when compared to ER and/or EMI. However, there is some ambiguity regarding the interpretation of gravity

measurements that may necessitate additional a- priori information. For example, a gravity anomaly from a distribution of small voids at a shallow depth can produce the same effect as a large void at larger depths. Nevertheless, gravity surveys remain a useful tool for karst evaluation as evidenced by their extensive presence in the literature.

2.2.2.5.*Seismic Methods*

Several methods rely on interpreting the subsurface based on the propagation of seismic waves. Seismic wave propagation produces mechanical strains that propagate at a velocity that is dependent on the material's elastic moduli and density. There are two (2) general types of seismic waves: 1) body waves; and 2) surface waves. Body waves travel through the interior of the domain while surface waves are propagated along the surface. Particle motion is parallel to the direction of the wave propagation in Primary waves (P-waves) and perpendicular for Secondary waves (S-waves) (Figure 2.27). The main types of surface waves commonly encountered in engineering contexts are Rayleigh and Love waves. Rayleigh waves move elliptically, and Love waves move similarly to S-waves with particle motion perpendicular to the direction of wave propagation. Both body and surface waves can be measured using an array of surface sensors such as geophones or accelerometers that are typically spiked into the ground (Figure 2.28). The acquired waveforms are used to determine elastic parameters of the materials through which they propagate. Seismic methods have long been used for mapping lithology as related to exploration for hydrocarbons (e.g., see history of seismic techniques in Sheriff and Geldart 1995). However, seismic methods have also been one of the most used geophysical tests for engineering applications due to the dependency of seismic wave propagation on stiffness, which is an important engineering parameter (Wightman et al. 2003). These methods are typically utilized to map and delineate strata, top of bedrock, faults/fractures, and voids/tunnels, as well as to measure elastic moduli for earthquake engineering or rock rippability purposes (e.g., Redpath 1973; Hawkins and Whiteley 1979; Granger 1990; Harrison and Hiltunen 2003; Hayashi et al. 2005; Hiltunen and Cramer 2008; Pérez-Santisteban et al. 2011; Parker, Jr and Hawman 2012; Galibert et al. 2014; Wood et al. 2017). The elastic moduli can also be correlated to other earth material properties for engineering design (e.g., Coe et al. 2018).

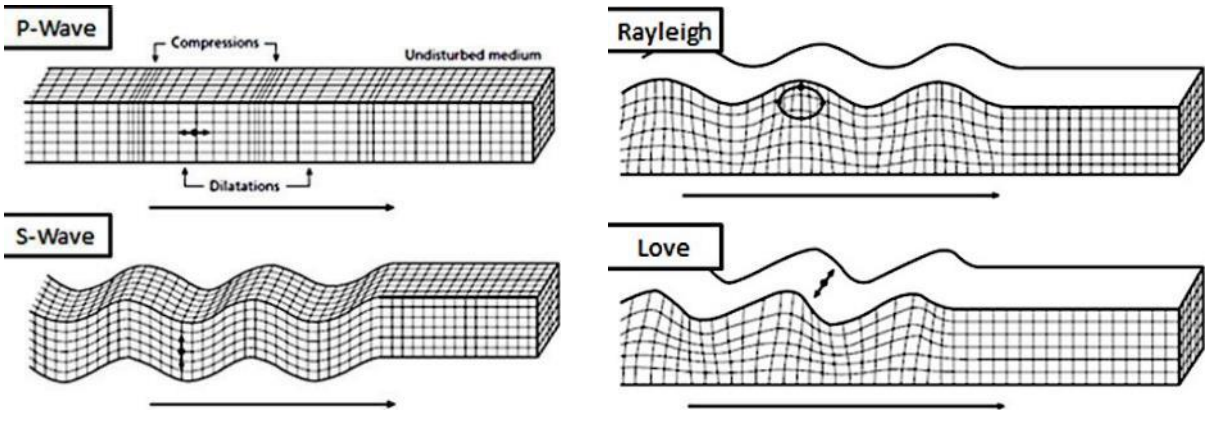

Figure 2.27. Elastic deformations and ground particle motions associated with seismic waves: (a) body waves; and (b) surface waves (Bolt 1982).

(a)

(b)

Figure 2.28. Seismic data acquisition: (a) surface geophones (courtesy of RT Clark, https://www.rtclark.com/); and (b) typical field survey (Yong et al. 2013).

Seismic methods are generally robust methods that can sample significantly large depths (e.g., hundreds of meters) depending on test method and site conditions. They are very useful when attempting to acquire information about geologic materials that are particularly hard to sample using traditional geotechnical techniques (e.g., Carr et al. 1998). Active methods generate seismic waves using various sources. Sledgehammers are the most common seismic sources, though air guns, explosives, mass shakers, accelerated weight drops (AWD), and vibroseis vehicles have also been used depending on the site conditions and particular needs of the survey. Passive methods rely on measurements of ambient seismic activity from background sources such as vehicular traffic, ocean tidal activity, and construction noise.

The most common surface-based seismic geophysical methods in geotechnical engineering include Seismic Reflection, Seismic Refraction, Spectral Analysis of Surface Waves (SASW), Multichannel Analysis of Surface Waves (MASW), and passive methods such as passive MASW, Microtremor Survey Method (MSM), Refraction Microtremor (ReMi), and the Horizontal-to- Vertical Spectral Ratio (HVSR). These methods differ primarily by which sets of wave types are analyzed (e.g., refracted body waves versus surface waves) and the way they are post- processed. However, despite some general differences between these methods (to be discussed in the following sections), all seismic methods suffer from similar limitations related to data post- processing and interpretation. First, the seismic waves propagating

through the site may interact in a complex manner such that it is difficult or impossible to separate the effects of the different wave types. In the case of active surveys, background seismic noise can result in poor signal-to-noise ratio and limited investigation depth. Vertical resolution suffers at larger depths since the source is located at the surface. The depth of investigation is also directly related to the length of the seismic survey. Deployment of a sufficiently long survey may prove problematic depending on the site conditions. Given these limitations and the similarity in data acquisition between the different seismic methods, it is advisable to acquire supplementary information by performing multiple seismic tests at a site to better constrain results.

The following sections provide additional information about the more commonly used seismic methods for karst investigations, including Seismic Reflection/Refraction and surface wave testing. The focus is on providing the analytical background necessary to understand how these methods are used to evaluate karst.

2.2.2.5.1 Seismic Reflection and Refraction

The seismic refraction technique relies on the selection of first arrivals of the waveforms recorded at the surface array of sensors. Generally, seismic waves radiate from an active source in a spherical manner. Depending on the polarization of the seismic source, either P-waves (vertical source) or S-waves (horizontal source) are generated. When these waves reach a subsurface interface separating media of different stiffnesses, the incident ray transforms into several new rays, including a reflected wave that bounces back towards sensors on the surface and a refracted wave that continues propagating further past the boundary (Figure 2.29). This behavior is described by Snell's Law, which states that for any ray striking an interface, the ratio of the sine of the angle of incidence to the velocity of propagation (i.e., the ray path parameter) within that medium remains a constant. Consequently, there are three (3) main pathways for body waves as they propagate through a domain (Figure 2.30):

- Direct waves which propagate along the near surface of the top layer
- Reflected waves that bounce off the boundaries between layers
- Refracted waves that bend and travel along the boundaries between layers

Refracted rays occur when the difference in stiffness between the two (2) layers is such that the refracted angle (θ_2 in Figure 2.29) equals the critical angle of 90 degrees. The critically refracted wave propagates along the interface of the boundary between the two (2) layers at the larger velocity. As this wave propagates, it becomes a source for the generation of additional body waves that then travel back up to the sensors on the ground surface (Figure 2.30).

The first arrival times of the received waveforms are selected and plotted as a function of offset distance along the survey (Figure 2.31). Initially, the first arrivals are from direct waves that propagate along the top layer. However, after the crossover distance (x_c) the critically refracted waves catch up to the direct wave and begin to arrive sooner due to propagating with a higher velocity component. In the simple case of a two-layer system, the time-distance graph can be interpreted to solve for the velocity of each layer

by taking the inverse of the time-distance slopes before and after the cross over point. Using the geometry of the ray paths and Snell's Law, the depth (h) to the layer interface can then be solved for based on the following expression:

$$h = \frac{1}{2}\frac{t_1 V_1 V_2}{\sqrt{V_2^2 - V_1^2}} \tag{2.6}$$

where V_1 and V_2 are the velocities of the top and bottom layer, respectively, and t_1 is the intercept time, which is extrapolated from time-distance graph in Figure 2.31 and represents the arrival time of the critically refracted waves at an offset equal to zero. Alternatively, the cross-over distance (x_c) can be used in lieu of an offset equal to zero, which avoids having to estimate t_1:

$$h = \frac{x_c}{2}\sqrt{\frac{V_2 - V_1}{V_2 + V_1}} \tag{2.7}$$

Equations 2.6 and 2.7 demonstrate the fact that the seismic-refraction method requires an increase in layer velocity with depth, otherwise a critically refracted wave will not occur nor will the solutions for h be mathematically possible. More complex layering profiles can be interpreted similarly with an increasing amount of complexity in the subsequent solution (e.g., see Redpath 1973 for development of these solutions). Additionally, there are other methods available to interpret the refraction data besides the conventional intercept-time approach, including the plus- minus method (Hagedoorn 1959), the generalized reciprocal method (GRM) (Palmer 1981), and more complicated tomographic techniques that solve an inversion problem based on a gridded model of the subsurface (White 1989). These approaches allow for greater flexibility in the subsurface model, including dipping interfaces, laterally heterogeneous stratigraphy, and extension into three dimensions.

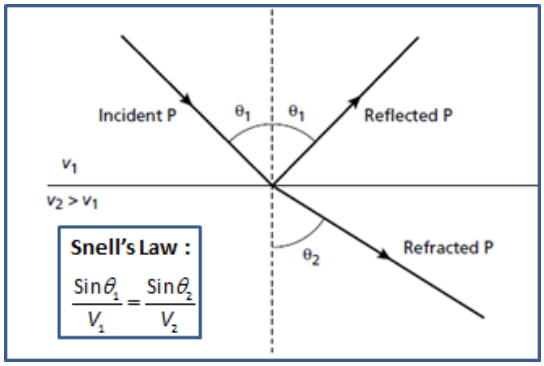

Figure 2.29. Seismic wave behavior at an interface between two layers with different stiffness (i.e., different seismic wave velocities).

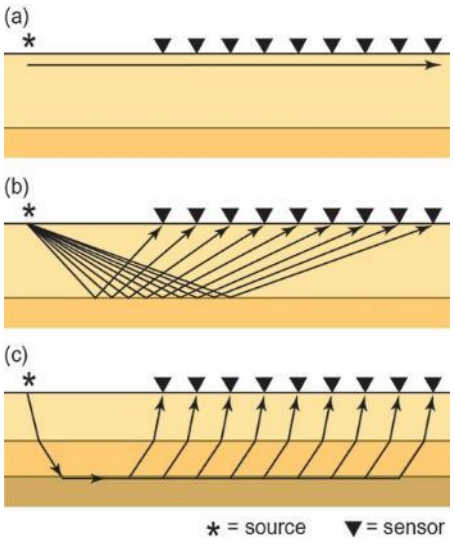

Figure 2.30. Body wave travel paths: (a) direct wave; (b) reflected wave; and (c) refracted wave (Peterie et al. 2014).

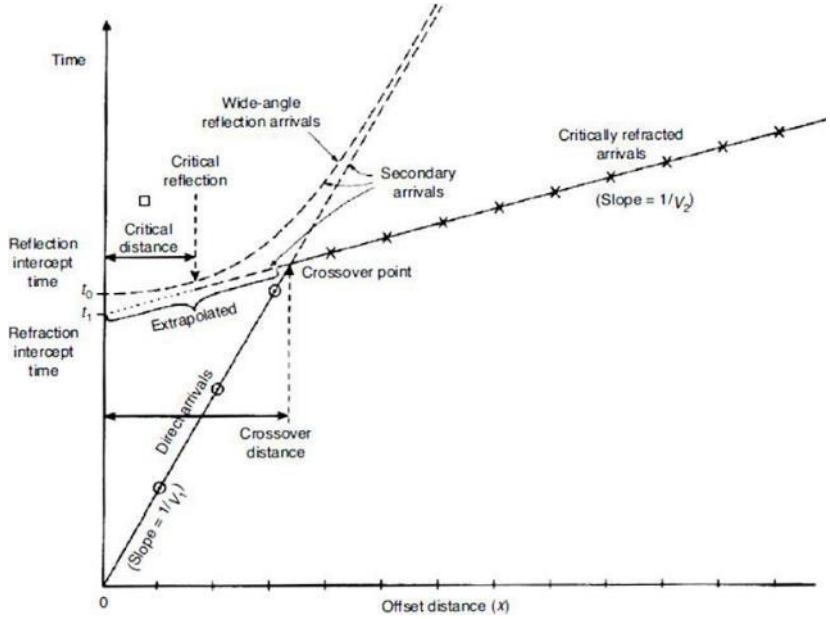

Figure 2.31. Time-distance graph of first arrival signals and interpreted layer velocities from the slopes of the arrival lines (Reynolds 2011).

Seismic reflection relies on interpretation of waves reflected from the boundaries between two (2) materials with different stiffnesses (Figure 2.32). This addresses the major limitation whereby the velocity profile must increase with depth to ensure a critically refracted wave can be developed. The path of least arrival time for a reflected wave will be from a point midway between the source and the receiver (called common depth point with a flat reflector) with the angle of incidence on the reflecting layer equal to the angle of reflection from the reflecting layer (Steeples and Miller 1988) (Figure 2.33). For each of the

multiple shots (S_1 - S_4) the reflection points for all ray paths to each of the receivers (D_1 - D_4) are the same. However, the paths traveled by the waves are different and the reflections will not occur at the same times on the recorded signals. This time delay is referred to as normal-moveout and is related to the subsurface velocities. A normal-moveout correction is typically applied to account for this time delay, allowing the summation of all traces to enhance the reflected energy and cancel spurious noise (Kearey et al. 2013). There are multiple data acquisition configurations to acquire reflection data, which controls sampling, post-processing, and accuracy of the recorded data (Figure 2.34). Consequently, a variety of filtering and data post-processing techniques exist (e.g., deconvolution, frequency filtering, migration, etc.) to improve data quality, differentiate between different incident waves, remove noise, and ensure reflection events are accurately represented in the cross section. Though outside the scope of this project, several sources contain a wealth of information regarding these post-processing efforts, including Telford et al. (1990), Baker (1999), and Kearney et al. (2013). The ultimate product of a seismic reflection survey is a corrected cross section (or 3D section) where the reflection events have been resolved to their true subsurface positions (Figure 2.35).

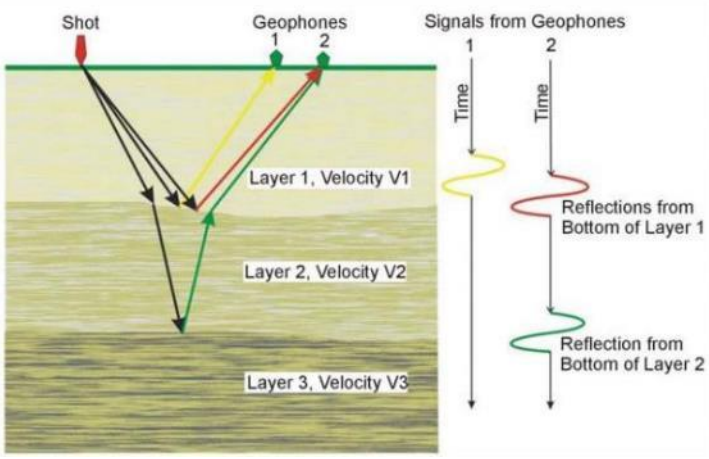

Figure 2.32. Basics of seismic reflection (Wightman et al. 2003).

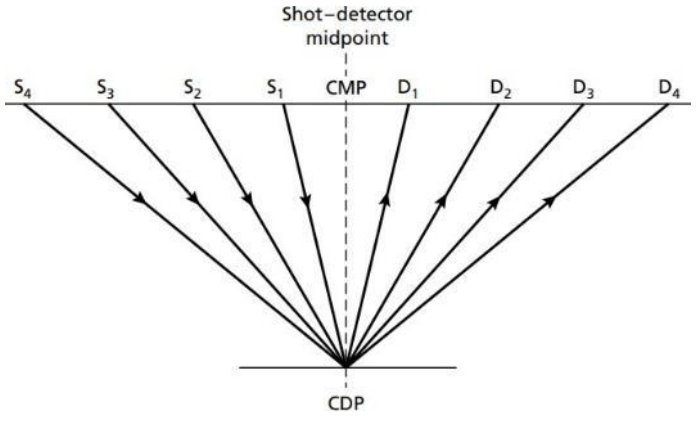

Figure 2.33. Common midpoint (CMP) reflection profiling (Kearey et al. 2013).

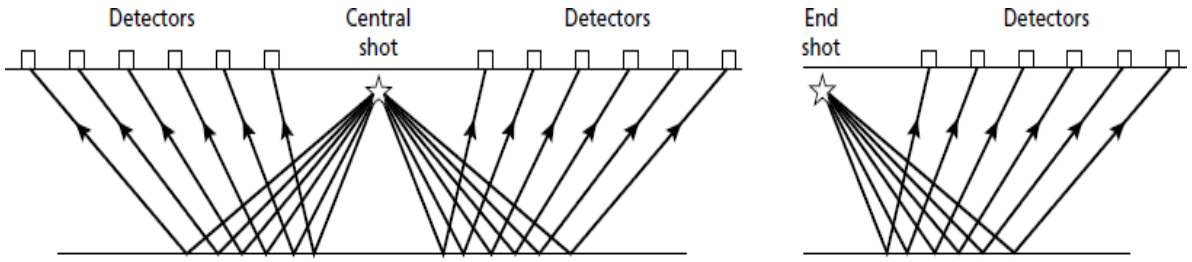

Figure 2.34. Survey configurations used in seismic reflection profiling (Kearey et al. 2013).

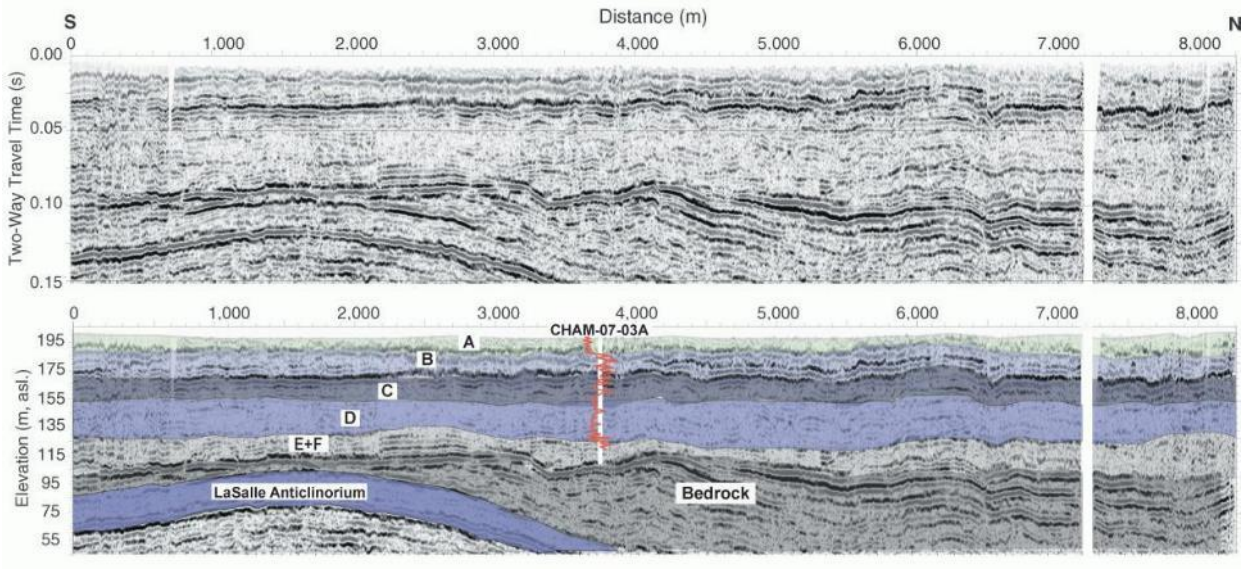

Figure 2.35. Example 2D seismic reflection profile with interpreted geologic units and bedrock topography (courtesy of Illinois State Geological Survey).

Use of both seismic reflection and refracted for karst detection is well documented during at least the last two (2) decades (e.g., Cook 1965; Greenfield 1979; Moore and Stewart 1983; Steeples et al. 1986; Van den Berghe et al. 1986; Evans et al. 1994; Carpenter et al. 1998; Johnston and Carpenter 1998; Šumanovac and Weisser 2001; Grandjean and Leparoux 2004; Miller et al. 2005; Nuzzo et al. 2007; Martínez-Moreno et al. 2014; Burberry et al. 2016). Figure 2.36 provides an example of seismic reflection and refraction profiles developed in karst settings. In both sets of results, the presence of sinkhole features is noted, allowing an estimate of its lateral extent.

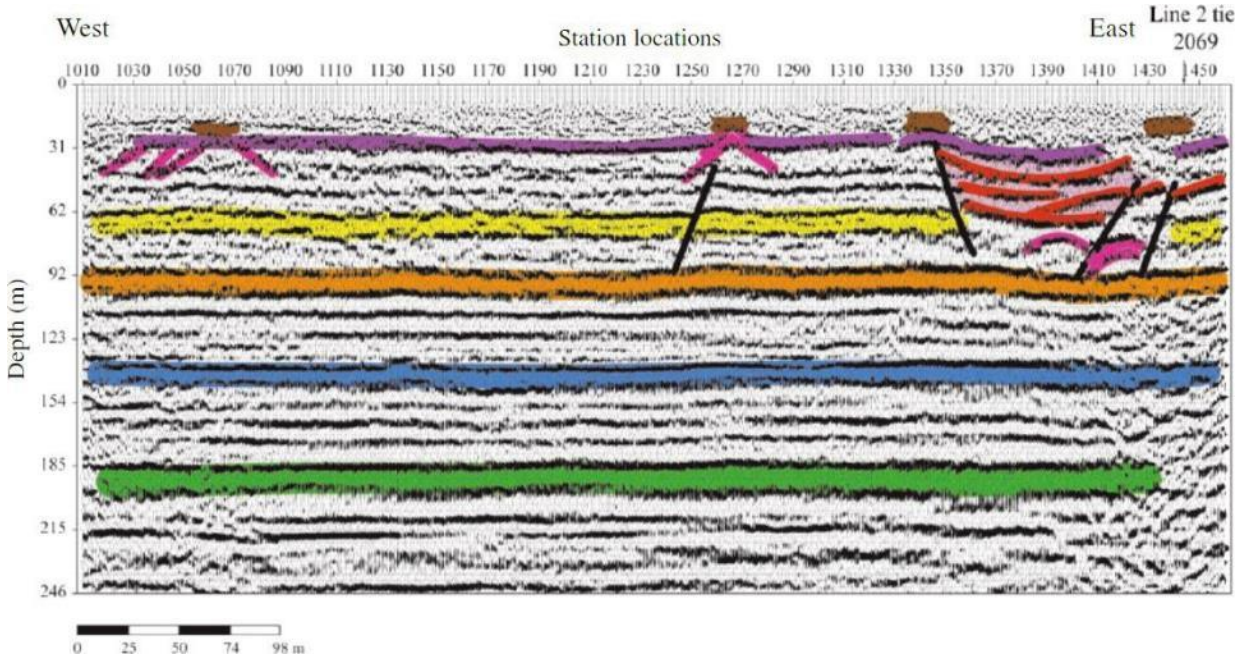

(a)

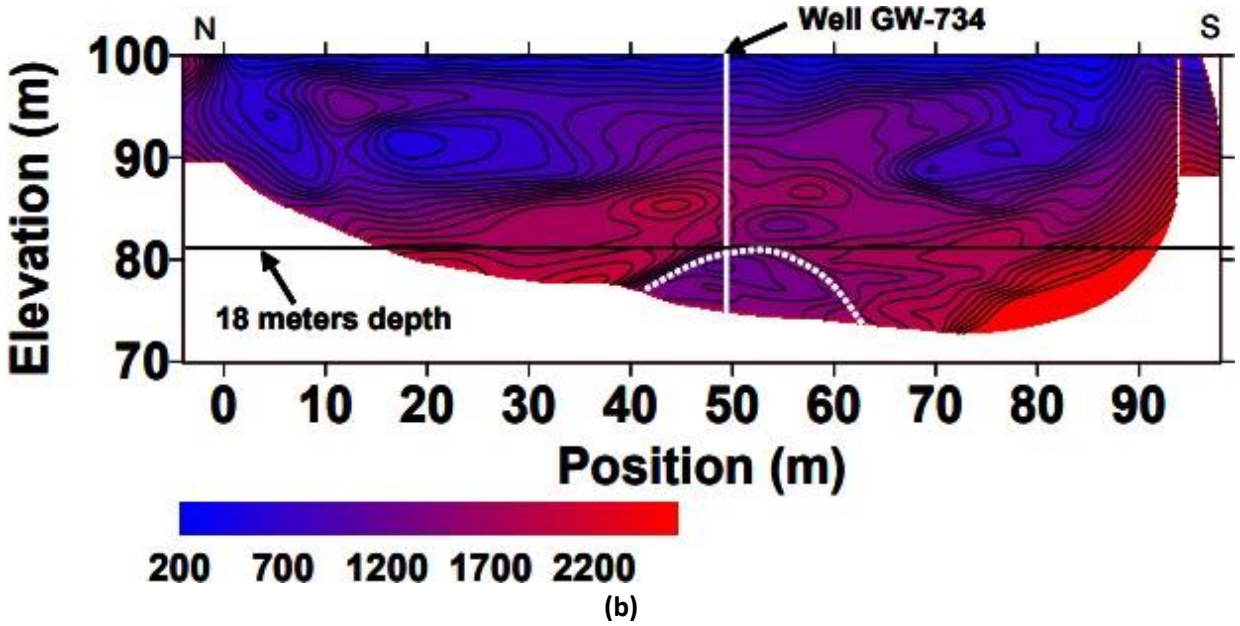

(b)

Figure 2.36. Example 2D seismic profiles in karst: (a) seismic reflection section indicating a subsidence feature between stations 1350 to 1450 (Miller et al. 2005); and (b) seismic refraction tomography section with mud-filled cavity indicated by dashed white lines (Sheehan et al. 2005).

2.2.2.5.2 Multiple Analyses of Surface Waves (MASW)

Surface waves account for more than two thirds of the total seismic energy generated by an impact source (Miller et al. 1955). It is for this reason that surface waves were originally considered as interference and noise to be filtered from the seismic records (Boiero et al. 2013). However, surface waves are larger in amplitude, longer in duration, and attenuate less quickly than body waves, which increases their effectiveness as a geophysical exploration tool. The pioneering work by Van der Pol (1951) and Jones (1955) began to realize the potential offered by harnessing surface waves to evaluate subsurface conditions. These efforts culminated in the development of the Spectral Analysis of Surface Waves (SASW) technique (Heisey et al. 1982) and later the Multichannel Analysis of Surface Waves (MASW) (Park et al. 1999; Xia et al. 1999) technique.

Surface wave propagation is governed by the mechanical properties of the subsurface materials sampled within approximately one wavelength (λ) of depth ($\lambda = V/f$ where V is phase velocity and f the frequency of the wave). Surface waves with greater wavelength will therefore penetrate more deeply into the subsurface (Figure 2.37). This behavior means that different wavelength components of a surface wave will propagate with different velocities (Heisey et al. 1982). This is commonly referred to as "dispersion" and evaluation of the velocity-frequency dependency of input surface waves allows a reconstruction of the subsurface stiffness variation.

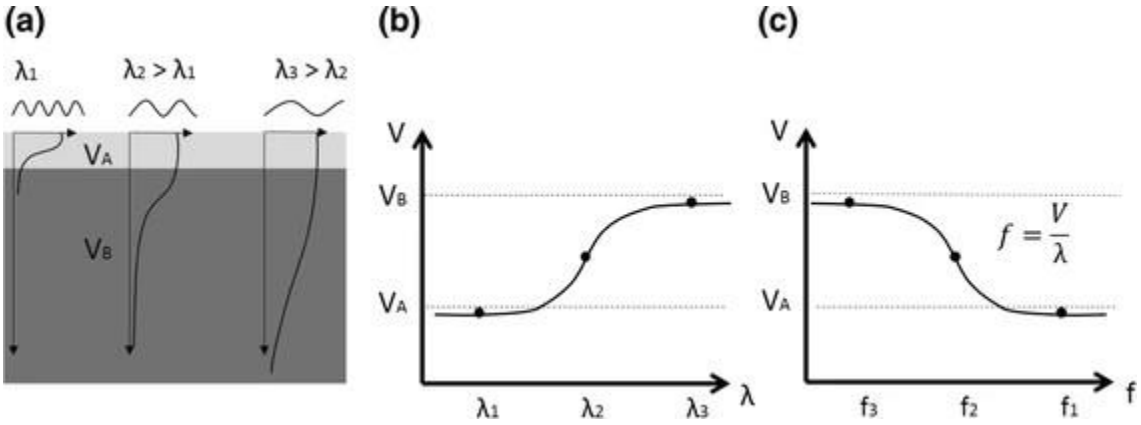

Figure 2.37. Dispersion of surface waves (Foti et al. 2018): (a) different sampling depths based on wavelength; (b) velocity-wavelength variation; and (c) velocity-frequency variation.

The MASW method proceeds by recording surface waves (typically Rayleigh waves generated by vertical impact sources) with a linear array of surface sensors (Figure 2.38). Once the propagation of surface waves is measured experimentally, the recorded waveforms are typically processed to extract dispersion information. Most techniques are transform-based approaches that transform the time-space (t-x) domain into another domain such as frequency-wavenumber (f-k method), frequency-phase velocity (phase-shift method), or frequency-slowness (p-ω method) (McMechan and Yedlin 1981; Gabriels et al. 1987; Park et al. 1998). The corresponding dispersion image is used to identify spectral maxima corresponding to

dispersion trends (Figure 2.39). Common practice uses the fundamental mode (i.e., lowest velocity for a given *f*) dispersion curves to simplify subsequent data processing.

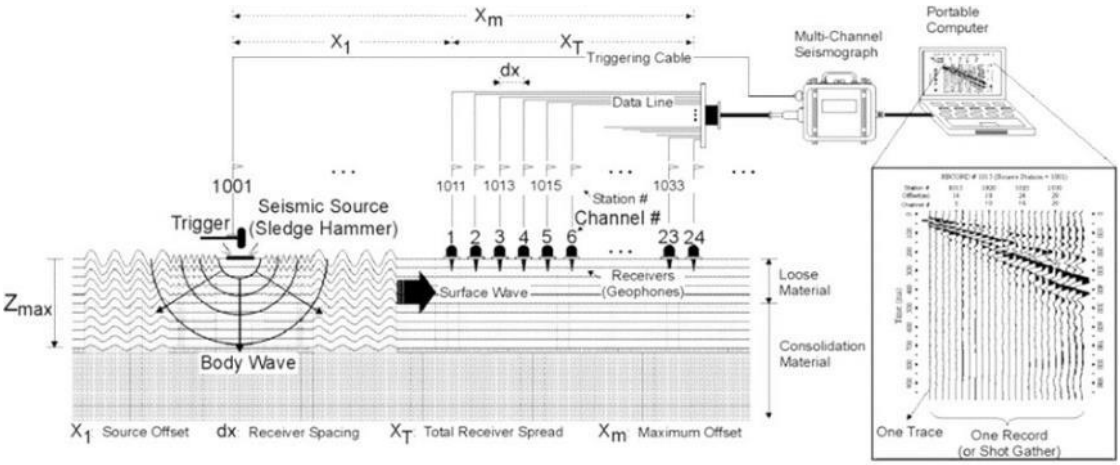

Figure 2.38. Typical active MASW survey schematic (Wightman et al. 2013).

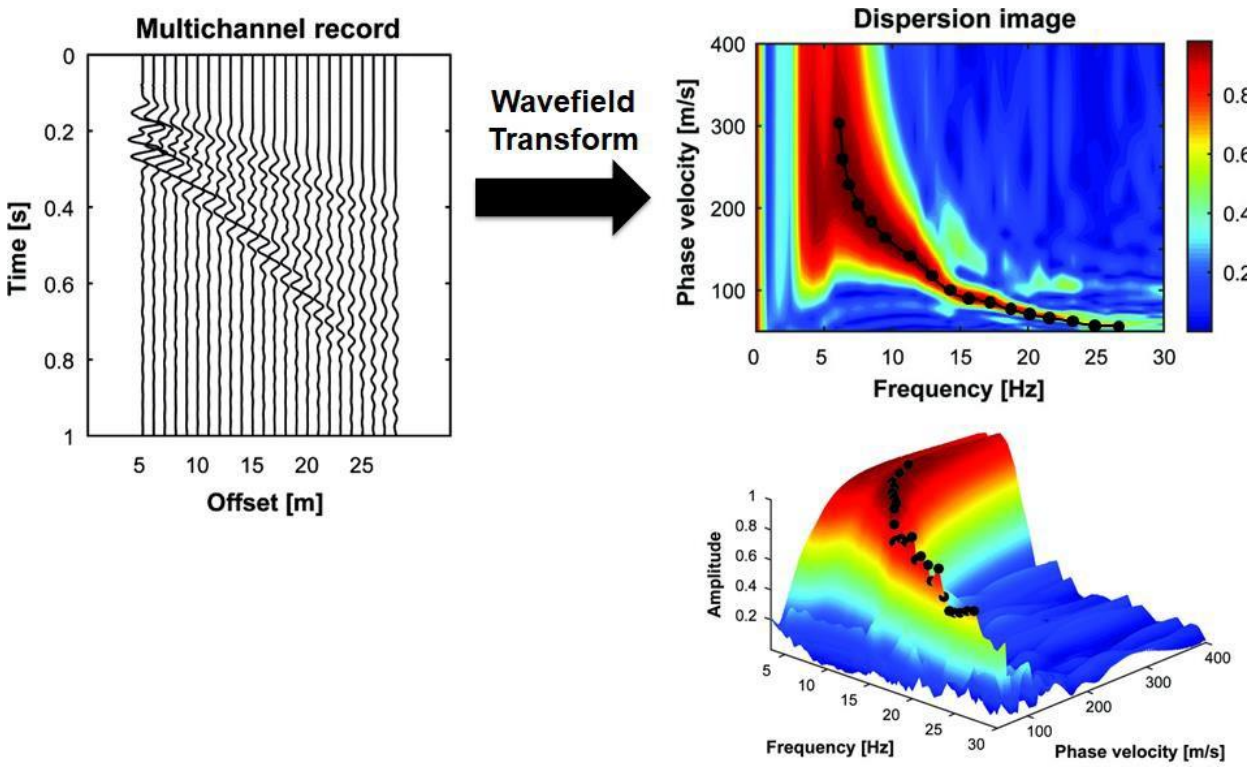

Figure 2.39. Development of dispersion image from a multichannel record and subsequent extraction of a dispersion curve (adapted from Olafsdottir et al. 2018).

The MASW method is comprised of three (3) main steps:

- Field data acquisition
- Dispersion analysis to extract the fundamental mode dispersion curve
- Inversion analysis to find the best theoretical velocity model matching the measured dispersion curve

During inversion, the measured experimental dispersion curve is compared to a theoretical dispersion curve using forward modeling with an idealized representation of the layering, density, and V_S of the soils at the site (Figure 2.40). V_S is the main parameter that is adjusted during inversion since the dispersion curve is most sensitive to it (Xia et al. 2007). The typical result is a 1D profile of V_S assumed to represent the conditions at the midpoint of the array of receivers (Figure 2.40). 2D or 3D V_S profiles can be developed by shifting the array of receivers along the site and interpolating between 1D profiles. As with ER, the key issue with MASW data post-processing and analysis returns to the uncertainty involved with the inversion process. This inverse problem is inherently ill-posed, non-linear, and mix-determined, without a unique solution (Cox and Teague 2016). Current MASW research efforts seek to address these issues through various means, including the incorporation of higher modes in the inversion, use of more sophisticated inversion schemes such as global search algorithms, machine learning, and/or joint inversion techniques (Foti et al. 2014). However, implicit in the preceding background discussion is the 1D nature of a typical dispersion-based surface wave analysis. A truly 3D spatially variable domain is relegated to a 1D computation of V_S. This is true no matter the complexity of the subsequent inversion algorithm. This occurs because dispersion processing and forward modeling assume a stratified medium with homogeneous elastic layers. As a result, lateral heterogeneity is misrepresented. This presents challenges when interpreting MASW results at sites with considerable heterogeneity, as is common in residual soils overlying carbonate rocks.

Despite the issues with inversion and spatial variability, MASW has become quite popular for the evaluation of subsurface conditions in geotechnical engineering applications (e.g., Hayashi et al. 2005; Debeglia et al. 2006; Park and Taylor 2010; Wood et al. 2017) due to the relative ease of surface wave data acquisition and processing. With respect to evaluating karst conditions, MASW has seen an extensive amount of use despite its relatively short history since development in the late 1990s (Miller et al. 2005; Debeglia et al. 2006; Lee et al. 2010; Park and Taylor 2010; Parker Jr. and Hawman 2012; Samyn et al. 2014; Jaafar et al. 2018; Varnavina et al. 2019; Wang et al. 2019). Figure 2.41 provides an example where a 2D V_S profile developed using MASW was used to identify areas of mechanical weakness in the deep limestone caused by karstification. It is evident in Figure 2.41 those limitations related to lateral resolution of MASW in spatially heterogenous strata do not prevent the identification of soft zones indicative of karst. Nevertheless, care should be exercised in the interpretation of such MASW results due to the spatial averaging effects introduced by the wavefield transformation and forward modeling (Foti et al. 2014).

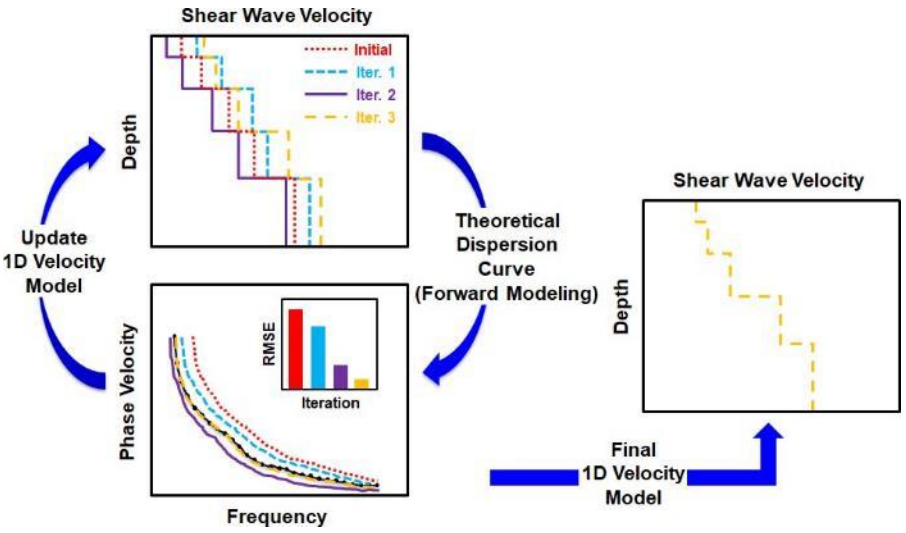

Figure 2.40. Schematic of the inversion of dispersion curve information to estimate the VS profile.

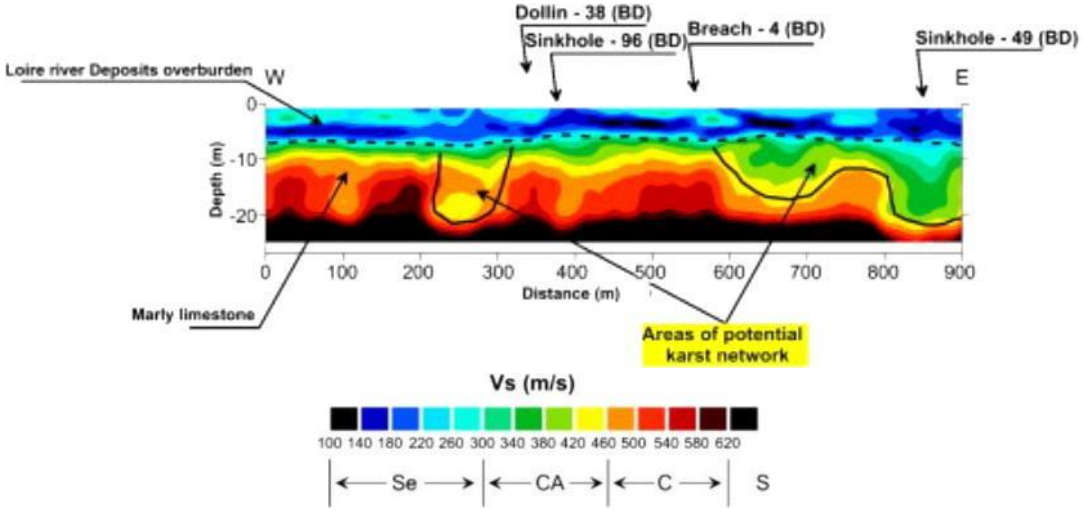

Figure 2.41. Examples of 2D MASW VS profile and interpretations of karst activity for a site in France (Samyn et al. 2014).

2.2.2.6.*Advances in Geophysical Testing*

Near-surface geophysics experienced a rapid expansion in the 1980s characterized by widespread developments in instrumentation (e.g., GPR), adaptation of techniques (e.g., shallow seismic reflection profiling), and acceptance as a tool for engineering investigations (Doll et al. 2012). Since then, the continual improvement offered by the technological revolution of the 1990s and onwards has resulted in a broad range of geophysical advancements (Doll et al. 2012):

- Increased hardware efficiencies: higher number of channels, lighter equipment, non- contact, and remote sensing/wireless equipment
- Improved resolution and inclusion of more dimensions: technological advancements in equipment have allowed for more rapid sampling and 2D, 3D, and even 4D (3D plus time lapse) acquisition
- Higher computational capabilities: the exponential rise in computational resources has increased the feasibility of more computationally expensive data post-processing and methods such as 3D numerical simulations of large domains, joint inversion of multiple datasets, and machine learning approaches
- Development of new tools: the rise of global manufacturing has decreased the cost of existing equipment and spurred the development/integration of other tools [e.g., unmanned aerial vehicles (UAV), drones, remote sensing equipment]

Given these continual changes, methods that were once considered impractical have become more prevalent. Consequently, there exists the potential for improvements in sinkhole/karst evaluation using some of the recent technological advancements in geophysical testing. The following sections discuss two approaches that are becoming increasingly common in the research literature and in the standard of geophysical practice due to the technological improvements within the last 30 to 40 years.

2.2.2.6.1 Joint Inversion

Many of the previously discussed geophysical methods rely on the solution to an inversion problem to evaluate the subsurface conditions from the measured response. In general, the goal of a geophysical inverse problem is to recover an earth model (***p***) that is consistent with the measured data (***d**obs*) (Menke 1989):

$$\boldsymbol{d_{obs}} = F(\boldsymbol{p}) \tag{2.8}$$

where the forward operator (*F*) is typically well-characterized since it is based on the physics governing the system response (e.g., elastic wave equation, gravitational forces, etc.). Therefore, reasonably accurate synthetic data can be generated for an arbitrary model using forward modeling. In all inverse problems, the input into the domain or model is known and measurements are available for the resulting output (***d**obs*). Then ***p*** can be subsequently determined by mathematically solving the inverse problem:

$$\boldsymbol{p} = F^{-1}(\boldsymbol{d_{obs}}) \tag{2.9}$$

However, the inverse operator (F^{-1}) may not exist or does not have a unique solution because it is inherently ill-posed (i.e., more model parameters than measured data parameters), nonlinear (i.e., relationship between model and measured data parameter cannot be represented using a linear mapping), and mix-determined (i.e., contradictory information for some model parameters and/or lack of information for others). An example of this non-uniqueness is provided in Figure 2.42 where three different subsurface V_S profiles exhibit the same fundamental-mode MASW dispersion curve. Use of a typical

fundamental-mode inversion scheme may result in any one of the three V_S profile as the final prediction. Yet it is clearly impossible for them all to simultaneously represent the true field condition. In a blind inversion, the amount of uncertainty present is therefore very high due to this non-uniqueness issue. A-priori information from boring/soundings can serve as "ground truth" to either further constrain the inversion process or as a quality control to check the reliability of the prediction. Though the MASW method has been and will continue to be used in this section for discussion, it should be noted that this discussion can be generalized to the other geophysical methods where an inverse problem is solved (Menke 1989).

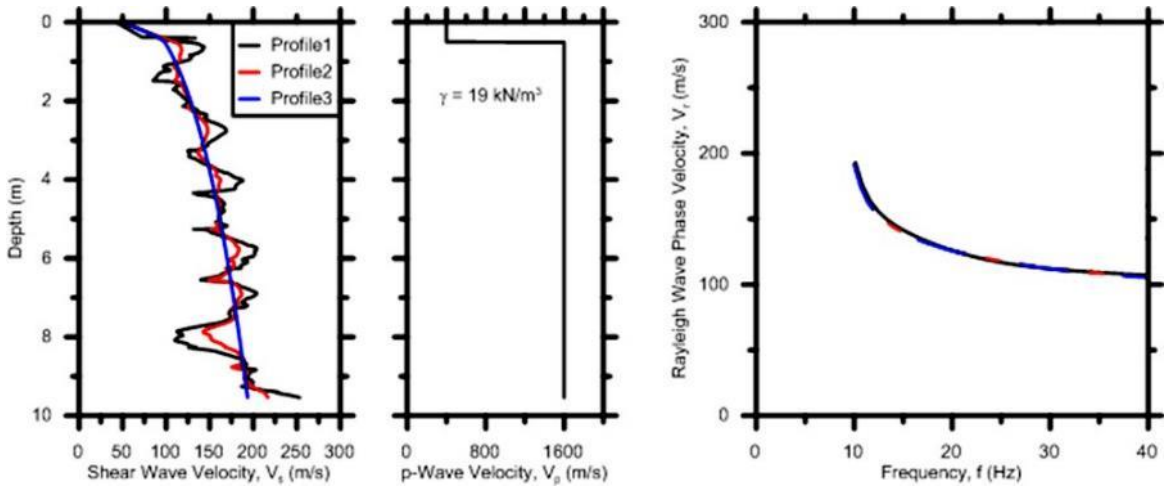

Figure 2.42. Example where three VS profiles exhibit the same fundamental-mode dispersion curve, leading to uncertainty in the inversion process (adapted from Coe et al. 2018).

Given the difficulties associated with inversion, an optimization algorithm is necessary to ensure the most probable layered earth model is selected whose theoretical dispersion curves most closely matches the measured experimental dispersion data. The function to be optimized (i.e., the objective function, misfit function, or fitness function) is typically some measure of the difference between observational data and synthetic data calculated for a trial model. An iterative gradient- based scheme is typically used in the optimization process (Figure 2.43). However, because of the difficulties, the objective function often incorporates some additional form of regularization, such as a measure of smoothness or distance from a prior model. Various other constraints may also be imposed upon the process. Different approaches can be used as part of the optimization process. For example, local search algorithms search near a starting model and calculate the root-mean-square (RMS) error to estimate model misfit. These search algorithms typically converge to a solution that fits the experimental data in an efficient manner. However, the starting model selected by the analyst can significantly affect the resulting V_S profile because the local search algorithm can get stuck in local minima without obtaining the lowest misfit model (Foti et al. 2014). To counteract this issue, several global search algorithms have been developed [e.g., uniform Monte-Carlo (Socco and Boiero 2008; Foti et al. 2009), genetic algorithm (Yamanaka and Ishida 1996), simulated annealing (Pei et al. 2007), and neighborhood algorithm (Wathelet et al. 2004)] that search a broader parameter space and avoid the solution converging to a local minimum. However, the analyst must

predefine the entire inversion parameter space of possible layered earth models for the global search. This parameterization must be broad enough to include all realistic earth models but also sufficiently constrained to prevent unrealistic models. Unfortunately, without a-priori information, it is very difficult to select appropriate site-specific inversion parameters in this manner.

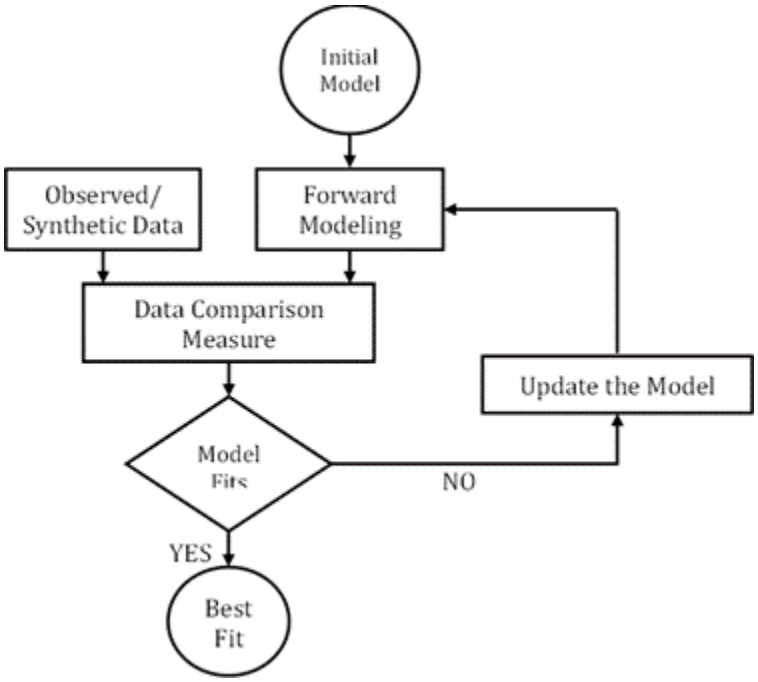

Figure 2.43. Inversion flow chart (Kordjazi 2019).

One promising area of study that has been explored to alleviate the issues of non-uniqueness is joint inversion of complementary geophysical data sets. Inversion of different data sets can be performed independently (i.e., sequentially) for each type of measurement or it can be performed jointly (i.e., simultaneously). The purpose of joint inversion is to develop one objective function for optimization from the individual objective functions representing the various data sets. In this manner, joint inversion can reduce the number of acceptable models and can produce mutually consistent estimates of the various unknown parameters because the results must explain all data simultaneously (Vozoff and Jupp 1975; Julia et al. 2000). Two factors contribute to these observations. First, different methods have different capabilities (e.g., resolution, sensitivity, etc.) and the incompatibilities for one type of data can often be resolved by another (Julia et al. 2000). Second, the noise sources and their impacts on data quality often differ between methods so that adding another method can improve the results more than adding more data of the same method. Given these factors, a considerable number of studies have explored joint inversion approaches (e.g., Gallardo and Meju 2003; Linde et al. 2006; Chen et al. 2007; Colombo and Stefano 2007; Wagner et al. 2007; Hamimu et al. 2011).

Joint inversion is often used in cases where different types of geophysical methods are combined [e.g., seismic, magnetotelluric (MT) and gravity data (Colombo and Stefano 2007; Moorkamp et al. 2011);

seismic and DC resistivity data (Gallardo and Meju 2003; Juhojuntti and Kamm 2015); seismic and gravity (Lines et al. 1988; Hayashi et al. 2005); etc.]. In these cases, data that are sensitive to different physical parameters are combined and a relationship between the corresponding physical parameters must be explicitly formulated. This can be accomplished in several ways. In one approach, a direct functional relationship between the parameters can be developed (Heincke et al. 2006; Colombo and Stefano 2007). For instance, water saturation and porosity have been assumed to provide a link between resistivity and seismic velocity in porous media (e.g., Tillmann and Stocker, 2000). Such a direct parameter relationship provides a strong coupling between data sets. In this case, the optimization model is expressed in terms of a single physical parameter and all other physical parameters needed to solve the forward problems are calculated using the analytical relationship between parameters. The resulting model update is then influenced by the misfit of all data sets. This form of coupling ensures the inversion process is highly influenced by all the data, but at the costs of major distortions in the resulting model should the assumed relationship be violated or is otherwise inappropriate.

Another joint inversion approach is to develop a structural constraint that enforces structural similarity between the different models (e.g., Gallardo and Meju 2003). The idea here is that even when the physical parameters affecting each of the data sets do not share a direct analytical link, the resulting images generated from each of the geophysical data sets should be structurally similar because they represent the same subsurface conditions. In that case, the objective function to be minimized during inversion can be defined as a structural constraint that measures the similarity between the different models. One example of such an approach is the use of the cross-gradient between the vector fields of two sets of measured properties (e.g., Gallardo and Meju 2004). Since the objective function minimized during inversion only provides a measure of the similarity between the models, a relatively loose coupling is developed between the data sets and the improvements over a single inversion approach are less extensive compared to direct parameter coupling (Gallardo et al. 2005). However, in cases where it is not possible to uniquely define a functional form for a direct parameter relationship, the cross-gradient approach provides an adequate coupling strategy for joint inversion.

One way in which joint inversion can be simplified is if the models for all the collected data are described by the same physical parameter. For example, seismic methods using body waves and surface waves are both usually modeled in terms of V_S and/or V_P (as a proxy for soil modulus/stiffness). Joint inversion of these data sets is therefore more straightforward compared to the case where different types of geophysical methods are used. The direct parameter relationship approach can be used with V_S and/or V_P as the coupling parameter. An additional advantage when focusing the joint inversion solely on seismic methods is that data collection is simplified because there is no need to deploy completely different sets of equipment at the site. Since additional equipment needs are minimized and data collection is simplified, joint inversion in this manner can be cost effective and highly efficient. However, some of the robustness of the joint inversion methodology is lost when all data sets are reliant on the same physical property and overall geophysical testing approach. For example, if seismic data quality is poor no matter which method is used to collect data (e.g., excessive background seismic noise at the site), joint inversion will not improve results. Nevertheless, the inherent limitations in the different seismic methods can sometimes be

mitigated through some of the strengths of the other datasets. For example, MASW can resolve velocity reversals that complicate analysis of seismic refraction results, whereas seismic reflection and refraction can consider lateral heterogeneities that are ignored in MASW results. A number of studies have explored the use of joint inversion approaches that combined MASW (or SASW) with the following seismic methods: seismic reflection (e.g., Dal Moro and Pipan 2007; Zhang et al. 2014); seismic refraction (e.g., Ivanov et al. 2006; Dal Moro 2008; Ivanov et al. 2013); Horizontal to Vertical Spectral Ratio (HVSR) method (e.g., Parolai et al. 2005; Arai and Tokimatsu 2005; Gouveia et al. 2016); and joint inversion of Rayleigh and Love waves (e.g., Joh et al. 2006; Boxberger et al. 2011; Dal Moro and Ferigo 2011; Hamimu et al. 2011). Many of these studies demonstrated an improvement in the overall qualities of the results from inversion after applying a joint inversion approach.

2.2.2.6.2 Full Wave Inversion (FWI)

The most used waveforms in geophysical studies include seismic stress waves and electromagnetic waves. The mechanical and physical properties of the intervening domain highly affect the way these waves are transmitted. Consequently, the entirety of the waveform records obtained in geophysical explorations contain encoded information necessary to evaluate subsurface conditions. Many inversion approaches for these waves rely entirely on first arrival information, which ignores information present in the later parts of the recordings and limits the accuracy/resolution of the resulting inverted section. Alternatively, a wavefield transform is applied to the acquired signals in the case of MASW, which introduces spatial averaging effects as previously noted. To address these issues, full waveform tomography was developed that bypasses the selection of first arrival information as in Seismic Refraction or the wavefield transform and subsequent selection of dispersion curves for MASW. In this approach, a Full Waveform Inversion (FWI) scheme is introduced to decode and acquire as much information as possible from the entirety of the acquired waveforms (Lailly 1983; Tarantola 1984). It is important to note that switching to a full waveform based tomographic approach does not necessitate changes to the current data acquisition schemes in seismic and GPR methods. Although FWI was introduced in the 1980's, it was not practically implementable until the advent of modern computers due to its expensive computational costs.

FWI generally proceeds as highlighted in Figure 2.43 and Figure 2.44. The relationship between the model $\boldsymbol{m}$ and the observed seismic wavefield ($\boldsymbol{d_{obs}}$) in FWI can be mathematically described as follows:

$$\boldsymbol{d_{obs}} = G(\boldsymbol{m}) * \boldsymbol{S} \tag{2.10}$$

where $G(\boldsymbol{m})$ denotes the impulse response of a model $\boldsymbol{m}$ (i.e., the Green's function of the model), $\boldsymbol{S}$ is the seismic source time function, and the symbol $*$ denotes a convolution operation in the time domain. Equation 2.10 can be simulated by numerically modeling wave propagation within the model domain using an appropriate scheme [e.g., staggered grid finite difference approach (Virieux, 1984), finite element approach (Marfurt, 1984), finite volume approach (Brossier et al., 2008), spectral element approach (Komatitsch & Vilotte, 1998), etc.] and theoretical framework [e.g., acoustic (Tarantola, 1984), elastic (Mora, 1987), viscoelastic (Carcione et al., 1988), or poroelastic (Yang & Malcolm, 2021) wave propagation]. Synthetic waveforms ($\boldsymbol{d_{syn}}$) computed from a subsurface model can be subsequently

compared to waveforms observed in the field ($\boldsymbol{d_{obs}}$). The process is repeated with model updates until a desired misfit ($\Delta\boldsymbol{d} = \boldsymbol{d_{syn}} - \boldsymbol{d_{obs}}$) is achieved between the synthetic and observed waveforms. In this manner, the entire recorded waveform is used to infer information about the domain, which increases resolution capabilities relative to ray-based (i.e., seismic refraction tomography) and dispersion-based methods [i.e., multichannel analysis of surface waves (MASW)].

The model $\boldsymbol{m}$ represents a set of physical parameters that govern wave propagation. Global optimization algorithms can be used to solve the inverse problem in FWI (Xing & Mazzotti, 2019). However, this becomes computationally intractable due to the large number of parameters in $\boldsymbol{m}$ for most wave propagation problems. Consequently, the FWI approach typically proceeds as a gradient-based local optimization whereby the minimum of a misfit function $E(\boldsymbol{m})$ (also referred to an objective function) is sought. Typically, $E(\boldsymbol{m})$ is a norm of the misfit vector $\Delta\boldsymbol{d}$, with the most common approach utilizing the least-squares norm (Tarantola, 2005):

$$E(\boldsymbol{m}) = \frac{1}{2}\Delta\boldsymbol{d}^{\dagger}\Delta\boldsymbol{d} \tag{2.11}$$

where the symbol † denotes the transpose conjugate. The operation in Equation 2.11 can be performed in the time domain by summing over the number of source-channel pairs and the number of time samples in the recorded wavefields. When summed over the frequency domain, the misfit function in Equation 2.11 is complex valued. Other misfit functions have also been explored that exhibit different sensitivity to various aspects of the recorded wavefield (e.g., amplitude, phase, etc.), selection of the starting model, and the inherent non-linearity of the full waveform inversion problem (e.g., Fichtner et al., 2008; Yuan et al., 2015; Borisov et al., 2017).

To perform the local optimization of the misfit function, a starting model ($\boldsymbol{m_o}$) is selected, and the minimum of the misfit function is sought in the vicinity of this $\boldsymbol{m_o}$. It is assumed based on the Born approximation that an updated model $\boldsymbol{m}$ of dimension M results from the addition of a perturbational model ($\Delta\boldsymbol{m}$) to $\boldsymbol{m_o}$, such that:

$$\boldsymbol{m}_{k+1} = \boldsymbol{m}_k + \alpha_k \Delta\boldsymbol{m}_k \tag{2.12}$$

where the step length α_k can be estimated by a line-search method or a trust-region globalization process (Bonnans et al., 2006). The misfit function can be evaluated in the vicinity of $\boldsymbol{m_o}$ based on a second-order Taylor series expansion:

$$E(\boldsymbol{m_o} + \Delta\boldsymbol{m}) = E(\boldsymbol{m_o}) + \frac{\partial E(\boldsymbol{m_o})}{\partial \boldsymbol{m}}\Delta\boldsymbol{m} + \frac{1}{2}\frac{\partial^2 E(\boldsymbol{m_o})}{\partial \boldsymbol{m}^2}\Delta\boldsymbol{m}^{\boldsymbol{T}}\Delta\boldsymbol{m} \tag{2.13}$$

where the $\partial^2 \boldsymbol{E}(\boldsymbol{m_o})/\partial \boldsymbol{m^2}$ term is referred to as the Hessian [$\boldsymbol{H}(\boldsymbol{m_o}) = \boldsymbol{H_o}$] and defines the curvature of the misfit function in the vicinity of $\boldsymbol{m_o}$. Taking the derivative of the resulting expression with respect to the model parameters $\boldsymbol{m}$ results in:

$$\frac{\partial E(\boldsymbol{m})}{\partial \boldsymbol{m}} = \nabla E_m = \frac{\partial E(\boldsymbol{m_o})}{\partial \boldsymbol{m}} + \boldsymbol{H}_o \Delta \boldsymbol{m} \tag{2.14}$$

The minimum of the misfit function in the vicinity of $\boldsymbol{m_o}$ can then be found by setting Equation 2.14 to zero, resulting in:

$$\Delta \boldsymbol{m} = -\boldsymbol{H_o^{-1}} \frac{\partial E(\boldsymbol{m_o})}{\partial \boldsymbol{m}} \tag{2.15}$$

The perturbation model $\Delta \boldsymbol{m}$ in Equation 2.15 can be inserted into Equation 2.12, which results in the Newton method for optimization of the model:

$$\boldsymbol{m}_{k+1} = \boldsymbol{m}_k - \alpha_k \boldsymbol{H_k^{-1}} \frac{\partial E(\boldsymbol{m_k})}{\partial \boldsymbol{m}} \tag{2.16}$$

Consequently, Equation 2.16 demonstrates that the Hessian matrix $\boldsymbol{H_k}$ must be inverted to determine the final model $\boldsymbol{m}$ that minimizes the misfit function. The Hessian can be computed from the following expression (see Pratt et al., 1998 for a detailed derivation):

$$\boldsymbol{H}(\boldsymbol{m}) = \boldsymbol{J}^T(\boldsymbol{m})\boldsymbol{J}(\boldsymbol{m}) + \frac{\partial \boldsymbol{J}}{\partial \boldsymbol{m}} \Delta \boldsymbol{d} \tag{2.17}$$

where $\boldsymbol{J(m)}$ represents the Jacobian operator (i.e., matrix of Fréchet derivatives, $\partial \boldsymbol{d_{syn}}/\partial \boldsymbol{m}$). A common approximation of the Hessian involves neglecting the second term in Equation 2.17, resulting in the so-called Gauss-Newton method (Epanomeritakis et al., 2008). However, even with this simplification, the Hessian is quite difficult to directly calculate due to the large number of parameters in $\boldsymbol{m}$ and resulting size of $\boldsymbol{J}(\boldsymbol{m})$. Moreover, the Hessian is often indeterminant even when approximated by the first term in Equation 2.17. Multiple attempts have been made to address this issue, including avoiding the use of $\boldsymbol{H^{-1}}(\boldsymbol{m})$ entirely in Equation 2.16 (i.e., the steepest decent method) and various approximations for $\boldsymbol{H^{-1}}(\boldsymbol{m})$ (e.g., Wang et al., 2016). The quality and rate of convergence for the inversion depends significantly on the Newton, Gauss-Newton, or gradient method used (Pratt et al., 1998).

The gradient of the misfit function with respect to model parameters [$\partial \boldsymbol{E}(\boldsymbol{m_k})/\partial \boldsymbol{m}$ in Equation 2.16] can be calculated efficiently using an adjoint-state algorithm (Mora, 1987; Pratt et al., 1998; Tarantola, 2005; Plessix, 2006). In this approach, two wavefield simulations are performed. The first simulates the forward-propagating wavefield (state variable) through the domain of interest (i.e., Equation 2.10). The second simulation computes the adjoint wavefield, which is the wavefield that is obtained when the time-reversed data residuals at the receiver positions are input as sources for modeling of wave propagation. Subsequently, the gradient can be calculated by correlating the state and the adjoint state wavefields.

The gradient is typically largest near the source and receiver positions, which can mask important information about the rest of the domain of interest. The inversion may fail to converge due to these artificially high gradients near the source/receivers. Consequently, the gradient is often preconditioned to reduce inversion artifacts (e.g., Guitton et al., 2012). Additional processing of the gradients may include scaling with depth to resolve deeper structures (Ben-Hadj-Ali et al., 2008) and regularization to provide the search for possible solutions with a priori information that comes from inferences about the wave propagation physics (Virieux et al., 2017). Further details regarding the general inversion framework (e.g., choice of regularization scheme, optimization algorithms, etc.) can be found in references from Santamarina and Fratta (2005), Fitchner (2011), and Modrak and Tromp (2016).

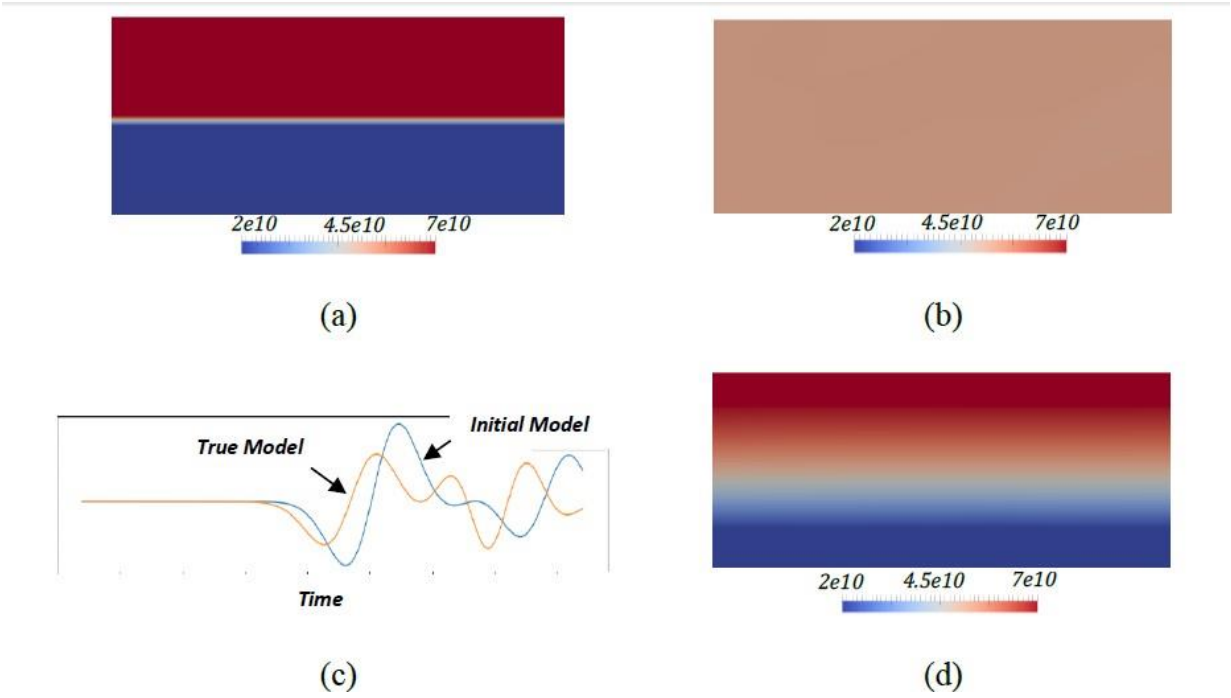

Figure 2.44. Example schematic of FWI (adapted from Afanasiev 2017): (a) true model; (b) starting (initial) model; (c) waveform misfit; and (d) inverted model.

Recent studies have reported the implementation of this method in exploration geophysics and geotechnical applications with promising degrees of success (Gélis et al. 2007; Virieux and Operto 2009, Romdhane et al. 2011; Kallivokas et al. 2013; Amrouche and Yamanaka 2015; Brossier et al. 2015; Fathi et al. 2016; Nguyen et al. 2016; Coe et al. 2019). In particular, the research team has also recently implemented 2D FWI to numerically evaluate the natural spatial variability present in conditions mimicking a liquefiable alluvial deposit (Coe et al. 2019), the presence of voids in drilled shafts (Kordjazi et al. 2019), and the geometry of unknown foundations (Mahvelati and Coe 2019). In each of these cases, the FWI approach demonstrated improved capabilities in reconstructing subsurface soil profiles with irregular interfaces resulting from heterogeneous features and/or natural spatial variability. Several recent publications have also highlighted the use of FWI with both seismic and radar waves to evaluate sinkhole

and karst features (e.g., Grasmuek et al. 2010; Buckman et al. 2012; McNeely et al. 2012; Grasmuek et al. 2013; Tran et al. 2013; Yoon et al. 2014; Loh et al. 2016; Tran et al. 2019). Figure 2.45 provides an example where FWI was used to evaluate a subsurface void in limestone at a field site in Florida. These results should suffer less from the spatial averaging effects previously discussed for surface waves.

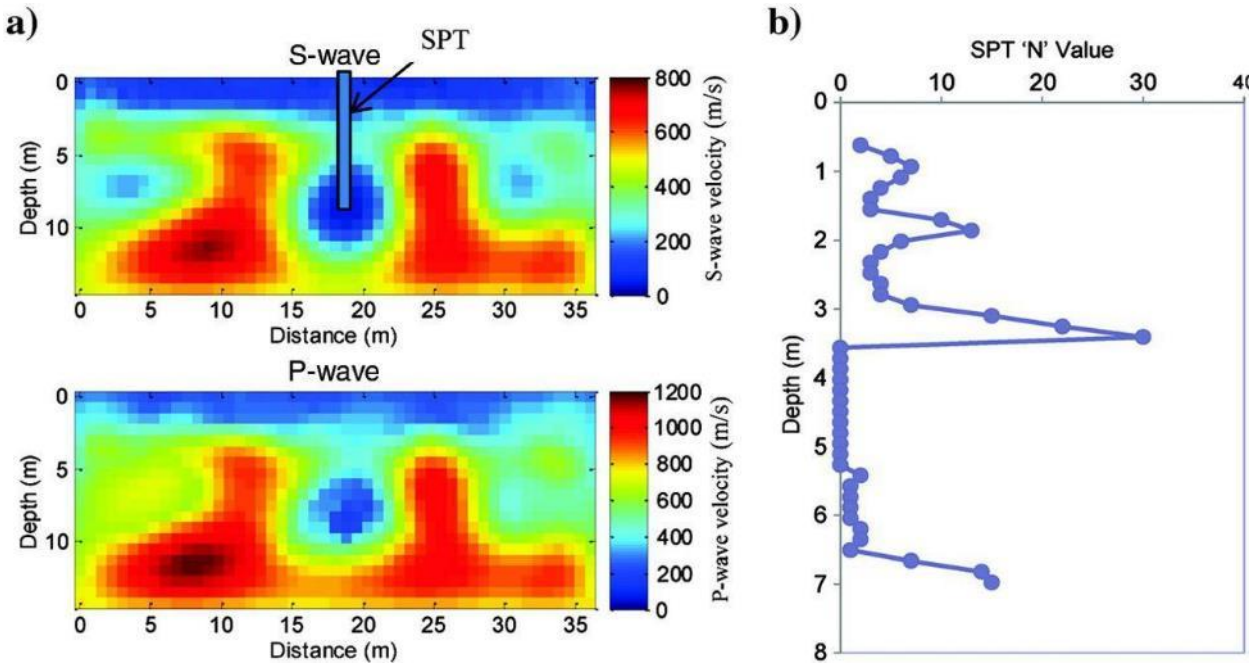

Figure 2.45. Example of FWI applied to evaluate an embedded void in limestone (Tran et al. 2013).

2.2.3. Other Karst Evaluation Techniques

Much of this report has focused on how geophysical methods can be used to evaluate subsurface conditions and monitor sinkhole formation. In many cases, geophysical methods can provide useful information on current karst conditions and possible mitigation strategies. However, other methods exist that are deployed in a monitoring fashion to help deduce subsurface activity and identify developing sinkholes. Monitoring of sinkhole areas should be performed at different stages of a project, including:

- Pre-construction inspection to identify any pre-existing anomalous karst features
- Monitoring of pre-identified features during construction
- Monitoring of additional features that form during and after construction

Each stage has different requirements in terms of site constraints and monitoring capabilities. For example, test borings are often used to evaluate subsurface conditions. When borings encounter low blow count materials, voids, or loss of drilling fluid circulation, they are usually interpreted as sinkhole indicators and typically trigger additional investigation and monitoring. However, it may be difficult or impossible to drill during the construction phase when there is a large amount of activity at the site and in the post-construction phase when a structure is limiting access for data acquisition at the location of a

developing sinkhole. Additionally, repeated measurements in the same location are not feasible for destructive approaches like drilling and in situ testing. Thus, as a monitoring tool, standard geotechnical investigations may not allow the spatial repeatability and temporal resolution necessary to monitor anomalous karst features. Geophysical methods may face similar limitations, though they are slightly more adaptable since they do not rely on destructive operations such as drilling. Consequently, other karst evaluation tools have been developed to monitor subsurface conditions.

Sinkholes are commonly associated with gradual, dissolution-induced land subsidence, which occurs before, during, and after the surface collapse (Paine et al. 2012). Characterization of the ongoing deformations is often the goal of monitoring sinkholes, as is the case with other geohazards such as landslides, embankments, and retaining systems. However, there is a shortage of literature available for sinkhole monitoring when compared with other natural instability phenomena like landslides (Desir et al. 2018). There is some published evidence confirming the feasibility of monitoring sinkhole precursor deformations to minimize the collapse risk (e.g., Closson et al. 2005; Buchignani et al. 2008; Jones and Blom 2014). In the case reported by Buchignani et al. (2008), precursor cracks and structural deformations were monitored on buildings six hours before a 35 m wide sinkhole developed at a site in central Italy, which prevented loss of life.

Deformation monitoring for sinkholes is generally classified into three (3) main groups based on the position of the devices and sensors being used (Gutiérrez et al. 2019):

- Subsurface methods
- Ground-based methods
- Remote Sensing methods

Subsurface methods refer to techniques such as borehole extensometers or Brillouin Optical Time Domain Reflectometry (BOTDR) that use sensors installed in the subsurface to detect underground deformation with no surface manifestation. Ground-based methods such as inclinometers, high precision leveling sensors, and Differential Global Positioning System (DGPS) are in direct contact with the ground surface and measure any differences in elevation. Finally, remote sensing techniques like LIDAR or Interferometric Synthetic Aperture Radar (InSAR) scan the ground surface by satellites, balloons, helicopters, planes, and unmanned aerial vehicles (UAV) to collect displacement data. There is no method that has been specifically developed to monitor sinkhole activity. Most of these sinkhole monitoring methods are derived from other fields, such as landslide monitoring (e.g., Lacasse and Nadim 2009). In the next section, a discussion is provided regarding the application of these techniques to monitor sinkhole activity. Since these methods are primarily outside the scope of TEM WO 015 this discussion is purposefully brief in scope.

2.2.3.1.*Subsurface Methods*

2.2.3.1.1 Brillouin Optical Time Domain Reflectometry (BOTDR)

Brillouin Optical Time Domain Reflectometry (BOTDR) is a distributed fiber optic strain sensing system, which can detect temporal and spatial changes of the ground surface (Pei et al. 2014). BOTDR uses the Brillouin scattering phenomenon to detect changes in temperature or axial strain along the optical fiber. When the strain occurs in the longitudinal direction of optical fiber, the backscattered light waves undergo a frequency shift that is proportional to the strain (Jiang et al. 2016). Linker et al. (2009) showed the potential of this method for fully automated early-warning detection of sinkhole formation in the Dead Sea region. Zhang et al. (2009) also used the BOTDR technique for monitoring and predicting potential sinkholes at a site in China. Their results showed a very good relationship between the strain in the optical fiber and the soil deflection when a sinkhole developed (Zhang et al. 2009). Guan et al. (2013) used a BOTDR system to detect karst deformations by burying a sensing fiber in a collapse prone soil and measuring the deformations caused by a soil void (Figure 2.46). Based on an analysis of the temporal and spatial variation of the optical fiber strain Guan et al. (2013) was able to monitor the location, size, and collapsing process of the void in soil.

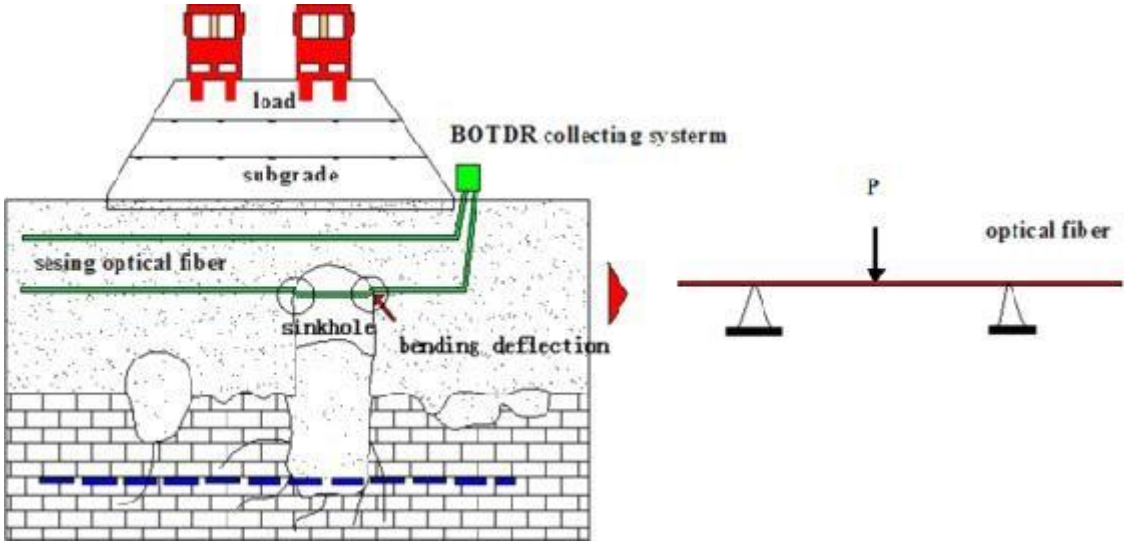

Figure 2.46. Schematic diagram of BOTDR setup to predict sinkhole formation (Guan et al. 2013).

2.2.3.1.2 Seismic Monitoring

Seismic monitoring typically consists of a geophone attached to a borehole at various depths within a site or an array of seismometers place somewhere in a karst-prone area. These sensors are used to record the magnitude of wave deflections caused by displaced strata from collapse activity. The seismic energy generated by the collapse events are often so small (e.g., Richter magnitudes of -3.0 and smaller) that the terminology “nanoseismic monitoring” has been used to refer to this methodology. There are several case studies that used this approach to detect concealed karst activity, but they all highlighted the difficulty in data interpretation given the limited signal-to-noise ratio, ambiguousness in the recordings, and minimal spatial density of the measurement locations (e.g., Malovichko et al. 2005; Wust-Bloch and

Joswig 2006; Nayak and Dreger 2014). The data is processed using similar filtering, muting, and scaling schemes used in the processing of microseismicity data to display the *f-t* distribution of signal energy. Pattern recognition schemes (Joswig 1990) are then applied to differentiate karst-related nanoseismic events from regional and local earthquakes as well as common noise sources. As an example of the capabilities of the approach, Malovichko et al. (2005) used six (6) underground and one (1) surface vertical geophones installed 1-2 km apart from each other near a mine in Russia to monitor karst activity. Based on the calculation of synthetic waveforms and their comparison with seismograms of the "low- frequency" events recorded in the field, they found evidence of a rockfall event at their site. Wust- Block and Joswig (2006) were able to locate individual sinkhole events and detect the presence of cavitation above the groundwater level progressing towards the surface.

2.2.3.2.*Ground-Based Methods*

2.2.3.2.1 High Precision Leveling

High precision leveling simply measures the difference in relative heights of successive points on the ground surface with the help of digital levels and the electronic reading of bar-coded staffs. The cost-effectiveness of this approach relative to other geodetic monitoring methods has led to its adoption to monitor vertical subsidence features in karst settings and other geologic environments prone to subsidence (e.g., De Zeeuw-van Dalfsen et al. 2013; Caputo et al. 2015; Islam et al. 2016; Desir et al. 2018). Desir et al. (2018) demonstrated the high potential of this method by monitoring five (5) active sinkholes related to dissolution of salt-bearing bedrock in the central sector of the Ebro Cenozoic basin in Spain. Desir et al. (2018) noted the following advantages of this method:

- High instrumental precision that allows the recognition of subsidence in slow moving sinkholes over practical measurement periods
- Reduced costs of the equipment
- Simplicity of the process, including installation of benchmarks, data acquisition and processing
- Limited time needed to collect the data by two (2) persons after discrete training
- Internal consistency of the data and lack of subjectivity in the interpretations

Gutierrez et al. (2019) also performed a series of high-precision level monitoring over a very active sinkhole zone in Alcala, Spain. They reported the efficiency of this technique when recording the slow vertical displacement over short periods of time. However, they also noted the high spatial resolution necessary (i.e., meter-scale spacing) for quality measurements (Gutiérrez et al. 2019).

2.2.3.2.2 Global Positioning Systems (GPS)

Global Positioning Systems (GPS) can perform automatic measurements of positions at high acquisition frequency with up to millimeter precision. However, the high costs associated with the deployment of the several antennae necessary for this level of precision severely limits its use for sinkhole early warning (Intrieri et al. 2015). Kent et al. (2013) provided a review of efforts with real-time subsidence monitoring using four (4) GPS reference stations along the portion of a Louisiana Department of Transportation and

Development (LADOTD) highway located in a sinkhole prone area. They reported GPS can provide informative and actionable monitoring to reduce the public hazards.

2.2.3.3.*Remote Sensing Methods*

2.2.3.3.1 Interferometric Synthetic Aperture Radar (InSAR)

Interferometric Synthetic Aperture Radar (InSAR) measures 3D surface displacements with nearly complete spatial continuity and takes advantage of a satellite's perspective to view large areas of Earth's surface quickly and efficiently (Simons and Rosen 2007). InSAR uses radar signals from Earth-orbiting Synthetic Aperture Radar (SAR) satellites to measure the phase difference between the returned signals from two images acquired over the same area (Figure 2.47). In this scenario, the phase difference is essentially related to the geometric path length difference to the image point, which depends on the topography. Consequently, the phase difference information (i.e., the interferogram) can be used to create surface deformation maps based on repeated time-lapse measurements at the same location as the satellite orbits. InSAR has been widely used to detect duration and magnitude of any precursory sinkhole-related surface subsidence (e.g., Conway and Cook 2013; Nof et al. 2013; Atzori et al. 2015; Baer et al. 2018).

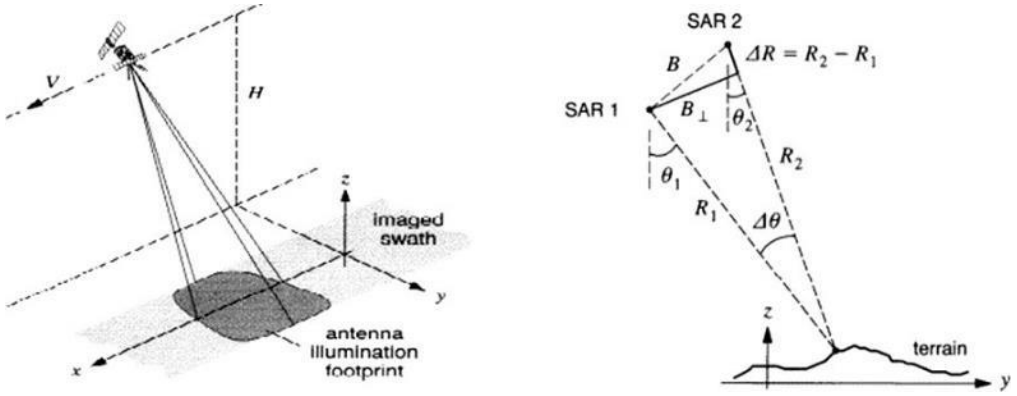

Figure 2.47. SAR imaging geometry and SAR interferometer concept (Bamler and Hartl 1998).

2.2.3.3.2 Close-range Photogrammetric Survey

Close-range photogrammetric surveys are another form of remote sensing that has been applied for karst activity detection. In this method, multiple overlapping images are taken from different perspectives with high-resolution digital cameras, producing measurements that can be used to create accurate 3D models of objects. For example, for each camera, each image point *P'* and the corresponding perspective center *O'* define the spatial direction of a ray to the corresponding object P (Luhmann et al. 2013) (Figure 2.48). The shape and position of an object can be subsequently determined with computational models that reconstruct bundles of rays. When combined with UAV technology, photogrammetry can be used to survey local-scale areas (approximately 100– 100,000 m^2) with an accuracy in the range of centimeters. In karst settings, the comparison of 3D surface models generated from photogrammetric surveys on different dates can be used to detect any changes in ground elevation. This approach has been highlighted

in several recent sinkhole-related case studies where photogrammetry was able to resolve subsidence features at a karst site (e.g., Al-Halbounia et al. 2017; Klawitter et al. 2017; Suh and Choi 2017).

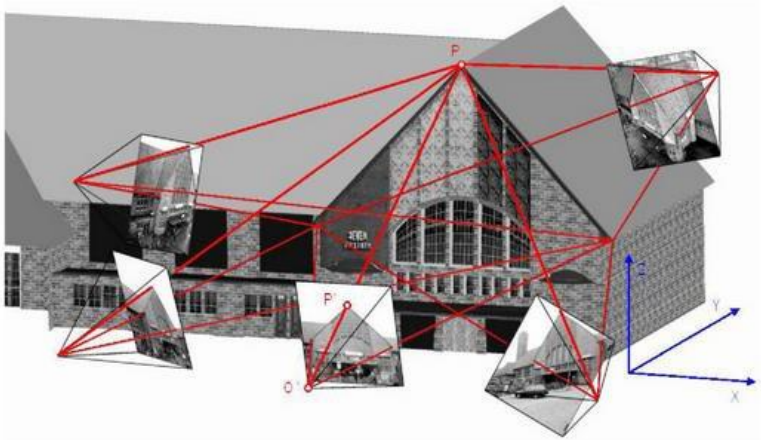

Figure 2.48. Principles of photogrammetric measurements (Luhmann et al. 2013).

2.2.3.3.3 LiDAR

LiDAR (Light Detection and Ranging) sends a pulsed laser to an object and measures the reflected light. Differences in the arrival times and wavelengths of the returning laser signals can be used to determine distance information. A 3D model of the object can be developed from the collection of points (i.e., the point cloud) that represent the backscattered laser signals. LiDAR can be applied from terrestrial or airborne measurement locations (Figure 2.49). With the continual advancements in UAV technology, LiDAR is increasingly being used in karst settings to generate high-resolution 3D models of sinkholes (e.g., Doctor and Young 2013; Hämmerle et al. 2014; Zhu et al. 2014; Silva et al. 2017 Moreno-Gómez et al. 2019). LiDAR can also be used in combination with other remote sensing or monitoring techniques to increase the quality of the 3D modeling and resulting analysis (e.g., Alexander et al. 2013).

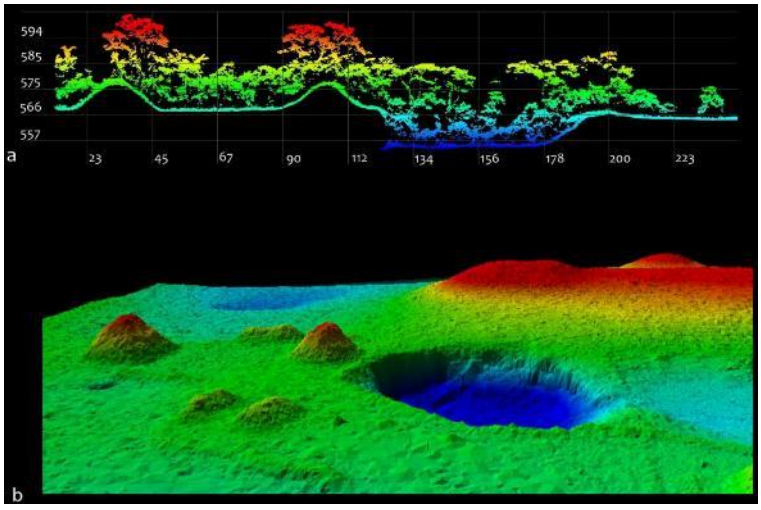

Figure 2.49. Example of LiDAR data in karst: (a) point cloud of cave and sinkhole; and (b) 3D image of sinkhole and surface structures (Moyes and Montgomery 2019).

2.3. Mitigation of Sinkholes

Natural and human-induced sinkholes can pose a great risk to human life. When sinkholes occur in urban areas they can result in irrecoverable damage to infrastructure and consequently lead to evacuations or deaths. In general, the design and construction of structures in karst regions confronts many problems due to unpredictable location, dimensions, and geometry of the karst structure and voids as well as the nature and thickness of the soil cover. Voids and cavities in both the bedrock and the soil are significant as potential sites for collapse (Waltham et al. 2005a,b). Consequently, sinkholes should be properly mitigated by applying preventive planning prior to any construction projects to reduce the risk of any damages. Sowers (1984) suggested a five-step mitigation process:

1. Optimize location: relocate the building or find an alternative site
2. Correct or mitigate the subsurface defects that are identified (e.g., grouting, cap grouting or dynamic compaction)
3. Modify the shallow foundation design into rigid mats that span a suspected sinkhole
4. Use deep foundations systems such as piles or drilled shafts
5. Minimize future sinkhole development process

The most practical solution for safe construction is to reduce the vulnerability of structures by constructing in a sinkhole-free zone. For example, a setback distance can be established around any suspected sinkholes (Zhou and Beck 2008). However, it may not always be feasible to avoid a site with suspected sinkhole activity or accommodate any proposed setbacks. In such cases, engineers can minimize sinkhole-related risk through design decisions, including:

- Incorporation of high tensile heavy-duty geogrids or geo-composites in layered systems under the sub-base of roads or embankments. The higher stiffness and tensile stress capabilities of these materials prevent sudden catastrophic sinkhole failures and instead typically provide a warning sign of sags under the road (Figure 2.50) (Kempton et al. 1996; Cooper and Saunders 2002).
- Application of rigid structures (e.g., reinforced concrete slabs) acting as ground bridges, to better distribute loads (Kannan 1999; Guerrero et al. 2004; Guerrero et al. 2008; Guitérrez et al. 2017).
- Incorporating bridges with larger individual piers or heavy-duty steel girder construction designed with sacrificial supporting piers to span a small subsidence event (Figure 2.50) (Cooper and Saunders 2002).
- Use of deep foundation systems either to transfer loads to deeper strata or to reduce the possibility of erosion of loose overburden soils (Kannan 1999; Tarquinio and Pearlman 2001; Bivens and Siegel 2007; Griffiths et al. 2011).

In addition to special design considerations, karst mitigation methods include remedial work on existing sinkholes or efforts to prevent or minimize their impact over time.

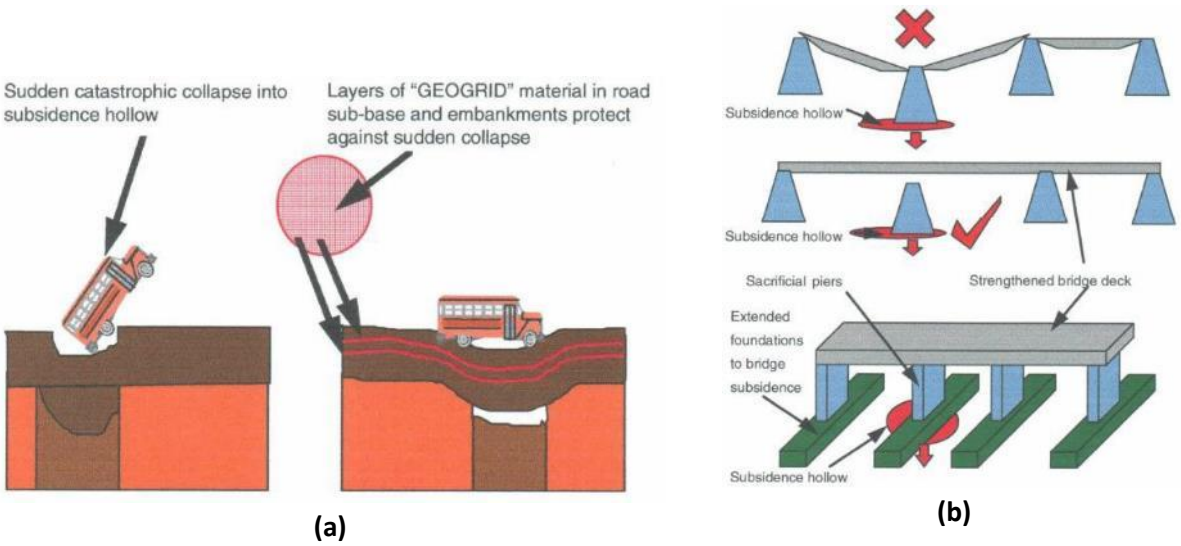

Figure 2.50. Examples of sinkhole resistant designs: (a) geosynthetics (Cooper and Calow 1998); and (b) sacrificial supports and extended foundations (Cooper and Saunders 2002).

2.3.1. Sinkhole Remediation Efforts

There are generally two (2) steps when addressing sinkhole issues at a site: 1) stabilize the soil subject to erosion (especially in contact with water) by increasing its strength; and 2) prevent additional sinkhole failure by removing the triggering mechanism and source. Most sinkhole/karst damage can be attributed to failures that develop entirely within the cover soil, which increases the applicability of ground improvement methods to address karst anomalies. However, as noted, soil treatment techniques such as grouting, and densification must be accompanied by appropriate drainage systems to adequately route water and prevent further developments of sinkhole (Zhou 2007). When exploring mitigation strategies, it is important to understand why the failure occurred so a durable repair can be made. As noted in this report, geophysical methods can develop further insights about the subsurface conditions and causes for sinkhole activity at a site. Some corrective measures to diminish triggering mechanisms for sinkholes include (Sowers 1996; Alcántara and Goudie 2010; Gutiérrez et al. 2017):

- Preventing water withdrawal and the decline of the water table
- Lining of canals and ditches
- Using flexible pipes with telescopic joints to prevent their breakage and subsequent source of additional water at the site
- Controlling irrigation
- Creating an impermeable surface with geo-membranes or geotextiles
- Construction of cutoff screens and grout curtains to avoid ground water circulation beneath structures

Most cases of sinkhole remediation attempt either to completely seal the outlet conduit at its base or to fill the void with graded material that will remain stable when stormwater subsequently drains through it (Waltham et al. 2005). Alternatively, various grouting mechanisms can be used to fill voids, create plugs, and increase soil compaction (Zhou and Beck 2008). Figure 2.51 provides examples of commonly used sinkhole remediation methods. Zhou et al. (2017) proposed a general process of selecting the most appropriate remediation method, which summarizes the efforts on this topic (Figure 2.52). Included in this process is development of a sinkhole conceptual site model (CSM) (U.S. Army Corps of Engineers 2012) and consideration for the purpose of the remediation, regulations, and costs. In the following sections some of the most common sinkhole remediation methods will be further discussed.

Sinkhole remediation	Typical diagrams
Shallow sinkholes with visible throats (Kutschke 2004, personnel communication)	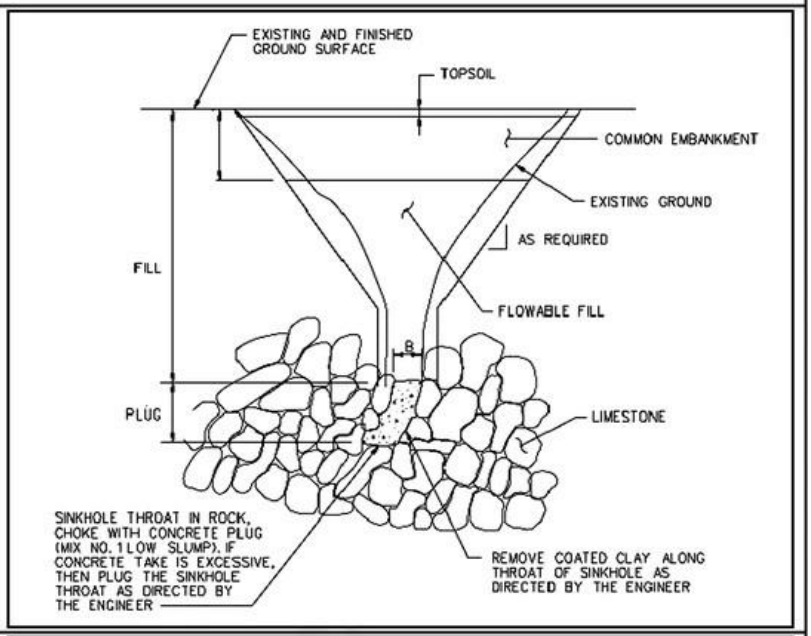
Deep sinkholes with known throats (Kutschke 2004, personnel communication)	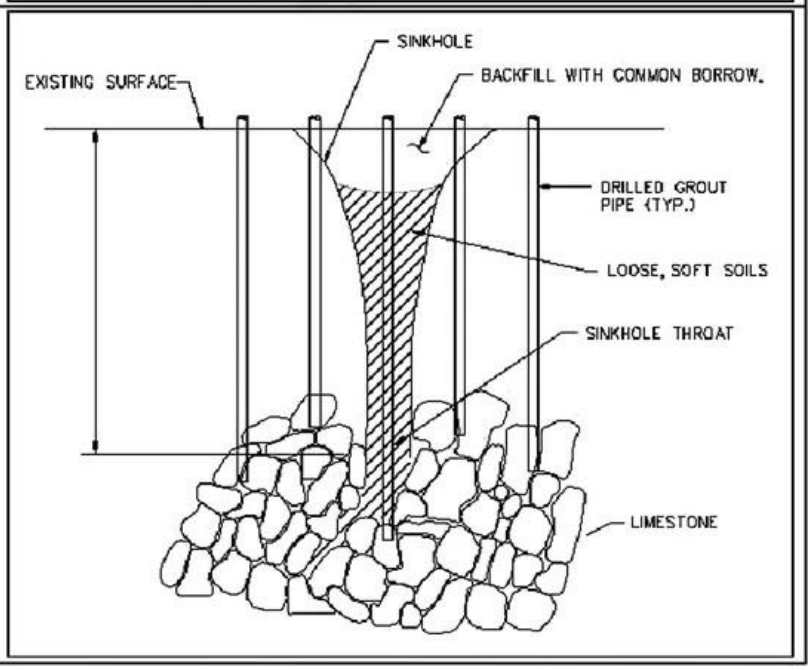

Figure 2.51. Examples of sinkhole remediation techniques (Zhou and Beck 2008).

Sinkhole remediation	Typical diagrams
Compaction grouting (Siegel et al. 1999)	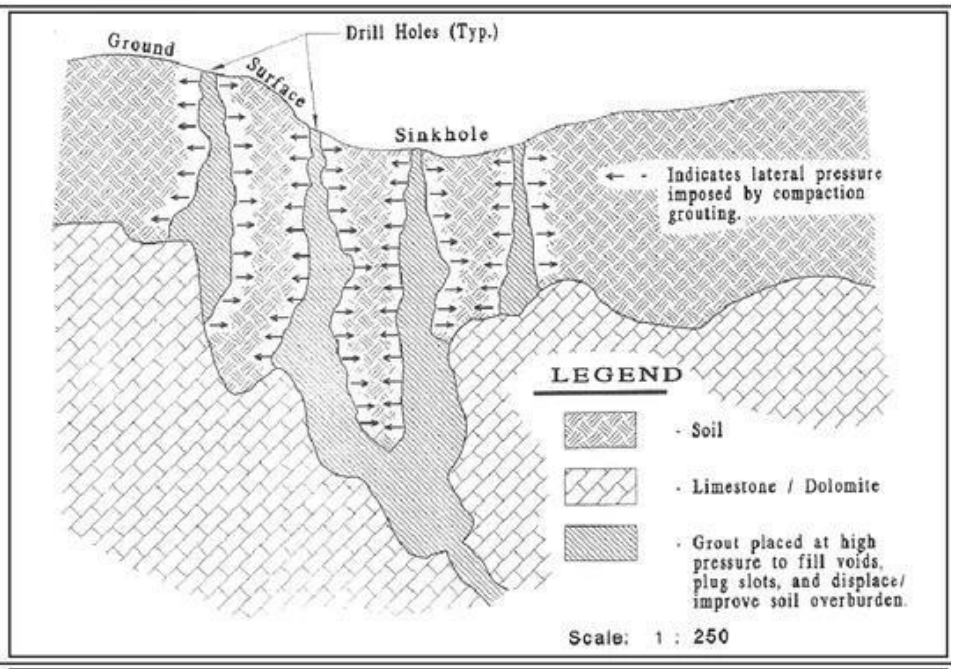
Cap grouting (Siegel et al. 1999)	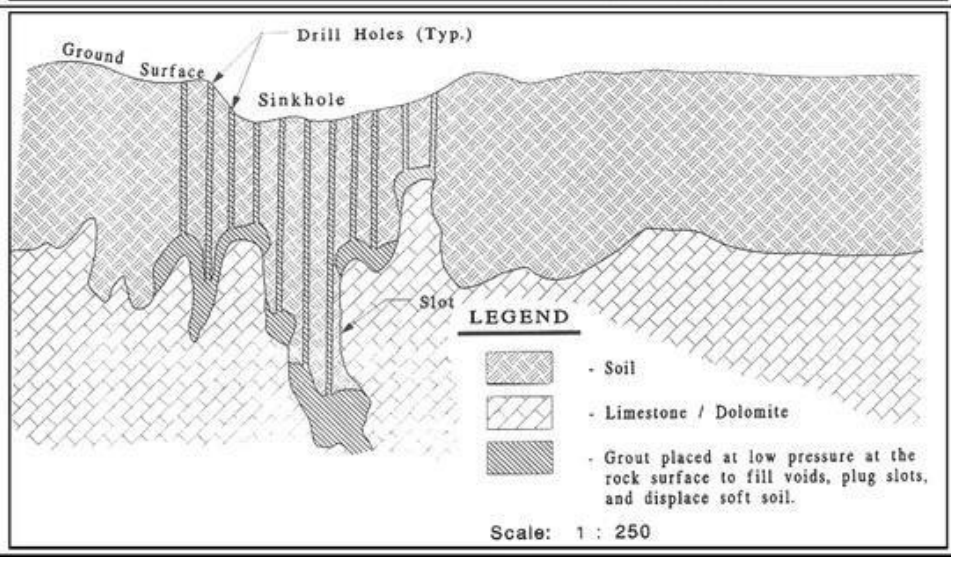

Figure 2.51 (continued). Examples of sinkhole remediation techniques (Zhou and Beck 2008).

Sinkhole remediation	Typical diagrams
Graded backfilling (Fort Campbell Environmental Division 2003)	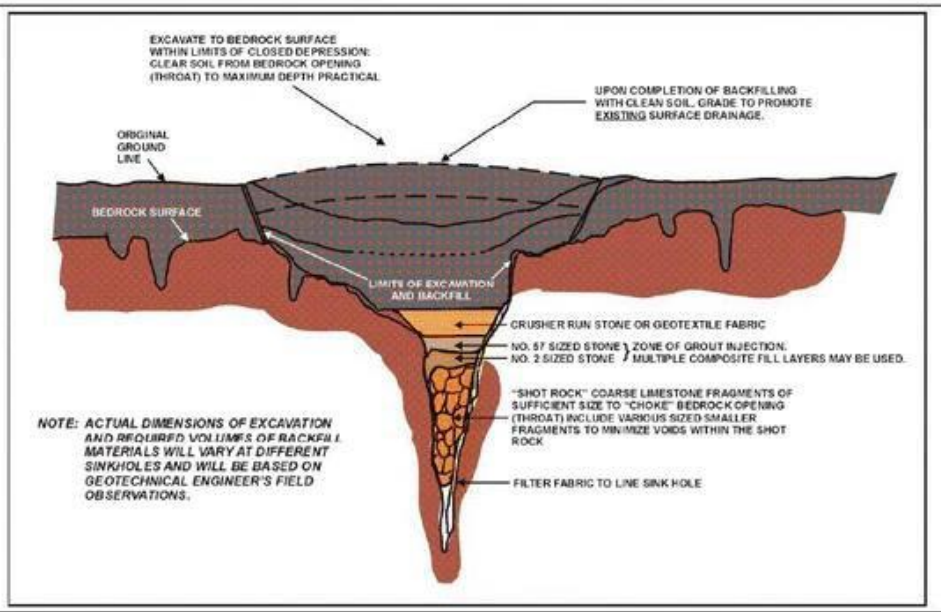
Dental filling by grout	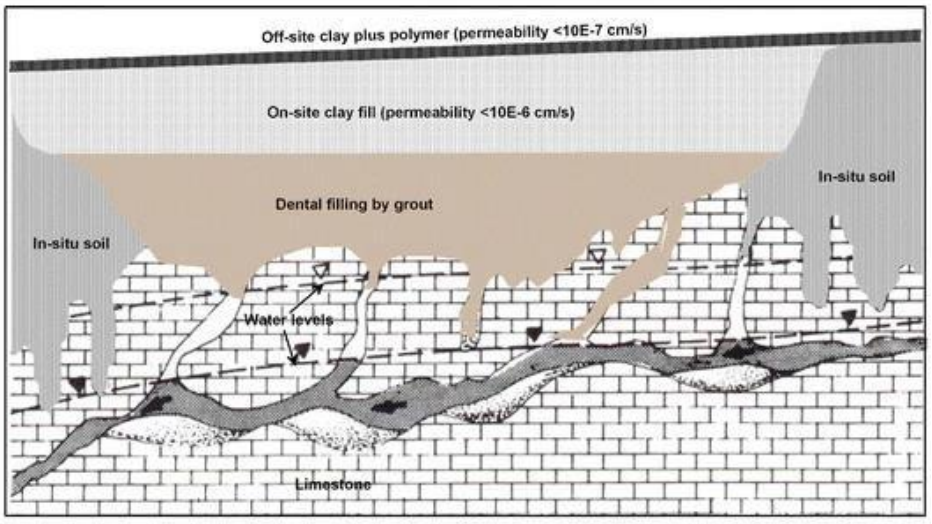

Figure 2.51 (continued). Examples of sinkhole remediation techniques (Zhou and Beck 2008).

Sinkhole remediation	Typical diagrams
Backfilling with drain pipes	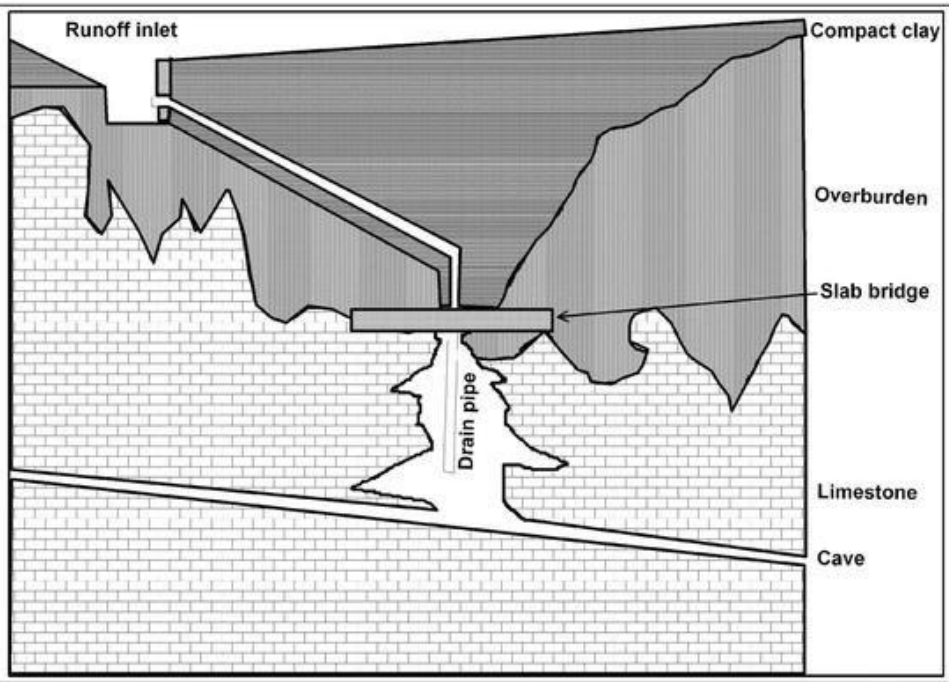
Designed filtration system (Beck and Zhou 2002)	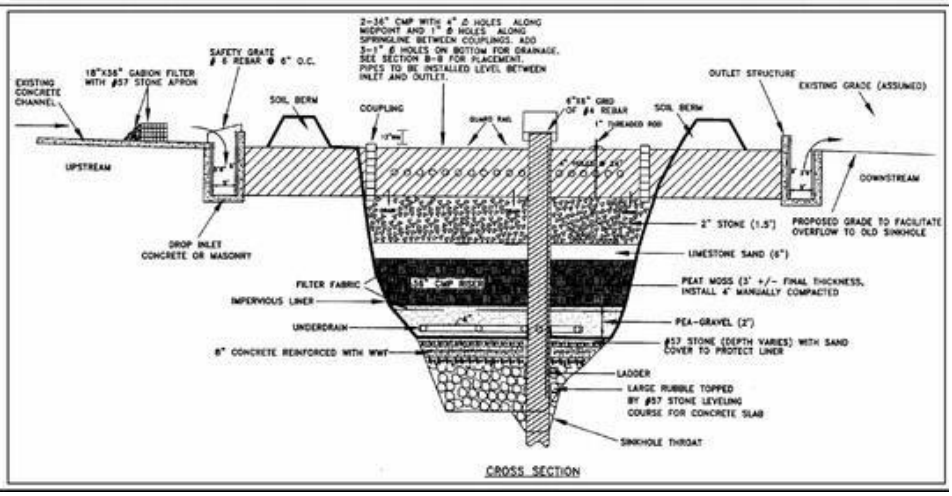

Figure 2.51 (continued). Examples of sinkhole remediation techniques (Zhou and Beck 2008).

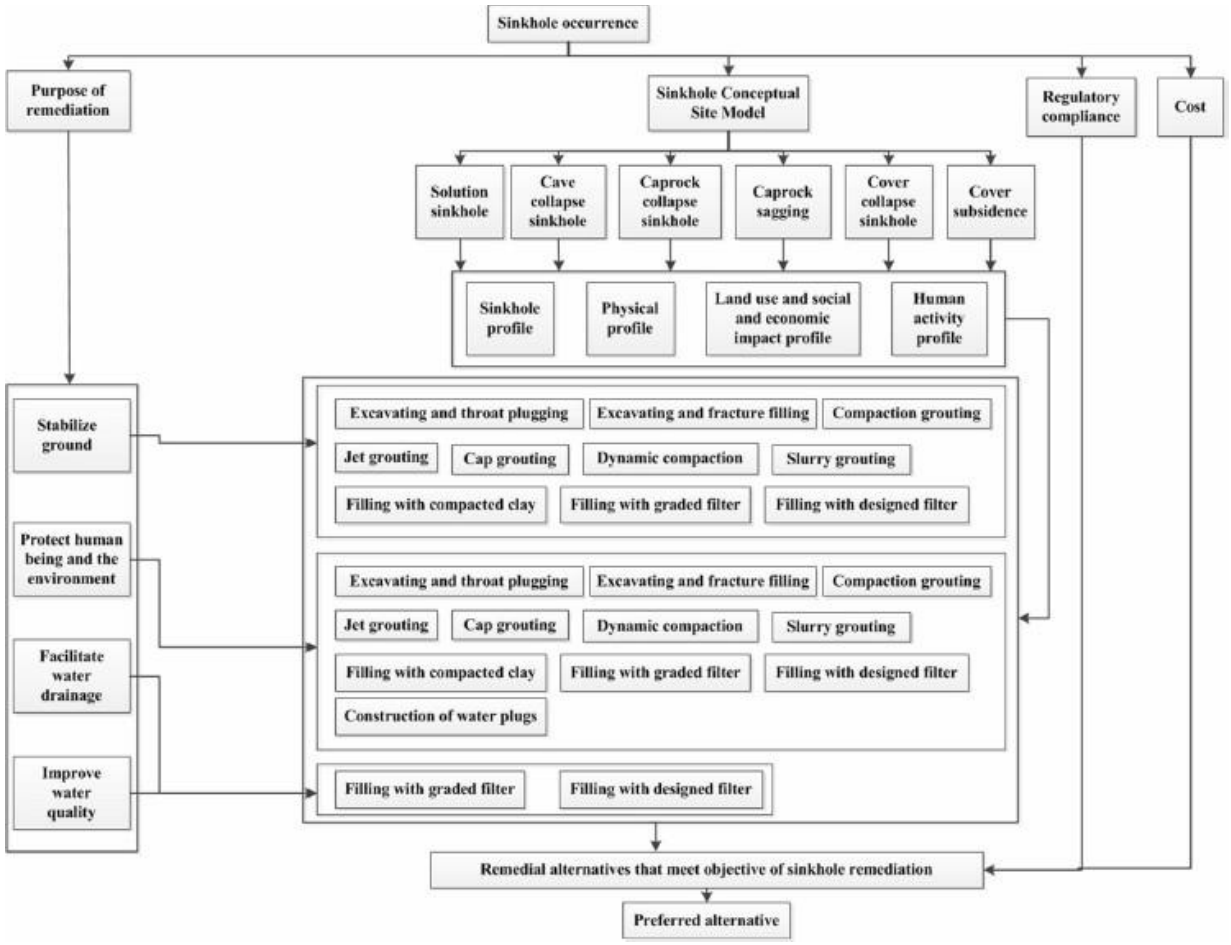

Figure 2.52. Recommended sinkhole remediation selection process (Zhou and Lei 2017).

2.3.1.1.*Inverted Filter Approach*

This method is the most intuitive and simplest solution to remediate an existing sinkhole capable of tolerating minor subsidence and for which the long-term effects of reactivation are minor (Zhou and Lei 2017). The inverted filter approach is typically used to block the throat of shallow sinkholes under the following circumstances (Zhou and Beck 2011):

- Shallow sinkholes within 10 m from natural ground surface
- Sinkholes of small (< 2 m diameter) or medium-size (2 m - 5 m diameter)
- Subsidence features of all sizes (< 2 m up to 15 m diameter)
- Existing infrastructure located at a distance, outside the area proposed for bulk excavation.

This process should be performed in a clay free zone to maximize its efficiency and lower the risk of failure. To initiate the inverted filter construction, the sinkhole area is excavated to expose either bedrock or its throat. An initial layer of rock/boulders in combination with sandy gravel is placed at the bottom of the excavation to block the throat (sometimes with a geosynthetic filter fabric).

The area is then returned to grade with layers of progressively finer material compacted in place and sealed with a geomembrane to prevent future water infiltration (Xeidakis et al. 2004) (Figure 2.51 labeled as "Graded Backfilling" and Figure 2.53). To improve the strength of the backfill, cement paste may be added to consolidate the filling material while the pit is being filled (Chen and Xiang 1991).

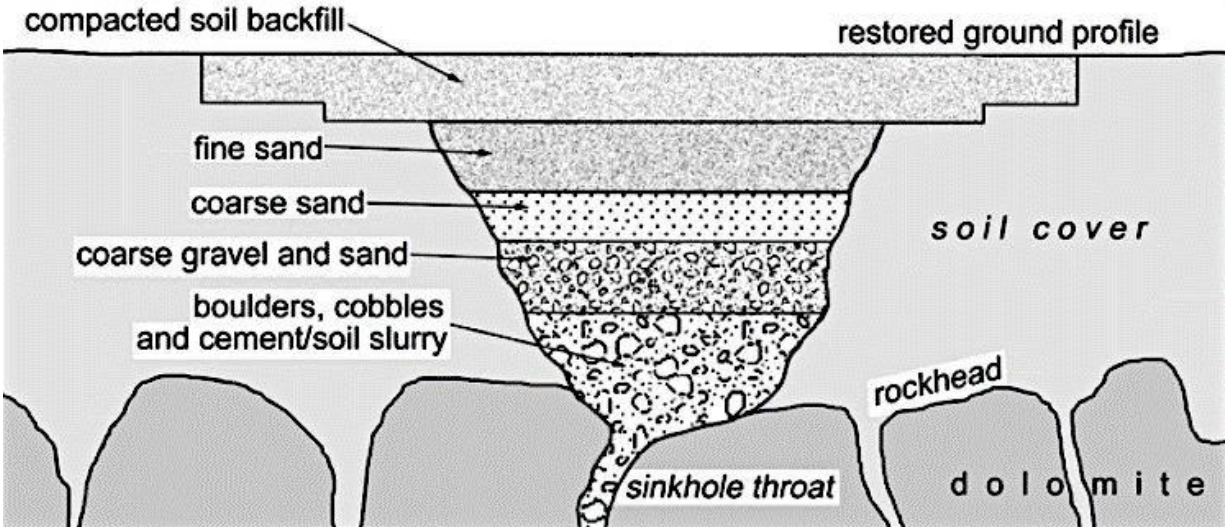

Figure 2.53. Schematic of an inverted filter to rehabilitate a small subsidence sinkhole over dolomite (Waltham et al. 2005).

2.3.1.2.*Grouting*

Innovations in grouting techniques have led to the consistent use of this ground improvement technique to address issues with sinkholes and karst. Grouting involves the injection of a cement- or chemical-based material to fill a cavity and seal any secondary karst voids and fissures. This typically increases the strength of the injected area and make it less permeable. The grout suspensions typically include water, cements, bentonite clay, sands and fillers, and other additives. Each country follows its own standards to define the desired properties and rheology of grout while understanding that site-specific conditions of the karst are also essential for grouting design (Nonveiller 1989). Generally, however, there are two (2) main types of grouts commonly employed for sinkhole prevention and remediation: (1) low mobility grout (LMG) (e.g., compaction grouting); and (2) high mobility grout (HMG) (e.g., slurry/cap grouting) (Gutiérrez et al. 2019). However, selection of both the grouting method and material is frequently left to the contractor because karst repairs are often performed on an emergency basis. This may result in less-than-optimal procedures and excessively high cost to the owner (Warner 2008). Additionally, due to the inherent uncertainty in mapping the extent of voids/fracture, there may be an enormous amount of grout loss from uncontrolled filling, particularly with high mobility grouts. Figure 2.54 provides a recommended flow chart for proper selection of grout technology for karst applications.

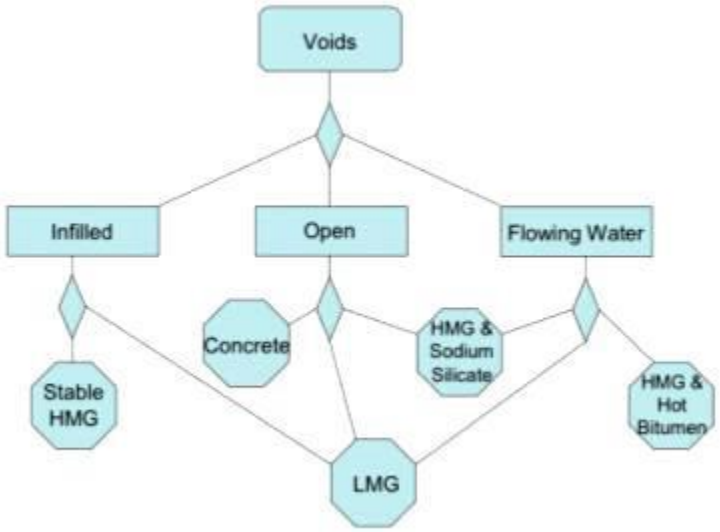

Figure 2.54. Recommended methods and grout technologies for karst features (U.S. Army Corps of Engineers 2017).

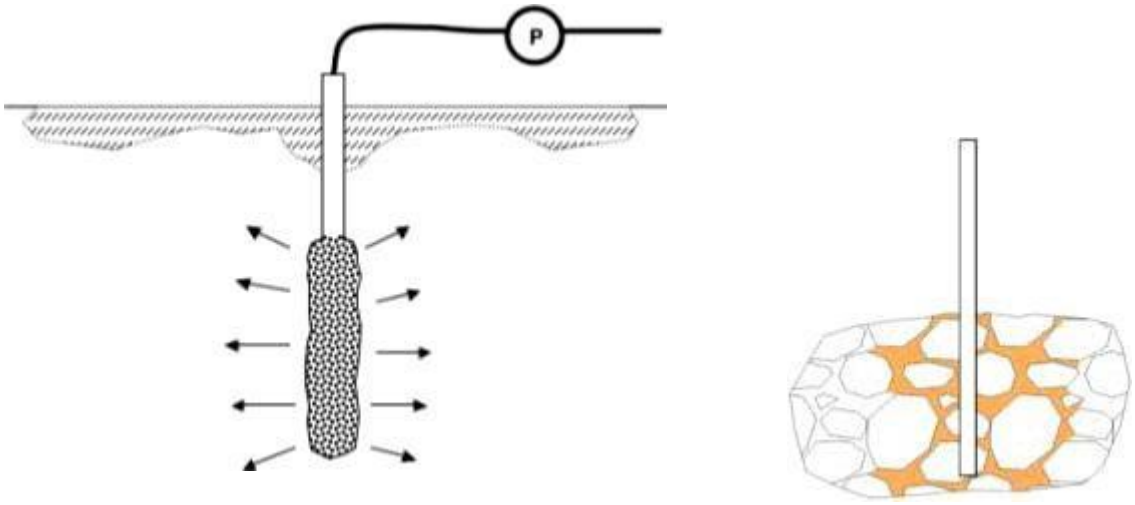

(a) **(b)**

Figure 2.55. Schematics of karst-related grouting operations: (a) compaction grouting; (b) slurry/cap grouting.

Compaction grouting is generally considered a relatively fast and economical method relative to other compaction methods. The process consists of injecting an LMG under high pressure to fill subsurface voids and compact the surrounding soil (Figure 2.51, Figure 2.55). It is generally used for pre-construction ground improvement, to halt foundation settlements, rectify sinkhole problems, and to lift and level slabs and foundations (U.S. Army Corps of Engineers 2017). The grout consistency, pressure of grout delivery, and grout placement strategy are important aspects of effective compaction grouting (Waltham et al. 2005). Additionally, special considerations should be accounted for in cases of high flow rates of water.

High pore pressures can develop that cause the soil to fail in an undrained state and cause it to move with the rapidly expanding grout front (Zisman and Clarey 2013).

On the other end of spectrum for grout rheology, HMG behaves much more like a fluid and is pumped into the subsurface under low pressure. Slurry grouting is generally the most appropriate for typical karst sites in which voids are found in both the rock and cover soils, and when structural loads are light to moderate (Fischer and Fischer 1996). In this method, the HMG is injected into the cavernous bedrock using cement-based mortar with aggregates with the aim of filling voids and preventing erosion of cover material (Kamal et al. 2011). Cap grouting is usually applied for treating an extensive area with small but distinct fractures located at the surface of the bedrock. It involves injection of HMG at the bedrock surface to form a seal over cavities and to prevent piping of soil (Figure 2.51, Figure 2.55). Cap grouting consumes less grout than compaction grouting (Bansah 2018).

2.3.1.3. *Deep Dynamic Compaction and Preloading*

Deep Dynamic Compaction (DDC) generates impact energy by dropping a heavy weight from a significant height to compact soils that are prone to significant settlement (Lukas 1995). The impact displaces the soil grains and rearranges them into a denser configuration (Indraratna et al. 2015). At sites with shallow karst features, DDC can be used to collapse voids and subsequently mitigate sinkholes prior to construction (Zhou and Beck 2011; Woods 2014; Fischer and Fischer 2015). However, though this approach may mitigate void formation in soils, the root cause of the void may remain. Consequently, a new void and then a subsidence sinkhole may develop in the in the future if no further action is taken to remediate the site (Sowers 1996). DDC is also inappropriate where vibrations may reach adjacent sites to induce new sinkholes. Another similar option to improve the ground is to preload the site with a temporary surcharge to consolidate weak and compressible soils. This method has been used on soft soils in shallow solution dolines and filled sinkholes (Sowers 1996), but its application is limited by the long timeframe required for effective pre-loading.

2.3.2. Role of Geophysics in Sinkhole Remediation

Many of the sinkhole remediation approaches discussed herein operate primarily below ground with little surficial evidence of their outcomes. For example, the various grouting methods primarily rely on field quality control measures that either verify the consistency of the grout and its mix design (e.g., compressive strength) or measure the pressure/volume/injection rate during operations (U.S. Army Corps of Engineers 2017). They also do not typically provide any obvious surficial visual representations that assure the desired sinkhole mitigation outcome was achieved. DDC and preloading efforts infer the remediation of sinkhole-related subsidence based on ground deformations. This contrasts with the inverted filter approach where an excavation is performed and construction of the filter proceeds from the bottom up with visual confirmation of the operations. Consequently, there is a need for quality control methods that can provide subsurface information to monitor sinkhole remediation efforts. Geotechnical subsurface investigation techniques such as SPT and CPT have long been employed to track pre- and post-ground improvement changes to the subsurface (e.g., Solymar 1984; Schmertmann et al. 1986; Tanaka and Sasaki 1989; Castelli 1991; Hayden and Welch 1991; Chow et al. 1992; Chow et al. 1994; Reed et al.

1998; Strauss et al. 2004; Miao et al. 2006; Russell et al. 2008; Hamidi et al. 2010; El- Kelesh et al. 2012; Chin et al. 2013; Miller and Roycroft 2014; Shen et al. 2019) (Figure 2.56). However, as was previously noted, SPT and CPT provide limited spatial coverage of a site, suffer from a lack of repeatability at the same location, and are destructive methods. Hence, geophysical approaches may be better suited to map a whole area and evaluate changes in conditions caused by ground improvement since they can address the issues with SPT/CPT.

As a result of the advantages offered by geophysical methods, they have been routinely used as a quality control measure for DDC, grouting, and other ground improvement techniques when these operations have been performed to address geotechnical issue such as excessively soft soils, tunneling, liquefaction, and other similar applications (e.g., Byle et al. 1991; Miao et al. 2006; Haramy et al. 2009; Hutchinson and Beird 2016; Xie et al. 2016; Yu et al. 2016; Lin et al. 2017; Mooney and Bearce 2017; Park et al. 2018; Qian et al. 2018; Lin et al. 2019; Park et al. 2019). This highlights their applicability for monitoring changes to subsurface conditions, particularly when mapping large areas over which ground improvement operations may generate spatially variable conditions. However, there is a limited amount of literature that documents the use of geophysics specifically to monitor ground improvement operations for sinkhole mitigation (e.g., Zheng et al. 2010; Harro and Kruse 2013; Bai et al. 2018). It is unclear the exact reason why case studies are limited for geophysical quality control of sinkhole remediation efforts. The fundamentals of the methodologies are unchanged from other ground improvement applications as are the geophysical methods themselves. Perhaps the highly variable nature of residual soils in karst contributes to complications with interpretation of ground improvement techniques. Even so, the limited amount of documentation of geophysics as a tool to monitor sinkhole remediation efforts highlights an area of research need.

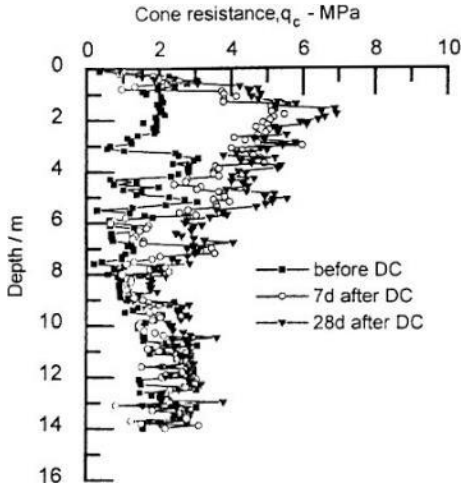

Figure 2.56. Example of changes to the subsurface monitored by CPT before and after DDC (Miao et al. 2006).

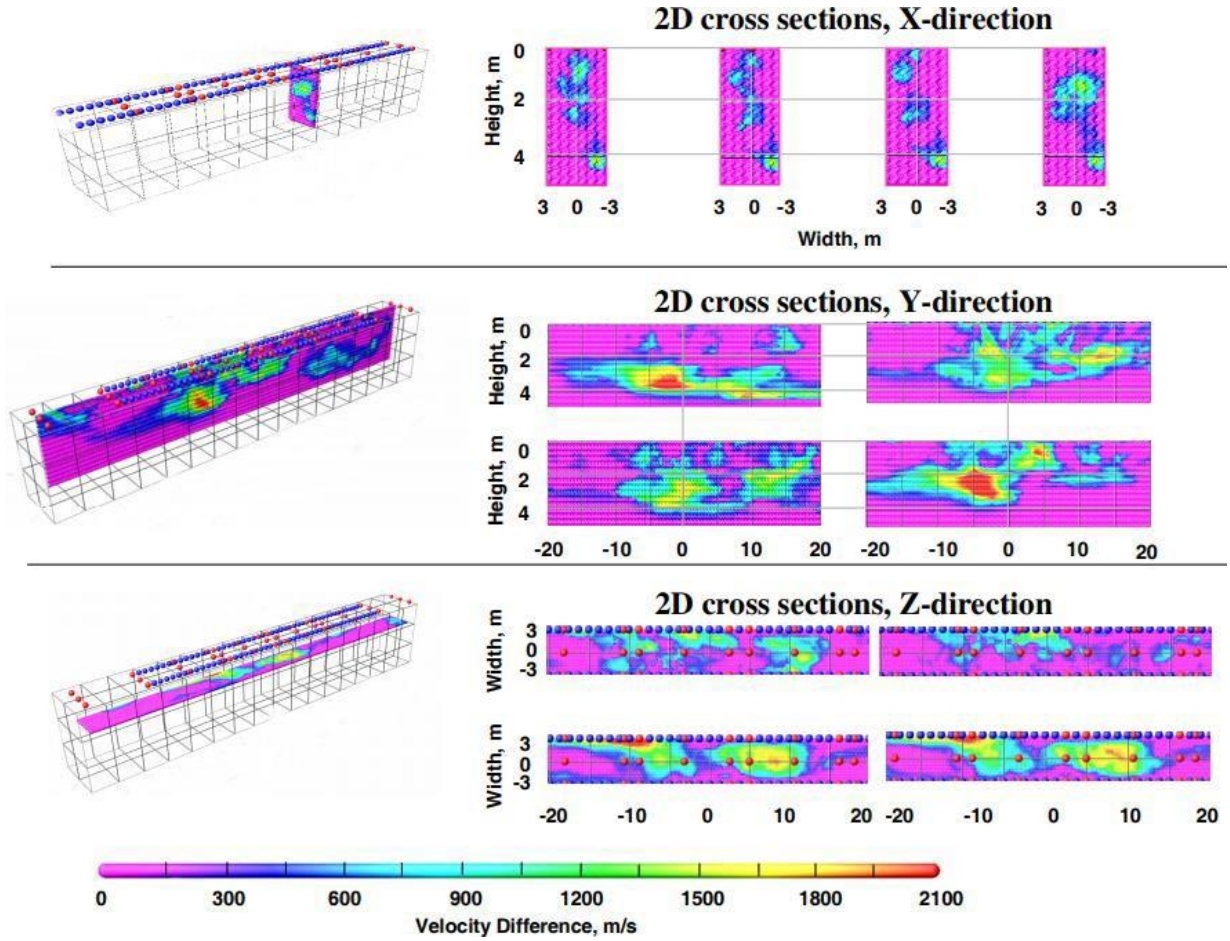

Figure 2.57. Example of changes to the subsurface monitored by seismic methods before and after compaction grouting (Haramy et al. 2009).

2.4. Summary

This chapter provides a thorough discussion of geophysical methods as they relate to karst/sinkhole evaluation and mitigation. The rapid technological advances of the recent decades have drastically improved instrumentation, equipment, and analytical capabilities. This has fueled an increase in the use of geophysics as a tool in engineering studies. Based on a review of the existing literature, several major topics were addressed in this chapter, including the formation of sinkholes, fundamentals of various geophysical methods, advances in geophysical testing, and sinkhole mitigation strategies. Some of the lessons learned from this review include:

- Standard geotechnical investigation techniques such as SPT and CPT are routinely used to characterize site conditions and evaluate karst/sinkhole features. However, they provide a spatially constrained measurement at a single location that may or may not be representative of general site conditions.
- There are five (5) major geophysical methods that are most applicable to karst/sinkhole evaluation: Electrical Resistivity (ER), Ground Penetrating Radar (GPR), Electromagnetic

Induction (EMI), Gravity surveys, and Seismic surveys (including reflection/refraction and surface wave methods).

- Each geophysical method excels at some aspect related to sinkhole evaluation but presents several limitations in its application. There is no “one size fits all” method and site- specific conditions should guide selection of an appropriate geophysical method.
- Advancements in computational capabilities has allowed the further development and deployment of analytical techniques such full waveform and joint inversion. These methods increase the resolution and can improve the accuracy of geophysical methods that primarily rely on the solution of an inverse problem. This increase in resolution and accuracy comes at a cost of higher computing and simulation efforts, which should only continue to decrease as computational resources continue to improve and decrease in cost.
- Sinkhole remediation typically requires a two-pronged approach whereby the sinkhole source or trigger is addressed, and any subsidence features are remediated. Most sinkhole remediation efforts include some form of ground improvement such as grouting or compaction.
- Geophysical methods have been often used to serve as a ground improvement quality control measure. In this manner, geophysics has been used to evaluate pre- and post-ground improvement changes to subsurface conditions. However, very little exists in the literature where these methods were used for this purpose directly for sinkhole applications, which represents an area of research need.

3. PENNDOT EXPERIENCES WITH SINKHOLES

A detailed investigation was performed on PennDOT District 6-0 projects related to sinkhole hazards to establish their experiences with sinkholes and karst. The projects highlighted the ways in which PennDOT has evaluated, mitigated, and provided for quality control of sinkhole hazards as well as the implementation of geophysics in their investigation. This chapter focuses on assessing the specifics of PennDOT experiences on these projects and on highlighting any areas of need. In this regard, the following questions related to PennDOT sinkhole experiences are discussed:

- What are the typically employed karst hazard identification, mitigation, and quality control techniques by PennDOT?
- What are the geophysical approaches that PennDOT used in the case of karst detection?
- What are the needs and recommendations to reduce the risk of karstic hazard occurrence in PennDOT projects?
- How can joint and/or full waveform inversion improve future PennDOT experiences?

3.1. Selection of Projects

Data for several projects in which there were signs of karst activity was provided by PennDOT. This included the following projects:

- 0029 & 202 at Matthews Rd
- 0029-SNK
- 0030-SNK
- 0076-SNK
- 0202-300
- 0202-320*
- 0202-330
- 0202-400
- 0202at Powderhorn Lane
- 0372-Coatesville Roadway Voids
- 9401-MG2 Ridge Pike*
- 0422-ITM
- 0422-SNK*
- 0422-SRB 23 over 422*
- 0476-RES
- 1010 Sweedsford Rd High Occupancy Permit (HOP) 97307*
- 3007-SKH*
- 3013-90S*
- 3051-78B*
- 7401-GAP*
- Chester Valley Trail*
- Church Road*
- Exton Bypass

All files related to these sinkhole projects were thoroughly examined as potential case histories and locations for the field testing originally proposed for this research study. To properly select the preferred projects, it was necessary to classify and compare different influential factors. The critical aspects affecting project selection were ultimately narrowed down based on the project goals, which necessitate access to sufficient a priori data of the conditions at the site and adequate site accessibility. Therefore, the following key aspects of the projects were used to guide selection (in the approximate order denoted):

- Availability of geotechnical data
- Site accessibility
- Availability of karst report

- Previous use of geophysics
- Sinkhole activity and remediation efforts

Those projects with asterisks in the list above did not have sufficient detailed information regarding the nature of the sinkhole activity, subsurface investigation to identify sinkholes, or mitigation strategies to warrant additional investigation for the purposes of this project. The remaining projects were reviewed to summarize PennDOT experiences with sinkholes.

3.2. PennDOT Experiences

The following sections provide the findings with respect to PennDOT District 6-0 experiences with sinkhole-related issues based on the projects examined for this study.

3.2.1. Types of Projects Affected by Sinkholes

Constructing highway-related projects over existing sinkholes or other karstic features is often unavoidable. Although the presence of karst and its potential manifestations are site-specific and should not be generalized, finding any patterns in the case histories regarding the most affected construction projects can provide essential information about long-term management of karst-related hazards for highway infrastructure. Table 3.1 summarizes the PennDOT projects in terms of what infrastructure was affected by the development of sinkholes. Remedial measures used to correct sinkhole problems in District 6 are mainly divided into bridging and drainage solutions as well as ground improvement/grouting, while relocation is less considered for PennDOT projects.

3.2.2. Pre- Versus Post-Construction Efforts

In general, addressing karst and its consequences in road construction projects can incorporate efforts into two phases of the project:

- Preconstruction (or proactive) measures: Activities or efforts that take place during initial site characterization before or during construction. These represent situations where karst and sinkhole activity have been previously identified for the project site and concern exists about long-term development of sinkholes once the structure has been constructed.
- Post-construction (or reactive) measures: Activities that take place after a structure has been constructed and in reaction to an active karst-related hazard.

Clearly, use of proactive methods during the design and maintenance of any structure located in karst has higher reliability in terms of the system's long-term stability and service. Understanding of karst processes and formulating remediation strategies in advance of a construction project can also lessen future maintenance costs and detrimental environmental impacts. However, due to financial and time constraints when carrying out projects, transportation agencies often deal with karst in highway design and construction by adopting post-construction approaches.

Table 3.1. Development of karst hazards at selected PennDOT District 6-0 case histories.

Project Title	Project Summary	Proposed/Affected Infrastructure	Pre- or Post-Construction Efforts
0029-202	Reconstruction of Matthews Rd, Chester County, PA	Roadway	Post-Construction
0029-SNK	Treatment of subsidence due to recurring sinkhole formation	Drainage and other underground facilities, temporary excavation and slopes, roadway	Post-Construction
0030 SNK	Emergency sinkhole repair and roadway construction	Stormwater pipes and roadway	Post-Construction
0076-SNK	I-76/202 Interchange Sinkhole Remediation	Stormwater and other underground facilities, slope, roadway	Post-Construction
0202-300	Widening SR 202 in both directions, reconstructing ramps, and constructing a connector road	Sinkholes were inside and outside of the project right-of-way or a significant distance from the proposed construction (Project involved the replacement/modification of 12 bridges and three culverts, and construction of sound barrier walls, retaining walls, and sign structures)	Pre-Construction
0202-330	Widening a SR 0202 bridge	Retaining wall, culvert, sound barrier	Pre-Construction
0202-400	Widening of SR 0202 and the construction of numerous new ramps	Roadway and structures	Pre-Construction
0202-Powderhorn Lane	Remediation of sinkhole	Drainage facilities and soil fill	Post-Construction
0372-Coatesville Roadway	Sinkhole remediation	Roadway	Post-Construction
0422-ITM	Roadway widening	Drainage facility and roadway	Pre-Construction
0476-RES	Reconstruction of the roadway due to sinkhole activity	Roadway and bridge	Pre-Construction
Exton Bypass (S.R. 6030)	Remediation and reconstruction of the bridge at the site where two sinkholes collapsed	Bridge	Post-Construction

Based on the review of the PennDOT projects in Table 3.1, 67% percent of the projects identify cases where karst-related characterization efforts occurred after the occurrence of an anomaly. The remaining 33% of the projects identify proactive measures where efforts were implemented during initial site investigation. It is important to note that there is no available information on the conducted karst assessment and remediation before construction of the projects where proactive measures have been documented. In other words, it cannot be stated conclusively that the karst-related issues in those projects occurred because of failure to perform any investigation of karst in the area or limitations in the existing subsurface investigation techniques. A detailed review of the projects that have carried out pre-construction karst investigation demonstrates that a lot of effort has gone into identifying and eliminating

areas with high karst risk in recent years. However, lack of post-remediation verification is apparent in the case histories as is the role of time in further creating karst-related anomalies that may reduce the effectiveness of each implemented treatment technique.

3.2.3. Site Characterization for Karst-Related Hazards

Mapping sinkholes in the absence of any clear evidence such as surface depressions, sudden drainage, or other karst features is a challenge. Despite the many techniques available to investigate subsurface conditions, none of the methods can be considered completely reliable to detect karst features and their applicability entirely depends on site characteristics, geology, and hydrological conditions. Standard penetration tests (SPTs) and cone penetration tests (CPTs) are the most common geotechnical subsurface investigation techniques for site characterization, including for sinkhole detection. However, these methods have a low probability of intercepting a raveling zone without a-priori information and may consequently miss evidence of sinkhole formation. In fact, there are no accepted criteria to guarantee the true discovery of the subsurface condition. To address the problem, the integration of geophysical and geotechnical investigation approaches can yield complementary information about the subsurface.

Based on a review of the previously mentioned PennDOT District 6-0 projects, test borings were typically drilled to provide information on the subsurface condition for both pre- and post-construction efforts. Also, most projects (10 out of 12) consisted of at least one geophysical exploration to help characterize the subsurface, especially for soft zones detected by boring logs. The geophysical results were used to recommend areas for further investigation where boring logs could verify any subsurface anomalies. Table 3.2 summarizes the geophysical techniques used in the reviewed projects. As can be seen, a wide range of geophysical techniques have been implemented to collect subsurface data and highlight the areas with a higher potential of sinkhole activity. The review also showed that the geophysical techniques were implemented during the design phase. It is notable that, in some cases, additional borings were requested after the geophysical investigation to confirm the existence of any karst features.

Table 3.2. Geophysical methods conducted for selected PennDOT District 6-0 case histories.

Project	Geophysical Methods						
					Seismic Methods		
	ERI	EM	GPR	Microgravity	Refraction	MASW	SASW
0029-202	-	-	-	-	-	-	-
0029-SNK	✓	-	-	✓	-	✓	-
0030-100 SNK	✓	-	-	✓	-	✓	-
0076-SNK	-	-	-	-	-	-	-
0202-300	✓	✓	-	-	-	-	-
0202-330	-	-	✓	-	-	-	✓
0202-400	-	-	✓	-	✓	-	-
0202-Powderhorn Lane	✓	-	-	-	-	-	-

0372-Coatesville Roadway	-	-	-	-	-	✓	-
0422-ITM	✓	-	-	-	-	-	-
0476-RES	-	-	-	-	-	✓	-
Exton Bypass (S.R. 6030)	-	✓	-	-	✓	-	-

The most common approach to evaluate subsurface conditions for sinkholes was one of the multiple methods that use seismic waves, including Seismic Refraction, Multichannel Analysis of Spectral Waves (MASW), and Spectral Analysis of Surface Waves (SASW). One of these methods was used in more than half of the projects where geophysics was performed. The most common of the seismic methods was MASW, which is unsurprising given the robust capabilities of MASW during data acquisition and subsequent analysis. Surface waves demonstrate high signal-to-noise ratio relative to body waves (e.g., refracted waves) and the multichannel acquisition improves the capabilities to resolve the spectral content of the waveforms. The next most used approach was Electrical Resistivity Imaging (ERI), which was used in half the projects where geophysics was performed. Again, this is unsurprising as the measured resistivity of geologic materials is highly related to the extent of voids and moisture present in those voids. ERI results are therefore often used to indicate the presence of loose, saturated soils in the subsurface that can point to sinkhole development.

A noteworthy point is how many of the case histories implemented multiple geophysical methods to provide complementary information and enhance the accuracy of subsurface images. However, the data from these methods were not integrated as part of a joint inversion process, despite the potential for even further improvements in the interpretation of the subsurface conditions. This will be further discussed in a later section of this report.

3.2.4. Sinkhole Mitigation

The characteristics of a sinkhole, including its dimension, depth, and type, as well as the intended use of the site, are key factors determining the repair strategy. The depth to rock also affects sinkhole development, the severity of its manifestation, and the need for and effectiveness of remediation efforts. These factors also affect the potential for future sinkhole reactivation once a particular mitigation technique has been employed. Detailed and comprehensive geotechnical and geological study of the site is of great importance when assessing the most appropriate sinkhole mitigation techniques. Apart from the avoidance of construction in karst-prone areas (which is not usually feasible), there are generally three basic approaches for sinkhole remediation:

- Eliminate sources of water that are driving the formation of a sinkhole
- Modify any passageways for water to cause sinkhole formation
- Reinforce the underlying soil and rock

Typically, the first priority is to remove the water source as the leading cause of karst failures, but such a strategy is not always possible. The next two approaches are named in order of priority, though the reinforcement option is typically more prevalent in projects. As mentioned before, there is no “one size

fits all" solution that can address all existing sinkhole hazards. Engineering judgment must be used based on the available budget, project goal, and site conditions to define the most appropriate treatment technique.

Based on the review of the sinkhole investigation and treatment reports located in the project files from Table 3.1, the following techniques were typically implemented in District 6-0 with the goal of addressing the existing subsidence features and mitigating future sinkhole subsidence activity:

- Geogrid and geotextile mat reinforcement
- Compaction
- Inverted filter (i.e., clogging swallow holes)
- Limited mobility grouting
- Compaction grouting

Table 3.3 presents the chosen mitigation techniques for the reviewed projects. Comprehensive karst reports containing a study of the geology of the area, site background, geophysical and geotechnical investigation, hydrological and groundwater assessment, and finally the presentation of the treatment method and its associated cost estimation were only available for approximately half of the projects in Table 3.1.

Table 3.3. Sinkhole mitigation techniques implemented for selected PennDOT District 6-0 case histories.

Project	Mitigation Technique					
	Compaction	Inverted Filter	Geotextile and Geogrid Reinforcement	Limited Mobility Grouting	Compaction Grouting	Excavation and Replacement
0029-202	-	-	✓	-	-	-
0029-SNK	-	✓	-	-	-	-
0030-100 SNK	-	-	-	✓	-	✓
0076-SNK	-	-	-	✓	-	-
0202-300	-	-	✓	-	-	-
0202-330	-	-	-	✓	✓	-
0202-400	-	-	-	-	✓	-
0202-Powderhorn Lane	✓	✓	-	-	-	-
0372-Coatesville Roadway	-	-	-	-	-	-
0422-ITM	✓	✓	-	-	-	-
0476-RES	-	-	-	✓	-	-
Exton Bypass (S.R. 6030)	-	✓	-	-	-	-

3.2.5. Quality Control of Sinkhole-Related Mitigation Efforts

In areas prone to karst, monitoring of potential sinkhole activity is typically implemented as part of pre-construction site characterization and may also be incorporated during construction. However, comprehensive post-construction monitoring and/or remediation verification efforts is not as commonly documented. At most of the sinkhole mitigation areas, logging, grout take checks, or some other instant methods are used to validate the efficiency of the treatment. However, these efforts may not provide a complete assessment of the effectiveness of the mitigation strategy. For example, the spatial extent of the grouting may be verified by test borings, and additional quality control may be necessary to ensure long-term performance of the repair. This is particularly the case given the importance of time on the formation of a sinkhole. Though a mitigation technique may allow the structure (e.g., foundation, roadway, etc.) to withstand design loads again in the short term, the long-term performance may be compromised by the continual formation of sinkholes if insufficient quality control is implemented during and after mitigation efforts. There is a tendency not to publish data on the performance of sinkhole remediation techniques and, unfortunately, the existing literature on this issue is sparse and can often only be found in non-accessible technical reports. Thus, it is unclear whether robust quality control efforts are indeed not typically performed or if they are just not published in accessible literature.

For the PennDOT projects in Table 3.1, quality control for mitigation operations were checked and recorded to assure compliance with specifications during the project and remediation stage. The following items were considered in the implementation of improvement methods:

- Checking the mechanical condition of drilling and grouting equipment
- Ground or structure movement monitoring like rotating laser level or other monitoring equipment capable of accurately measuring movements of 0.01 feet
- Inspection of treatment procedure performance measures (e.g., grouting rate, pressure, and volumes) by the department's representative
- Measurements of material properties such as slump or strength test for grout or tensile test for geotextiles

Some additional verification testing programs have been performed during the projects to increase the final quality of the operations. For instance, in the case of limited mobility grouting, a grouting test program must be done prior to the start of the project to determine ground response during grouting and to evaluate whether the equipment, methods, and grout mix proposed by the Contractor achieve the desired coherent limited mobility grout mass at each injection stage. Some of the karst reports discuss how the Contractor compared the volumes and pressures of grout injection at primary holes within adjacent secondary and/or tertiary holes. For instance, when compared with primary grout injection holes, secondary limited mobility grout holes are generally expected to have decreased grout takes and increased injection pressures within a given stratum. In the case of any failures and unsatisfactory results, the Contractor was responsible for adjusting the material, equipment, procedure, or adding additional grout holes and performing a new test program at no additional cost to PennDOT.

3.3. PennDOT Needs

The project files provided by PennDOT helped summarize the experience with sinkhole activity in District 6-0. These experiences were compared to the standard of practice and to state-of-the-art methods identified in the literature review efforts to establish potential needs for PennDOT to improve its evaluation and mitigation of sinkhole hazards. The following discussion highlights these findings.

3.3.1. General Findings

The subsurface investigation and site reconnaissance results of the District 6-0 projects indicate the subject areas have a risk of sinkhole development due to the presence of loose soil conditions, observed open sinkholes and depressions, and historical documentation of sinkhole activity in the vicinity of project sites. In response to ongoing surface subsidence activity, it became necessary for PennDOT to repair, stabilize, or design karst-resistant highway structures, pavements, and related assets. Based on the review of available reports, the conducted surveys were completed using standard and/or routinely accepted practices of the geophysical and geotechnical industry. However, this still inherently poses some limitations due to unforeseen site-specific conditions and the challenges associated with analyzing and interpreting geotechnical and geophysical test results. Additionally, subsurface conditions were typically not directly monitored in a comprehensive manner for quality control of mitigation efforts to ensure long-term performance of the infrastructure after repair. This may be particularly beneficial to prevent future sinkhole occurrence given the influence of altered subsurface conditions and subsurface drainage patterns due to grading and construction activities. In this regard, two important issues should be considered for future projects which may contribute to reductions in potential sinkhole hazards for District 6-0 projects:

1. There are inherent limitations in the use of routine geophysical and geotechnical techniques to identify anomalous zones indicative of incipient or active sinkhole activity. The amount of uncertainty present in the results from these techniques can negatively affect the ability to make accurate assessments of the spatial extent of a sinkhole and the cause of its development. Implementation of advanced analytical techniques for various geophysical methods can help to enhance performance and reliability. Current geophysical research has pushed developments that attempt to map the subsurface conditions with more resolution and higher reliability. This includes the use of integrated geophysical methods for joint inversion, methods to better constrain data by existing ground truth information, and use of high-performance computing (HPC) to better simulate subsurface conditions with full waveform tomographic methods.

2. Another issue is the lack of awareness of long-term karst activity and changes in conditions, especially after performing treatment procedures and ending a project. Focusing all the attention on karst conditions during the project is a process that is well considered in most operations. However, due to the area's geological and hydrological conditions, the potential hazards of sinkhole events are still present and need to be monitored over longer time intervals. Moreover, it is important to verify the effects of any mitigation efforts to ensure long-term performance.

The following sections discuss these issues in more detail and describe the role of the TEM WO 015 research efforts addressing some of the PennDOT sinkhole evaluation and mitigation needs.

3.3.2. Role of Advanced Geophysical Analytical Techniques

As noted in Table 3.2, PennDOT has often used geophysical techniques to detect sinkholes or other anomalies. For most projects, more than one geophysical method was used to provide complementary information. However, each method has its own limitations and current standard of practice analytical techniques can fail to provide more in-depth engineering information regarding the extent of sinkhole conditions. Additionally, the interpretation of each dataset introduces some subjectivity that reduces the reliability of the prediction of subsurface conditions. Thus, there exists a need to address these shortcomings and better improve the capabilities of existing geophysical efforts often employed to investigate sinkholes. The literature review identified two primary ways by which the data already being collected from PennDOT sinkhole projects can be further improved to address the issues: (1) integrated data processing of geophysical data (i.e., joint inversion); and (2) advanced inversion techniques such as full waveform tomography.

3.3.2.1 *Joint Inversion*

As previously highlighted in the literature review, joint inversion of complementary geophysical data sets has been used with increasing frequency to address the limitations of current geophysical investigation techniques. The purpose of joint inversion is to develop one objective function for optimization from the individual objective functions representing the various data sets. In this manner, joint inversion can better constrain the inversion results and can produce mutually consistent estimates of soil properties because the results must explain all data simultaneously. This occurs because the different methods have different capabilities (e.g., resolution, sensitivity, etc.) and the incompatibilities for one type of data can often be resolved by another. Joint inversion is often used in cases where different types of geophysical methods are combined (e.g., seismic and microgravity), though it is also possible to jointly invert datasets from similar methods (e.g., seismic refraction and MASW). Since PennDOT is already often using multiple geophysical techniques on sinkhole projects, the application of joint inversion would not incur any penalties in terms of additional data acquisition efforts relative to current standard of practice for PennDOT. Instead, the additional efforts would focus on development of an appropriate workflow and optimization scheme by which to jointly invert the data. Many studies presented in the literature review have demonstrated an improvement in the overall qualities of the results from inversion after applying a joint inversion approach. Therefore, the use of joint inversion represents a potential way by which to address the limitations in the current standards of practice with only a relatively modest increase in effort. The goal of TEM WO 015 was to explore how to effectively develop useful joint inversion workflows with the most common geophysical methods used for PennDOT projects and to evaluate the improvements offered with a joint inversion approach relative to the current standard of PennDOT practice.

3.3.2.2. *Full Waveform Tomography*

Another advancement in geophysical analytical techniques that can address PennDOT's needs and improve subsurface characterization of sinkholes is full waveform tomography. The physical properties of geologic materials highly affect the way both stress and electromagnetic waves propagate through the subsurface. Consequently, a Full Waveform Inversion (FWI) scheme can be introduced with seismic and GPR methods to decode and acquire as much information as possible from the entirety of the acquired waveforms. FWI proceeds with an initial selection for a starting model based on any available knowledge of the domain. Numerical simulations are then used to model wave propagation and generate a set of synthetic signals. The inversion proceeds by comparing these synthetic waveforms and the waveforms collected from the field and making changes to the numerical model to minimize the misfit between the synthetic and observed waveforms. A full waveform based tomographic approach does not necessitate major changes to the current data acquisition schemes of seismic and GPR methods. Rather, increased efforts are necessary to define an effective inversion workflow, selection of an appropriate misfit function, and proper development of the numerical simulation. As with joint inversion, the literature review in Chapter 2 highlighted several studies that have demonstrated the increased resolution capabilities of FWI relative to standard analytical methods for both GPR and seismic methods. The goal of TEM WO 015 was to explore the development of effective full waveform tomography workflows based on the seismic and GPR methods used in PennDOT projects and to evaluate how they can address the limitations with the current standard of PennDOT practice.

3.3.3. Improvements to Quality Control of Sinkhole Mitigation Efforts

Based on the review of PennDOT projects in Table 3.1 and from the literature review efforts in Chapter 2, little data exists on verifying the efficacy of the various sinkhole mitigating approaches. Generally, the verification tests that are performed as quality control for mitigation efforts include drilling of test borings in the improved areas, grout take checks, and other similar efforts. The data from these verification tests are limited in scope in terms of delineating the treatment level, spatial extent of the mitigation efforts, and overall quality of the construction. Additionally, the review of the PennDOT projects highlighted in Table 3.1 indicate that no long-term monitoring methods have been utilized to monitor sinkhole activity, resulting in repeated damage to structures and roads even when previous mitigation efforts have been implemented. Given these issues, it is difficult to evaluate whether repeated long-term sinkhole activity at a site represents the development of new, unrelated sinkholes, or if such sinkhole activity is due to insufficient quality of the original mitigation efforts and/or unanticipated changes to the site conditions from the mitigation efforts themselves.

At this time, there is no instrument or approach that has been specifically developed for long-term monitoring of sinkholes. The existing literature identifies subsurface and ground-based methods (e.g., borehole extensometers, inclinometers, etc.) and remote sensing (e.g., LiDAR, InSAR, etc.) techniques as potential alternatives that have been used in several other applications. Subsurface and ground-based methods are comparatively lower in cost to implement relative to remote sensing methods. However, remote sensing offers a more comprehensive assessment of a site in terms of spatial coverage of ground displacement data. In any case, long-term monitoring efforts can potentially prevent damage to highway

infrastructure by identifying potential problematic sites where ground displacement indicates the possible development of an active sinkhole.

With respect to the issue of verification of mitigation efforts, advanced geophysical techniques can provide useful information about site subsurface conditions prior to and after mitigation. In this way, a more comprehensive assessment can be performed regarding the effectiveness of the proposed mitigation strategy and the potential for future development of additional sinkholes. The efforts of TEM WO 015 examined how joint inversion techniques and full waveform tomography can specifically aid with quality control of sinkhole mitigation efforts. Long-term monitoring of sinkhole activity at either a localized site scale or at a regional scale across District 6-0 was beyond the scope of the project.

4. FIELD TESTING

Efforts to identify potential field sites occurred concurrently with the review of PennDOT sinkhole case histories summarized in Chapter 3. Project selection was ultimately narrowed down based on the availability of geotechnical data, karst reports, previous use of geophysics, nature of the sinkhole activity and remediation efforts, and site accessibility. Issues with site accessibility can severely limit the resolution, depth, or functionality of some geophysical tests. These issues can include cultural features like human-made objects (e.g., fencing, barriers, etc.), vegetation density, groundwater existence and its salinity, traffic, soil type, and topography. Consequently, an initial assessment of site accessibility was performed using satellite imagery and the street view feature from Google Earth®. A small subset of sites from the list of case histories in Chapter 3 was selected for additional field reconnaissance by the Temple research team (SR 0029-SNK, SR 0202-300, SR 0030-SNK, and SR 0076-SNK). The site visits occurred on Tuesday, October 13th, 2020, in coordination with the PennDOT project technical advisor. As the project progressed, the PennDOT technical advisor communicated an active sinkhole project that had resulted in the closure of a lane of Chemical Road (S.R. 3015 Segment 61, SB) in Montgomery County (Plymouth Township; Latitude 40.105040, Longitude -75.286643) and a planned emergency grouting contract. As with the other case history projects, initial virtual reconnaissance was performed using satellite imagery and street view in Google Earth®. Given the timeliness of the efforts taking place at the site and based on favorable conditions inferred from the virtual reconnaissance, in-person site reconnaissance was performed on Friday, January 29th, 2021. Based on these efforts, the list of potential field sites was narrowed down to two finalists: SR 0076-SNK and SR 3015-SNK. Ultimately, the Chemical Road site was selected because the active sinkholes had led to a road closure, which allowed for excellent access for the geophysical methods undertaken in this research project. Additionally, with grouting operations planned for the site, it would be possible to perform geophysical testing for pre- and post-grouting conditions and evaluate the effectiveness of full waveform tomography as a quality control tool for ground improvement efforts.

4.1. Chemical Road Sinkhole Project Site Conditions

Figure 4.1 provides a satellite image of the Chemical Road sinkhole project site. The site is located at Exit 19 (Plymouth Meeting) for I-476, which is the last exit before the I-276 and toll plaza and interchange. Chemical Road is situated between Ridge Pike and West Germantown Pike and is the primary link between those major thoroughfares. The main entrances to the Metroplex shopping center are also accessed from Chemical Road approximately 400 m from the project site location. Chemical Road is supported by a 20 ft. high embankment at the project site, with the bed of ephemeral Plymouth Creek located at the toe of the corresponding slope and the Cross County Trail located immediately north of the creek (Figure 4.2). The shoulder at the southern part of roadway grades upward to the parking lot of 3025 Chemical Road (Figure 4.2).

The satellite image in Figure 4.1 highlights the approximate location of the sinkholes present at the time. Sinkhole 1 was observed in the westbound travel lane and led to closure of one lane of traffic in that direction (Figure 4.3). At the time of observation for site selection, the depression caused by Sinkhole 1

was approximately 14.5 m long and 4.0 m wide and located at the top of the roadway embankment. Sinkhole 2 formed on the eastbound travel lanes at the southern part of the project. The development of this sinkhole caused a large depression in the roadway that spanned approximately 3.5 m in width engulfing the southernmost lane and was approximately 4.5 m in length (Figure 4.3). During repair of Sinkhole 2, several inches of settlement of the roadway, curb, and guiderail was observed, which led to closure of all lanes of traffic (Figure 4.3). Sinkhole 3 in the dry bed of Plymouth Creek at the toe of the roadway embankment was also mapped in the same timeframe.

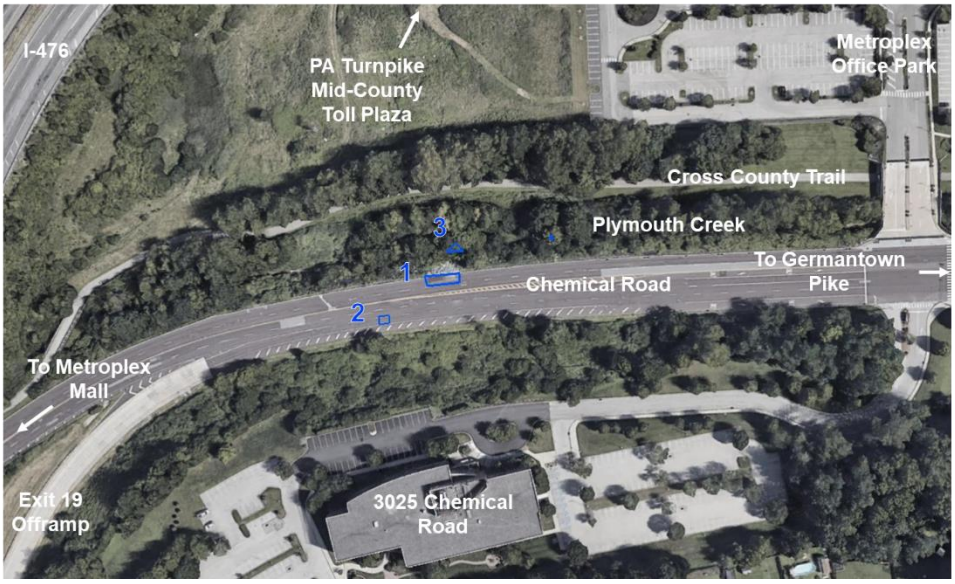

Figure 4.1. Chemical Road sinkhole project location with observed sinkhole activity delineated and numbered in blue.

(a) **(b)**

Figure 4.2. Chemical Road: (a) Looking east from northernmost lane towards Plymouth Creek; (b) Looking south towards 3025 Chemical Road.

(a) **(b)**

(c)

Figure 4.3. Sinkhole activity at the Chemical Road site: (a, b) Sinkhole 2 that developed on eastbound lane of Chemical Road; (c) Sinkhole 1.

4.2. Previous Site Investigation Efforts at Chemical Road

In response to the sinkhole activity, PennDOT closed the road to traffic and TRC Engineers, Inc. performed an extensive subsurface investigation program to evaluate the extent of remediation efforts necessary to stabilize the depressions in the roadway. Prior to drilling operations, Schnabel Engineering conducted a geophysical site investigation program on behalf of PennDOT between March 8 and 22, 2021 (Figure 4.4) to target locations for the drilling program and identify the length of proposed remediation efforts. These efforts included electrical resistivity imaging (ERI), multi-channel analysis of surface waves (MASW), and ground-penetrating radar (GPR). A total of four lines were investigated using ERI, including two lines in the adjacent Plymouth Creek bed north of Chemical Road, one line on the southbound lane, and one line along the shoulder of the northbound lane serving as the off-ramp from I-476. The MASW data was collected over a series of four lines that spanned the width of the roadway across the southbound and northbound lanes. GPR data was collected along several lines and covered the zones at the MASW lines. In addition to the geophysical site investigation, a total of 17 test borings were drilled with an Acker XLS Track Mounted Rig drilling between March 29 and April 7, 2021 (Figure 4.4). Continuous sampling was performed using standard penetration testing (SPT) and rock coring when the underlying dolomite was reached.

Raw data from the Schnabel MASW and ERI testing was shared with Temple research team and a small subset of the data was processed to provide an initial working model of site subsurface conditions. All future references to the data collected by Schnabel will herein be referred to as the Department's data. Finalized subsurface results were not initially requested or viewed by the Temple research team to avoid bias when interpreting the geophysical dataset acquired in this research study. Consequently, the geophysical testing efforts in this research study were performed without the aid of an interpreted subsurface profile beyond the boring logs provided by PennDOT during site selection and the results from the small subset of the Department's geophysical data processed by the research team.

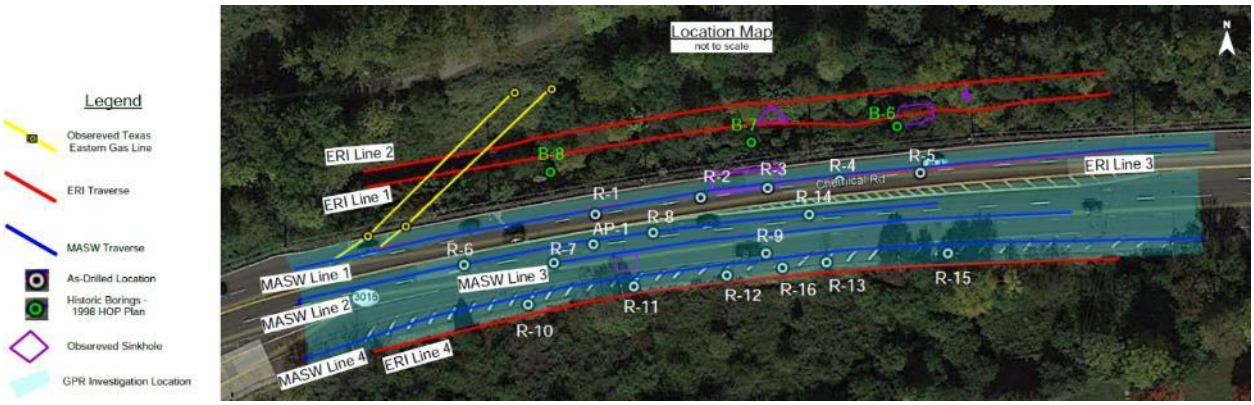

Figure 4.4. PennDOT geophysical and test boring investigation efforts at Chemical Road.

The Department's subsurface investigation efforts generally revealed highly variable conditions with multiple probable weathered zones indicative of karst activity. SPT indicated the presence of soft/loose and wet soils and rock coring indicated fractured, weathered rock of variable thickness with the top of the intact dolomite located as shallow as 10.5 ft below the ground surface at boring R-6 to as deep as 46.5 ft at boring R-2. The test borings along the northbound lane of Chemical Road (i.e., near the shoulder of the I-476 offramp) generally encountered intact dolomite at shallower depths than the southbound lanes closet to the creek bed. Multiple test borings indicated evidence of soil-filled voids, solutioned fractures, and pinnacling in the dolomite.

4.3. Temple Chemical Road Geophysical Testing

Field testing for this project was accomplished over two time periods:

1. June and July 2021 while the roadway was closed prior to any grouting for sinkhole remediation efforts
2. December 2021 immediately after the grouting remediation efforts were completed and prior to the roadway opening

Generally, the site conditions were less active during the first assessment period and the research team was able to mobilize and acquire a larger amount of data without disruptions. The second assessment period was more abbreviated and was subject to increased activity at the site as the roadway was prepared to be reopened after grouting efforts were completed.

4.3.1. Pre-Grouting Efforts

Initial pre-grouting efforts at the site were generally accomplished with minimal interruptions caused by site activities. Instead, weather and access to equipment were more critical factors during this time as some of the equipment was rented from geophysical rental companies, Schnabel, and/or another Temple faculty. Additionally, the pre-grouting field efforts served as a testbed to learn about any issues in the proposed workplan that could be modified to improve future data acquisition efforts.

4.3.1.1. *Seismic Methods*

Seismic measurements were re-acquired along the same survey lines completed by Schnabel Engineering (Figure 4.4). However, the length of the geophone spread was larger and included more receivers. For the acquisition of vertically polarized Rayleigh waves, the seismic data acquisition equipment consisted of a 48-channel landstreamer system with 4.5 Hz vertical geophones spaced at a 1.0 m interval, resulting in a total array length of 47.0 m (Figure 4.5). The input of vertically polarized Rayleigh waves was generated using the same PEG-40 accelerated weight drop (AWD) source used by Schnabel in their field efforts (Figure 4.5). Typically, at least five shots were stacked at each location to improve the signal-to-noise ratio (*SNR*). The acquisition of the seismic data followed a pattern that allowed for simultaneous acquisition of data that could be processed using MASW, SR, and FWI. This necessitated the use of shots in between

geophone locations as well as on either end of the array of geophones, as detailed in the procedure below and show in Figure 4.6:

1. Arrange array of geophones at the starting location.
2. Shot #1 is generated at an offset of -6.0 m from the first geophone of the array.
3. Subsequent shots (#2 – #25) are spaced at 2.0 m and generated in between geophones along the array.
4. The final shot #26 is generated at an offset of 6.0 m from the final geophone of the array.
5. The entire array is then shifted by 2.0 m along the acquisition line and the shot at an offset of 6.0 m is repeated.
6. Step 5 is repeated until the entire array has been shifted by 46.0 m such that the new locations of geophones 1/2 are the same as the old locations of geophones 47/48 prior to the shifting.
7. Steps 1-5 are repeated for the new array location.

(a) **(b)**

Figure 4.5. Seismic data acquisition: (a) landstreamer with vertically polarized 4.5 Hz geophones; and (b) PEG-40 AWD source.

The results of this procedure are a total of 192 data files and four overlapping sections of the 48-channel array spanning a total distance of 182.0 m of spatial coverage along the line. FWI and SR can then be implemented with the interior shots, and a pseudo-2D MASW cross section can be developed from all the data files where the array was shifted with a source shot located 6.0 m in front of the array. This procedure was followed for initial data acquisition efforts along MASW Line 4 as originally designated by the Schnabel subsurface investigation (Figure 4.4). However, this approach took multiple days to implement and there was a growing concern that an insufficient amount of FWI data would be acquired for the pre-remediation conditions at the site if the procedure was followed for the remaining lines. Consequently, the steps of the procedure that replicated data files for use in developing a pseudo-2D MASW shear wave velocity (V_S) profile were no longer implemented. The MASW results from Schnabel would instead be used as a basis of comparison for the FWI and SR results in lieu of MASW results derived from data files acquired by the Temple research team. Additionally, MASW Lines 2 and 3 were skipped since the 3D data acquisition efforts would cover that section of the roadway. This left only MASW Line 1 to replicate the areas explored

by Schnabel across the roadway and existing sinkholes (Figure 4.4). The Temple research team performed the data acquisition along MASW Line 1 using modified procedures that only implemented FWI and SR data recovery. Unfortunately, onsite construction operations and storage of equipment/materials limited how much of the line could be accessed by the Temple research team. Data acquisition was completed after 78 data files and only 139.0 m of spatial coverage with FWI and SR data acquisition.

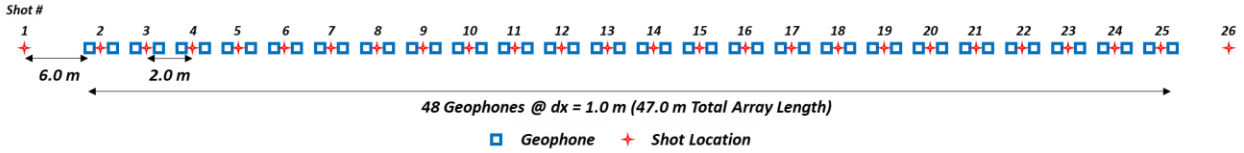

Figure 4.6. Seismic data acquisition layout for one section of an entire 2D line.

(a) **(b)**

Figure 4.7. Love wave data acquisition: (a) array placed along grassy area next to roadway shoulder; and (b) custom Love wave base plate as used at another site.

In between the acquisition of MASW Lines 1 and 4, the Temple research team also acquired several other seismic lines. The accuracy of an FWI analysis suffers at the ends of the array as fewer receivers are affected by the ray-paths between the source and receivers (Virieux et al. 2017). Consequently, anomalous conditions near the center of the array are more likely to be reconstructed properly by FWI. During the acquisition of MASW Line 4, there was never a circumstance where interior FWI shots were collected on an array that was centered on the active sinkhole at the site. For this reason, the Temple research team decided to perform one line that centered around the sinkhole. For that line, only steps 1-4 of the previous procedure were used to generate 24 interior shots spaced along the array at an equidistant 2.0 m and two exterior shots spaced 6.0 m away from either end of the array (Figure 4.6). Additionally, this data acquisition was repeated with a 48-channel array of horizontally polarized geophones along the grassy area immediately adjacent to the shoulder of the roadway approximately 3.0 m from the previous array (Figure 4.7). For this data acquisition, horizontal impacts of a 20 lb

sledgehammer were performed on a custom base plate to generate Love waves (Figure 4.7). The Love wave data acquisition was moved to the grassy area after initial efforts to perform the testing on asphalt resulted in poor *SNR*. Once moved to the grassy area, the horizontally polarized geophones and custom base plate could be readily spiked into the ground to improve *SNR*. This data acquisition would allow the Temple research team to compare the accuracy, robustness, and computational costs of Rayleigh and Love wave FWI and SR. Additionally, Love wave MASW was also acquired by using a source offset of 6.0 m from one end of the array and performing multiple shifts of the array. This array was initially centered at the same location as the first geophone of the FWI array and was shifted by 2.0 m and shots acquired until it was centered on the last geophone of the FWI array.

In addition to multichannel 2D data, 3D data acquisition was also performed at the Chemical Road site. The 3D data acquisition layout as originally proposed consisted of six lines spaced at an offset of 3.0 m so that they spanned 15.0 m along the width of the roadway and shoulder (Figure 4.8). Within each line was proposed a 48-channel array of vertically polarized geophones spaced at a 1.5 m interval, resulting in an array length of 70.5 m. Together, the overall spatial coverage of the proposed 3D array would be 15.0 m by 70.5 m. For each line, exterior shots were proposed at a 0.75 m offset from either end of the array. Interior shots were then proposed in between every other geophone resulting in 3.0 m between shots. When repeated across the entire 3D layout, this shot pattern would create a grid of 3.0 m by 3.0 m. However, the proposed workplan required access to a total of 288 receivers. Despite trying to source additional geophones, the research team was limited to a total of 72 vertically polarized geophones. Consequently, modifications were necessary to the proposed 3D workplan. These modifications represented a compromise between resolution, spatial extent of the 3D array, and length of time necessary to acquire the data. It was decided to maintain a 1.5 m spacing between geophones along the array to ensure high resolution of the resulting reconstructed subsurface profile and the 3.0 m by 3.0 m grid of source locations. However, this meant that each of the six lines consisted of only a 24-channel array of 4.5 Hz vertically polarized geophones spaced at a 1.5 m receiver spacing rather than the 48-channel array originally proposed. This results in a shorter overall length of 34.5 m along each array instead of 70.5 m. However, the 3D layout was arranged such that Sinkhole 2 at the site would be located within the footprint of the 3D array. The other complication was that only three lines could be set up at a given time (i.e., 24 geophones per line x 3 lines = 72 geophones). To get around this issue, the 3D data acquisition was performed with the first half of the 3D receiver array in place. After this was completed, all the shots were repeated after the geophones were moved to the next half of the 3D layout (Figure 4.9). Fortunately, the repeatability of the PEG-40 AWD seismic source ensured consistency of the shots for this approach.

During completion of the 3D array, the research team also decided to attempt an additional 3D array. This new 3D array was immediately adjacent to the previous 3D array and spanned a part of the roadway not covered by the shortened lines in Figure 4.9. However, given the limited amount of time that was left before construction began, this 3D array was arranged in a coarser grid pattern. As before, only three lines were set up with 24 vertically polarized geophones spaced at 1.5 m along each line, resulting in a length of 34.5 m. This time the three lines were offset by 7.5 m so that the entire grid spanned a spatial extent of 15.0 m by 34.5 m like the earlier 3D layout with six lines. The resulting shot pattern followed closely the

first 3D array (i.e., two exterior shots spaced at 0.75 m from either end of the array and interior shots located every 3.0 m thereafter). However, the shots were now located on a 3.0 m by 7.5 m grid instead of 3.0 m by 3.0 m.

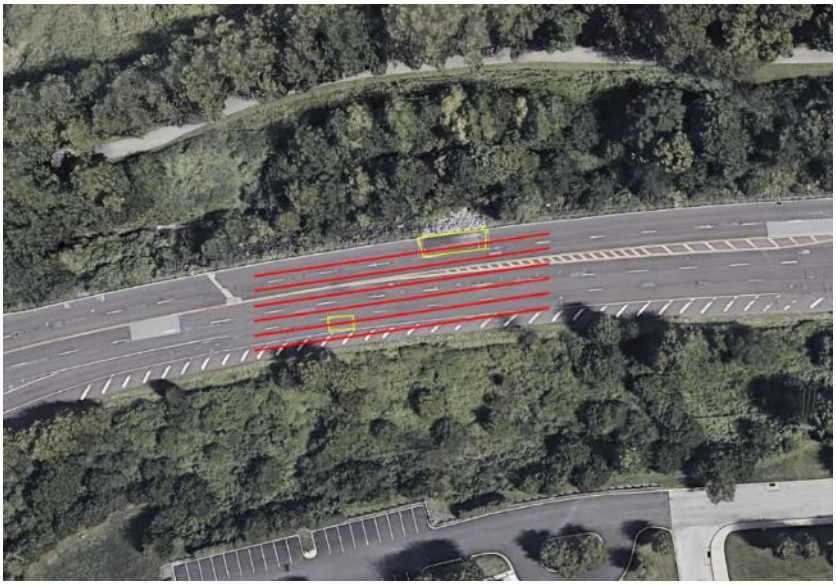

(a)

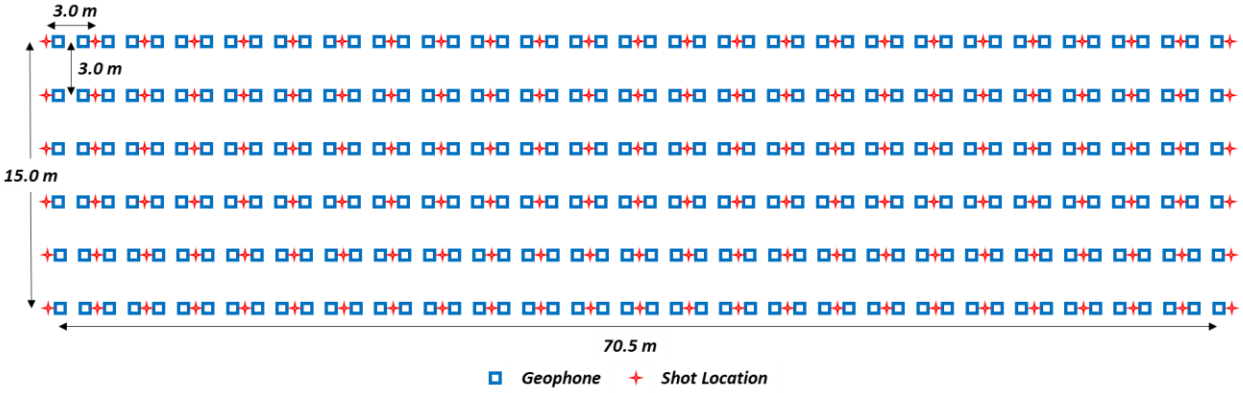

(b)

Figure 4.8. Proposed 3D FWI data acquisition layout: (a) site map; and (b) source-receiver geometry.

(a)

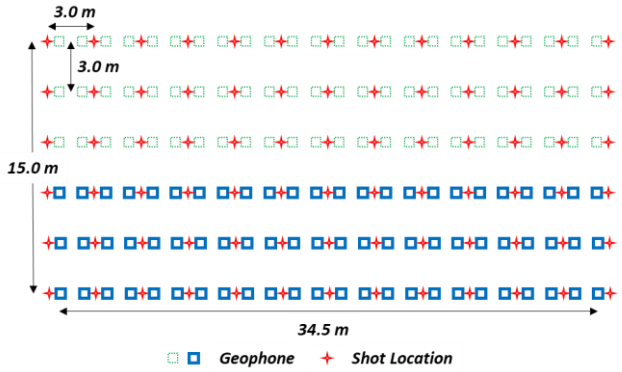

(b)

Figure 4.9. Actual 3D FWI data acquisition layout: (a) site map with end and middle points of lines indicated by red circles; and (b) source-receiver geometry with different color geophones representing the two-part data acquisition process.

In addition to multi-channel 2D data, ambient noise data were also acquired at multiple locations at the site to be processed using the HSVR approach. The ambient noise measurements in this study were performed using a three-component Tromino® seismometer, a common tool employed in many HVSR studies (Bignardi et al. 2016). Due to time limitations with site access and weather conditions, a limited number of locations were tested. The seismometer was placed immediately adjacent to test borings R-10, R-11, R-12, and R-15 when deployed on the roadway asphalt (Figure 4.4). The seismometer was also deployed in the same location but offset by approximately 3.0 m so that the seismometer was located on soil along the roadway shoulder. This additional set of recordings were acquired to explore whether the asphalt negatively affected the H/V curves after data processing. To obtain good coupling, short spikes were used to couple the seismometer to the asphalt, while longer ones were attached for deployment on

soil. Additionally, the seismometer was covered with a bucket to reduce the effect of wind and placed inside a small hole in the topsoil for recordings along the shoulder.

4.3.1.2. *Ground Penetrating Radar*

The research team repeated GPR measurements at approximately the same locations as the Department's investigation. However, a lower frequency antenna (MALÅ Pro Ex system with 250 MHz shielded antenna) was used to increase the depth of investigation. A total of 22 GPR lines were acquired along the roadway and two along the Cross County Trail adjacent to Plymouth Creek. The 22 GPR lines on the roadway were roughly divided such that each travel lane had two GPR lines within the lane and one GPR line one either side of the lane (i.e., either on white or yellow dotted markings). One of the GPR lines along the trail was in the grassy section immediately adjacent to the trail and the other was located on the edge of the paving. Each GPR line on the roadway was acquired over a 175.0 m distance that was approximately the same as the ERI lines collected by Schnabel. The two GPR lines collected on the trail spanned a length of approximately 200.0 m. No GPR lines were acquired directly in Plymouth Creek as originally intended because there were too many obstructions to be able to traverse the creek with the GPR antenna.

4.3.1.3. *Electromagnetic Method (EM)*

EM data was acquired on both the roadway and the creek trail using a GSSI EMP-400 profiler. The GPR lines were retraced and the built-in GPR antenna on the EMP-400 profile was used to track location.

4.3.1.4. *Gravity*

Three gravity lines were acquired along MASW Line 1, MASW Lines 2/3, and MASW Line 4 with the same start and end points as the MASW lines (i.e., approximately 200.0 m in length) (Figure 4.4). Rather than perform separate gravity lines collocated with MASW Line 2 and Line 3, a single gravity line was acquired that was located between those two MASW lines (Figure 4.10). For the gravity line located between MASW Line 2/3, a 2.5 m spacing was used and four 15-second measurements were recorded and averaged. Repeat measurements were also made at 11 of the stations throughout the gravity line to quantify the uncertainty in the measurements. Additionally, a base station was established at a survey marker at the far end of the site and measurements were collected there after 10 field measurements along each line (i.e., approximately every 45 minutes). This data acquisition took an entire day to accomplish. With only one remaining day to collect the gravity lines along MASW Line 1 and MASW Line 4, the spacing between stations was increased to 5.0 m for those gravity lines, resulting in 41 measurement locations instead of the 81 for MASW Line 2/3. Additionally, three 10-second measurements were performed at each station instead of the four 15-second measurements.

Figure 4.10. Gravity surveys, including location of base station.

4.3.2. Post-Grouting Efforts

The duration of post-grouting geophysical testing was much more compressed compared to the pre-grouting efforts. During this time, the Temple research team had to work around several PennDOT and contractor personnel, resulting in some interruptions to geophysical data acquisition. Given the abbreviated timeframe and number of field operations taking place, the Temple research team focused entirely on seismic and gravity methods, which were generally thought to be the most promising, were directly related to stiffness/density of the underlying materials and were the fastest to collect. This approach ensured acquisition of sufficient subsurface data to compare pre- and post-grouting stiffness/density changes in the areas around the sinkholes.

4.3.2.1. *Seismic Methods*

Post-grouting seismic data acquisition generally followed the same procedures and reoccupied the same line locations as the pre-grouting investigations. The most significant deviation was with the overall number of lines performed as well as the seismic source. A 20 lb sledgehammer was used in lieu of the PEG-40 to avoid unnecessary indentations/impressions on the newly paved roadway surface (Figure 4.11). A small sacrificial piece of rubber was also used as a base plate for the sledgehammer blows. The following seismic lines were reperformed, with the following deviations from the pre-grouting efforts noted:

1. MASW lines 1 and 4: This data acquisition followed the modified procedures of the pre-grouting efforts whereby the data acquired did not explicitly perform a pseudo-2D MASW acquisition. Instead, the data acquisition acquired two exterior shots and several interior shots within a 48-channel linear array, and then the entire array was shifted until the first two geophones matched the locations of the last two geophones of the previous array location. This was repeated until the entire length of the line was traversed.
2. 3D FWI: The pre-grouting layout and procedures were followed. Data were only acquired for the section of roadway with Sinkhole 2 due to time constraints and limitations on access.
3. HVSR: The same test boring locations were tested on the roadway and along the grassy shoulder with the same Tromino seismometer. The pre-grouting data acquisition parameters were used.

Figure 4.11. Seismic shots for post-grouting seismic data acquisition efforts.

4.3.2.2. *Gravity*

Post-grouting data acquisition efforts were very similar to the pre-grouting efforts. The same three gravity lines were acquired along MASW Line 1, MASW Line 2/3, and MASW Line 4. However, a 5.0 m spacing between measurements was used for MASW Line 2/3 instead of the 2.5 m spacing for the pre-grouting efforts. Again, three 10-second measurements were taken at each station and averaged. Unfortunately, due to lack of time, GPS measurements were only acquired along a subset of the MASW Line 1 measurement locations. Consequently, it proved impossible to completely correct the gravity measurements for any changes in elevation between pre- and post-grouting. Even as little as inches of elevation change can create additional uncertainty in the interpretation of the gravity results if not accounted for during data processing.

5. DATA PROCESSING AND ANALYSIS OF TEST RESULTS

Data processing for geophysical testing is highly dependent on the method used and the way the data will be used to deduce information regarding the subsurface conditions. For example, some methods require very little processing and the data collected in the field can be directly plotted to develop a qualitative assessment of the subsurface conditions. Other methods require extensive processing of the data, including filtering, application of correction/adjustment factors, and/or computer simulations of the underlying physical processes involved. This chapter provides a detailed discussion of the factors involved to derive subsurface models from processing of the data acquired by the Temple research team. Additionally, the results obtained from the data processing are provided and analyzed to interpret subsurface conditions at Chemical Road.

5.1. Geophysical Data Processing

The following sections discuss the data processing efforts specific to each method used by the Temple research team at Chemical Road with a general progression from methods that entail simpler processing techniques to those that utilize more complex procedures.

5.1.1. Electromagnetic (EM) Method

The EM measurements in this study were collected using a GSSI EMP-400 profiler, which is 1.4 m long with a transmitter-receiver coil spacing of 1.25 m. During data acquisition, the transmitter is energized at a fixed frequency and creates magnetic field loops in the subsurface. This, in turn, produces electrical field loops and a corresponding secondary magnetic field. The combined primary and secondary magnetic fields measured in the receiver are proportional to the bulk ground electrical conductivity *(σ_a)* (McNeill, 1980). At the Chemical Road site, the EMP-400 profiler was set up to acquire data simultaneously using 8 kHz and 15 kHz frequencies, which nominally correspond to different depths of investigation depending on the conductivity of the site. The magnitude of the in-phase and quadrature components of the induced secondary field, as well as the apparent conductivity were stored by the data acquisition system for each reading along with a time stamp and survey grid information. GPS data were also recorded using the internal GPS of the data acquisition system.

Data processing consisted of applying a de-spiking filter that removed abnormally large readings based on user-prescribed settings. This ensured large positive/negative σ_a values were not present in the resulting site maps. Though not physically meaningful, the meter may report negative σ_a for several reasons: (1) if σ_a is sufficiently low such that the quadrature response falls below the system noise level; (2) if in the vicinity of strong lateral heterogeneities (e.g., underlying utilities) as the assumption of a homogeneous ground used to develop the relationship between quadrature response and conductivity is violated; and (3) if the site exhibits generally high conductivity, the linear relationship between quadrature response and conductivity breaks down. Excessively large σ_a values on the other hand may be attributed to high amplitude noise variations that exist over a small period of time. The final product is either a geo-coded map or survey schematic with measurements of σ_a across the site.

5.1.2. Ground Penetrating Radar (GPR)

The GPR measurements in this study were acquired using a MALÅ Pro Ex system with 250 MHz shielded antenna along 22 lines spanning the roadway. As the GPR antenna was dragged across an acquisition line, traces were acquired at an interval of approximately 0.1 m. Data from the receiver were sampled at an interval of 0.08728 ns for a total of 2024 samples, resulting in a trace time window of 176.57 ns. Data processing followed a typical sequence as highlighted in the GPR literature (e.g., Benedetto et al. 2017):

- Time-zero Correction: Correct the arrival time of the GPR wave directly transmitted from source to receiver along the ground.
- Zero Offset Removal: Removal of initial direct current (DC) signal component and any very low-frequency signal trend.
- Band-pass Filtering: Removal of frequencies outside the main bandwidth of the GPR antenna to increase signal-to-noise ratio.
- Time-varying Gain: Correction of signal amplitudes using automatic gain control to account for geometric attenuation and intrinsic material damping of the electromagnetic wave.
- Trim Time Window: Reduction of the time window after gain control is applied such that the latter part of the recordings with no coherent reflection signals (i.e., only background noise) are removed.
- Time-depth Conversion: The time axis was corrected to depth by assuming a representative GPR velocity value based on the existing subsurface information.

The MATLAB code *matGPR* was used to perform these processing steps and to plot the data (Tzanis 2010). The final product is a series of depth profiles that portray reflection signals underlying the site from contrasts in the dielectric/conductivity properties of the subsurface.

5.1.3. Gravity

Gravity data were collected along three MASW survey lines with the Scintrex CG-5 Autograv relative gravimeter. Details of the data collection were provided in the previous chapter. The pre-grouting gravity data were processed following standard land-gravity survey procedures (e.g., Long and Kaufmann, 2013), which included corrections for the effects of tide, gravimeter drift, free-air (elevation) effect and the regional gravity trend. Each measurement was first corrected for earth tide using the method of Longman (1959). Then, the gravimeter drift was determined by fitting a fourth-order polynomial of the time series of all base-station measurements and corrected for by subtracting it from each station measurement. At each station, four 15-second measurements were recorded, so they were averaged to give the station measurement. Free-air correction, which adjusts the gravity measurements to what would have been measured at mean sea level, was then applied to each station measurement relative to the base-station elevation using the second-order free-air formula (Longman and Kaufmann, 2013). The data were then corrected for the regional gravity trend by fitting a plane through all the free-air-corrected values and subtracting it at each measurement station. This step was necessary because the surface elevation around the survey site at the several-kilometer scale generally increases from southeast to northwest, creating a positive-to-negative gravity trend in the southeast-northwest direction (more negative where the

elevation is higher because of more mass pulling upwards opposite to the direction of Earth's gravity field). The final data product is the residual gravity anomaly at each measurement station relative to the base station.

The post-grouting gravity data were processed in the same way as the pre-grouting data. However, accurate elevation data needed for free-air correction were obtained only for approximately 2/3 of MASW Line 1 due to time constraints. Therefore, residual gravity anomalies for MASW Line 2/3, Line 4 and part of Line 1 are not reported here.

The uncertainty of the residual gravity anomaly for each measurement station was estimated by accounting for the uncertainty in the elevation at the base station and at each station, free-air correction, and the root-mean-square difference of repeat measurements at 11 stations on each line. Note that the free-air correction depends on the elevation difference between the base and each measurement station, hence the uncertainty arising from the free-air correction is different for each measurement station. The estimated uncertainty is ±0.013-0.015 mGal.

5.1.4. Seismic Methods

Seismic geophysical testing was the major focus of TEM WO 015. Consequently, multiple seismic methods were used at Chemical Road. The following sections detail the specifics of data processing for each of the seismic methods.

5.1.4.1. *Horizontal-to-Vertical Spectral Ratio (HVSR)*

The following discussion has been adapted from a publication in the proceedings from the ASCE Geo-Congress 2023: Alidoust, P., Mahvelati, S., Coe, J. T., Muto, A., McInnes, S., Painter, M., and Kubiak, K. (2023). "HVSR Measurements to Investigate Sinkholes and Treatment Efforts Along a Roadway." *Proceedings Geo-Congress 2023*, Los Angeles, CA.

The ambient noise measurements in this study were performed using a three-component Tromino® seismometer, a common tool employed in many HVSR studies (Giacomo and Gallipoli 2005, Gosar 2007, Bignardi et al. 2016). The seismometer was placed immediately adjacent to the location of previous test borings when deployed on the roadway asphalt (Figure 5.1). The seismometer was also deployed on soil along the roadway shoulder to acquire an additional set of recordings in case the asphalt negatively affected the H/V curves. To obtain good coupling, short spikes were used to couple the seismometer to the asphalt, while longer ones were attached for deployment on soil. Additionally, the seismometer was covered with a bucket to reduce the effect of wind and placed inside a small hole in the topsoil for recordings along the shoulder. The recording duration was 30 minutes at a sampling frequency of 128 Hz for each location. Following the completion of grouting, HVSR measurements were repeated at the same locations to investigate changes in the subsurface stiffness based on changes to the H/V curves, including $f_{o,HVSR}$.

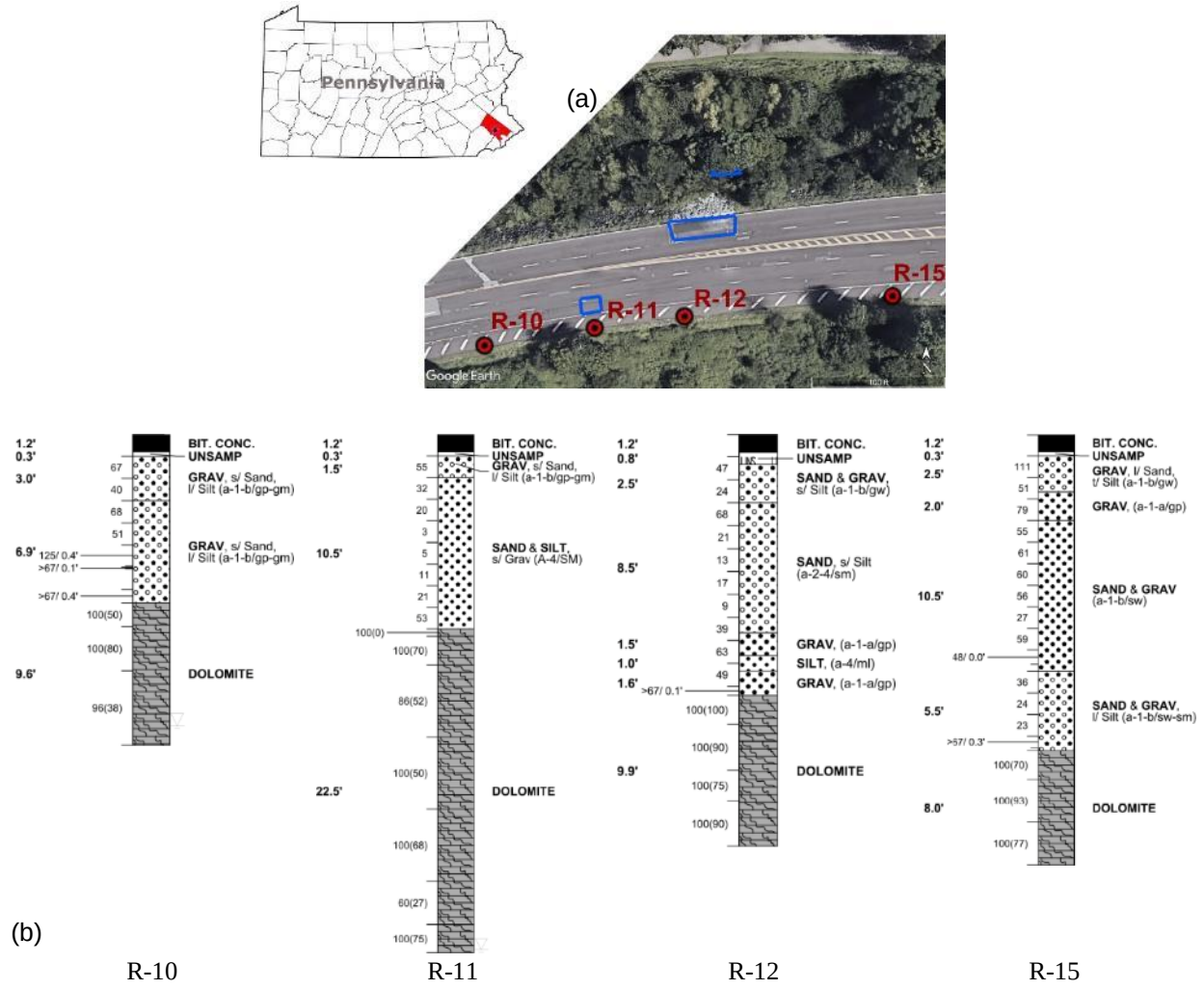

Figure 5.1. Project site: (a) location of site, test borings, and sinkholes (outlined in blue); and (b) interpreted subsurface profile [including blow counts and % Recovery (RQD)].

The open-source Python package *hvsrpy* was used to process the HVSR measurements (Vantassel 2021). This package utilizes a lognormal distribution to characterize $f_{o,HVSR}$ and an automatic frequency-domain window-rejection technique. This algorithm reduces variance and improves data quality while not over-rejecting good windows in low-variance data sets (Cox et al. 2020). Each recording was broken down into 40-second windows. Unsmoothed edges of the truncated windows can cause artifacts during the computation of Fourier spectra (Dal Moro 2015). Therefore, each window was tapered with a cosine taper function (width = 0.1) and band-pass filtered (0.1-80 Hz). Fourier amplitude curves were then computed for the vertical and horizontal components. The Fourier amplitude spectra were smoothed as described in Konno and Ohmachi (1998). The geometric mean method was used to combine the two horizontal spectra into a representative horizontal spectrum. A set of H/V curves was produced for each 40-second window by dividing the horizontal spectrum by vertical spectrum. H/V curves that exhibited standard deviations greater than two were rejected. The rejection and re-calculation of statistics was repeated for several iterations until convergence (i.e., no more windows rejected). Figure 5.2 shows an example of the

data processing for one recording. More details on the automated frequency-domain window-rejection algorithm and lognormal statistics are provided in Cox et al. (2020).

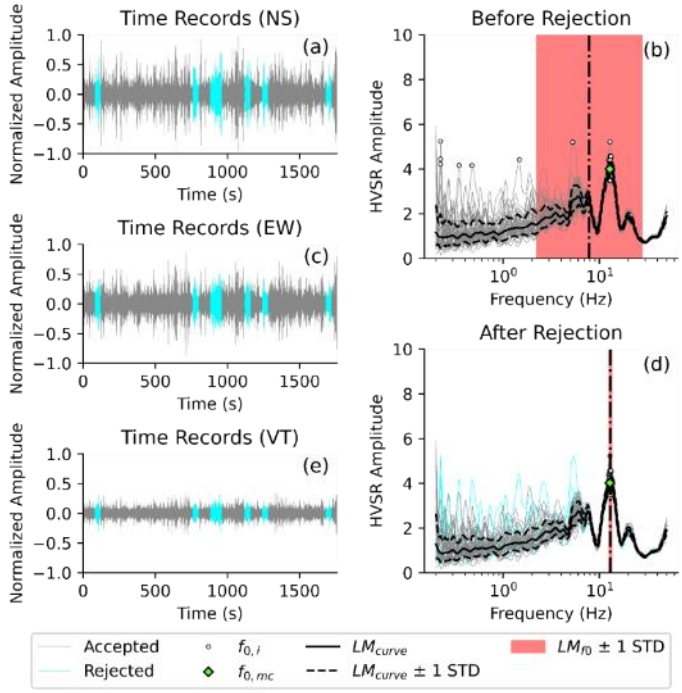

Notes:
LM_{curve} = lognormal median curve
LM_{curve} ± 1 STD = uncertainty in LM_{curve} expressed with positive/negative standard deviations
$f_{0,i}$ = peaks of accepted time windows
$f_{0,mc}$ = peak of the median curve
LM_{f0} ± 1 STD = uncertainty in LM_{f0} expressed with positive/negative standard deviations

Figure 5.2. Sample recording processed using hvsrpy: (a) north-south (NS) component; (c) east-west (EW) component; (e) vertical (VT) component; (b) H/V curves before rejection algorithm; and (d) H/V curves after rejection algorithm.

5.1.4.2. *Multichannel Analysis of Surface Waves (MASW)*

The MASW results in this study were graciously shared by Schnabel with the Temple research team. These results had been previously shared with PennDOT as per the Schnabel final report detailing the geophysical testing performed in support of the site remediation efforts. As per their report, the MASW analyses were performed using the *SurfSeis* surface wave recognition and modeling program (Kansas Geological Survey). Overtone images were generated using a wavefield transformation and dispersion curves were then picked and adjusted manually. Inversion was performed using a local search method. Then the inversion models from each source/receiver array location were combined to form a two-dimensional cross-section model of the subsurface shear wave velocity for each MASW line.

5.1.4.3. *Full Waveform Inversion (FWI)*

The *SalvusProject* module of the Salvus software suite from Mondaic group was used to perform FWI. The module employs the robust spectral-element method (SEM) formulation for solving the Visco-elastic wave propagation equations (Afanasiev et al. 2019). To mimic natural wave propagation and due to high attenuation of waves at the site, constant quality factor values were used to account for the intrinsic

damping of the site and enhance the output accuracy. However, these quality factors were not updated during the inversion process to minimize interference with the velocity values.

To address the non-uniqueness of geophysical modeling and the non-convexity of misfit functions, it is recommended to incorporate a-priori knowledge into the initial models. This helps accelerate convergence and avoid getting trapped in local minima. In this study, the results from the MASW were used to guide the search algorithm in the vicinity of the true model and decrease uncertainties. The simulation also incorporated specific boundary conditions: the top boundary was set as a free surface, while the bottom and sides of the domain were equipped with Clayton and Engquist absorbing boundaries (Clayton and Engquist 1977) for stability.

For the inversion part of the FWI study, a quasi-Newton method called the limited-memory Broyden-Fletcher-Goldfarb-Shanno (L-BFGS) algorithm (Nocedal and Wright 1999) was employed to update all model parameters separately including Vp, Vs, and density. This algorithm efficiently approximates the Hessian matrix and balances the gradient to converge to the global minima. To reduce computational costs, the common practice in the inversion of FWI data suggests focusing on a smaller subset of the domain known as the "region of interest" for model updating. However, in this study, the entire domain was updated to model sites where no prior site investigation results exist.

To achieve more accurate results, an optimal transport misfit function was used to assess the similarity between synthetic and field waveforms. A hierarchical inversion approach was adopted, introducing frequencies gradually during the inversion process (Bunks et al. 1995). Starting with lower frequencies and progressively increasing them allows the updating process to converge to an initial estimate of the subsurface structure that captures the larger features. In this study, the inversion began with a center frequency of 20 Hz, followed by 30 Hz, 40 Hz, and finally 50 Hz. Each iteration of the inversion continued until no further improvement in the misfit value was observed for all events.

To mitigate the high computational cost of FWI, the forward and inverse modeling steps were performed remotely in parallel mode using the High-Performance Computing (HPC) resources at Temple University. The computations were distributed among sixteen cores of the computer servers in the Temple HPC cluster, which provides 88 CPU cores (Intel® Xeon Gold 6238 processors) with up to 1.5 TB of RAM and 0.5 PB of shared memory.

5.2. Geophysical Results

The following sections present the results from the TEM WO 015 geophysical testing at Chemical Road as well as a brief discussion related to analysis and interpretation of the results. For corroboration purposes, the geophysical results from the Department’s investigation were reviewed after the Temple research team obtained their results. It should be noted that data processing is still ongoing for three-dimensional (3D) FWI due to the complexity of the modeling and computational costs. The results from those efforts will be incorporated into future deliverable reports as well as a more thorough discussion of the implications for site subsurface interpretation.

5.2.1. Electromagnetic (EM) Method

Figure 5.3 presents the site map of apparent conductivity based on the 15 kHz transmission data from the EMP-400 profiler. The map also includes the approximate locations of the two sinkholes at the site. The 8 kHz data did not exhibit any meaningful differences, indicating that the effective depths of operation using both frequencies were similar (i.e., generally less than or equal to approximately 3 m for the EMP-400 profiler). The results generally suggest that the northern end of the site closet to the embankment is more conductive than the southern end of the site closet to the grass shoulder. These results are generally corroborated by the Department's ERI results that indicated the presence of very low resistivity zones closer to the surface near MASW Line 1 (ERI Line 3) at the northern part of the site. Sinkhole 1 on the westbound travel lane closest to the roadway embankment was in this highly conductive low resistivity section. Interestingly, Sinkhole 2 was located over the zone where σ_a measurements were quite low (i.e., high resistivity). Generally, soft, and wet soils indicative of karst and sinkhole activity are often attributed to low resistivity zones. However, depending on the characteristics of a sinkhole, it may present as resistive relative to the surrounding rock. For example, an air-filled cavity would tend to exhibit very low conductivity despite it being a by-product of rock dissolution associated with karst and sinkholes (van Schoor 2002). It should be noted that during site reconnaissance Sinkhole 2 did present some evidence of the presence of void features in the underlying subsurface (Figure 5.4). It is possible that the low conductivity at that area of the site can be partially attributed to air-filled voids caused by the sinkhole formation. Given the limited depth of investigation and presentation of the results, the EM method only provided a qualitative assessment of the subsurface sinkhole features.

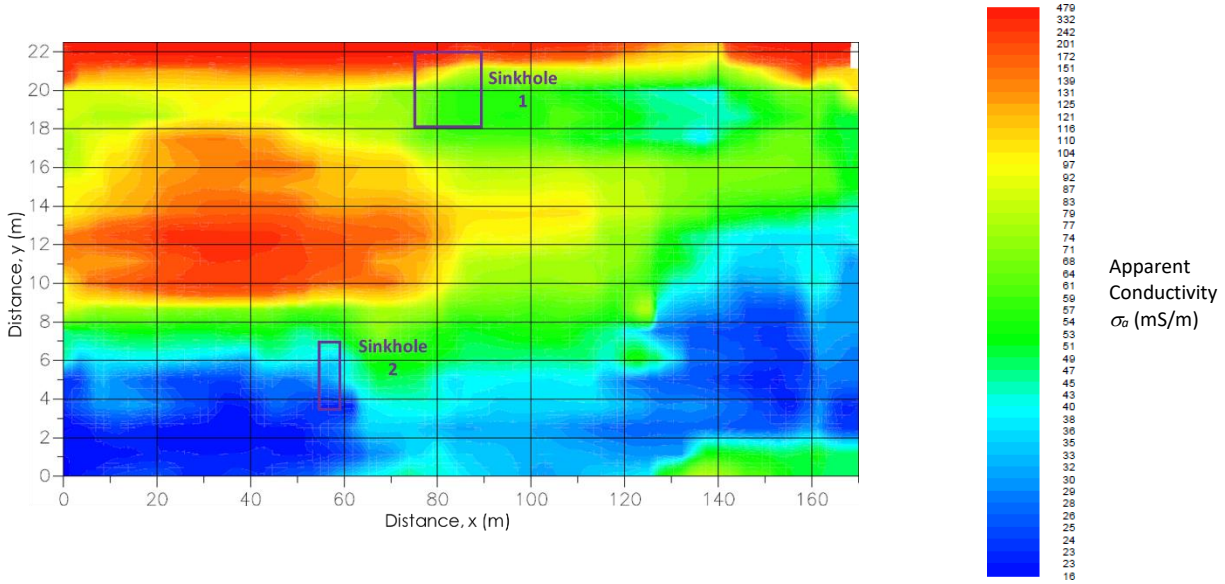

Figure 5.3. Apparent conductivity (σ_a) site map for Chemical Road and approximate sinkhole locations indicated by purple boundaries. Note that the axes origin corresponds to the starting point of ERI Line 4 offset by approximately two meters so that testing was conductive only over the asphalt roadway.

Figure 5.4. Evidence of void features at Sinkhole 2.

5.2.2. Ground Penetrating Radar (GPR)

Generally, the GPR data acquired at Chemical Road suffered from poor signal-to-noise ratio as may be expected at a highly conductive site and exhibited a range of anomalous features attributed to different subsurface conditions. Figure 5.5 provides two representative examples of GPR results from the site, one near MASW Line 1 and the other near MASW Line 4. Both sets of results do provide some evidence of subsurface disturbances in the general vicinity of the two sinkholes on site. For the MASW Line 1 results, the sinkhole is located at approximately 75 m along the survey line. Evidence of a surface depression as well as subsurface disturbance is present there with a total length that matches well with the surface-measured length of the roadway depression caused by Sinkhole 1. The results along MASW Line 4 also exhibit this to a certain extent (note the surface disturbance at approximately 55 m along the survey line), but the sinkhole target is much smaller in scale and less visible as a result. Given the poor quality of the GPR data, the B-scans only provide nominal information regarding the subsurface sinkhole features.

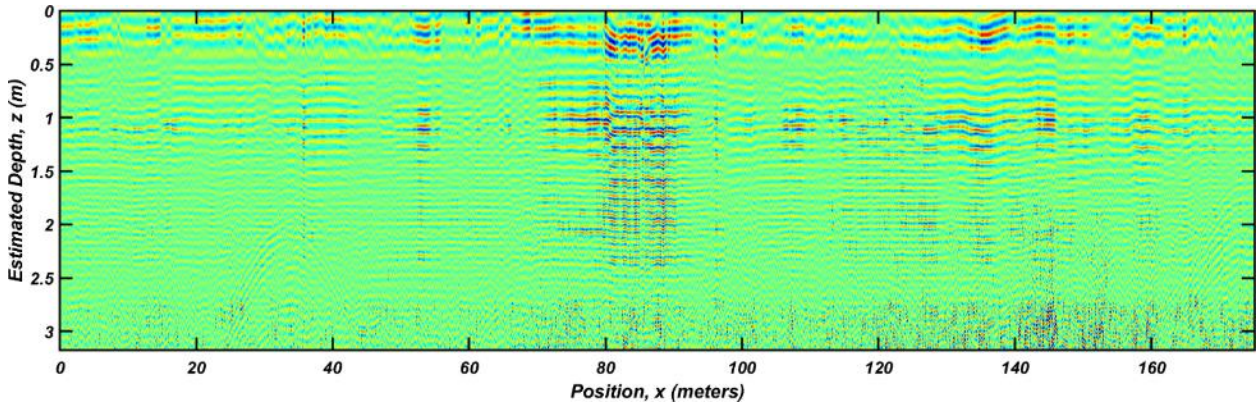

(a)

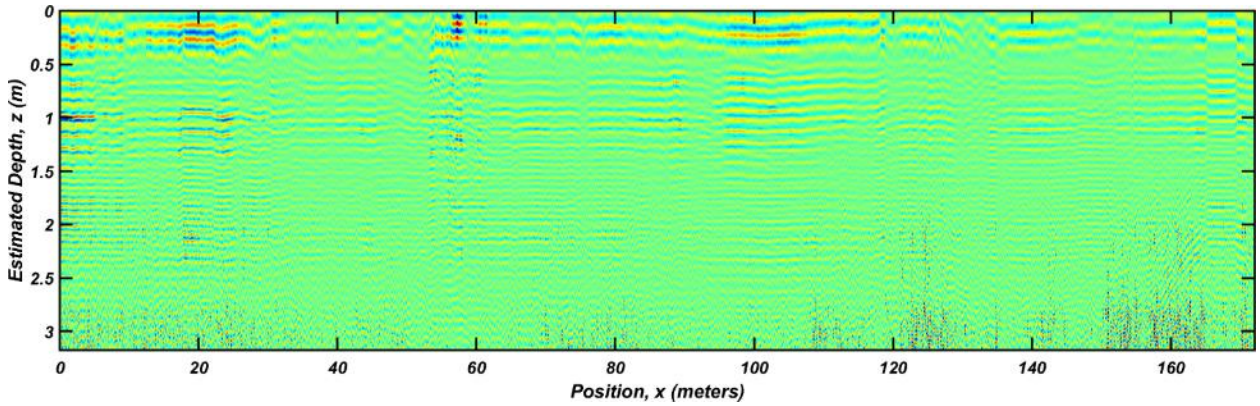

(b)

Figure 5.5. Representative GPR B-scans at two positions along the Chemical Road site: (a) adjacent to MASW Line 1 (approximately 21 m measured from edge of grass shoulder); and (b) adjacent to MASW Line 4 (approximately 9 m measured from edge of grass shoulder).

5.2.3. Gravity

Figure 5.6 presents the pre-grouting gravity results in two forms: (1) as an x-y scatter plot with the residual gravity (including the estimated measurement uncertainty) plotted along the survey position; and (2) as color-coded circles at the corresponding measurement positions on a site map. For the site map, the red and blue colors of the circles indicate mass deficits (e.g., voids or low-density materials) and excesses, respectively. As noted in these pre-grouting results, there is clear evidence indicating mass deficits in the immediate vicinity of Sinkhole 2 between 40 – 120 m along all the survey lines. This evidence is less conclusive in the immediate area encompassing Sinkhole 1. The lack of mass deficits present in the residual gravity measurements may be associated with previous efforts to backfill Sinkhole 1.

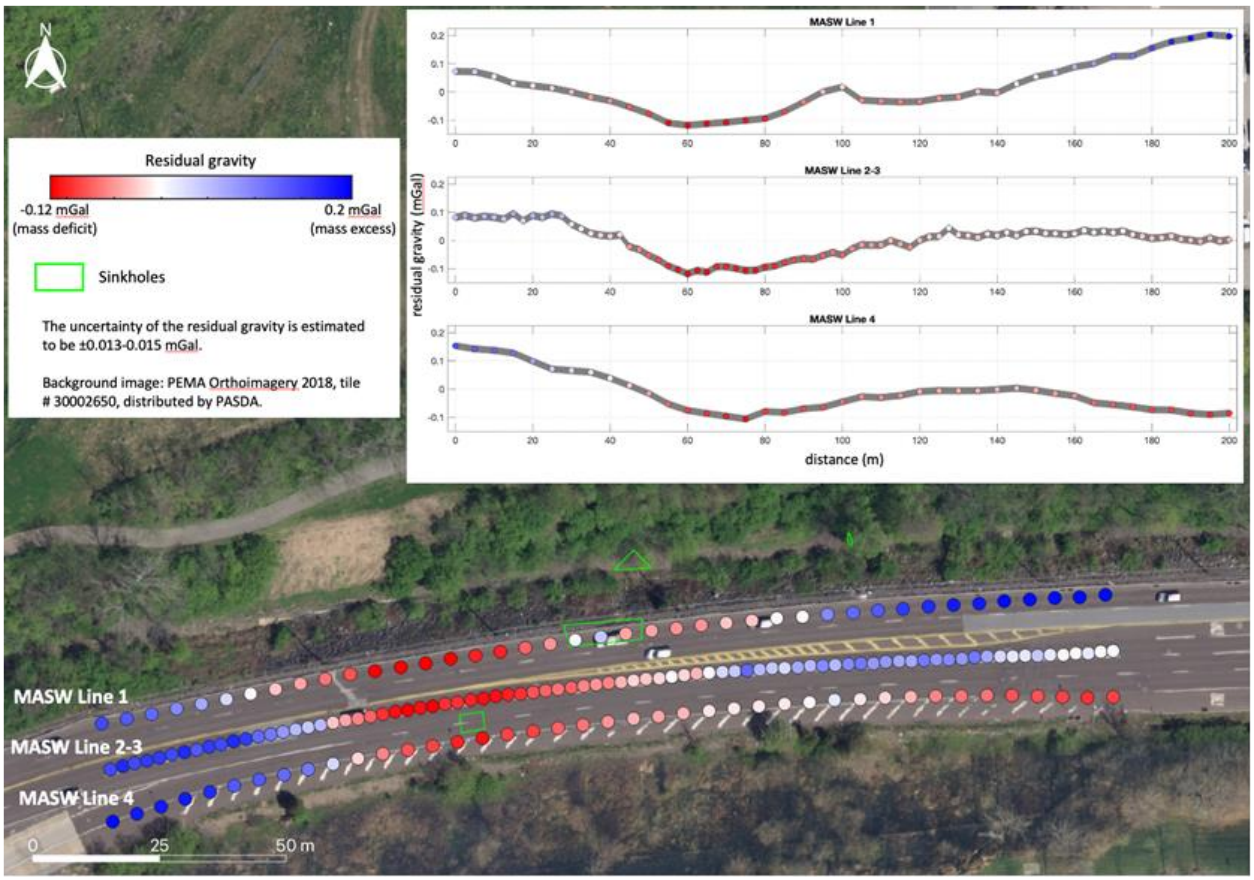

Figure 5.6. Map of the survey site and pre-grouting gravity residual values along each of the survey lines. Gray bands in the inset plot indicate the uncertainty of the gravity measurements.

Figure 5.7 plots the residual gravity measurements prior to and after grouting at the site, again with the associated measurement uncertainty presented as grey bands at each data point. The figure shows that after the grouting, the residual gravities increased by about 0.03-0.05 mGal between 50 and 110 m along MASW Line 1. This increase is relatively modest given the measurement uncertainty. The "scale" of the density changes caused by grouting may not be as significant relative to other factors that change gravity readings. So even though these changes in residual gravity would be expected given the increased subsurface mass from grouting, the amount of material replaced by any grouting may need to be abnormally high to register changes in residual gravity that are well above the scale of measurement uncertainty present in any gravity survey.

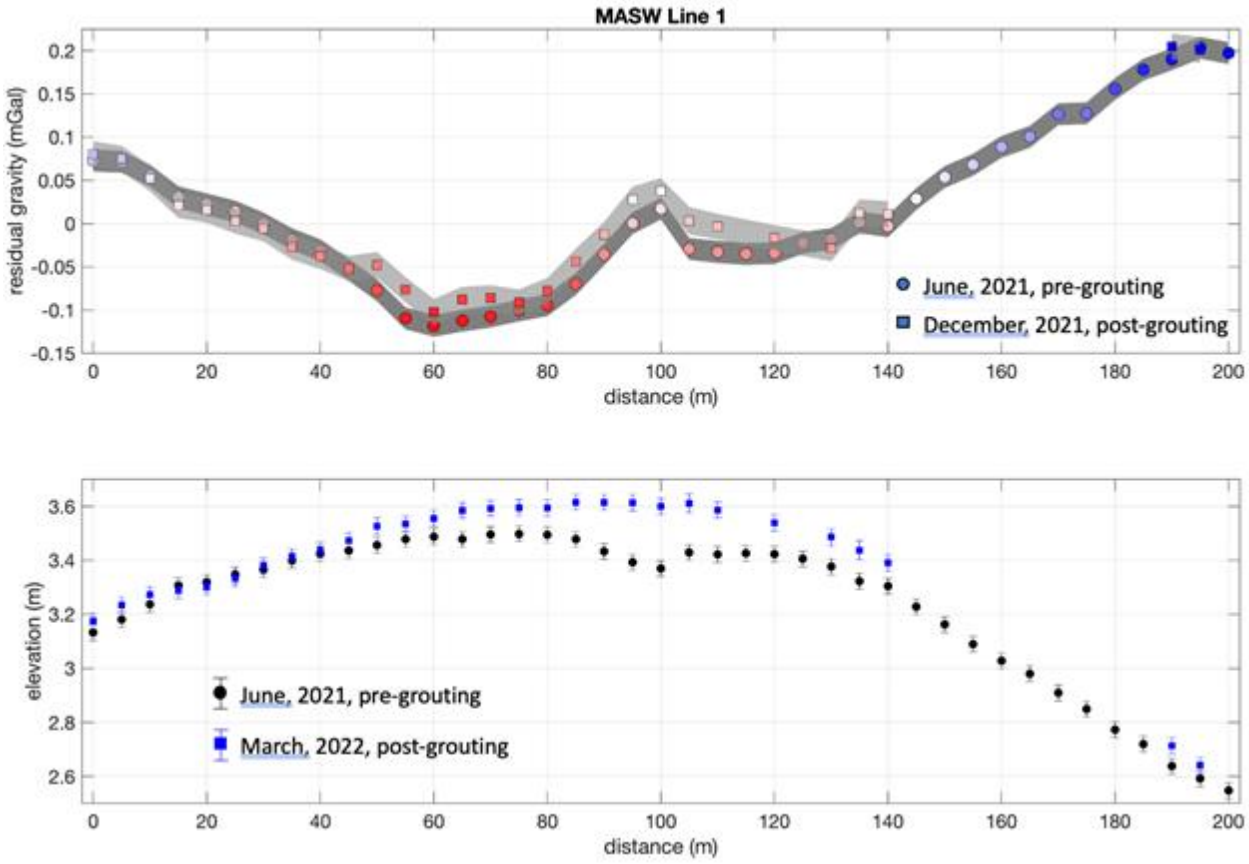

Figure 5.7. Pre-grouting (circles) and post-grouting (squares) residual gravities (top) and elevation measurements (bottom) along MASW Line 1.

5.2.4. Seismic Methods

5.2.4.1. *Horizontal-to-Vertical Spectral Ratio (HVSR)*

The following discussion has been adapted from a publication in the proceedings from the ASCE Geo-Congress 2023: Alidoust, P., Mahvelati, S., Coe, J. T., Muto, A., McInnes, S., Painter, M., and Kubiak, K. (2023). "HVSR Measurements to Investigate Sinkholes and Treatment Efforts Along a Roadway." *Proceedings Geo-Congress 2023*, Los Angeles, CA.

Figure 5.8 presents the processed H/V curves and shows evidence of larger standard deviation (LM_{curve}±1 STD) in the post-grouting measurements relative to the pre-grouting measurements. This was the case despite rejection of time windows that exhibited evidence of near-field anthropogenic waveforms. Possible sources for the additional uncertainty between post- and pre-grouting measurements include differences in seismometer coupling, adverse weather conditions, and complexity of subsurface conditions (e.g., the extent and spatial variability with which grout flowed into voids, interaction of grout

with nearby buried utilities, etc.). Such sources have been noted in the literature to increase H/V uncertainty (e.g., Cox et al. 2020).

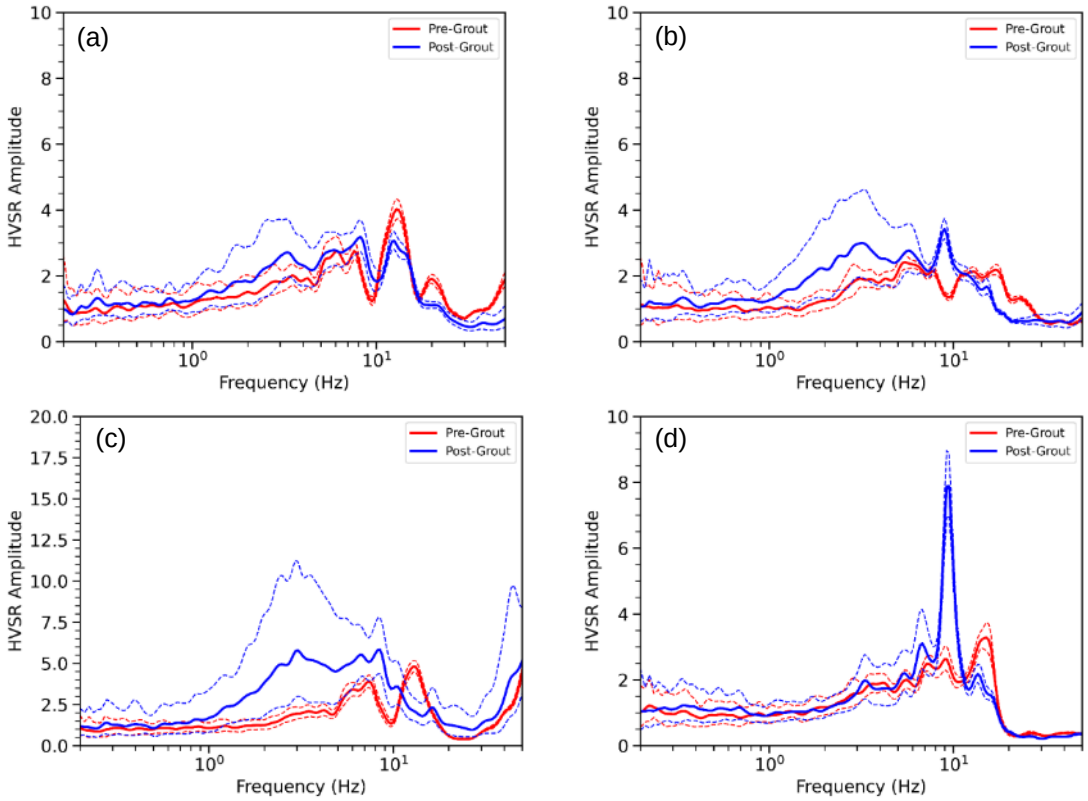

Figure 5.8. Comparison of processed H/V curves for pre- and post-grouting conditions (asphalt coupling) adjacent to (a) borehole R-10; (b) borehole R-11; (c) borehole R-12; and (d) borehole R-15. Note: Dotted lines indicate the uncertainty in the H/V curve (LM_{curve}±1 STD).

Even accounting for the larger scatter, Figure 5.8 shows a general increase in H/V amplitude at lower frequencies after grouting, particularly next to the Sinkhole 2 (test borings R-11 and R-12). Both pre- and post-grouting HVSR measurements were obtained on weekends during which the site had similar levels of anthropic activity (e.g., no construction, similar nearby traffic, etc.). The increase in H/V amplitude also occurs over a large span of frequencies and above the range typically associated with adverse weather conditions (< 2 - 3 Hz). Consequently, the increase in H/V amplitude can be reasonably attributed to physical changes in the subsurface despite the increased uncertainty present in the post-grouting measurements. Stratigraphically, this increase in H/V amplitude can be explained by a grouting-related velocity increase in the soft zones noted in Figure 5.1. The resulting subsurface stiffness profile would more closely resemble a gradually increasing pattern with depth, which has been shown in other studies to result in H/V amplitudes larger than one over a broad range of frequencies (e.g., Castellaro and Mulargia 2009).

The increase in H/V amplitude occurs over a broad enough frequency that a distinct peak is not readily visible in the results (Figure 5.8); thus, it hinders the extraction of a reliable $f_{o,HVSR}$ estimate based on the six clarity criteria established in SESAME (2004). Prior to grouting, a reliable estimate for $f_{o,HVSR}$ was possible based on SESAME (2004) for all test locations except for test boring R-11 right next to Sinkhole 2 at the site. The lack of a distinct H/V peak for post-grouting measurements can be attributed to the tendency of the grout to decrease the severity of large impedance contrasts. The results near borehole R-15, however, were quite different suggesting perhaps a localized anomaly or differences in grouting. The increase in H/V amplitude was much more narrowly defined and a distinct peak could be reliably interpreted based on SESAME (2004). The cause of this peak was interpreted as stratigraphic since anthropogenic artifacts appear as sharp/narrow spikes in all three spectral components (NS, EW, and VT), which was not observed in this recording. When compared to the pre-grouting $f_{o,HVSR}$ (≈ 12 Hz), the post-grouting $f_{o,HVSR}$ shifted to a lower frequency (≈ 9 Hz), which implies V_S decreased throughout the subsurface (based on $f_{o,HVSR} = f_0 = V_S/4H$ and a consistent bedrock depth, H). This is unlikely after the introduction of low mobility grout. Instead, it should be noted that the microtremor (i.e., ambient vibration) wavefield is a complex function of many variables and $f_{o,HVSR}$ may not always equal to f_0, particularly when large stiffness contrasts are reduced in the subsurface (Molnar et al. 2022). Interestingly, the shift in $f_{o,HVSR}$ near test boring R-15 could be explained mathematically if the post-grouting operations altered the site response such that $f_{o,HVSR}$ was now directly related to the next higher resonant site frequency (i.e., $f_1 = 3V_S/4H$) instead of f_0 (assuming V_S and H did not drastically change). Additional modeling and/or joint inversion with other geophysical data would be necessary to definitively ascribe the cause of the distinct H/V peak present in the post-grouting measurements near test boring R-15.

5.2.4.2. *Multichannel Analysis of Surface Waves (MASW)*

Figure 5.9 presents the Department's MASW results. The figure contains both the pre- and post-grouting Vs profiles along each of the four lines collected across the site. The pre-grouting MASW results indicate the depth to rock at the site generally decreased towards the southern lanes and grass shoulder. Each profile also exhibited low Vs values comparable with those of soft wet soils and/or fractured rocks pervasive in karst conditions. The low Vs values were typically located between approximately 50 m to 100 m along the survey lines and overlapped with the locations of both sinkholes at the site. Overall, the post-grouting MASW results exhibited a marked increase in Vs in the near surface (i.e., upper 5 m). This increase was as much as 10%, particularly in the low velocity zone previously identified in the pre-grouting results. These results indicate that the grouting operations stiffened the surrounding soils and filled in low velocity anomalous areas. Interestingly, this did not seem to affect the southwestern end of the site as appreciably as the northern areas of the site. This can be attributed to the already higher Vs values present at that end of the site, which may have necessitated less overall grout during remediation efforts.

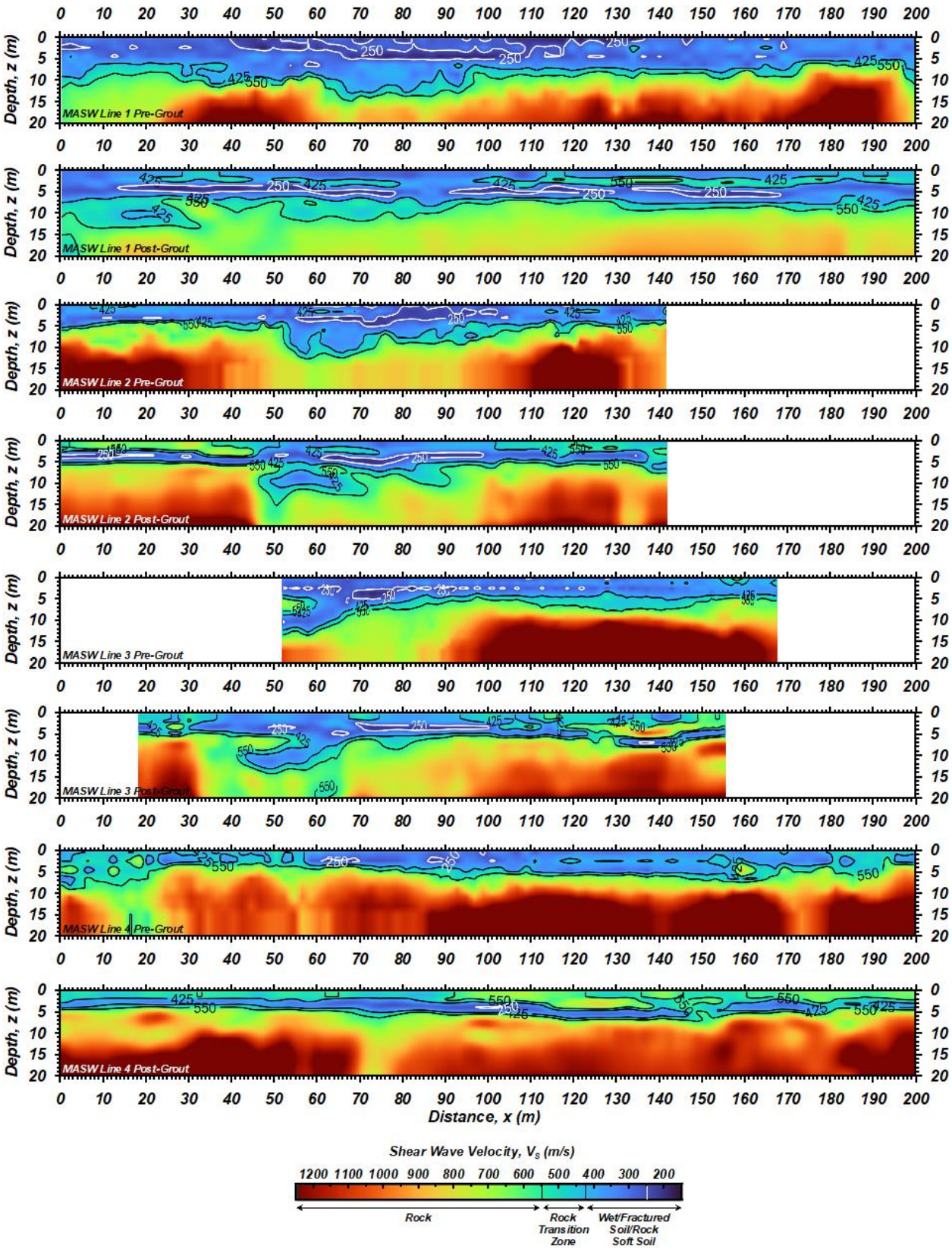

Figure 5.9. Comparison of pre- and post-grouting 2D MASW results across the site.

5.2.4.3. *Full Waveform Inversion*

Figure 5.10 compares the pre- and post-grouting FWI results along Line 1 near the northern section of the site. This survey crossed the Sinkhole 1 at approximately 115 – 130 m based on its relative location with respect to the first shot location of Line 1. The pre-grout FWI results clearly delineate a very low velocity zone in the upper 5 m throughout that location along the survey line, as well as beyond. The post-grouting results indicate that the overall area of the low velocity zone is decreased. Similarly, the FWI results along Line 4 (Figure 5.11) also provide evidence that the grouting efforts decreased the presence of low velocity zones in the immediate near surface, likely due to filling in weak and/or soft seams associated with soil infill into fractured karst rock.

Figures 5.12 – 5.14 compare the FWI results with the MASW results. Generally, both sets of results agree well in that they indicate an overall increase in stiffness of the subsurface conditions. However, there are some notable differences. For example, along Line 1, the FWI results suggest that the pre-grouting low velocity anomalous regions are more extensive than supported by the MASW results. Consequently, despite both sets of results indicating improvement in subsurface stiffness from the grouting efforts, the FWI results seem to indicate a more extensive post-improvement low-velocity zone across the site and in the immediate vicinity of the treated sinkhole. This is unsurprising since the pre-grouting FWI results indicated lower velocities overall than the pre-grouting MASW results. The Line 4 pre-grouting FWI results also indicate more extensive anomalous low velocities in the upper 5 m of the site. However, the improvements in Vs caused by the grouting operations are comparable in the FWI results and MASW results. When compared to their pre-grouting baseline Vs, the MASW and FWI post-grouting results across the site support that additional remediation was unnecessary given the extent and depth of ground improvement.

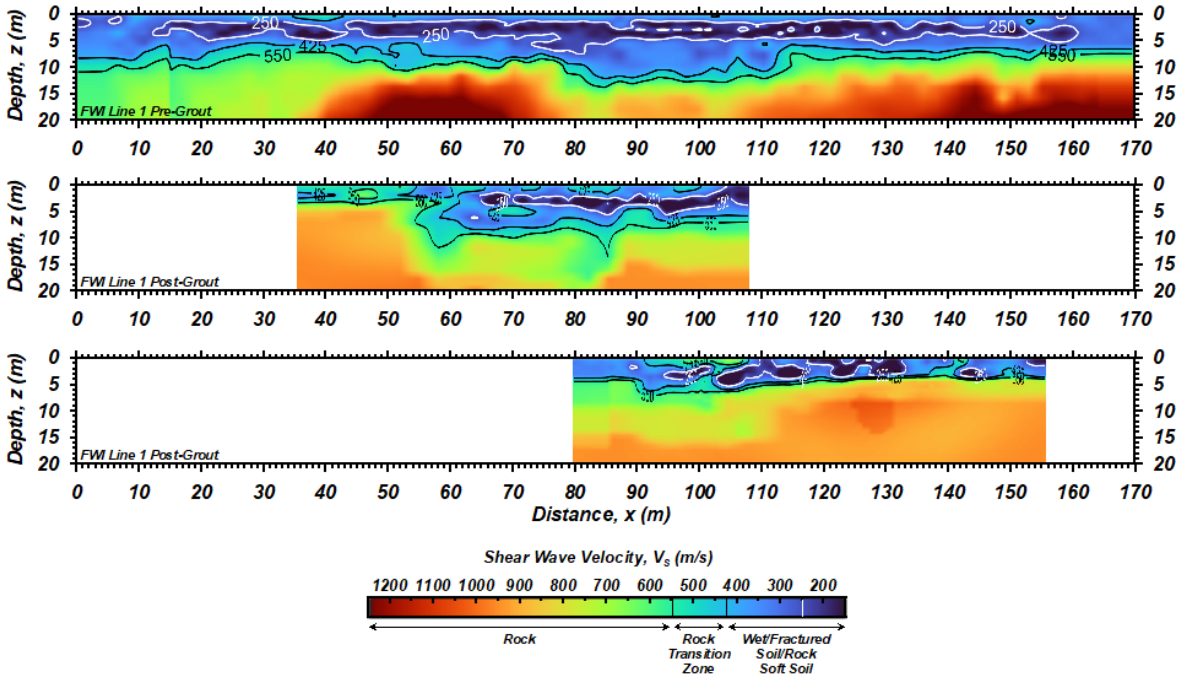

Figure 5.10. Comparison of pre- and post-grouting FWI Line 1 results.

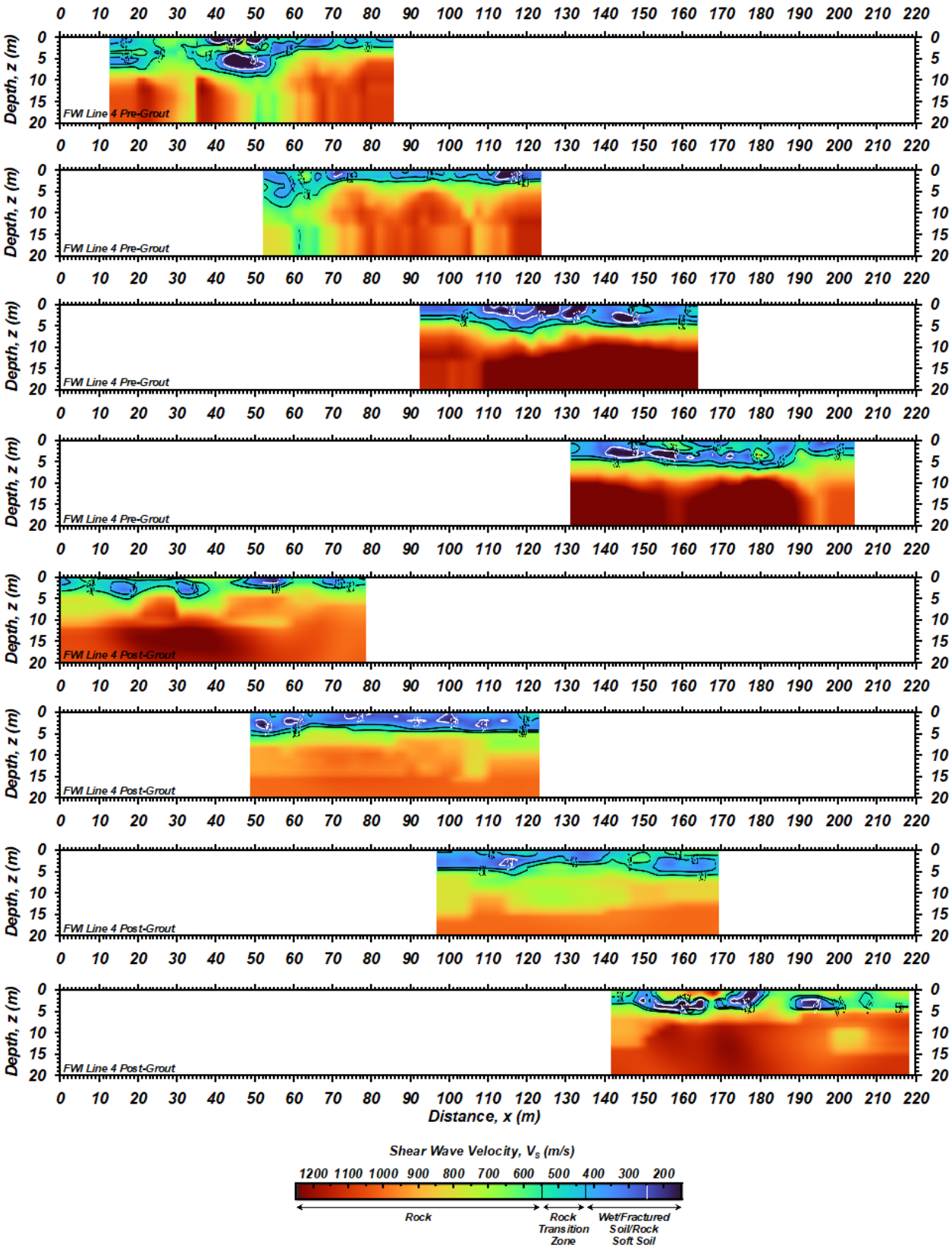

Figure 5.11. Comparison of pre- and post-grouting FWI Line 4 results.

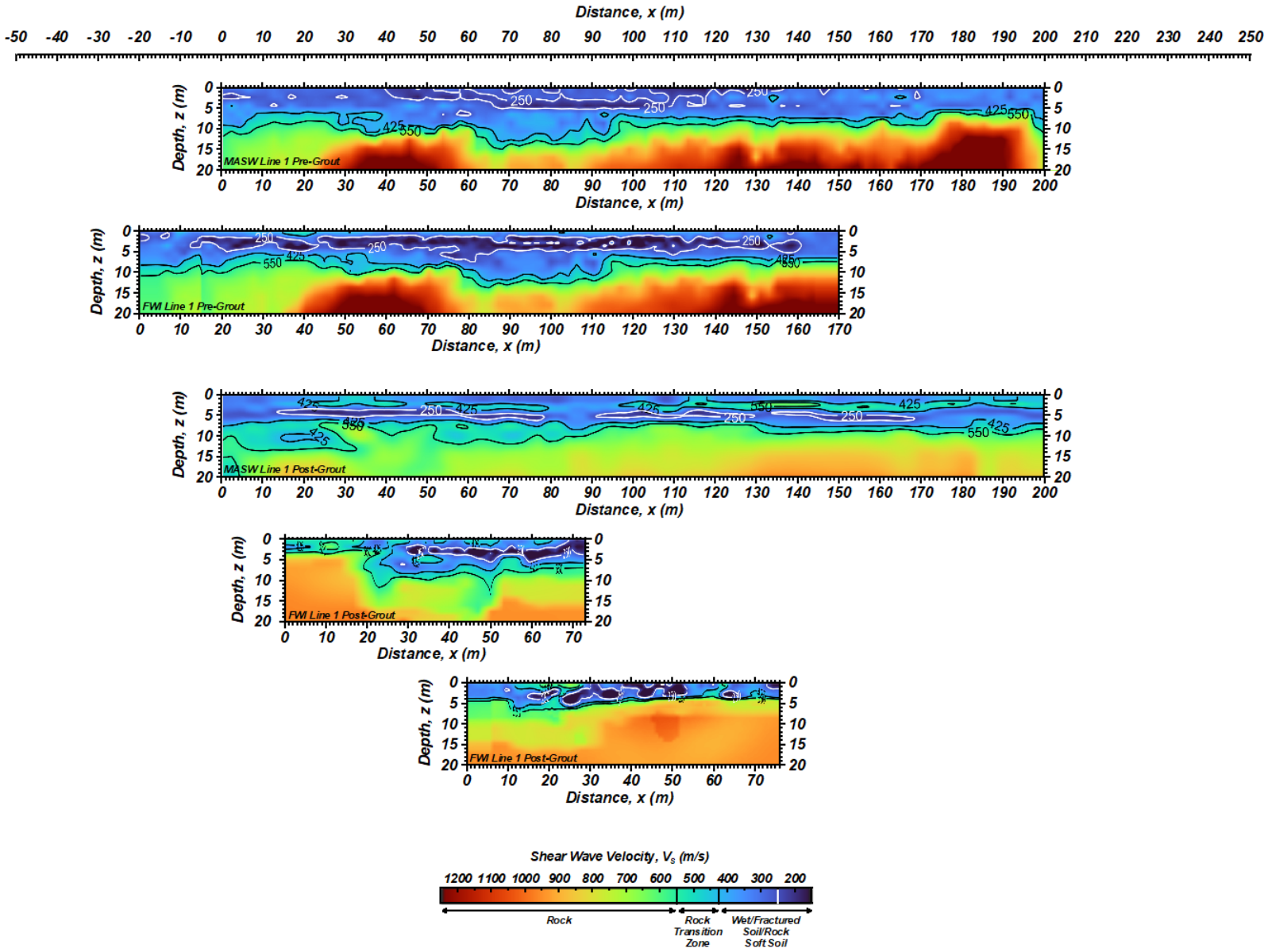

Figure 5.12. Comparison of pre- and post-grouting FWI and MASW Line 1 results.

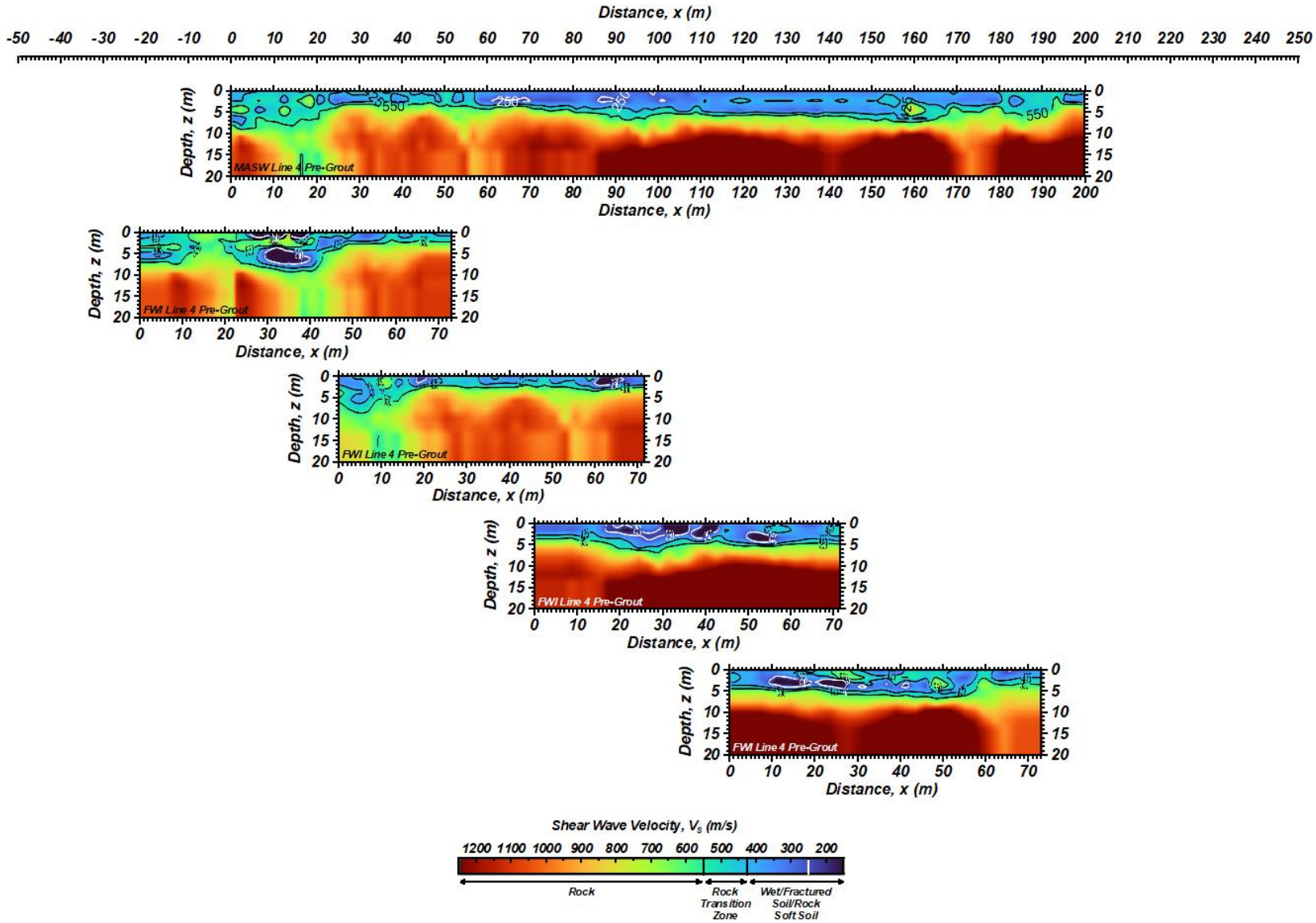

Figure 5.13. Comparison of pre-grouting FWI and MASW Line 4 results.

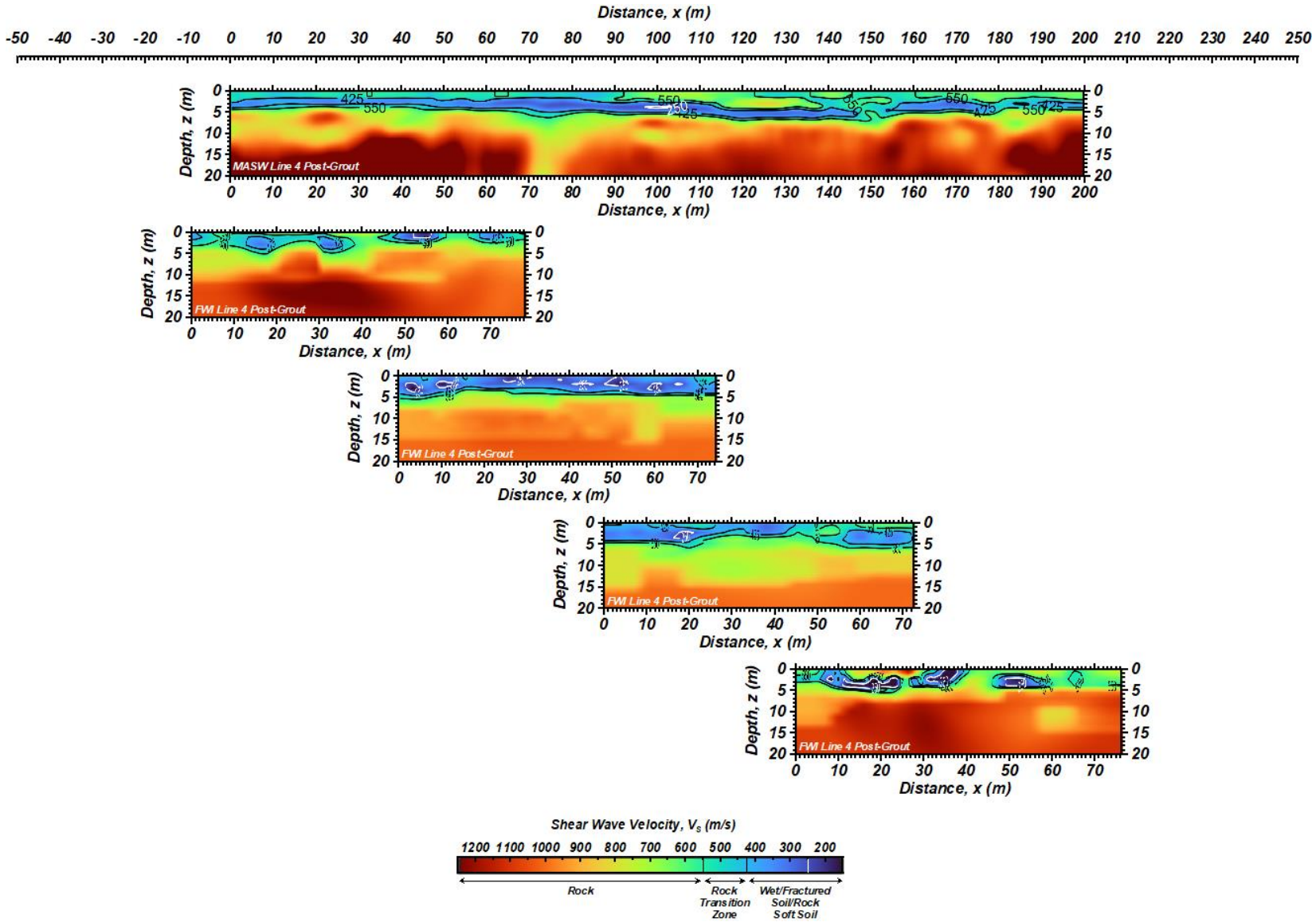

Figure 5.14. Comparison of post-grouting FWI and MASW Line 4 results.

Figures 5.15 and 5.16 present the pre- and post-grouting FWI results for the 3D arrays acquired near Sinkhole 2. These 3D results largely corroborate the results obtained from the 2D survey lines with evidence of a very low velocity zone in the upper 5 m throughout the site. The post-grouting results clearly indicate this low velocity zone has been drastically reduced due to the treatment efforts. The 3D results provide a more comprehensive interpretation of these effects that does not suffer from having to interpolate between 2D surveys. For example, the pre-grouting results in Figure 5.15 clearly indicate a dipping rock interface as the site is traversed from south to north (i.e., from the grassy shoulder to the edge of the roadway embankment). But by visualizing a slice through the 3D subsurface model that traverses along the direction from Sinkhole 2 towards Sinkhole 1 [Figure 5.15(h)], the presence of an interconnected zone of low velocities suggests both sinkholes developed along a similar fracture/void network caused by the karst activity at the site. This is also supported by the fact that Sinkhole 3 on Plymouth Creek is located along the same trajectory following Sinkhole 2 to Sinkhole 1. These soft seams and weak infill were stiffened by the grout treatment efforts, resulting in a drastic reduction in the presence of the low velocity zones along the trajectory from Sinkhole 2 to Sinkhole 1 [compare Figure 5.15(h) and 5.16(h)]. When compared to pre-grouting subsurface conditions, the 3D FWI post-grouting results in Figure 5.16 support the conclusion derived from the 2D results that additional remediation was unnecessary given the extent and depth of ground improvement.

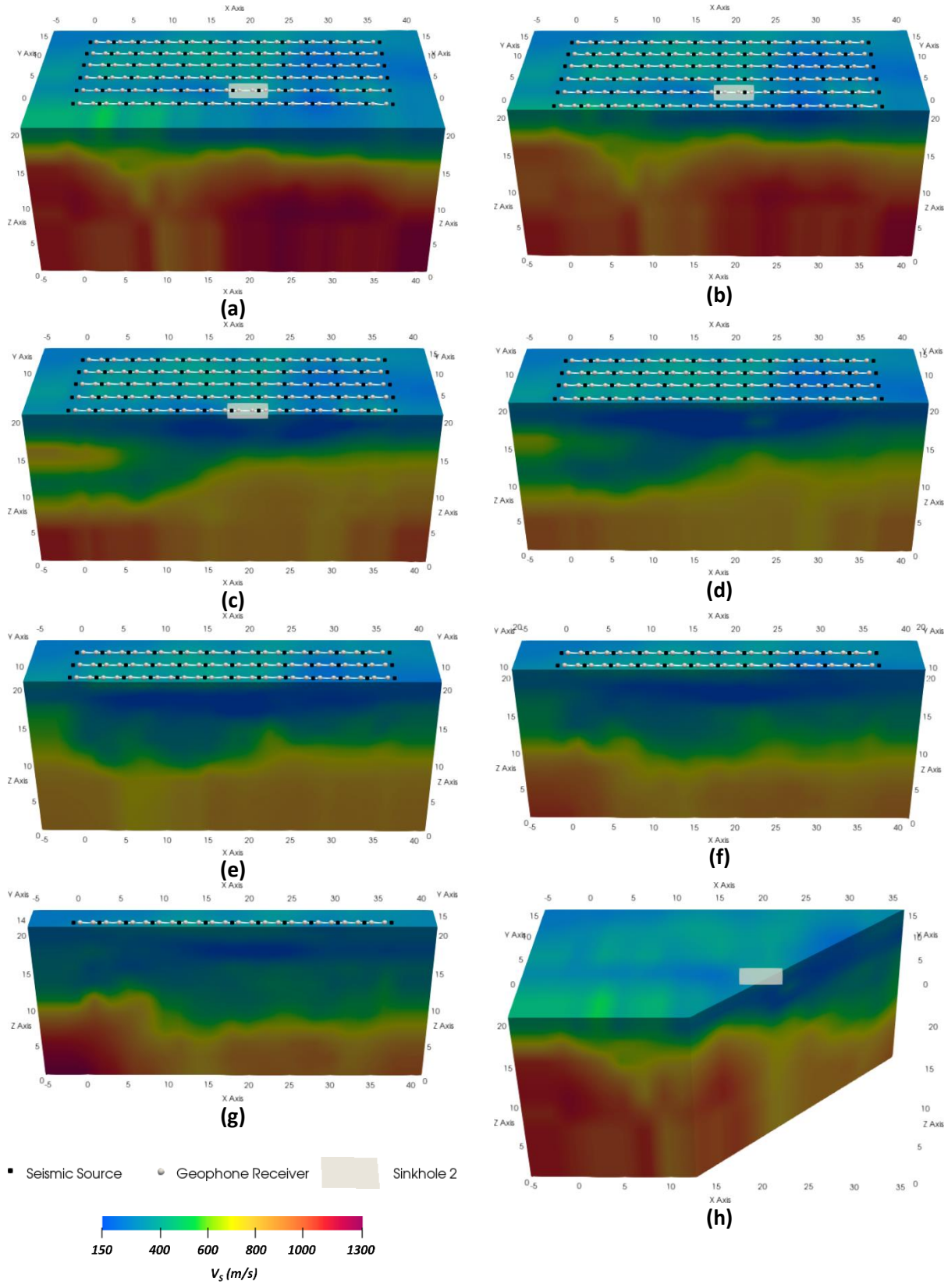

Figure 5.15. Pre-grouting 3D FWI results.

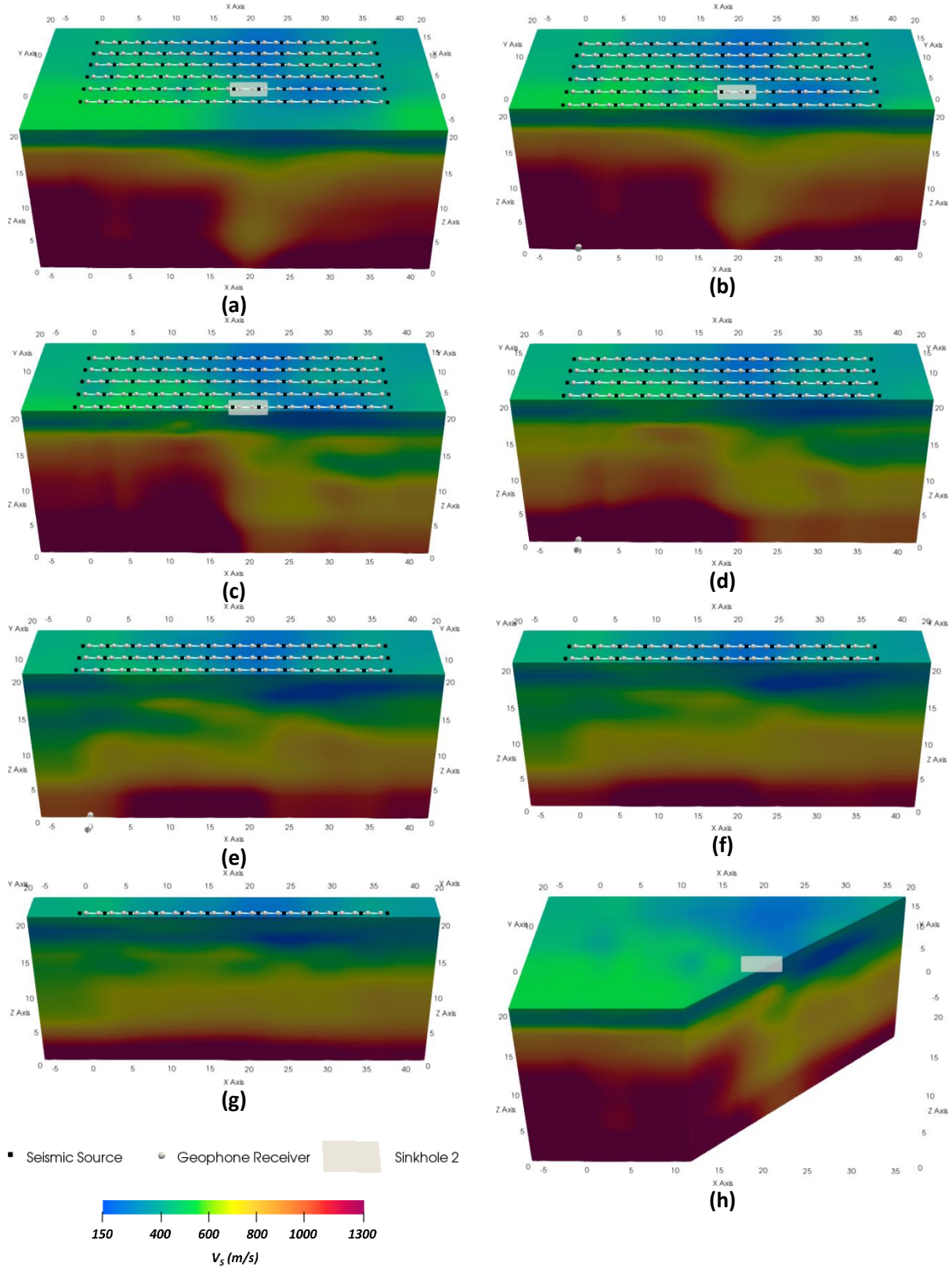

Figure 5.16. Post-grouting 3D FWI results.

5.3. Summary

Overall, the results provided in this chapter highlight the inherent difficulties of geophysical methods when applied to sinkholes. It has long been known that sinkholes in karstic areas are a difficult geophysical target (e.g., van Schoor 2002). That is particularly the case at an urban site such as Chemical Road where many subsurface features such as utilities present obstacles to accurately assessing anomalous soil conditions. Nevertheless, the methods used in this study helped support site characterization efforts both prior to and after grouting operations. The stiffness information offered by the seismic methods provided compelling evidence of improvements caused by the grouting efforts. Pre- and post-grouting gravity measurements also served as evidence of these improvements though they were less compelling due to measurement uncertainties.

6. NUMERICAL AND ANALYTICAL EFFORTS TO DEVELOP RECOMMENDATIONS

A comprehensive numerical and analytical study regarding the implementation of full waveform inversion (FWI) and joint inversion at the Chemical Road site was undertaken in conjunction with the field efforts summarized in Chapter 5. These efforts simulated site conditions to aid selecting appropriate parameters for use in the FWI algorithm when applied to the acquired field data. They also served as compelling evidence to develop recommendations regarding the implementation of FWI and joint inversion for future PennDOT sinkhole projects. The following sections summarize the numerical and theoretical efforts and provide a discussion of these recommendations.

6.1. Role of Numerical Modeling in Geophysical Inversion

Geophysical inversion refers to the recovery of subsurface physical properties such as density, stiffness, electrical resistivity, etc., from observed geophysical data. Such inversion problems present several challenges:

- Ill-posed: The problem does not have a unique solution that is insensitive to the initial conditions
- Ill-conditioned: A small change in the inputs (the independent variables) results in a large change in the dependent variable.
- Non-linear: The relationship between dependent and independent variables follows a non-linear function

The accuracy of results derived from geophysical inversion problems are therefore highly dependent on many factors associated with the algorithm used to solve the inversion problem (Liu et al., 2017). Complicating matters is the fact that “ground truth” is rarely known with absolute certainty under typical field conditions due to the limitations of subsurface investigations.

Given the issues, numerical simulations and analytical solutions play a key role when evaluating the effectiveness of inversion strategies. The process of forward modeling involves the solution of known physics-based governing equations using numerical techniques such as finite element or finite difference methods. A reliable set of observed data can be derived from forward modeling on a known synthetic domain. When such a domain is fully defined such that all subsurface physical properties are known to the user, the effectiveness of various inversion strategies can be reliably evaluated. Similarly, for simple models it may be possible to derive analytical solutions for comparison purposes. The remainder of this chapter focuses on such efforts for the FWI algorithm implemented on the seismic data acquired at Chemical Road. Also included is a discussion of joint inversion of Rayleigh and Love seismic waves.

6.2. Implementation of Full Waveform Inversion

FWI implementation must choose from a variety of objective functions, nonlinear optimization algorithms, preconditioning strategies, regularization methods and multiscale schemes. The ability of FWI to accurately evaluate subsurface conditions is largely affected by choices related to the optimization

algorithm and parameterization (Métivier et al., 2013; Métivier & Brossier, 2016; Liu et al., 2017). Though the FWI literature does explore some methodological comparisons of algorithms and parameter selections there is still some uncertainty regarding the most appropriate FWI implementation strategy and a one-size-fits-all approach may not result in the most effective or computationally efficient algorithm. This is particularly the case with near-surface geotechnical problems where the observed wavefields are quite complex due to the short acquisition times and relatively small arrays used for data acquisition relative to FWI efforts at a regional or global scale. Consequently, the Temple research team developed a numerical model for and used it to explore the effectiveness of different FWI implementation strategies. This primarily consisted of testing different initial models and misfit functions since the existing literature does not provide a clear consensus for which ones to select. Other parameters and algorithm choices are also discussed but their selection was primarily driven by support in the FWI literature or limitations related to availability in commercial and open-source FWI software.

6.2.1. Numerical Model

A two-dimensional (2D) synthetic domain (Figure 6.1) was generated with an anomalous subsurface karst feature and used as a testbed for the appropriate selection of FWI parameters. The model domain represented a stiff soil and spanned 40 m in length and had a depth of 10 m. To represent a sinkhole, an ellipse-shaped anomalous karst feature was centered laterally on the domain 2.0 m below the surface. The ellipse shape of the anomaly had axis radii of 1.5 m and 5 m along the *z* and *x* axes, respectively (Figure 6.1). Table 6.1 provides the specific subsurface properties of the soil and karst feature within the domain.

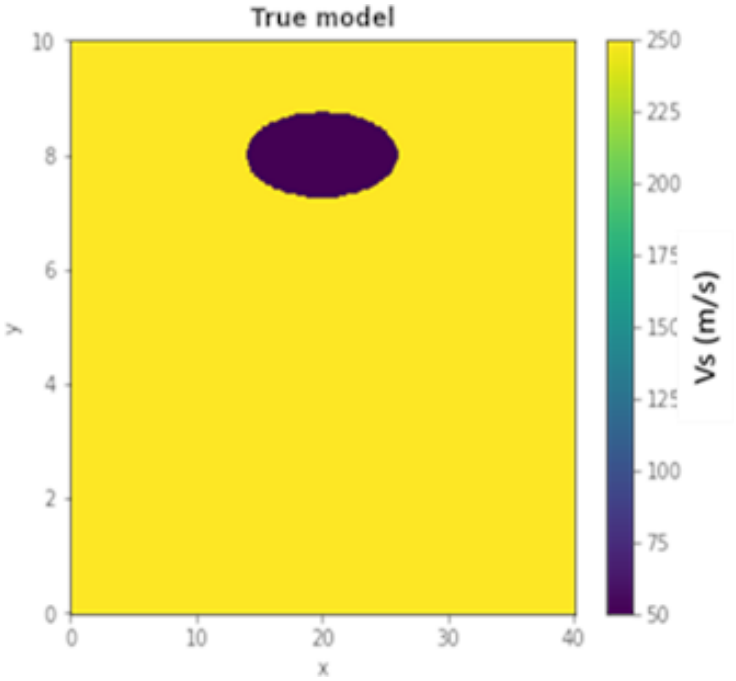

Figure 6.1. Numerical model used to simulate a karst anomaly for testing FWI implementation strategies.

Table 6.1. Material properties for the numerical model used in this study.

Material	Background Soil	Karst Anomaly
Density (kg/m^3)	2000	1000
V_P (m/s)	500	100
V_S (m/s)	250	50

6.2.2. Selection of Initial Model and Misfit Function

As noted previously, gradient-based local optimization methods typically require fewer forward problems than their global counterparts, making them significantly faster for FWI. However, they are more likely to become stuck in a local minimum that prevents them from advancing toward the correct solution. The most used misfit function in FWI is the L2 norm misfit function, which computes the squared difference between the observed and synthetic data as in Equation 2-2. However, the non-convexity of the L2 norm misfit function contributes to its increased likelihood to a phenomenon known as cycle-skipping. When the synthetic data produced by the initial model deviates by over half a cycle from the observed data (which is the case in complex geologies), L2-norm-based FWI converges to a local minimum and an erroneous velocity model. It is important to note that the effectiveness of a particular misfit function is inherently related to the availability of an initial model that closely approximates ground truth. In such a scenario, the inversion will most likely converge to the true model since the algorithm is starting much closer to the global minimum where cycle-skipping is no longer a concern. However, it is practically impossible to guarantee a starting model that is so close to the true model given the limitations of subsurface investigations in geotechnical engineering and the complex subsurface conditions found in near surface settings. This is particularly the case in karst settings where many anomalous features such as voids may be present. Consequently, the Temple research team explicitly explored the interplay between starting model and misfit function in the case of an anomalous karst target present in the subsurface with the goal of locating a misfit function more resilient than the L2-norm.

The use of misfit function based on optimal transport theory has recently gained significant popularity in the field of geophysics due to its ability to potentially reduce the problem of local minima (Métivier et al, 2016). The concept behind this method is to find an optimal mapping between two distributions that minimizes the total transportation cost (i.e., the Monge–Kantorovich transportation problem). This approach has found numerous applications in various fields, including economics, physics, and computer science (Villani 2021). In seismic signal processing, Engquist and Froese (2013) were the first to propose using the Wasserstein distance, which is based on the optimal transport theory, as a replacement for the problematic L2 distance. The distance measure in this context is not solely based on the difference of the oscillatory signals but includes all possible mappings that can shift and distort the original signal to match the target signal. This makes the optimal transport misfit capable of capturing information on travel time shifts and amplitude variations in the signal. However, the Wasserstein distance assumes that the compared signals are positive, and that no energy is lost in the process of mapping one signal to the other,

which are not valid assumptions for seismic signals. To address this shortcoming, Métivier et al. (2016) proposed the strategy of using a variant of Wasserstein distance that relies on the dual formulation of the Monge–Kantorovich problem and is defined as a maximization problem over the space of bounded functions with variations bounded by the unity. The proposed misfit function can be implemented using the following equations:

$$f_{W1}(m) = \sum_{s=1}^{S} W_1\left(d_{cal}^{s}[m]\,, d_{obs}^{s}\right) \tag{6.1}$$

$$W_1(d_{cal}^{s}[m]\,, d_{obs}^{s}) = \max_{\psi BLip_1} \int_t \int_{x_r} \psi(x_r, t) d_{cal}^{s}\,(x_r, t) - d_{obs}^{s}(x_r, t) dx_r dt \tag{6.2}$$

where *d* presents the observed and calculated shot-gathers, the variable x_r is linked to the receiver position while the variable *t* is representative of time. The superscript *s* corresponds to the shot-gather number in a seismic survey containing *S* shot-gathers. The notation [*m*] indicates the reliance of the calculated data on the model parameter *m*. Also, $BLip_1$ shows the space of bounded 1-Lipschitz functions. Given the existing gaps in the implementation of this misfit function, the current study aims to address the efficacy of this method in evaluating a sinkhole feature.

6.2.3. Data Acquisition and Processing

For data acquisition, a total of 17 surface receivers were positioned on both sides of the sinkhole. These receivers were placed at regular intervals of 2.0 m, with the first receiver located at coordinates (5.0, 0.0). Concurrently, 17 source impulse signals were introduced as seismic sources into the model. The signals were generated using a vertically polarized Ricker wavelet with a central frequency of 40 Hz (Figure 6.2). The source signals were also spaced 2.0 m apart, starting from coordinates (4.0, 0.0). This arrangement of sources and receivers closely resembles a commonly employed configuration in surface-based seismic geophysical testing.

To test the performance of optimal transport misfit function under different scenarios, two distinct initial models were considered. The first model closely resembled the true model, except for the anomalous zone (Figure 6.3) and the other one was derived from a pseudo-2D subsurface V_S profile using the multichannel analysis of surface wave (MASW) method on the recorded synthetically propagated waves (Figure 6.3). An MASW V_S profile was used as one of the starting models because it is a commonly employed geophysical method for karst characterization and the dataset acquired for FWI analysis can be readily processed using a dispersion-based analysis. Thus, MASW results represent a logical starting point in real-world applications of FWI. However, MASW spatially averages the properties of the domain, and the resulting subsurface model may not adequately reconstruct the subsurface in complex conditions with significant lateral variations. For example, the MASW-based initial model in Figure 6.3 exhibits a velocity inversion layer near the surface indicative of the karst anomaly in the true model but with inaccurate geometry and V_S. This makes the MASW V_S profile an ideal case to examine the robustness of the optimal transport misfit function relative to the L2 norm misfit function.

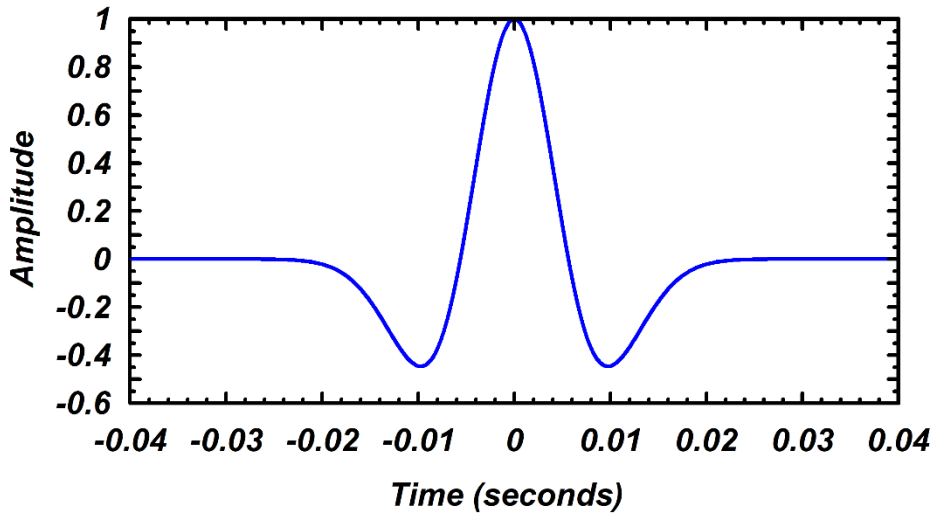

Figure 6.2. Ricker wavelet used to generate initial waveforms for numerical modeling.

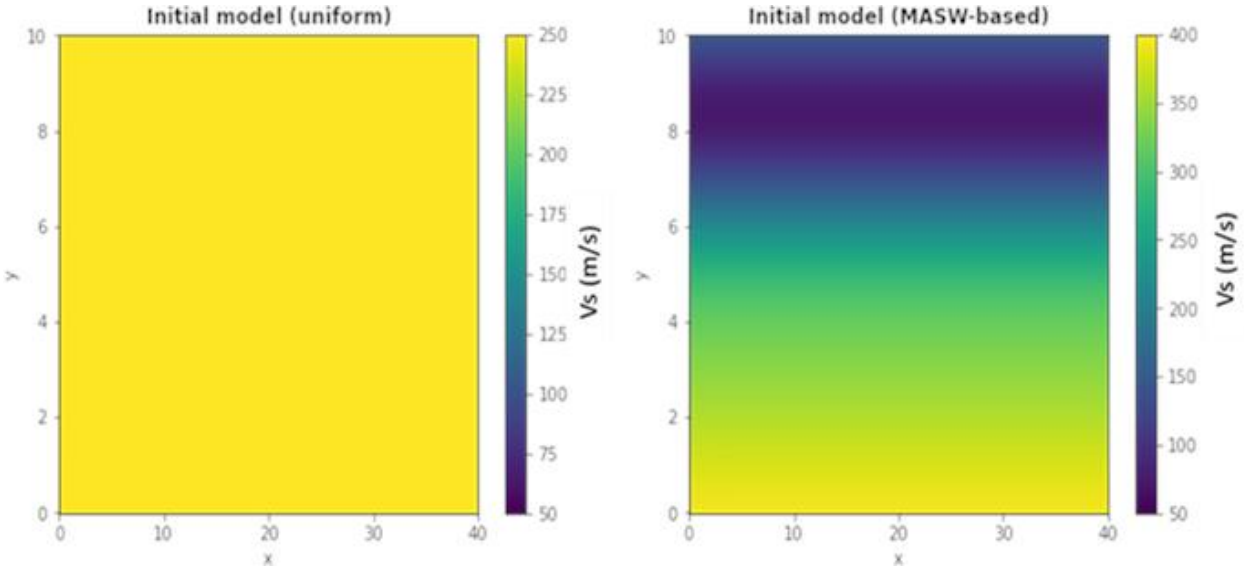

Figure 6.3. Starting models for FWI implementation on the synthetic model from Figure 6.1: (left) Uniform starting model; and (right) MASW starting model.

The *SalvusProject* module of the *Salvus* software suite from Mondaic group was employed in this study (Afanasiev et al., 2019). *Salvus* utilizes the robust spectral-element method (SEM) formulation for solving the elastic wave propagation equations. The observed waveforms from forward modeling simulations of the true model were subsequently processed using the Geometrics *SeisImager/SW* software package to develop and extract dispersion curves to conduct MASW. Additionally, the open-source software package *Geopsy* was used for the inversion of the dispersion data. This software utilizes a global search algorithm,

known as the neighborhood algorithm, to effectively invert for the velocity parameter (Wathelet *et al.* 2020).

For FWI, a quasi-newton method referred to as the limited-memory Broyden–Fletcher–Goldfarb–Shanno (L-BFGS) algorithm (Nocedal & Wright, 2006) was used to update the subsurface properties. This algorithm efficiently approximates the Hessian matrix and attempts to balance the gradient in a way to ensure convergence towards the global minima. To reduce the computational cost of FWI, it is a common practice to target a smaller subset of the domain, commonly referred to as the region of interest, for model updating during the inversion. The selection of this region is directly related to a-priori knowledge of the site. However, for this numerical study it was assumed that there were no previous site investigations, and the entire domain should be updated, resulting in increased uncertainty as it expands the search area. The top boundary condition was set as a free surface, while the bottom and sides of the domain were equipped with absorbing boundaries. A hierarchical inversion scheme was adopted in this study following a multiscale approach that interpreted first lower frequency waveform energy and then progressively introduced higher frequency data (e.g., Groos et al., 2017). The first stage of inversion used a center frequency of 10 Hz, followed by 20 Hz, 30 Hz, and ultimately 40 Hz. Each inversion stage persisted until there was no improvement in the misfit value for all the events.

Forward and inverse modeling were executed remotely in parallel modes by using the High-Performance Computing (HPC) resources at Temple University. The computations submitted to ten cores of the compute servers of the Temple HPC cluster. Compute is an interactive-use server that provides 88 CPU cores [Intel® Xeon Gold 6238 (Cascade Lake) processors] with up to 1.5 TB of RAM and 0.5 PB shared memory.

6.2.4. Results and Discussion

The final V_S profiles derived from the FWI procedures for the theoretical model are displayed in Figure 6.4. For models developed from uniform initial conditions [Figure 6.4(a-b)], the general location of the anomaly is accurately imaged, although there is a tendency to overestimate the extent of the anomalous zone, particularly in the L2-based result. The absence of data coverage on both ends of the domain, caused by the positions of the sources and receivers, resulted in the presence of additional low velocity zones and erroneous velocities near the boundaries no matter what misfit function and starting model selected. Additionally, since no constraints were imposed to the velocity inversion range, the background soil property could freely update in both models, resulting in minor deviations from the true values. However, the situation becomes more complicated when the initial model significantly deviates from the true model.

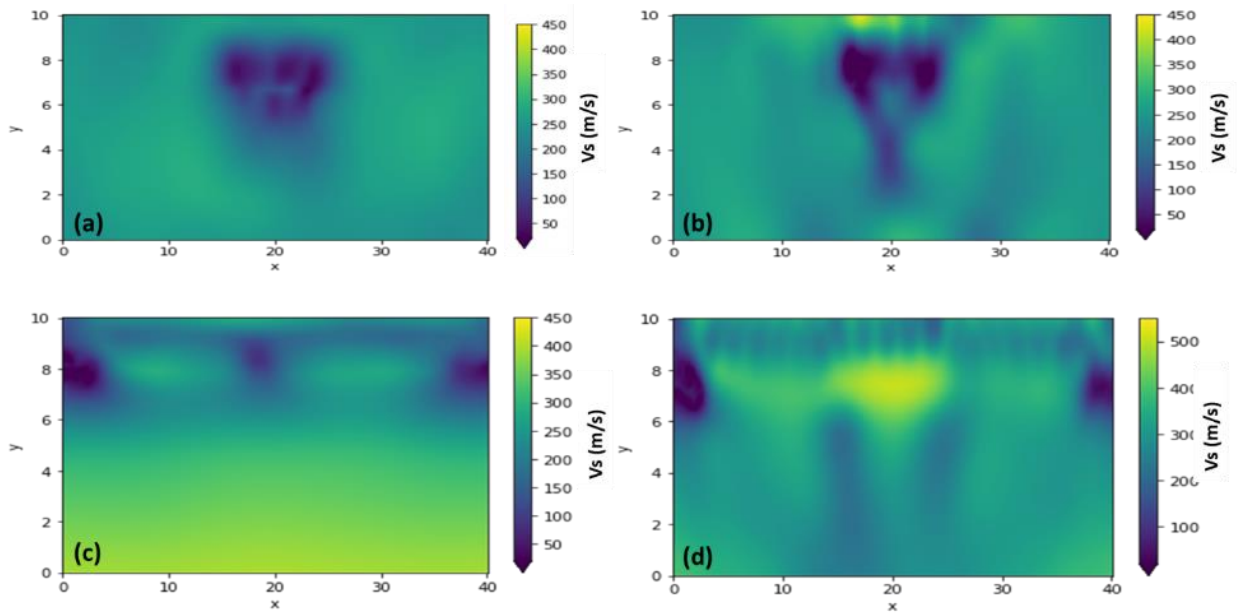

Figure 6.4. FWI V_S results using different misfit functions and starting models: (a) optimal transport with uniform starting model; (b) L2 norm with uniform starting model; (c) optimal transport with MASW starting model; and (d) L2 with MASW starting model.

In Figure 6.4(c), the results obtained using the optimal transport misfit function demonstrate its ability to overcome local minima and detect the low velocity zone. However, the extent of the velocity anomaly is not as large as expected and the performance of the optimal transport misfit function is better when an initial model is selected that more closely approximates the true model. The L2 norm results encountered difficulties during the inversion process and indicated a higher velocity region at the location of the low-velocity anomaly in the true model [Figure 6.4(d)]. This highlights the extent with which the L2 norm misfit function can become caught in a local minimum with a velocity structure that is drastically unrealistic. The observed performance differences can be attributed to the nature of each function. By its very nature, the optimal transport misfit function tends to be more resistant to local minima and can more accurately depict non-linear relationships in the data. On the other hand, the L2 misfit function is more prone to cycle skipping, especially when the phase difference between observed and predicted waveforms deviates by over half a cycle. Despite the limitations in accurately capturing the extent of the anomaly, the optimal transport approach still managed to detect the presence of the lower velocity zone, while the L2 approach failed to do so and produced misleading results.

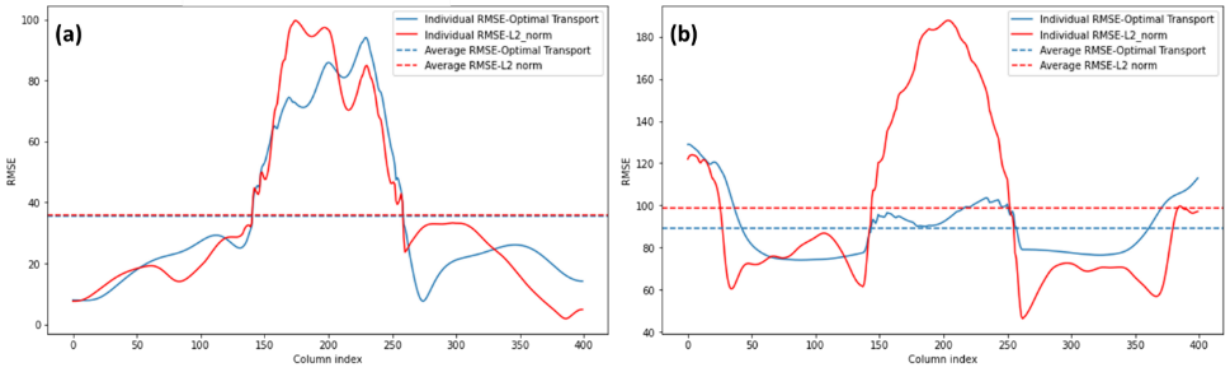

Figure 6.5. Calculated RMSE as a function of location: (a) uniform starting model; and (b) MASW starting model.

In addition to visual inspection of the reconstructed subsurface models, it is important to use statistical metrics for a more objective assessment of the results, reducing uncertainty in interpretations. In this study, the output mesh for each scenario was divided into 400 elements, and their associated matrix columns were compared elementwise with the true model to calculate the root mean square error (RMSE) as a function of location along the domain. This metric provides a quantitative measure of the fit between the observed and modeled data, with lower values indicating a better fit. Figure 6.5 displays the RMSE values for each column of the output matrices, as well as the average RMSE for each scenario. It can be observed that when the initial model is close to the true model, both the L2 and optimal transport functions perform similarly. However, this does not hold true when the starting model deviates significantly. In the case of the MASW-based initial model, the RMSE value for the optimal transport function is lower than that of the L2 norm misfit function, indicating its superiority in complex conditions. The practical implication of this finding is that resolving subsurface features using FWI in complicated settings might benefit from utilizing the optimum transport function to enhance output reliability. Given that a priori knowledge of the subsurface conditions is not always feasible, it may be prudent to shift away from the L2 norm misfit function to ensure unrealistic subsurface models indicative of local minima are not reconstructed using FWI.

6.2.5. Other Issues Related to FWI Implementation

Forward modeling of wave propagation is an essential aspect of the FWI methodology, and it is repeated multiple times as the inversion proceeds through multiple iterations to minimize the misfit function. One of the most popular methods to discretize the governing wave equation for Equation 2-1 is the finite difference method (Virieux, 1984), though other more sophisticated approaches such as finite-element or finite-volume methods may be beneficial in certain applications, particularly with respect to the implementation of boundary conditions (Virieux & Operto, 2009). Ultimately, the discretization scheme does not drastically affect the accuracy of the forward modeling (e.g., Kordjazi et al., 2020) and its selection can be a matter of user preference and availability in commercial and open-source software. For example, the Temple research team has experience with commercial software based on spectral element

methods [e.g., *Salvus* (Afanasiev et al., 2019)] as well as open-source software that utilizes the finite difference method [e.g., *DENISE Black Edition* (Koehn et al., 2012)].

Forward modeling can also be performed in either the frequency or time domain. Relative to time-domain FWI (Tarantola, 1984) , frequency-domain FWI (Pratt et al., 1998) can be more naturally implemented using a multiscale approach whereby the inversion is performed using lower frequency waveform content first, followed by increasingly higher frequencies. Such a multiscale approach has been shown to improve the convergence of the inversion (Groos et al., 2017). However, it should be noted that time-domain FWI is still capable of such a multiscale approach (as was implemented in the numerical efforts summarized in the previous section), it just requires finer discretization of time and space to avoid numerical dispersion or instability resulting in the need for a larger amount of computing resources and memory requirements. The *Salvus* software suite used in this study is an example of a commercial time-domain FWI code that can implement a hierarchical multiscale approach.

In the simplest case of acoustic wave propagation, the P-wave velocity (V_P) is the only model parameter that is discretized over the FWI domain. The number of model parameters increases as the complexity of the framework used to model wave propagation increases. This complexity is necessary to better capture the more complex wavefields present in most subsurface domains, which include different types of body waves, converted waves from layer boundaries, guided waves, and surface waves. Failure to include these phenomena in the wave modeling may lead to inaccurate model updating, inversion artifacts, and lack of convergence to meaningful subsurface models. In the case of elastic wave propagation, the model parameters include V_P, shear wave velocity (V_S), and density (ρ). Viscoelastic wave propagation introduces an attenuation factor [quality factor (Q)] as a model parameter to account for the intrinsic damping of geologic materials. Some studies have demonstrated improvements in the recovered subsurface profiles when viscoelastic wave propagation is used in forward modeling (e.g., Groos et al., 2017), though application of viscoelastic FWI remains largely relegated to research applications and/or large-scale domains such as those associated with hydrocarbon exploration or planetary geophysics (e.g., P. Yang et al., 2016). Consequently, elastic FWI was implemented in this study.

As noted previously, nonlinear minimization problems are usually solved using Newton-based methods whereby the nearest local minimum of the objective function is found using a local descent algorithm from a given starting point (Equation 2-3). These methods are based on a guided exploration of the probable models following the descent directions of the misfit function. Typically, the descent direction is approximated using a first-order derivative of the misfit function (e.g., the gradient) as in the steepest-descent or the nonlinear conjugate gradient algorithm. A more complex approach to define the descent direction uses approximations of the inverse Hessian (Equation 2-8) to account for the curvature of the misfit function. Examples of these include the L-BFGS algorithm implemented in this study and the truncated Newton method implemented in other studies. Comparisons between different optimization algorithms in FWI can be found in the literature. For example, Métivier & Brossier (2016) found that the nonlinear conjugate gradient performed better when attempting to locate the minimum for a complex analytical function but converged in a more irregular pattern. The L-BFGS algorithm path exhibited a more regular pattern towards the local minimum, but the truncated Newton method proposed the most

efficient path. The steepest descent algorithm converged the slowest and needed the greatest number of iterations compared with the three other methods. Similar patterns were noted when the algorithms were applied to a synthetic case study of a real field site. However, the authors commented that this performance was observed when initial models that were relatively good fits with the true model were selected. In real case applications, the initial model can be poorer and the difference between the algorithms may be less obvious and/or they all may fail to produce a reliable subsurface model. FWI efforts in this study employed the L-BFGS algorithm due to the consistency and regularity of its path towards solution convergence observed in the literature.

One final aspect that drastically affects the efficacy and efficiency of FWI is survey design. The zone of influence in which gradients can be calculated during FWI is dependent on the source-receiver geometry used to record waveforms (Figure 6.6). The spatial coverage offered by the survey design must therefore ensure sufficient waveforms are collected in the field to characterize the domain of interest and prevent convergence issues during the nonlinear optimization scheme employed in FWI. However, there exists a tradeoff between sufficient spatial coverage and adequate numbers of source/receiver and the amount of time necessary for data acquisition in the field and subsequent computational costs. Each source introduced into a domain to acquire waveforms represents additional time necessary for data acquisition. Each source also serves as a new "event" for which the data must be pre-processed (e.g., amplitude corrections, filtering, etc.) and for which the FWI algorithm must march through the optimization algorithm to match the observed waveforms. The optimal configuration of source and receivers for an FWI survey is still an open topic of research and previous efforts have indicated that optimal survey design is likely application- and domain-specific. For example, Kordjazi and Coe (2021) used a sequential optimal experimental design approach to develop a benefit-cost curve for a crosshole tomography survey and found that an increase in the number of crosshole sources directly increased the computational efforts but did not continually lead to appreciable improvements in the inverted images and subsequent interpretation of defect geometry and location. Given the preceding discussion and lack of formalized consensus for optimal survey design, the FWI efforts in this study utilized the same data acquisition approach as would be implemented in a seismic refraction survey. From a practicality standpoint, such a survey design aligns favorably with other seismic data needs, including seismic refraction and MASW, which lessens the impact of the amount of time necessary for data acquisition.

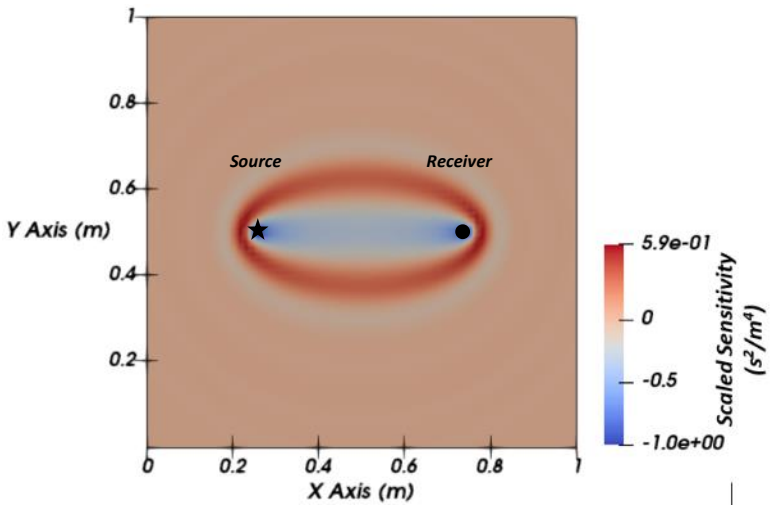

Figure 6.6. Influence zone (scaled sensitivity) for an FWI source and receiver pair within a homogeneous domain.

6.3. Joint Inversion of Rayleigh and Love Waves

As noted in Chapter 2, joint inversion of different geophysical datasets has shown promise as a tool in subsurface characterization and can alleviate the issues of non-uniqueness in geophysical inversion problems (e.g., Gallardo and Meju 2003; Linde et al. 2006; Chen et al. 2007; Colombo and Stefano 2007; Wagner et al. 2007; Hamimu et al. 2011). Many of these studies demonstrated an improvement in the subsurface results after applying a joint inversion approach to geophysical datasets such as electrical resistivity, GPR, and seismic methods that are commonly implemented for sinkhole evaluation. Unfortunately, as data processing efforts began for this study, a major obstacle was encountered in the implementation of joint inversion. Since the fundamental physics and theory behind the gravity method, electrical resistivity, GPR, and seismic methods (such as MASW) are so different, the implementation of joint inversion for different combinations of these geophysical methods is highly specialized. Consequently, no commercially developed software package was readily located that can implement joint inversion of such disparate datasets. This left only the option of research-based open-source software. Many open-source codes with the potential for joint inversion were scattered across the web in settings ranging from poorly documented GitHub repositories to citable peer-reviewed literature [e.g., pyGIMLi (Rücker et al. 2017)]. However, such codes often merely provided a framework or workflow for the joint inversion and relied either on external dependencies for some of the steps or on the user to develop more application-specific subroutines. For example, the forward modeling of different geophysical methods may have been implemented, but the mathematical basis for the inversion problem itself may have been missing. Because software development was beyond the scope of this study, joint inversion was therefore limited to the joint inversion of Rayleigh and Love waves, for which the open-source software package *Geopsy* was readily available. Previous efforts had explored joint inversion of Rayleigh and Love waves (e.g., Joh et al. 2006; Boxberger et al. 2011; Dal Moro and Ferigo 2011; Hamimu et al. 2011) but did not specifically explore its application in karst.

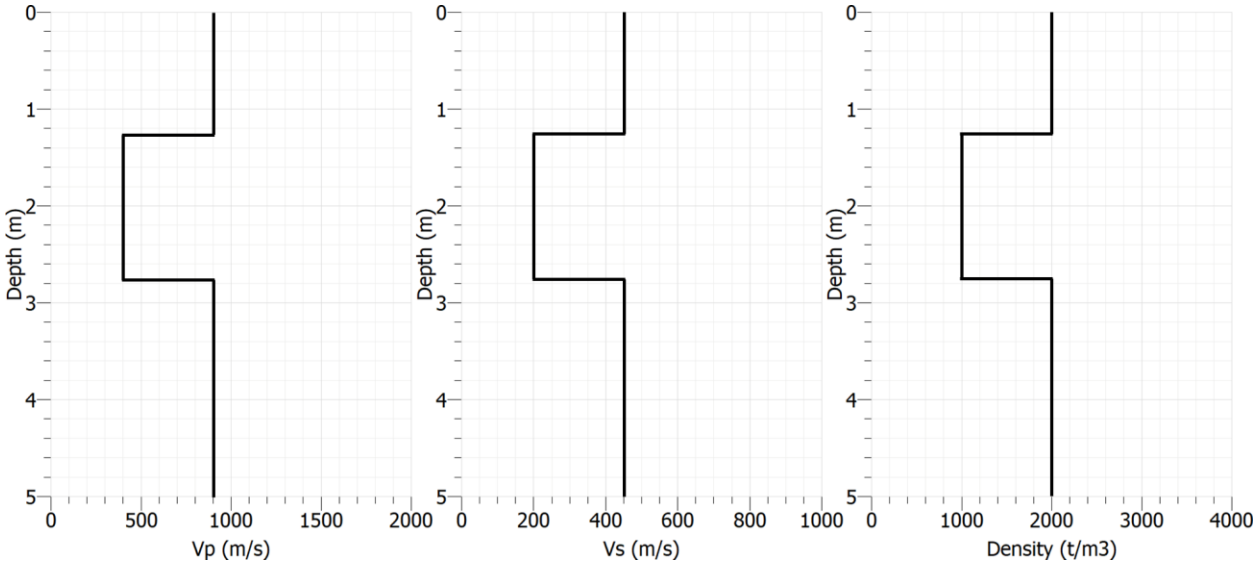

(a)

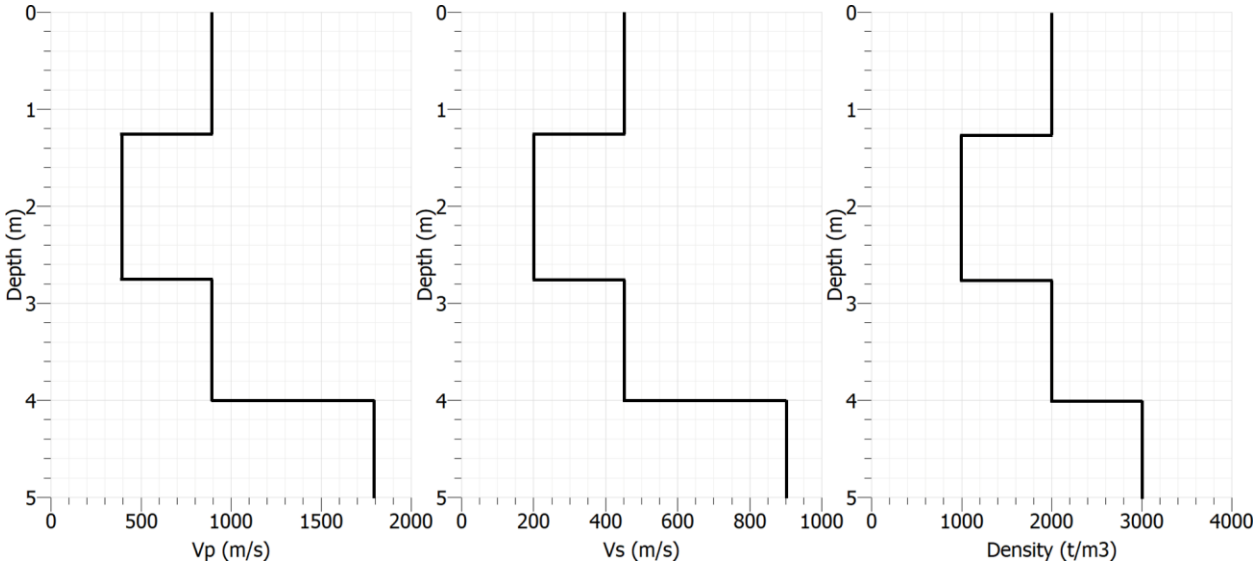

(b)

Figure 6.7. One-dimensional numerical models used to simulate a karst anomaly for testing joint inversion of Rayleigh and Love waves: (1) background soil with karst anomaly; (b) background soil with karst anomaly and intact bedrock interface.

Joint inversion of Rayleigh and Love waves was implemented using theoretical simulations to explore its capabilities much like FWI. However, only one-dimensional simulations were performed since MASW inherently produces a one-dimensional (1D) model of the subsurface within the spatial extent of its array. Figure 6.1 was used as inspiration for the 1D models of karst anomalies for joint Rayleigh and Love wave inversion. However, the *Vs*, V_p, and density were adjusted to better represent the stiffer conditions encountered at the Chemical Road site and a second model was added where a bedrock interface was included (Figure 6.7). These models were then used to generate theoretical Rayleigh and Love wave

dispersion curves using the *gpdc* module of the *Geopsy* software package. These theoretical dispersion curves were assumed to represent the observed dispersion curves from waveforms acquired at a site with the 1D subsurface profiles in Figure 6.7. The *Geopsy* software package was then used to perform inversion of the observed dispersion curves using the global search algorithm implemented within the *dinver* module. The Rayleigh and Love wave dispersion curves were independently inverted and then jointly inverted. Equal weight was assigned to the Rayleigh and Love wave dispersion curves when defining the joint misfit function in the joint inversion algorithm.

Figure 6.8 presents the V_s inversion results for the 1D model with background soil and a soft anomalous layer indicative of a void feature or other karst activity. The black line indicates the V_s profile with the smallest dispersion misfit, which is assumed to represent the actual subsurface conditions. Each plot also includes all V_s profiles within 0.1% of the minimum dispersion misfit to give an indication of the uncertainty and variability in the results. For practical purposes, such small differences in misfit render all V_s profiles within a given plot as likely solutions for the inversion. In the case of this first model, all the minimum misfit V_s profiles match the ground truth V_s in Figure 6.7(a) almost identically. The V_s results using Rayleigh inversion [Figure 6.8(a)] indicate slightly less variability, particularly for the layer of soil beneath the anomalous karst layer. The Love wave V_s results in Figure 6.8(b) below 2.75 m still indicate a V_s equal to 450 m/s, but with a larger amount of variation for other inversion results with similar misfit. Nevertheless, the overall amount of variability in the results is very low. Unsurprisingly, this carries over to the joint inversion results in Figure 6.8(c), with very little difference in the results relative to the V_s profile derived from individual Rayleigh and Love wave inversions and relative to the ground truth model in Figure 6.7(a). This indicates that very little is gained from performing joint inversion of Rayleigh and Love waves for this model since the individual inversions are already well-constrained and converge to the true model quite readily.

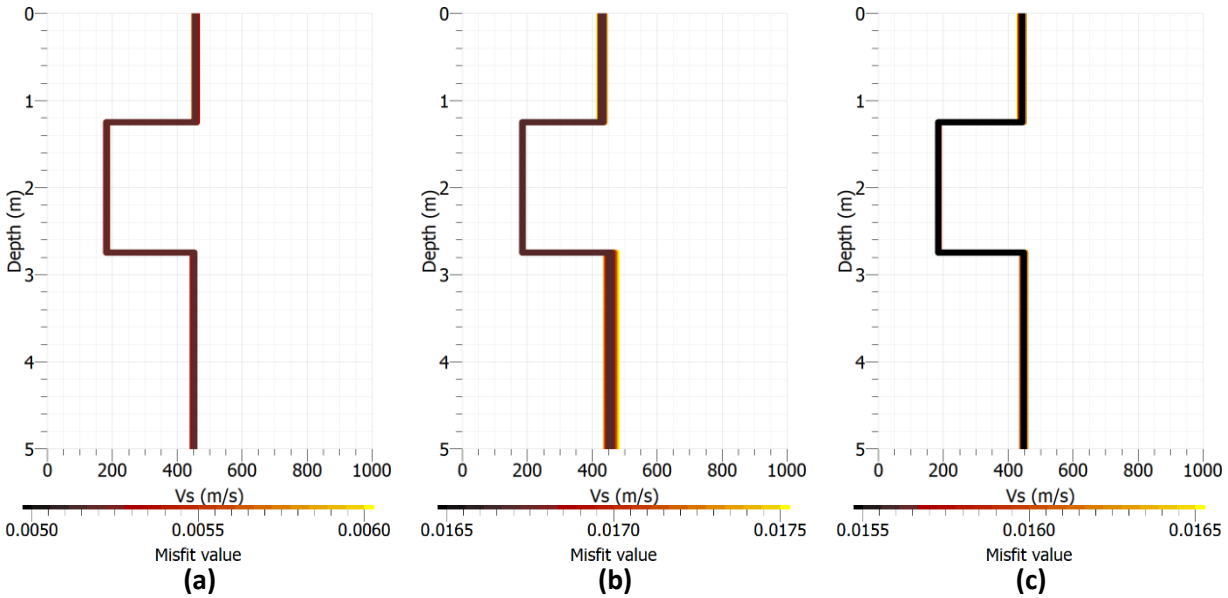

Figure 6.8. V_s Results for background soil with karst anomaly model: (a) Rayleigh wave inversion; (b) Love wave inversion; and (c) joint inversion of Rayleigh and Love waves.

The results in Figure 6.9 for the second ground truth model (soil, karst anomaly, and underlying intact bedrock interface) suggest a more pronounced effect from joint inversion of Rayleigh and Love waves. Immediately apparent is the much larger amount of scatter associated with the Rayleigh wave inversion results in Figure 6.9(a). The small anomalous layer of karst activity between 1.25 m to 2.75 m creates issues for accurately identifying the V_s of the background soil present below that depth and above the intact bedrock interface in all the results. This layer of soil is typically estimated as approximately 300 m/s instead of the true value of 450 m/s no matter which inversion technique is used. However, the Rayleigh wave inversion results in Figure 6.9(a) really struggle to converge to a consistent estimate for this layer with quite drastically different interpretations (e.g., ≈ 300 m/s versus ≈ 600-700 m/s) despite a practically negligible difference in dispersion misfit of less than 0.1%. The Love wave inversion results in Figure 6.9(b) do not exhibit this level of uncertainty, indicating that Love waves in this ground truth model are more consistent with respect to their dispersive behavior. Both Rayleigh and Love wave inversion results provide similar estimates for the Vs of the upper soil layer, anomalous karst layer, and the intact bedrock, though the Love wave inversion results do exhibit more variability with respect to the interpreted V_s of the intact bedrock layer. Consequently, the joint inversion results in Figure 6.9(c) do not provide a different interpretation of the overall subsurface conditions. Instead, a joint inversion approach takes advantage of the complementary information provided by the Rayleigh and Love wave results to better constrain the scatter in V_s results for the bottom soil layer and the intact bedrock layer. Therefore, the results for this model demonstrate how joint inversion can increase confidence in the resulting V_s profiles even if the overall interpretation of the subsurface conditions is unchanged.

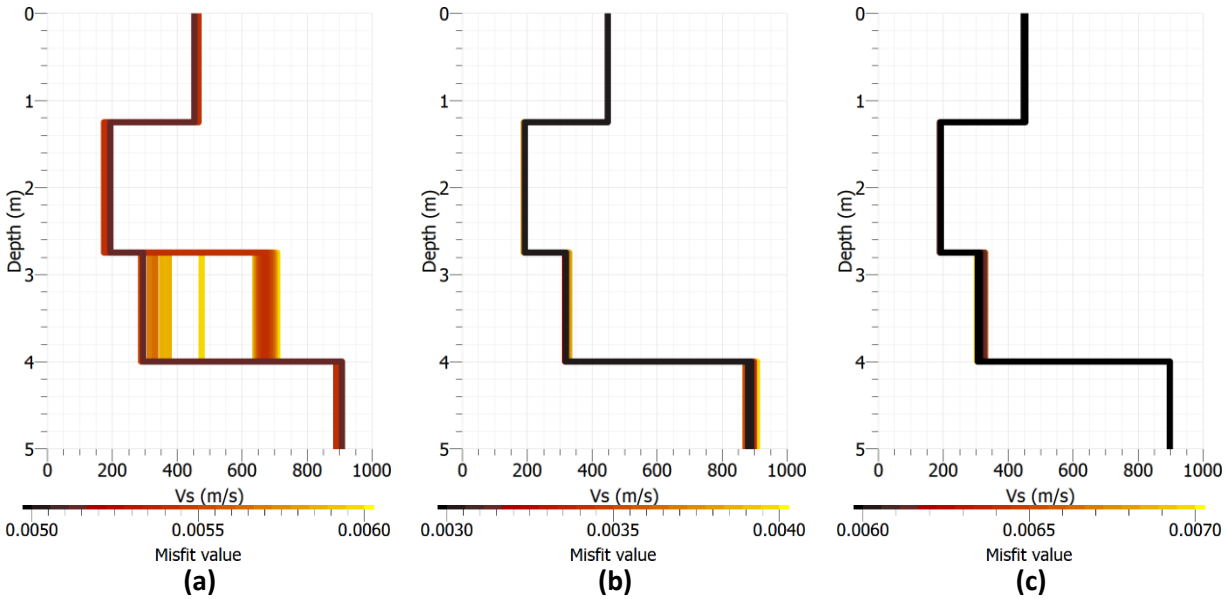

Figure 6.9. V_s Results for background soil with karst anomaly and bedrock interface model: (a) Rayleigh wave inversion; (b) Love wave inversion; and (c) joint inversion of Rayleigh and Love waves.

6.4. Recommendations

Based on the simulation efforts and extensive review of existing literature on FWI, the following approach is recommended for implementation of FWI on domains with potential karst anomalous features:

- Elastic wave propagation
- Interior and exterior source locations with spatial density like seismic refraction survey
- L-FBGS algorithm
- Optimal transport misfit function
- Multiscale approach with multiple central frequency sources during inversion (between 10 Hz – 40 Hz)

Though it is possible that deviations from these recommendations can still result in effective FWI results, it is expected that following these recommendations represents a good compromise between inversion robustness and computational costs. Many of the recommendations represent commonly employed techniques in FWI for other near surface and global applications and implementation is possible across a wide range of commercially availability and open-source software. For other aspects, there was insufficient evidence in both the literature and the numerical simulations to definitively make recommendations. For example, it was noted that a finite difference versus a finite element scheme has limited effects on the accuracy of the FWI results. Consequently, the Temple research team recommends that choices regarding numerical discretization, spatial extent of survey and number of sources/receivers, the use of viscoelastic wave propagation, and time-domain versus frequency-domain FWI be decided based on user experience, ease of implementation for the given domain, site conditions, and the limitations of the selected FWI software package.

With respect to joint inversion, the Temple research team struggled to locate software packages that are flexible enough to jointly invert such disparate datasets as gravity, electrical resistivity, GPR, and MASW, while also being sufficiently developed and documented to minimize the need for significant specialized coding efforts to run the inversions. Only the open-source *Geopsy* package was identified to meet the second criterion at the expense of the flexibility to analyze data from fundamentally different geophysical tests. *Geopsy* readily allows for joint inversion of multiple dispersion curves, including from different wave types, but is relegated to applications with only seismic data. Subsequent efforts with joint inversion of Rayleigh and Love waves highlighted the benefits of this approach in subsurface conditions with karst. Overall, the interpretations of the underlying subsurface conditions were unchanged by joint inversion. However, the joint inversion process better constrained the resulting V_s profiles and reduced uncertainty in some layers of the tested models. This benefit was model-specific and dependent on the extent to which one wave types was better suited to capture the dispersive behavior of a particular subsurface profile. It is not expected that the additional benefit from joint inversion will be exhibited at all sites, particularly if both Rayleigh and Love wave results exhibit similar levels of uncertainty. But in situations where one wave type has more trouble converging to a stable solution, the complementary information provided by the other wave type can better constrain the inversion and allow for greater confidence in the jointly inverted *Vs* profiles. In neither of the two 1D models tested in this study did joint inversion led to poorer outcomes relative to individually inverted Rayleigh and Love wave results. Based on this fact and the modest increase in data collection and pre-processing efforts to acquire both Rayleigh and Love wave data at a site, the Temple research team recommends that joint inversion of Rayleigh and Love waves be implemented more consistently when characterizing karst sites. This recommendation can be

qualified by acknowledging that karst sites where data acquisition efforts are constrained to the roadway (as was largely the case at the Chemical Road site) do not lend themselves well to joint inversion of both Rayleigh and Love waves since the generation of Love waves is much more difficult to accomplish. The generation of Love waves is better suited for soil sites where spikes can be used to couple a base plate more firmly to the ground for horizontal strikes [e.g., Figure 4.7(b)]. In these cases, the use of angled base plates where sledgehammer strikes include a vertical and horizontal component and the use of multicomponent geophones that record both vertical and horizontal ground motion are recommended to reduce the data collection efforts.

6.5. Summary

The implementation of advanced inversion techniques such as FWI and joint inversion requires an appreciable number of decisions regarding data acquisition, survey design, optimization algorithm, and parameterization, all of which can influence the accuracy and efficiency. Exacerbating this issue is the limited amount of implementation of such techniques on near surface geotechnical domains with anomalous conditions. A numerical and theoretical study was undertaken that attempted to explore the many issues in FWI and joint inversion implementation in anticipation of processing the field data. The results of this study aided the development of recommendations regarding FWI and joint inversion implementation at Chemical Road. Though a one-size-fits-all approach is not recommended given the complex interplay between various factors affecting advanced inversion techniques (e.g., starting model, misfit function, optimization algorithm, subsurface/site conditions, etc.) it is anticipated that the lessons learned in this study will be generally relevant to other sites with active karst features.

7. RECOMMENDATIONS FOR IMPLEMENTATION

The objective of this research project was to provide the Pennsylvania Department of Transportation (PennDOT) with recommendations regarding the use of advanced geophysical techniques such as full waveform tomography and joint inversion of geophysical datasets to better characterize sinkholes hazards. A more generalized discussion regarding implementation of the lessons learned in this study is provided herein, starting with a global summary of the project findings and followed by specific recommendations for full waveform inversion (FWI) and joint inversion.

7.1. General Findings and Recommendations

Though the overall focus of this study was FWI and joint inversion, many general findings were observed based on the literature review of PennDOT District 6-0 projects and application of multiple geophysical techniques at the selected Chemical Road site:

- Test borings were typically drilled in PennDOT District 6-0 projects to provide information regarding sinkhole activity and karst. Most projects reviewed in this study consisted of at least one geophysical exploration to help characterize the subsurface typically during the design phase. Multichannel Analysis of Surface Waves (MASW) was the most common geophysical test and Electrical Resistivity Imaging (ERI) was the second most common.

- For the District 6-0 projects reviewed in this project, the following techniques were typically implemented to address existing subsidence features and mitigate future sinkhole subsidence activity: geogrid and geotextile mat reinforcement; compaction; inverted filter (i.e., clogging swallow holes); limited/low mobility grouting; and compaction grouting.

- The District 6-0 projects reviewed in this study showed that quality control of sinkhole mitigation operations was typically accomplished using the following approaches: checking the mechanical condition of drilling and grouting equipment; ground or structure movement monitoring; inspection of treatment procedure performance measures (e.g., grouting rate, pressure, and volumes); and measurements of material properties (e.g., grout slump or strength tests, geotextile tensile tests). Post-remediation verification testing with geophysics was typically not performed though it was prevalent during the treatment design stage to guide construction efforts and post-remediation test borings have been used on quite a few projects.

- The Electromagnetic (EM) results at Chemical Road only provided a qualitative assessment of the subsurface sinkhole features and largely corroborated ERI results. Sinkhole 1 was located in a part of the site that exhibited high conductivity (i.e., low resistivity), which pointed to the presence of soft, wet soils that can result from karst activity. Interestingly, the EM results mapped Sinkhole 2 to a part of the site with lower conductivity, which suggested an air-filled cavity beneath the surface. Evidence of such an air-filled cavity was present at the site immediately beneath the roadway at the location of Sinkhole 2. Consideration of EM for future sinkhole sites should be

limited to situations where there is a lack of a distinct surface manifestation of the sinkhole that prevents an estimation of its size/location or to identify between potentially air-filled or soil-filled voids in the subsurface.

- Ground Penetrating Radar (GPR) suffered from poor performance due to the highly conductive subsurface materials present throughout much of the site. Some evidence of subsurface depressions was present, but interpretation of the GPR results proved largely inconclusive. GPR should be considered as a useful tool for future karst studies when the subsurface soils are more likely to exhibit low conductivity (e.g., granular soils) so better signal quality is encountered. A review of previous test borings from the design stage of the structure or from nearby sites can aid determining the potential extent of highly conductive subsurface soils.

- The pre-grouting gravity results presented clear evidence of mass deficits in the immediate vicinity of Sinkhole 2 but was inconclusive for Sinkhole 1. Post-grouting gravity results showed a modest increase in the residual gravity measurements across the sites as would be expected by the addition of new grout material to the subsurface. The use of the gravity method should be reserved for projects where time is not the most critical factor since the acquisition of gravity data is so involved and time-consuming. Emergency repair projects are not ideal in that regard due to their urgency.

- The post-grouting Horizontal-to-Vertical Spectral Ratio (HVSR) results exhibited a general increase in H/V amplitude at lower frequencies that could be reasonably attributed to a grouting-related velocity increase in the soft zones encountered in the test borings. However, the increase in H/V amplitude occurs over a broad frequency band and hinders the extraction of a reliable estimate for the site frequency. The lack of a distinct H/V peak for post-grouting measurements was attributed to the tendency of the grout to decrease the severity of large stiffness contrasts in the subsurface. HVSR data was rapidly acquired and did provide additional corroboration of the subsurface conditions, so its use is encouraged in future sinkhole projects particularly as a rapid tool to assess pre- and post-treatment changes in the subsurface conditions.

- The Department's MASW results indicated that the depth to rock generally decreased towards the eastbound travel lanes closet to the roadway grass shoulder. The locations of the sinkholes coincided with locations where low V_s values were encountered within the subsurface. Post-grouting MASW results exhibited as much as a 10% increase relative to the pre-grouting V_s due to the increased stiffness of the grouting and filling in of anomalous soft zones. MASW and ERI proved the most versatile of the geophysical methods implemented on behalf of the Department, which strengthens the rationale for why these two methods were the most commonly employed in previous District 6-0 sinkhole projects. They provided complementary information and demonstrated the most value when it came to interpreting subsurface conditions given the time investment in data acquisition and processing. The results from this study support the continued use of MASW and ERI data for future sinkhole projects.

- The FWI results generally corroborated the MASW results with a few notable exceptions. First, the FWI results tended to exhibit lower values for V_s across the site both before and after grouting. Second, the FWI results suggested that post-grouting anomalous soft zones were more spatially extensive than the MASW results. However, when compared to their pre-grouting baseline *Vs*, the MASW and FWI post-grouting results across the site support that additional remediation was unnecessary given the extent and depth of ground improvement. The 3D FWI results allowed a better visualization of a karst-related network of anomalous soft zones between Sinkholes 2 and 1.

More specific recommendations related to FWI and joint inversion are discussed in the following sections based on the lessons learned from the field testing (Chapter 5) and the numerical/theoretical analysis (Chapter 6).

7.2. Full Waveform Inversion

Simulation efforts were used to develop a more specific set of recommendations for the FWI workflow to be implemented in future karst projects. Though an extensive array of models was not developed, the following recommendations were formed based on the simulation efforts and an extensive review of recent FWI literature:

- Elastic wave propagation is sufficient to develop suitable estimates of subsurface conditions even though geologic materials inherently exhibit internal damping akin to viscoelastic materials.

- The source/receiver geometry should follow typical seismic refraction practice to ensure sufficient waveform coverage and resolution.

- The most commonly used optimization algorithm in FWI (L-FBGS algorithm) is sufficient to develop suitable estimates of subsurface conditions.

- The most commonly employed misfit function (L2-norm) exhibits strong dependency on the starting model used for FWI. The more recently introduced optimal transport misfit function is more robust against errors in the starting model and is recommended as the default misfit function to be used for the optimization process. In either case, the starting model should be derived from some other seismic method such as MASW.

- The FWI should implement a multiscale approach where low frequency components of the wavefield are inverted before moving to higher frequency components. The results in this study demonstrated that a frequency range between 10 Hz – 40 Hz is sufficient to derive suitable estimates of subsurface conditions

- Any remaining choices regarding the FWI workflow (e.g., numerical discretization, spatial extent of survey, time-domain versus frequency-domain analysis, etc.) should be decided based on user

experience, ease of implementation for the given domain, site conditions, and the limitations of the selected FWI software package.

- The amount of time necessary to acquire data for a FWI survey is comparable to a 2D MASW survey or seismic refraction survey. There is also some efficiency gained if the waveform data acquired from an FWI survey is also processed to develop dispersion curves for an MASW analysis. Consequently, the main hurdle with respect to implementation of FWI remains the large computational costs and the steep learning curve for the commercially available or open-source software packages. The latter can be addressed with sufficient training, and many vendors of commercial FWI software include that in the baseline costs for software licensing. However, the issue of computational costs remains a challenge. For the purposes of this study, the inversions were completed in parallel mode using the High-Performance Computing (HPC) resources at Temple University. The computations were distributed anywhere between ten to sixteen cores of the *Compute* servers in the Temple HPC cluster, which provides 88 CPU cores (Intel® Xeon Gold 6238 processors) with up to 1.5 terabytes (TB) of RAM and 0.5 petabytes (PB) of shared memory. On average, each set of 2D FWI results necessitated approximately 10 hours for the inversion to complete (60 iterations per inversion with each iteration taking 10 minutes). An additional one to two hours was necessary for pre-processing to remove noisy data, apply filters, and other similar tasks. This represents at least two orders of magnitude difference when compared to typical 2D MASW surveys where the inversions take several minutes for global search algorithms and only a handful of seconds for a local search algorithm. In the case of 3D FWI, the comparison is even more lopsided since it took approximately 50 hours for the inversions performed in this study (25 iterations per inversion with each iteration taking 2 hours). Though computational capabilities are ever evolving with the continued development of central processing units (CPU) and graphics processing units (GPU) , the length of time necessary to complete the FWI in this study will not drastically change in the foreseeable future. Consequently, FWI is recommended only in cases where time is not the most critical aspect of the project. For example, use of FWI to guide emergency repair projects is not recommended given the amount of time necessary to run the inversions.

7.3. Joint Inversion

The open-source *Geopsy* package was the only software package identified that was readily available and did not require extensive specialized coding efforts to perform joint inversion. Unfortunately, that meant that only joint inversion of seismic data was implemented in this study. Moreover, the field conditions at this site prevented the collocation of Rayleigh and Love wave MASW surveys directly over known sinkhole locations since these locations were always over the existing roadway. The stiff asphalt prevented good coupling for the horizontal base plate necessary to generate Love waves. Therefore, analytical efforts were used to explore joint inversion of Rayleigh and Love wave dispersion curves on two models that represent karst conditions like the Chemical Road site. The following recommendations were formed based on these analytical efforts and an extensive review of recent literature related to joint inversion of seismic data:

- Joint inversion of Rayleigh and Love waves did not alter the interpreted subsurface profile in either of the models. Instead, the joint inversion process offered increased confidence in the results due to the additional constraints placed on the inversion and the resulting reduction in V_s uncertainty for some of the layers within the two models. In neither case did performing a joint inversion negatively impact the final resulting subsurface profile.

- The potential for improvements offered by joint inversion of Rayleigh and Love waves is site-specific and will depend on the extent with which a particular wave type is better suited to reveal the dispersive conditions at the site. At sites where the specific subsurface conditions cause one wave type to struggle with converging towards a stable solution during MASW inversion, the use of joint inversion may better constrain the resulting subsurface profile and increase confidence in the interpreted subsurface conditions.

- Acquisition of Rayleigh and Love waves requires a similar amount of effort and time. The only difference in equipment is that the receivers must be polarized to capture the appropriate ground motion (i.e., vertical for Rayleigh waves and horizontal for Love waves) and an adequate source is necessary to generate the appropriate input seismic energy. The use of angled base plates where the sledgehammer strikes include a vertical and horizontal component and the use of multicomponent geophones that record both vertical and horizontal ground motion are recommended to increase efficiency during data collection efforts.

- It takes approximately the same amount of time (a few minutes) to run a global inversion of Rayleigh wave dispersion information, Love wave dispersion information, or joint inversion of both. So computational run times are trivial in all scenarios and the only real difference between them are the data collection efforts as previously described and any data pre-processing (e.g., removing noisy data, applying filters, etc.). Data pre-processing efforts are again comparable for all scenarios.

- Given the potential improvements offered by joint inversion and the modest increase in data collection and pre-processing efforts for both Rayleigh and Love waves at a site, it is recommended that joint inversion of Rayleigh and Love waves be implemented when feasible at karst sites.

8. REFERENCES

Afanasiev, M. (2017). Multi-scale full-waveform inversion. Ph.D. Dissertation, ETH Zurich.

Afanasiev, M., Boehm, C., Van Driel, M., Krischer, L., Rietmann, M., May, D.A., Knepley, M.G., and Fichtner, A., (2019). “Modular and flexible spectral-element waveform modelling in two and three dimensions.” Geophysical Journal International, 216 (3), 1675–1692.

Afanasiev, M., Boehm, C., Van Driel, M., Krischer, L., Rietmann, M., May, D.A., Knepley, M.G., and Fichtner, A., (2019). “Modular and flexible spectral-element waveform modelling in two and three dimensions.” Geophysical Journal International, 216 (3), 1675–1692.

Ahmed, S. and P. J. Carpenter (2003). "Geophysical response of filled sinkholes, soil pipes and associated bedrock fractures in thinly mantled karst, east-central Illinois." Environmental Geology 44(6): 705-716.

Alcántara, I. and A. S. Goudie (2010). Geomorphological hazards and disaster prevention, Cambridge University Press.

Alexander, S. C., Rahimi, M., Larson, E., Bomberger, C., Greenwaldt, B., and Alexander Jr, C. (2013). “Combining LiDAR, aerial photography, and Pictometry® tools for karst features database management.” Proceedings 13th Sinkhole Conference, NCKRI Symposium 2, 441-448.

Al-Halbouni, D., E. P. Holohan, L. Saberi, H. Alrshdan, A. Sawarieh, D. Closson, T. R. Walter and T. Dahm (2017). "Sinkholes, subsidence and subrosion on the eastern shore of the Dead Sea as revealed by a close-range photogrammetric survey." Geomorphology 285: 305-324.

Amrouche, M., and Yamanaka, H. (2015). "Two-dimensional shallow soil profiling using time-domain waveform inversion." Geophysics, 80(1), EN27-EN41.

Anchuela, Ó. P., Casas-Sainz, A. M., Soriano, M. A., and Pocoví-Juan, A. (2009). “Mapping subsurface karst features with GPR: results and limitations.” Environmental Geology, 58(2), 391-399.

Anchuela, Ó. P., Sainz, A. C., Juan, A. P., and Garbí, H. G. (2015). “Assessing karst hazards in urbanized areas. Case study and methodological considerations in the mantle karst from Zaragoza city (NE Spain).” Engineering geology, 184, 29-42.

Arai, H. and K. Tokimatsu (2005). "S-wave velocity profiling by joint inversion of microtremor dispersion curve and horizontal-to-vertical (H/V) spectrum." Bulletin of the Seismological Society of America 95(5): 1766-1778.

Arai, H., and Tokimatsu, K. (2005). “S-wave velocity profiling by joint inversion of microtremor dispersion curve and horizontal-to-vertical (h/v) spectrum.” Bulletin of the Seismological Society of America, 95, 1766–1778.

Archie, G. E. (1942). "The electrical resistivity log as an aid in determining some reservoir characteristics." Transactions of the AIME 146(01): 54-62.

Arzi, A.A. (1975). “Microgravimetry for Engineering Applications.” Geophys. Prosp., 23(3), 408-425.

ASTM (2020). “D6429: Standard Guide for Selecting Surface Geophysical Methods.” ASTM International, West Conshohocken, PA.

Atzori, S., G. Baer, A. Antonioli and S. Salvi (2015). "InSAR-based modeling and analysis of sinkholes along the Dead Sea coastline." Geophysical Research Letters 42(20): 8383-8390.

Baer, G., Y. Magen, R. Nof, E. Raz, V. Lyakhovsky and E. Shalev (2018). "InSAR measurements and viscoelastic modeling of sinkhole precursory subsidence: Implications for sinkhole formation, early warning, and sediment properties." Journal of Geophysical Research: Earth Surface 123(4): 678-693.

Bai, M., Chen, Y., Wang, C., Li, X., and Tian, G. (2018). "Radar spectral analysis and evaluation of the effect of grouting treatment in karst caves and soil caves." Environmental Earth Sciences, 77(24), 795.

Baker, G. S. (1999). Processing near-surface seismic-reflection data: A primer. Society of Exploration Geophysicists.

Bamler, R. and P. Hartl (1998). "Synthetic aperture radar interferometry." Inverse problems 14(4): R1.

Bansah, K. J. (2018). "Imaging and mitigating karst features." Ph.D. Dissertation, Missouri S&T.

Batayneh, A. T., A. A. Abueladas and K. A. Moumani (2002). "Use of ground-penetrating radar for assessment of potential sinkhole conditions: an example from Ghor al Haditha area, Jordan." Environmental Geology 41(8): 977-983.

Bates, R. L. and J. A. Jackson (1984). Dictionary of geological terms, Anchor Books.

Beck, B. F., and Zhou, W. (2002). Management of the discharge and quality of highway stormwater runoff in karst areas. FHWA Report DTFH61–93-R-00183, U.S. Department of Transportation, Washington D.C.

Benedetto, A., Benedetto, F., and Tosti, F. (2012). “GPR applications for geotechnical stability of transportation infrastructures.” Nondestructive Testing and Evaluation, 27(3), 253-262.

Benedetto, A., Tosti, F., Bianchini Ciampoli, L., and D’Amico, F. (2017). “An overview of ground-penetrating radar signal processing techniques for road inspections.” Signal Processing, 132, 201-209.

Ben-Hadj-Ali, H., Operto, S., & Virieux, J. (2008). Velocity model building by 3D frequency-domain, full-waveform inversion of wide-aperture seismic data. *Geophysics*, *73*(5), VE101–VE117.

Benson, A.K., and Baer, J.L. (1989). “Close order gravity surveys – a mean of fault definition in valley fill sediments.” Proc. 23rd Symp. On Engineering Geology and Soil Engineering, 219–240.

Benson, A.K., and Floyd, A.R. (2000). “Application of gravity and magnetic methods to assess geological hazards and natural resource potential in the Mosida Hills, Utah County, Utah.” Geophysics, 65(5), 1514–1526.

Benson, R.C., Kaufmann, R.D., Yuhr, L, and Hopkins, R. (2003). “Locating and characterizing abandoned mines using microgravity.” Geophysical Technologies for Detecting Underground Coal Mine Voids Forum, Lexington, KY.

Beres, M., and Haeni, F. P. (1991). “Application of ground-penetrating radar methods in hydrogeologic studies.” Ground Water, 29(3), 375–386.

Beres, M., Luetscher, M., and Olivier, R. (2001). “Integration of ground penetrating radar and microgravimetric methods to map shallow caves.” J. Appl. Geophys., 46(4), 249–262.

Bignardi, S., Mantovani, A., and Zeid, N. (2016). "OpenHVSR: imaging the subsurface 2D/3D elastic properties through multiple HVSR modeling and inversion." Comp. & Geosci., 93, 103–113.

Bignardi, S., Mantovani, A., and Zeid, N. (2016). “OpenHVSR: imaging the subsurface 2D/3D elastic properties through multiple HVSR modeling and inversion.” Comp. & Geosci., 93, 103–113.

Bivens, M. J., and Siegel, T. C. (2007). “Case Histories of Micropile in Karst: The Influence of Installation on Design and Performance.” Proceedings Geo-Denver 2007, pp. 1-8.

Blatt, H. and R. L. Jones (1975). "Proportions of exposed igneous, metamorphic, and sedimentary rocks." Geological Society of America Bulletin 86(8): 1085-1088.

Boiero, D., E. Wiarda and P. Vermeer (2013). "Surface-and guided-wave inversion for near-surface modeling in land and shallow marine seismic data." The Leading Edge 32(6): 638-646.

Bolt, B. (1982). Inside the Earth (BA Bolt, Ed.), San Francisco: WH Freeman.

Bonnans, J. F., Gilbert, J. C., Lemarécha, C., & Sagastizábal, C. A. (2006). *Numerical optimization: Theoretical and practical aspects* (2nd ed). Springer.

Borisov, D., Modrak, R., Gao, F., & Tromp, J. (2017). 3D elastic full-waveform inversion of surface waves in the presence of irregular topography using an envelope-based misfit function. *Geophysics*, *83*(1), R1–R11.

Bosch, F. P., and Müller, I. (2005). “Improved karst exploration by VLF-EM-gradient survey: comparison with other geophysical methods.” Near Surface Geophysics, 3(4), 299-310.

Boxberger, T., M. Picozzi and S. Parolai (2011). "Shallow geology characterization using Rayleigh and Love wave dispersion curves derived from seismic noise array measurements." Journal of Applied Geophysics 75(2): 345-354.

Boxberger, T., Picozzi, M., and Parolai, S. (2011). "Shallow geology characterization using Rayleigh and Love wave dispersion curves derived from seismic noise array measurements." Journal of Applied Geophysics, 75, 345-354.

Boxberger, T., Picozzi, M., and Parolai, S. (2011). “Shallow geology characterization using Rayleigh and Love wave dispersion curves derived from seismic noise array measurements.” Journal of Applied Geophysics, 75, 345-354.

Bozdağ, E., Trampert, J., and Tromp, J. (2011). “Misfit functions for full waveform inversion based on instantaneous phase and envelope measurements.” Geophysical Journal International, 185(2), 845-870.

Briaud, J., Medina-Cetina, Z., Hurlebaus, S., Everett, T., Tucker, S., Yousefpour, N., and Arjwech, R. (2012). “Unknown Foundation Determination for Scour.” Report No. FHWA/TX-12/0-6604-1, Texas Department of Transportation, Austin, TX.

Brossier, R., Operto, S., and Virieux, J. (2015). “Velocity model building from seismic reflection data by full-waveform inversion.” Geophysical Prospecting, 63(2), 354-367.

Brossier, R., Virieux, J., & Operto, S. (2008). Parsimonious finite-volume frequency-domain method for 2-D P–SV-wave modelling. *Geophysical Journal International*, *175*(2), 541–559.

Buchignani, V., G. A. Avanzi, R. Giannecchini and A. Puccinelli (2008). "Evaporite karst and sinkholes: a synthesis on the case of Camaiore (Italy)." Environmental Geology 53(5): 1037-1044.

Buckman, C., Lahti, R., Michelsen, F., and Shea, L. (2012). “Full Waveform Non-Linear P and S Wave Seismic Tomography Investigation Performed to Identify Karst Features and Bedrock Topography within Stormwater Basin in Western US.” Proceedings 25th Symposium on the Application of Geophysics to Engineering and Environmental Problems, pp. cp-329.

Bullock, P. J., and Dillman, A. (2003). “Sinkhole detection in Florida Using GPR and CPT.” In Proc. Int. Conf. on Applied Geophysics (ICAG), 1-12.

Bunks, C., Saleck, F.M., Zaleski, S., and Chavent, G., (1995). “Multiscale seismic waveform inversion.” Geophysics, 60 (5), 1457–1473.

Burberry, C. M., Jackson, C. A. L., and Chandler, S. R. (2016). “Seismic reflection imaging of karst in the Persian Gulf: Implications for the characterization of carbonate reservoirs.” AAPG Bulletin, 100(10), 1561-1584.

Burchette, T. P. (2012). “Carbonate rocks and petroleum reservoirs: a geological perspective from the industry.” Geological Society, London, Special Publications, 370(1), 17-37.

Butler, D.K. (1980). “Microgravimetry for geotechnical applications.” Miscellaneous Paper GL-80-6, U.S. Army Engineer Waterways Experiment Station, Vicksburg, MS.

Butler, D.K. (1984). “Microgravimetric and gravity gradient techniques for detection of subsurface cavities.” Geophysics, 49(7), 1084–1096.

Butler, D.K. (2007). “Engineering And Environmental Applications Of The Potential Field Methods Of Geophysics.” Proc. SAGEEP 2007, Denver, Colorado.

Byle, M., Blakita, P. M., and Winter, E. (1991). "Seismic Testing Methods for Evaluation of Deep Foundation Improvement by Compaction Grouting." In Deep Foundation Improvements: Design, Construction, and Testing, edited by Esrig, M. and Bachus, R., ASTM International, West Conshohocken, PA, pp. 234-247.

Camacho, A.G., Vieira, R., Montesonos, F.G., and Cuellar, V. (1994). “A gravimetric 3D global inversion for cavity detection.” Geophys. Prosp., 42(2), 113–130.

Caputo, R., A. Pellegrinelli, C. Bignami, A. Bondesan, A. Mantovani, S. Stramondo and P. Russo (2015). "High-precision levelling, DInSAR and geomorphological effects in the Emilia 2012 epicentral area." Geomorphology 235: 106-117.

Carbonel, D., V. Rodríguez, F. Gutiérrez, J. P. McCalpin, R. Linares, C. Roqué, M. Zarroca, J. Guerrero and I. Sasowsky (2014). "Evaluation of trenching, ground penetrating radar (GPR) and electrical resistivity tomography (ERT) for sinkhole characterization." Earth Surface Processes and Landforms 39(2): 214-227.

Carcione, J. M., Kosloff, D., & Kosloff, R. (1988). Wave propagation simulation in a linear viscoelastic medium. *Geophysical Journal International*, *95*(3), 597–611.

Carmichael, R.W., and Henry, G. (1977). “Gravity Exploration for Groundwater and Bedrock Topography in Glaciated Areas.” Geophysics, 42(4), 850-859.

Carpenter, P. J., Doll, W. E., and Kaufmann, R. D. (1998). “Geophysical Character of Buried Sinkholes on the Oak Ridge Reservation, Tennessee.” Journal of Environmental and Engineering Geophysics, 3(3), 133-145.

Carr, B. J., Hajnal, Z., and Prugger, A. (1998). “Shear-wave studies in glacial till.” Geophysics, 63(4), 1273-1284.

Carriere, S. D., Chalikakis, K., Sénéchal, G., Danquigny, C., and Emblanch, C. (2013). “Combining electrical resistivity tomography and ground penetrating radar to study geological structuring of karst unsaturated zone.” Journal of Applied Geophysics, 94, 31-41.

Caselle, C., Bonetto, S., Comina, C., and Stocco, S. (2020). “GPR surveys for the prevention of karst risk in underground gypsum quarries.” Tunnelling and Underground Space Technology, 95, 103137.

Castellaro, S. and Mulargia, F. (2009). “The effect of velocity inversions on H/V.” Pure & App. Geophys., 166 (4), 567–592.

Castelli, R.J. (1991). "Vibratory Deep Compaction of Underwater Fill." Deep Foundation Improvements: Design, Construction, and Testing, ASTM STP 1089, Melvin I. Esrig and Robert C Bachus, Eds., American Society for Testing and Materials, Philadelphia, pp. 279-319.

Chambers, J. E., Gunn, D. A., Wilkinson, P. B., Meldrum, P. I., Haslam, E., Holyoake, S., Kirkham, M., Kuras, O., Merritt, A., and Wragg, J. (2014). “4D electrical resistivity tomography monitoring of soil moisture dynamics in an operational railway embankment.” Near Surface Geophysics, 12(1), 61-72.

Chen, C.W., Rondenay, S., Weeraratne, D.S., and Snyder, D.B. (2007). “New constraints on the upper mantle structure of the Slave Craton from Rayleigh wave inversion.” Geophys. Res. Lett., 34, L10301.

Chen, J. and S. Xiang (1991). Sinkhole collapse resulting from pumping of karst groundwater: a problem and its solution. Proceedings 4th International Conference on Land Subsidence, Houston.

Chin, K. H., Disla, H. P., and Cote, B. (2013). "Design and Construction of Compaction Grouting for Foundation Soil Improvements." International Conference on Case Histories in Geotechnical Engineering, 1-9.

Chow, Y. K., Yong, D. M., Yong, K. Y., and Lee, S. L. (1992). "Dynamic compaction analysis." Journal of Geotechnical Engineering, 118(8), 1141-1157.

Chow, Y.K., Yong, D.M., Yong, K.Y. and Lee, S.L. (1994). "Dynamic compaction of loose granular soils: effect of print spacing." Journal of the Geotechnical Engineering, 120(7), 1115–1133.

Clayton, R. and Engquist, B., (1977). “Absorbing Boundary Conditions for Acoustic and Elastic Wave Equations.” Bulletin of the Seismological Society of America, 67 (6), 1529–1540.

Closson, D., N. A. Karaki, Y. Klinger and M. J. Hussein (2005). "Subsidence and sinkhole hazard assessment in the southern Dead Sea area, Jordan." Pure and Applied geophysics 162(2): 221-248.

Coe, J. T., Brandenberg, S. J., Ahdi, S., and Kordjazi, A. (2018). Geophysical Methods for Determining the Geotechnical Engineering Properties of Earth Materials. Report No. CA-17-2111, California Department of Transportation, Sacramento, CA.

Coe, J. T., Mahvelati, S., and Kordjazi, A. (2019). “Full Waveform Inversion to Evaluate Liquefaction Triggering in Soils Exhibiting Natural Spatial Stiffness Variability.” Proceedings 7th International Conference on Earthquake Geotechnical Engineering, Rome, Italy.

Colombo, D., and Stefano, M.D. (2007). “Geophysical modeling via simultaneous joint inversion of seismic, gravity, and electromagnetic data: application to prestack depth imaging.” Leading Edge, 26(3), 326–331.

Colombo, D., and Stefano, M.D. (2007). “Geophysical modeling via simultaneous joint inversion of seismic, gravity, and electromagnetic data: application to prestack depth imaging.” Leading Edge, 26(3), 326–331.

Comas, X., N. Terry, M. Warren, R. Kolka, A. Kristiyono, N. Sudiana, D. Nurjaman and T. Darusman (2015). "Imaging tropical peatlands in Indonesia using ground-penetrating radar (GPR) and electrical resistivity imaging (ERI): implications for carbon stock estimates and peat soil characterization." Biogeosciences. 12: 2995-3007.

Conway, B. D. and J. P. Cook (2013). "Monitoring evaporite karst activity and land subsidence in the Holbrook Basin, Arizona using interferometric synthetic aperture radar (InSAR)." KIP Talks and Conferences. 78.

Cook, J. C. (1965). “Seismic mapping of underground cavities using reflection amplitudes. Geophysics.” 30(4), 527-538.

Cooper A.H. (2018) Evaporites. In: Bobrowsky P.T., Marker B. (eds) Encyclopedia of Engineering Geology. Encyclopedia of Earth Sciences Series. Springer, Cham.

Cooper, A. and R. Calow (1998). Avoiding gypsum geohazards: guidance for planning and construction. BGS Technical Report WC/98/5.

Cooper, A. H. and J. M. Saunders (2002). "Road and bridge construction across gypsum karst in England." Engineering Geology 65(2-3): 217-223.

Corwin, D.L. (2008). “Past, present, and future trends in soil electrical conductivity measurements using geophysical methods.” In: Allred, B.J., Daniels, J.J., Ehsani, M.R. (Eds.), Handbook of Agricultural Geophysics. CRC Press, Taylor and Francis Group, Boca Raton, Florida, pp. 17–44.

Cox, B. R. and D. P. Teague (2016). "Layering ratios: a systematic approach to the inversion of surface wave data in the absence of a priori information." Geophysical Journal International 207(1): 422-438.

Cox, B., Cheng, T., and Vantassel, J. (2020). “A statistical representation and frequency-domain window-rejection algorithm for single-station HVSR measurements.” Geophys. J. Int., 221 (3), 2170–2183.

Culshaw, M. and A. Waltham (1987). "Natural and artificial cavities as ground engineering hazards." Quarterly Journal of Engineering Geology and Hydrogeology 20(2): 139-150.

Dal Moro, G. (2008). "Vs and Vp vertical profiling via joint inversion of Rayleigh waves and refraction travel times by means of bi-objective evolutionary algorithm." Journal of Applied Geophysics, 66, 15-24.

Dal Moro, G. (2008). “Vs and Vp vertical profiling via joint inversion of Rayleigh waves and refraction travel times by means of bi-objective evolutionary algorithm.” Journal of Applied Geophysics, 66, 15-24.

Dal Moro, G. (2015). “Joint analysis of Rayleigh-wave dispersion and HVSR of lunar seismic data from the Apollo 14 and 16 sites.” Icarus, 254, 338–349.

Dal Moro, G. and M. Pipan (2007). "Joint inversion of surface wave dispersion curves and reflection travel times via multi-objective evolutionary algorithms." Journal of Applied Geophysics 61(1): 56-81.

Dal Moro, G. and M. Pipan (2007). “Joint inversion of surface wave dispersion curves and reflection travel times via multi-objective evolutionary algorithms.” Journal of Applied Geophysics 61(1): 56-81.

Dal Moro, G., and Ferigo, F. (2011). "Joint analysis of Rayleigh- and Love-wave dispersion: Issues, criteria and improvements." Journal of Applied Geophysics, 75, 573-589.

Dal Moro, G., and Ferigo, F. (2011). “Joint analysis of Rayleigh- and Love-wave dispersion: Issues, criteria and improvements.” Journal of Applied Geophysics, 75, 573-589.

Dal Moro, G., and Pipan, M. (2007). “Joint inversion of surface wave dispersion curves and reflection travel times via multi-objective evolutionary algorithms.” Journal of Applied Geophysics, 61, 56-81.

Dal Moro, G., and Pipan, M. (2007). “Joint inversion of surface wave dispersion curves and reflection travel times via multi-objective evolutionary algorithms.” Journal of Applied Geophysics, 61, 56-81.

Davis, J. L., and Annan, A. P. (1989). “Ground-penetrating radar for high-resolution mapping of soil and rock stratigraphy.” Geophysical prospecting, 37(5), 531-551.

Davis, K., Li, Y., and Batzle, M. (2008). “Time-lapse gravity monitoring: A systematic 4D approach with application to aquifer storage and recovery.” Geophysics, 73(6), WA61-WA69. doi: 10.1190/1.2987376.

De Zeeuw-van Dalfsen, E., H. Rymer, E. Sturkell, R. Pedersen, A. Hooper, F. Sigmundsson and B. Ófeigsson (2013). "Geodetic data shed light on ongoing caldera subsidence at Askja, Iceland." Bulletin of volcanology 75(5): 709.

Debeglia, N., A. Bitri and P. Thierry (2006). "Karst investigations using microgravity and MASW; Application to Orléans, France." Near Surface Geophysics 4(4): 215-225.

Desir, G., F. Gutiérrez, J. Merino, D. Carbonel, A. Benito-Calvo, J. Guerrero and I. Fabregat (2018). "Rapid subsidence in damaging sinkholes: Measurement by high-precision leveling and the role of salt dissolution." Geomorphology 303: 393-409.

Diaz, C.M., Diaz, G.M. and Chilcoat, L. (1998). "Repair of Liquefaction Induced Lateral Spreading and Settlement Using Compaction Grouting." Proc. Geot. Earthquake Engrg. and Soil Dyn. III, 691-702.

Dobecki, T. L. and S. B. Upchurch (2006). "Geophysical applications to detect sinkholes and ground subsidence." The Leading Edge 25(3): 336-341.

Doctor, D. H., and Young, J. A. (2013). “An evaluation of automated GIS tools for delineating karst sinkholes and closed depressions from 1-meter LIDAR-derived digital elevation data.” Proceedings 13th Sinkhole Conference, NCKRI Symposium 2, 449-458.

Doll, W. E., Miller, R. D., and Bradford, J. (2012). “The emergence and future of near-surface geophysics.” The Leading Edge, 31(6), 684-692.

Domenico, S. N. (1967). “Detail gravity profile across San Andreas fault zone.” Geophysics, 32(2), 297-301.

Doolittle, J. A., and Brevik, E. C. (2014). “The use of electromagnetic induction techniques in soils studies.” Geoderma, 223, 33-45.

Doolittle, J. A., and Collins, M. E. (1998). “A comparison of EM induction and GPR methods in areas of karst.” Geoderma, 85(1), 83-102.

Early, K. R., and Dyer, K. R. (1964). “The use of a resistivity survey on a foundation site underlain by karst dolomite.” Geotechnique, 14(4), 341-348.

Eaton, G.P., Martin, N.W., and Murphy, M.A. (1965). “Application of Gravity Measurements to Some Problems in Engineering Geology.” Bull. Assoc. Eng. Geol., 3, 6-21.

Eide, E.S., and Hjelmstad, J.F. (2002). “3D Utility mapping using electronically scanned antenna array.” In 9th International Conference on Ground Penetrating Radar, Santa Barbara, CA.

El-Kelesh, A. M., Matsui, T., and Tokida, K. I. (2012). "Field investigation into effectiveness of compaction grouting." Journal of Geotechnical and Geoenvironmental Engineering, 138(4), 451-460.

Epanomeritakis, I., Akçelik, V., Ghattas, O., & Bielak, J. (2008). A Newton-CG method for large-scale three-dimensional elastic full-waveform seismic inversion. *Inverse Problems*, *24*(3), 034015.

Erkan, K., Jekeli, C., and Shum, C.K. (2012). “Fusion of gravity gradient and magnetic field data for discrimination of anomalies using deformation analysis.” Geophysics, 77(3), F13-F20. doi: 10.1190/geo2010-0184.1.

Evans, M. W., Snyder, S. W., and Hine, A. C. (1994). “High-resolution seismic expression of karst evolution within the Upper Floridan aquifer system; Crooked Lake, Polk County, Florida.” Journal of Sedimentary Research, 64(2b), 232-244.

Evans, R. D. (2010). Optimising ground penetrating radar (gpr) to assess pavements, Eng.D. Dissertation, Loughborough University.

Evjen, H.M. (1936). “The place of the vertical gradient in gravitational interpretations.” Geophysics, 1(1), 127-136.

Fajklewicz, Z. J. (1976). “Gravity Vertical Gradient Measurements for the Detection of Small Geologic and Anthropomorphic Forms.” Geophysics, 41(5), 1016-1030.

Fathi, A., Poursartip, B., Stokoe, II, K.H., and Kallivokas, L.F. (2016). “Three-dimensional P- and S-wave velocity profiling of geotechnical sites using full-waveform inversion driven by field data.” Soil Dynamics and Earthquake Engineering, 87, 63-81.

Fichtner, A. (2011). Full seismic waveform modeling and inversion. Springer-Verlag Berlin Heidelberg, 343 p.

Fichtner, A., Kennett, B. L. N., Igel, H., & Bunge, H.-P. (2008). Theoretical background for continental- and global-scale full-waveform inversion in the time–frequency domain. *Geophysical Journal International*, *175*(2), 665–685.

Fischer, J. and J. Fischer (1996). Karst site remediation grouting. International Journal of Rock Mechanics and Mining Sciences and Geomechanics Abstracts.

Fischer, J. J., and Fischer, J. A. (2015). “Concepts For Geotechnical Investigation in Karst.” Proceedings 14th Sinkhole Conference. Rochester: NCKRI Symposium 5, 549-557.

Fort Campbell Environmental Division (2003). Class V injection well management plan for sinkholes, Fort Campbell Environmental Division, Kentucky.

Foshee, J., and Bixler, B. (1994). “Cover-subsidence sinkhole evaluation of state road 434, longwood, Florida.” Journal of geotechnical engineering, 120(11), 2026-2040.

Foti, S., Comina, C., Boiero, D., and Socco, L.V. (2009). “Non-uniqueness in surface-wave inversion and consequences on seismic site response analyses.” Soil Dyn. Earthq. Eng., 29, 982–993.

Foti, S., Hollender, F., Garofalo, F., Albarello, D., Asten, M., Bard, P.Y., Comina, C., Cornou, C., Cox, B., Di Giulio, G. and Forbriger, T. (2018). “Guidelines for the good practice of surface wave analysis: A product of the InterPACIFIC project.” Bulletin of Earthquake Engineering, 16(6), 2367-2420.

Foti, S., Lai, C., Rix, G., and Strobbia, C. (2014). Surface Wave Methods for Near-Surface Characterization. CRC Press.

Fountain, L. W., Herzig, F. X., and Owen, T. E. (1975). Detection of Subsurface Cavities by Surface Remote Sensing Techniques. Report No. FHWA-RD-75-80, Federal Highway Administration, Washington, D. C.

Fretwell, J. D., and Stewart, M. T. (1981). “Resistivity study of a coastal karst terrain, Florida.” Groundwater, 19(2), 156-162.

Gabriels, P., Snieder, R., and Nolet, G. (1987). "In situ measurements of shearwave velocity in sediments with higher-mode Rayleigh waves." Geophys, Prospect., 35(2), 187-196.

Galibert, P. Y., Valois, R., Mendes, M., and Guérin, R. (2014). “Seismic study of the low-permeability volume in southern France karst systems.” Geophysics, 79(1), EN1-EN13.

Gallardo, L. A. and M. A. Meju (2004). "Joint two-dimensional DC resistivity and seismic travel time inversion with cross-gradients constraints." Journal of Geophysical Research: Solid Earth 109(B3).

Gallardo, L.A., and Meju, M.A. (2003). “Characterization of heterogeneous near-surface materials by joint 2D inversion of DC resistivity and seismic data.” Geophys. Res. Lett., 30(13), 1658.

Gallardo, L.A., and Meju, M.A. (2003). “Characterization of heterogeneous near-surface materials by joint 2D inversion of DC resistivity and seismic data.” Geophys. Res. Lett., 30(13), 1658.

Gallardo, L.A., and Meju, M.A. (2004). “Joint two-dimensional DC resistivity and seismic travel time inversion with cross-gradients constraints.” J. Geophys. Res., 109, B03311.

Gallardo, L.A., Meju, M.A., and Perez-Flores, M.A. (2005). “A quadratic programming approach for joint image reconstruction: mathematical and geophysical examples.” Inverse Problems, 21, 435–452.

Galve, J. P., J. Remondo and F. Gutiérrez (2011). "Improving sinkhole hazard models incorporating magnitude–frequency relationships and nearest neighbor analysis." Geomorphology 134(1-2): 157-170.

Gélis, C., J. Virieux and G. Grandjean (2007). "Two-dimensional elastic full waveform inversion using Born and Rytov formulations in the frequency domain." Geophysical Journal International 168(2): 605-633.

Giacomo, D. Di and Gallipoli, M. (2005). “Analysis and Modeling of HVSR in the Presence of a Velocity Inversion: The Case of Venosa, Italy.” Bull. Seis. Soc. America , 95 (6), 2364–2372.

Gosar, A., (2007). “Microtremor HVSR study for assessing site effects in the Bovec basin (NW Slovenia) related to 1998 Mw5. 6 and 2004 Mw5. 2 earthquakes.” Eng. Geology, 178–193.

Gouveia, F., I. Lopes and R. C. Gomes (2016). "Deeper VS profile from joint analysis of Rayleigh wave data." Engineering geology 202: 85-98.

Gouveia, F., Lopes, I., and Carrilho Gomes, R. (2016). "Deeper Vs profile from joint analysis of Rayleigh wave data." Engineering Geology, 202, 85-98.

Grandjean, G., and Leparoux, D. (2004). “The potential of seismic methods for detecting cavities and buried objects: experimentation at a test site.” Journal of Applied Geophysics, 56(2), 93-106.

Granger, G. D. (1990). “Geophysics in the assessment of road materials borrow sites.” Exploration Geophysics, 21(2), 111-119.

Grasmueck, M., Coll, M., Eberli, G. P., and Pomar, K. (2010). “Diffraction Imaging of Vertical Fractures and Karst With Full-resolution 3D GPR, Cassis Quarry, France.” Proceedings 72nd EAGE Conference and Exhibition-Workshops and Fieldtrips, pp. cp-161.

Grasmueck, M., Quintà, M. C., Pomar, K., and Eberli, G. P. (2013). “Diffraction imaging of sub-vertical fractures and karst with full-resolution 3D Ground-Penetrating Radar.” Geophysical Prospecting, 61(5), 907-918.

Greenfield, R. J. (1979). “Review of geophysical approaches to the detection of karst.” Bulletin of the association of engineering geologists, 16(3), 393-408.

Greenhalgh, S. A., Bing, Z., and Green, A. (2006). “Solutions, algorithms and inter-relations for local minimization search geophysical inversion.” Journal of Geophysics and Engineering, 3(2), 101-113.

Griffiths, D. V., Dotson, D., and Huang, J. (2011). “Probabilistic finite element analysis of a raft foundation supported by drilled shafts in karst.” Proceedings Geo-Risk 2011: Risk Assessment and Management, pp. 233-239.

Groos, L., Schäfer, M., Forbriger, T., & Bohlen, T. (2017). Application of a complete workflow for 2D elastic full-waveform inversion to recorded shallow-seismic Rayleigh waves. *Geophysics*, *82*(2), R109–R117.

Guan, Z., X. Jiang and M. Gao (2013). "A calibration test of karst collapse monitoring device by optical time domain reflectometry (BOTDR) technique." Proceedings of the Thirteenth Multidisciplinary Conference on Sinkholes and the Engineering and Environmental Impacts of Karst.

Guerrero, J., F. Gutiérrez, J. Bonachea and P. Lucha (2008). "A sinkhole susceptibility zonation based on paleokarst analysis along a stretch of the Madrid–Barcelona high-speed railway built over gypsum-and salt-bearing evaporites (NE Spain)." Engineering Geology 102(1-2): 62-73.

Guerrero, J., Gutierrez, F., and Lucha, P. (2004). “Paleosubsidence and active subsidence due to evaporite dissolution in the Zaragoza area (Huerva River valley, NE Spain): processes, spatial distribution and protection measures for transport routes.” Engineering Geology, 72(3-4), 309-329.

Guitton, A., Ayeni, G., & Díaz, E. (2012). Constrained full-waveform inversion by model reparameterization. *Geophysics*, *77*(2), R117–R127.

Gunn, J. (2004). Encyclopedia of caves and karst science, Taylor and Francis.

Gutiérrez, F., A. Benito-Calvo, D. Carbonel, G. Desir, J. Sevil, J. Guerrero, A. Martínez-Fernández, T. Karamplaglidis, Á. García-Arnay and I. Fabregat (2019). "Review on sinkhole monitoring and performance of remediation measures by high-precision leveling and terrestrial laser scanner in the salt karst of the Ebro Valley, Spain." Engineering Geology 248: 283-308.

Gutiérrez, F., J. Guerrero and P. Lucha (2008). "A genetic classification of sinkholes illustrated from evaporite paleokarst exposures in Spain." Environmental Geology 53(5): 993-1006.

Gutiérrez, F., M. Parise, J. De Waele and H. Jourde (2014). "A review on natural and human-induced geohazards and impacts in karst." Earth-Science Reviews 138: 61-88.

Hagedoorn, J. G. (1959). "The Plus-Minus Method of Interpreting Seismic Refraction Sections". Geophysical Prospecting, 7(2), 158–182.

Hall, D.H., and Hajnal, Z. (1962). “The Gravimeter in Studies of Buried Valleys.” Geophysics, 27(6), 939-951.

Hamidi, B., Nikraz, H., and Varaksin, S. (2010). "Correlations between CPT and PMT at a Dynamic Compaction Project." Proceedings of the 2nd International Symposium on Cone Penetration Testing (CPT'10), 1-8.

Hamimu, L., J. Safani and M. Nawawi (2011). "Improving the accurate assessment of a shear-wave velocity reversal profile using joint inversion of the effective Rayleigh wave and multimode Love wave dispersion curves." Near Surface Geophysics 9(1): 1-14.

Hamimu, L., Safani, J., and Nawawi, M. (2011). "Improving the accurate assessment of a shear-wave velocity reversal profile using joint inversion of the effective Rayleigh wave and multimode Love wave dispersion cruves." Near Surface Geophysics, 9(1), 1-14.

Hämmerle, M., Höfle, B., Fuchs, J., Schröder-Ritzrau, A., Vollweiler, N., and Frank, N. (2014). “Comparison of kinect and terrestrial lidar capturing natural karst cave 3-d objects.” IEEE Geoscience and Remote Sensing Letters, 11(11), 1896-1900.

Haramy, K. Y., Henwood, J. T., and Szynakiewicz, T. (2009). "Assessing the effectiveness of compaction grouting using seismic methods." Proceedings International Foundation Congress and Equipment Expo 2019, pp. 241-248.

Harrison, H. D., and Hiltunen, D. R. (2003). “Characterization of karst terrane via SASW seismic wave method.” In Sinkholes and the Engineering and Environmental Impacts of Karst, 519-528.

Harro, D., and Kruse, S. (2013). "Improved imaging of covered karst with the multi-electrode resistivity implant technique." Proceedings 13th Sinkhole Conference, NCKRI Symposium 2, 213-220.

Hawkins, L. V., and Whiteley, R. J. (1979). “Estimation of rippability and excavation conditions in calcrete deposits with seismic refraction methods.” Exploration Geophysics, 10(3), 223-224.

Hayashi, K., Matsuoka, T., and Hatakeyama, H. (2005). “Joint Analysis of a Surface-wave Method and Micro-gravity Survey.” JEEG, 10(2), 175-184.

Hayashi, K., Matsuoka, T., and Hatakeyama, H. (2005). “Joint Analysis of a Surface-wave Method and Micro-gravity Survey.” JEEG, 10(2), 175-184.

Hayden, R.F. and Welch, C.H. (1991). "Design and Installation of Stone Columns at Naval Air Station." Deep Foundation Improvements: Design, Construction, and Testing, ASTM STP 1089, Melvin I. Esrig and Robert C Bachus, Eds., American Society for Testing and Materials, Philadelphia, pp. 172-184.

Heiland, C. A. (1943). "A rapid method for measuring the profile components of horizontal and vertical gravity gradients." Geophysics, 8(2), 119-133.

Heincke, B., Jegen, M., and Hobbs, R. (2006). “Joint inversion of mt, gravity and seismic data applied to sub-basalt imaging.” SEG Tech. Prog. Expand. Abstracts, 25(1), 784–789.

Heisey, J., K. Stokoe and A. Meyer (1982). "Moduli of pavement systems from spectral analysis of surface waves." Transportation research record 852(22-31): 147.

Hill, S. A. (2005). Resolving Sinkhole Issues: A State Government Perspective. Sinkholes and the Engineering and Environmental Impacts of Karst: 520-528.

Hiltunen, D. R., and Cramer, B. J. (2008). “Application of seismic refraction tomography in karst terrane.” Journal of Geotechnical and Geoenvironmental Engineering, 134(7), 938-948.

Hinze, W.J. (1990). “The Role of Gravity and Magnetic Methods in Engineering and Environmental Studies,” In: Geotechnical and Environmental Geophysics, Vol 1: Review and Tutorial, Ward, S.H., ed., Society of Exploration Geophysicists, Tulsa, OK.

Holman, J. A. (1995). Ancient Life of the Great Lakes Basin: Precambrian to Pleistocene, University of Michigan Press.

Holzer, T. L. (1991). Mitigating losses from land subsidence in the United States, National Academies.

Hoover, R. A. (2003). “Geophysical choices for karst investigations.” In Sinkholes and the Engineering and Environmental Impacts of Karst, 529-538.

Hudyma, N., Ruelke, T. J., and Samakur, C. (2005). “Characterization of a Sinkhole Prone Retention Pond Using Multiple Geophysical Surveys and Closely Spaced Borings.” In Sinkholes and the Engineering and Environmental Impacts of Karst, 555-561.

Huismann, J. A., Hubbard, S. S., Redman, J. D., and Annan, A. P. (2003). “Measuring soil water content with ground penetrating radar.” Vadose zone journal, 2(4), 476-491.

Hutchinson, P. J., and Beird, M. H. (2016). "3D mapping with MASW." The Leading Edge, 35(4), 350-352.

Indraratna, B., J. Chu and C. Rujikiatkamjorn (2015). "Ground Improvement Case Histories: Compaction, Grouting and Geosynthetics." Ground Improvement Case Histories: Compaction, Grouting and Geosynthetics.

Intrieri, E., G. Gigli, M. Nocentini, L. Lombardi, F. Mugnai, F. Fidolini and N. Casagli (2015). "Sinkhole monitoring and early warning: An experimental and successful GB-InSAR application." Geomorphology 241: 304-314.

Islam, M. T., E. Sturkell, P. LaFemina, H. Geirsson, F. Sigmundsson and H. Ólafsson (2016). "Continuous subsidence in the Thingvellir rift graben, Iceland: Geodetic observations since 1967 compared to rheological models of plate spreading." Journal of Geophysical Research: Solid Earth 121(1): 321-338.

Ismail, A., and Anderson, N. (2012). “2-D and 3-D Resistivity Imaging of Karst Sites in Missouri, USAResistivity Imaging of Karst Sites.” Environmental and Engineering Geoscience, 18(3), 281-293.

Ivanov, J., Miller, R.D., Xia, J., Steeples, D., and Park, C.B. (2006). "Joint analysis of refractions with surface waves: An inverse solution to the refraction-traveltime problem." Geophysics, 71(6), R131-R138.

Ivanov, J., R. D. Miller, J. Xia, D. Steeples and C. B. Park (2006). "Joint analysis of refractions with surface waves: An inverse solution to the refraction-traveltime problem." Geophysics 71(6): R131-R138.

Ivanov, J., Schwenk, J.T., Peterie, S.L., and Xia, J. (2013). "The joint analysis of refractions with surface waves (JARS) method for finding solutions to the inverse refraction problem." The Leading Edge, 32(6), 692-697.

Ivanov, J., Schwenk, J.T., Peterie, S.L., and Xia, J. (2013). “The joint analysis of refractions with surface waves (JARS) method for finding solutions to the inverse refraction problem.” The Leading Edge, 32(6), 692-697.

Jaafar, R., Anderson, N., and Torgashov, E. (2018). “Imaging in karst terrain utilizing the electrical-resistivity and multichannel analysis of surface-wave methods.” In SEG Technical Program Expanded Abstracts 2018, 2877-2881.

Jardani, A., Revil, A., Santos, F., Fauchard, C., and Dupont, J. P. (2007). “Detection of preferential infiltration pathways in sinkholes using joint inversion of self-potential and EM-34 conductivity data.” Geophysical Prospecting, 55(5), 749-760.

Jiang, X., Y. Gao, Y. Wu and M. Lei (2016). "Use of Brillouin optical time domain reflectometry to monitor soil-cave and sinkhole formation." Environmental earth sciences 75(3): 225.

Joh, S-H., Stokoe, II, K.H., Lee, I-W., Kang, T-H., Rosenblad, B., and Bay, J.A. (2006). "Joint Inversion for Apparent Phase Velocities of Rayleigh and Love Waves." Proceedings GeoCongress 2006, Atlanta, GA.

Johnson, K. S. (2005). "Subsidence hazards due to evaporite dissolution in the United States." Environmental geology 48(3): 395-409.

Johnston, M. A., and Carpenter, P. J. (1998). “Use of seismic refraction surveys to identify mine subsidence fractures in glacial drift and bedrock.” Journal of Environmental and Engineering Geophysics, 2, 213-222.

Jol, H. M., ed. (2009). Ground penetrating radar theory and applications. Elsevier Science.

Jones, C. E. and R. G. Blom (2014). "Bayou Corne, Louisiana, sinkhole: Precursory deformation measured by radar interferometry." Geology 42(2): 111-114.

Jones, R. (1955). “A vibration method for measuring the thickness of concrete road slabs in situ.” Magazine of Concrete Research, 7(20), 97-102.

Joswig M. (1990). “Pattern recognition for earthquake detection.” Bull. seism. Soc. Am., 80, 170–186.

Juhojuntti, N., and Kamm, J. (2015). "Joint inversion of seismic refraction and resistivity data using layered models - Applications to groundwater investigation." Geophysics, 80(1), EN43-EN55.

Juhojuntti, N., and Kamm, J. (2015). “Joint inversion of seismic refraction and resistivity data using layered models - Applications to groundwater investigation.” Geophysics, 80(1), EN43- EN55.

Julia, J., Ammon, C.J., Herrman, R.B., and Correig, A.M. (2000). “Joint inversion of receiver function and surface wave dispersion observations.” Geophysical Journal International, 143, pp. 99–112.

Julia, J., Ammon, C.J., Herrman, R.B., and Correig, A.M. (2000). “Joint inversion of receiver function and surface wave dispersion observations.” Geophysical Journal International, 143, pp. 99–112.

Kachanoski, R. G., Wesenbeeck, I. V., and Gregorich, E. G. (1988). “Estimating spatial variations of soil water content using noncontacting electromagnetic inductive methods.” Canadian Journal of Soil Science, 68(4), 715-722.

Kallivokas, L.F., Fathi, A., Kucukcoban, S., Stokoe II, K.H., Bielak, J., and Ghattas, O. (2013). "Site characterization using full waveform inversion." Soil Dynamics and Earthquake Engineering, 47, 62-82.

Kamal, H., M. El-Hawary, A. Abdul-Jaleel, S. Abdul-Salam and M. Taha (2011). "Development of Cement Grout mixes for treatment of underground cavities in Kuwait." International Journal of Civil and Structural Engineering 2(2): 424-434.

Kannan, R. C. (1999). “Designing foundations around sinkholes.” Engineering Geology, 52(1-2), 75-82.

Kannan, R. C. (2005). Essential elements of estimating engineering properties of karst for foundation design. Sinkholes and the Engineering and Environmental Impacts of Karst: 322-330.

Kearey, P., M. Brooks and I. Hill (2013). An introduction to geophysical exploration, John Wiley and Sons.

Kempton, G., Lawson, C. R., Jones, C. J. F. P., and Demerdash, M. (1996). “The use of geosynthetics to prevent the structural collapse of fills over areas prone to subsidence.” Geosynthetics: Applications, Design and Construction. AA Balkema, Rotterdam, 1086.

Kent, J. D., and Larry Dunaway (2013). Real-Time GPS Network Monitors Bayou Corne Sinkhole Event, Eos, Transactions American Geophysical Union,. 94(43).

Kidanu, S. T., E. V. Torgashov, A. V. Varnavina and N. L. Anderson (2016). "ERT-based investigation of a sinkhole in Greene County, Missouri." AIMS Geosciences 2(2): 99-115.

Kiflu, H., Wightman, M., and Kruse, S. (2013). “Statistical analysis of GPR and SPT methods for sinkhole investigation in covered karst terrain, west-central Florida, USA.” Proceedings 13th Sinkhole Conference, Carlsbad, New Mexico.

Kirsch, A. (1996). An Introduction to the Mathematical Theory of Inverse Problems. Basel Springer.

Klawitter, M., Pistellato, D., Webster, A., and Esterle, J. (2017). “Application of photogrammetry for mapping of solution collapse breccia pipes on the Colorado Plateau, USA.” The Photogrammetric Record, 32(160), 443-458.

Klein, C. and A. R. Philpotts (2013). Earth materials: introduction to mineralogy and petrology, Cambridge University Press.

Kochanov, W. E. (2015). "Sinkholes in Pennsylvania." Philadelphia Department of conservation and natural resources Educational series 11.

Komatitsch, D., & Vilotte, J.-P. (1998). The spectral element method: An efficient tool to simulate the seismic response of 2D and 3D geological structures. *Bulletin of the Seismological Society of America*, *88*(2), 368–392.

Konno, K. and Ohmachi, T. (1998). “Ground-motion characteristics estimated from spectral ratio between horizontal and vertical components of microtremor.” Bull. Seis. Soc. of America, 88 (1), 228–241.

Kordjazi, A. (2019). Novel application of nondestructive testing to evaluate anomalous conditions in drilled shafts and the geologic materials underlying their excavations. Ph.D. Dissertation, Temple University.

Kordjazi, A., Coe, J. T., & Afanasiev, M. (2020). The Use of the Spectral Element Method for Modeling Stress Wave Propagation in Non-Destructive Testing Applications for Drilled Shafts. 434–443.

Kordjazi, A., Coe, J. T., and Afanasiev, M. (2019). “Full Waveform Inversion of Cross-Hole Stress Waves for Structural Integrity Testing of Drilled Shafts.” Proceedings DFI 44th Annual Conference, Chicago, IL.

Kruse, S., M. Grasmueck, M. Weiss and D. Viggiano (2006). "Sinkhole structure imaging in covered karst terrain." Geophysical Research Letters 33(16).

Lacasse, S. and F. Nadim (2009). Landslide risk assessment and mitigation strategy. Landslides–disaster risk reduction, Springer: 31-61.

Lailly, P. (1983). “The seismic inverse problem as a sequence of before stack migrations.” In SIAM conference on inverse scattering: theory and application, Philadelphia, PA.

Lee, R., Callahan, P., Shelly, B., Iqbal, A., and Kribbs, G. (2010). “MASW Survey Identifies Causes of Sink Activity Along I-476 (Blue Route), Montgomery County, Pennsylvania.” In Proceedings of GeoFlorida 2010: Advances in Analysis, Modeling and Design, 1350-1359.

Lee, W.H.K., and Stewart, S.W. (1981). Principles and Applications of Microearthquake Networks. Academic Press, New York.

Li, Y., and Oldenburg, D. W. (1998). “3-D inversion of gravity data.” Geophysics, 63(1), 109-119.

Liang, D., Gan, F., Zhang, W., and Jia, L. (2018). “The application of HVSR method in detecting sediment thickness in karst collapse area of Pearl River Delta, China.” Environmental Earth Sciences, 77, 1-9.

Lin, C. H., Lin, C. P., Dai, Y. Z., and Chien, C. J. (2017). "Application of surface wave method in assessment of ground modification with improvement columns." Journal of Applied Geophysics, 142, 14-22.

Lin, C. H., Lin, C. P., Ngui, Y. J., Wang, H., Wu, P. L., He, G. J., and Liu, H. C. (2019). "Diameter assessment of soilcrete column using in-hole electrical resistivity tomography." Géotechnique, 1-13.

Linde, N., Binley, A., Tryggvason, A., Pedersen, L.B., and Revil, A. (2006). “Improved hydrogeophysical characterization using joint inversion of crosshole electrical resistance and ground-penetrating radar traveltime data.” Water Resour. Res., 42, W12404.

Linde, N., Binley, A., Tryggvason, A., Pedersen, L.B., and Revil, A. (2006). “Improved hydrogeophysical characterization using joint inversion of crosshole electrical resistance and ground-penetrating radar traveltime data.” Water Resour. Res., 42, W12404.

Lines, L.R., Schultz, A.K., and Treitel, S. (1988). "Cooperative inversion of geophysical data." Geophysics, 53(1), 8-20.

Lines, L.R., Schultz, A.K., and Treitel, S. (1988). “Cooperative inversion of geophysical data.” Geophysics, 53(1), 8-20.

Linker, R. and A. Klar (2009). Detection of sinkhole formation via Brillouin Optical-Fiber Time-Domain Reflectrometry (BOTDR). EGU General Assembly Conference Abstracts.

Liu, Y., Teng, J., Xu, T., Badal, J., Liu, Q., & Zhou, B. (2017). Effects of Conjugate Gradient Methods and Step-Length Formulas on the Multiscale Full Waveform Inversion in Time Domain: Numerical Experiments. *Pure and Applied Geophysics*, *174*(5), 1983–2006.

Loh, F. C., Chuah, B. L., Zhou, J., Manning, T., Wolfarth, S., and Priyambodo, D. (2016). “Subsea Karst Detection and Imaging Improvement Using Full Waveform Inversion.” Proceedings 78th EAGE Conference and Exhibition 2016, pp. 1-5.

Loke, M. (1999). "Electrical imaging surveys for environmental and engineering studies." A practical guide to 2.

Long, L., and Kaufmann, R. (2013). Acquisition and Analysis of Terrestrial Gravity Data, Cambridge: Cambridge University Press.

Longman, I. M. (1959). “Formulas for computing the tidal accelerations due to the moon and sun.” Journal Geophysical Research, 64, 2351–2355.

Luhmann, T., S. Robson, S. Kyle and J. Boehm (2013). Close-range photogrammetry and 3D imaging, Walter de Gruyter.

Lukas, R. (1995). Dynamic Compaction, Geotechnical Engineering Circular No. 1. FHWA-SA-95-037, Federal Highway Administration, Washington, D.C.

Mahvelati, S., and Coe, J. T. (2019). “Comparison of Dispersion-Based Analysis of Surface Waves and Full Waveform Inversion in Characterizing Unknown Foundations.” Proceedings Geo-Congress 2019, pp. 158-166.

Maierhofer, C. (2003). “Nondestructive evaluation of concrete infrastructure with ground penetrating radar.” Journal of Materials in Civil Engineering, 15(3), 287-297.

Majzoub, A. F., Stafford, K. W., Brown, W. A., and Ehrhart, J. T. (2017). “Characterization and delineation of gypsum karst geohazards using 2D electrical resistivity tomography in Culberson County, Texas, USA.” Journal of Environmental and Engineering Geophysics, 22(4), 411-420.

Malovichko, D., Y. Potvin and M. Hudyma (2005). Study of “low-frequency” seismic events sources in the mines of the Verkhnekamskoye potash deposit. Controlling seismic risk. Proceedings of the Sixth International Symposium on Rockbursts and Seismicity in Mines, Citeseer.

Mankhemthong, N., Doser, D.I., and Baker, M.R. (2012). “Practical Estimation of Near-surface Bulk Density Variations Across the Border Ranges Fault System, Central Kenai Peninsula, Alaska.” JEEG, 17(3), 151-158.

Marfurt, K. J. (1984). Accuracy of finite-difference and finite-element modeling of the scalar and elastic wave equations. *Geophysics*, *49*(5), 533–549.

Martín-Crespo, T. and D. Gomez-Ortiz (2007). "Collapse hazard assessment in evaporitic materials from ground penetrating radar: a case study." Environmental geology 53(1): 57-66.

Martinez, J. D., K. S. Johnson and J. T. Neal (1998). "Sinkholes in evaporite rocks: surface subsidence can develop within a matter of days when highly soluble rocks dissolve because of either natural or human causes." American Scientist 86(1): 38-51.

Martínez-Moreno, F., J. Galindo-Zaldívar, A. Pedrera, T. Teixido, P. Ruano, J. Peña, L. González-Castillo, A. Ruiz-Constán, M. López-Chicano and W. Martín-Rosales (2014). "Integrated geophysical methods for studying the karst system of Gruta de las Maravillas (Aracena, Southwest Spain)." Journal of Applied Geophysics 107: 149-162.

McMechan, G. A., and Yedlin, M.J. (1981). “Analysis of dispersive wave by wave field transformation.” Geophysics, 46, 869–874.

McNeely, J., Keho, T., Tonellot, T., Ley, R., and Chen, J. (2012). “3D acoustic waveform inversion of land data: a case study from Saudi Arabia.” SEG Technical Program Expanded Abstracts 2012, pp. 1-5.

McNeill, J. D. (1990). “Use of electromagnetic methods for groundwater studies.” Geotechnical and Environmental Geophysics, 1(5), 191-218.

McNeill, J.D. (1980). Electromagnetic Terrain Conductivity Measurement at Low Induction Numbers. Technical Note TN-6. Geonics Ltd: Ontario.

Menke, W. (1989), Geophysical Data Analysis: Discrete Inverse Theory, Elsevier, New York.

Métivier, L., & Brossier, R. (2016). The SEISCOPE optimization toolbox: A large-scale nonlinear optimization library based on reverse communication. *Geophysics*, *81*(2), F1–F15.

Métivier, L., and Brossier, R. (2016). “The SEISCOPE optimization toolbox: A large-scale nonlinear optimization library based on reverse communication.” Geophysics, 81, F1-F15.

Métivier, L., Brossier, R., Virieux, J., & Operto, S. (2013). Full Waveform Inversion and the Truncated Newton Method. *SIAM Journal on Scientific Computing*, *35*(2), B401–B437.

Métivier, L., Brossier, R., Virieux, J., and Operto, S. (2013). “Full waveform inversion and the truncated Newton method.” SIAM Journal on Scientific Computing, 35(2), B401-B437.

Miao, L., Chen, G., and Hong, Z. (2006). "Application of dynamic compaction in highway: a case study." Geotechnical and Geological Engineering, 24(1), 91-99.

Mickus, K. (2003). “The gravity method in engineering and environmental geophysics.” Proc. Geophysics 2003, Federal Highway Administration and Florida Department of Transportation.

Miller, E. A., and Roycroft, G. A. (2004). "Compaction grouting test program for liquefaction control." Journal of Geotechnical and Geoenvironmental Engineering, 130(4), 355-361.

Miller, G., H. Pursey and E. C. Bullard (1955). "On the partition of energy between elastic waves in a semi-infinite solid." Proceedings of the Royal Society of London. Series A. Mathematical and Physical Sciences 233(1192): 55-69.

Miller, R. D., Xia, J., and Park, C. B. (2005). “Seismic techniques to detect dissolution features (karst) at a proposed power-plant site.” In Near-surface geophysics, 663-680.

Mitrofan, H., Povară, I., and Mafteiu, M. (2008). “Geoelectrical investigations by means of resistivity methods in karst areas in Romania.” Environmental Geology, 55(2), 405-413.

Mochales, T., Casas, A.M., Pueyo, E.L., Pueyo, O., Román, M.T., Pocoví, A., Soriano, M.A., and Ansón, D. (2008). “Detection of underground cavities by combining gravity, magnetic and ground penetrating radar surveys: a case study from the Zaragoza area, NE Spain.” Environ. Geol., 53(5), 1067-1077.

Modrak, R. and Tromp, J. (2016). “Seismic waveform inversion best practices: regional, global and exploration test cases.” Geophys. J. Int., Vol. 206, pp. 1864-1889.

Molnar, S., Sirohey, A., Assaf, J., Bard, P.Y., Castellaro, S., Cornou, C., Cox, B., Guillier, B., Hassani, B., Kawase, H. and Matsushima, S. (2022). “A review of the microtremor horizontal-to-vertical spectral ratio (MHVSR) method.” J. of Seismology, pp.1-33.

Mooney, M. A., and Bearce, R. G. (2017). "Assessment of jet grout column diameter during construction using electrical resistivity imaging." Proceedings Grouting 2017, pp. 42-51.

Moore, D. L., and Stewart, M. T. (1983). “Geophysical signatures of fracture traces in a karst aquifer (Florida, USA).” Journal of Hydrology, 61(1-3), 325-340.

Moorkamp, M., Heincke, B., Jegen, M., Roberts, A.W., and Hobbs, R.W. (2011). "A framework for 3-D joint inversion of MT, gravity, and seismic refraction data." Geophysical Journal International, 184, 477-493.

Moorkamp, M., Heincke, B., Jegen, M., Roberts, A.W., and Hobbs, R.W. (2011). "A framework for 3-D joint inversion of MT, gravity, and seismic refraction data." Geophysical Journal International, 184, 477-493.

Mora, P. (1987). Nonlinear two-dimensional elastic inversion of multioffset seismic data. *Geophysics*, *52*(9), 1211–1228.

Moreno-Gómez, M., Liedl, R., and Stefan, C. (2019). “A New GIS-Based Model for Karst Dolines Mapping Using LiDAR; Application of a Multidepth Threshold Approach in the Yucatan Karst, Mexico.” Remote Sensing, 11(10), 1147.

Moyes, H., and Montgomery, S. (2019). “Locating cave entrances using lidar-derived local relief modeling. Geosciences.” 9(2), 98.

Mundell, J. A., and Hebert, G. J. (2010). “Subsurface Imaging Of Karst Geology For Energy Infrastructure Expansion.” In 23rd EEGS Symposium on the Application of Geophysics to Engineering and Environmental Problems.

Nabighian, M.N., Ander, M.E, Grauch, V.J.S., Hansen, R.O., LaFehr, T.R., Li, Y., Pearson, W.C., Peirce, J.W., Phillips, J.D. and Ruder, M.E. (2005). “Historical development of the gravity method in exploration.” Geophysics, 70(6), 63ND-89ND. doi: 10.1190/1.2133785.

Nakamura Y. (1989). “A method for dynamic characteristics estimation of subsurface using microtremor on the ground surface.” Q. Rep. Railway Tech. Res. Inst., 30(1), 25–33.

Nam, B. H. (2019). "Special Contribution Detection and Geotechnical Characterization of Sinkhole: Central Florida Case Study."

Nam, B. H., and Shamet, R. (2020). “A preliminary sinkhole raveling chart.” Engineering Geology, 105513.

Nayak, A. and D. S. Dreger (2014). "Moment tensor inversion of seismic events associated with the sinkhole at Napoleonville salt dome, Louisiana." Bulletin of the Seismological Society of America 104(4): 1763-1776.

Nearing, G. S., Tuller, M., Jones, S. B., Heinse, R., and Meding, M. S. (2013). “Electromagnetic induction for mapping textural contrasts of mine tailing deposits.” Journal of Applied Geophysics, 89, 11-20.

Nesse, William D. (2011). Introduction to Mineralogy, 2nd Edition. Oxford University Press.

Neumann, R. (1977). “Microgravity method applied to the detection of cavities.” Proc. Symp. Detect. Subsurf. Cavities, D. K. Butler, (Ed.), US Army Engineer Waterways Experiment Station, Vicksburg, MS.

Newton, J. G. (1987). Development of sinkholes resulting from man's activities in the eastern United States, US Geological Survey.

Nguyen, T.D., Tran, K.T., and McVay, M. (2016). "Evaluation of unknown foundations using surface-based full waveform tomography." Journal of Bridge Engineering, 21(5), 10.1061/(ASCE)BE.1943-5592.0000866, 04016013.

Nocedal, J. and Wright, S., (1999). Numerical optimization. New York: Springer New York.

Nocedal, J., & Wright, S. J. (2006). *Numerical Optimization* (2nd ed). Springer.

Nof, R. N., G. Baer, A. Ziv, E. Raz, S. Atzori and S. Salvi (2013). "Sinkhole precursors along the Dead Sea, Israel, revealed by SAR interferometry." Geology 41(9): 1019-1022.

Nonveiller, E. (1989). Grouting, Theory and Practice. 250 p, Elsevier, Amsterdam, Oxford, New York, Tokyo.

Nuzzo, L., G. Leucci and S. Negri (2007). "GPR, VES and refraction seismic surveys in the karstic area “Spedicaturo” near Nociglia (Lecce, Italy)." Near Surface Geophysics 5(1): 67-76.

Nyquist, J. E., Peake, J. S., and Roth, M. J. (2007). “Comparison of an optimized resistivity array with dipole-dipole soundings in karst terrain.” Geophysics, 72(4), F139-F144.

Nyquist, J. E., Roth, M. J., and Petruccione, J. L. (1999). “Characterization of shallow karst terrain using multi-frequency electromagnetic induction: two examples from Eastern Pennsylvania.” In SEG Technical Program Expanded Abstracts, 547-550.

Ojakangas, R. W. (1982). Minnesota's geology, U of Minnesota Press.

Olafsdottir, E. A., Erlingsson, S., and Bessason, B. (2018). “Tool for analysis of multichannel analysis of surface waves (MASW) field data and evaluation of shear wave velocity profiles of soils.” Canadian Geotechnical Journal, 55(2), 217-233.

Olhoeft, G. R., Smith, S., Hyslip, J. P., and Selig, E. T. (2004). “GPR in railroad investigations.” In IEEE Proceedings of the Tenth International Conference on Grounds Penetrating Radar.

Oosterveld, M. (1981). “Mapping salinity using resistivity and electromagnetic inductive techniques.” Canadian Journal of Soil Science, 61(1), 67-78.

Orfanos, C., and Apostolopoulos, G. (2011). “2D–3D resistivity and microgravity measurements for the detection of an ancient tunnel in the Lavrion area, Greece.” Near Surf. Geophys., 9(5), 449-457.

Paine, J.G., Buckley, S.M., Collins, E.W., and Wilson, C.R. (2012). “Assessing Collapse Risk in Evaporite Sinkhole-prone Areas Using Microgravimetry and Radar Interferometry.” JEEG, 17(2), 75-87.

Pajot, G., de Viron, O., Diament, M., Lequentrec-Lalancette, M.-F., and Mikhailov, V. (2008). “Noise reduction through joint processing of gravity and gravity gradient data.” Geophysics, 73(3), I23-I34. doi: 10.1190/1.2905222.

Palacky, G. (1987). "Clay mapping using electromagnetic methods." First Break 5(8): 295-306.

Palmer, D. (1981). “An introduction to the generalized reciprocal method of seismic refraction interpretation.” Geophysics, 46(11), 1508-1518.

Pan, J.-J. (1989). “Gravity anomalies of irregularly shaped two-dimensional bodies with constant horizontal density gradient.” Geophysics, 54(4), 528-530. doi: 10.1190/1.1442680.

Papadopoulos, N. G., Tsourlos, P., Papazachos, C., Tsokas, G. N., Sarris, A., and Kim, J. H. (2011). “An algorithm for fast 3D inversion of surface electrical resistivity tomography data: application on imaging buried antiquities.” Geophysical Prospecting, 59(3), 557-575.

Papadopoulos, N. G., Yi, M. J., Kim, J. H., Tsourlos, P., and Tsokas, G. N. (2010). “Geophysical investigation of tumuli by means of surface 3D electrical resistivity tomography.” Journal of Applied Geophysics, 70(3), 192-205.

Park, C. (2019). “ParkSEIS-3D for 3D MASW surveys.” FastTIMES, 24(4), 67-70.

Park, C. and M. Carnevale (2014). "Multichannel analysis of surface waves (MASW): Symposium on the application of geophysics to engineering and environmental problems (SAGEEP)." Boston, March: 16-20.

Park, C. B. and C. Taylor (2010). 3D MASW Characterization of Sinkhole: A Pilot Study at USF Geology Park, Tampa, Fl. Symposium on the Application of Geophysics to Engineering and Environmental Problems 2010, Society of Exploration Geophysicists.

Park, C. B., Miller, R. D., and Xia, J. (1999). “Multichannel analysis of surface waves.” Geophysics, 64(3), 800-808.

Park, C. B., R. D. Miller and J. Xia (1999). "Multichannel analysis of surface waves." Geophysics 64(3): 800-808.

Park, C., Cirone, A., and Rodrigues, R. (2019). "Roadside Active-Passive MASW Surveys to Evaluate Soil Grouting." Proceedings Geo-Congress 2019, pp. 354-366.

Park, C., Richter, J., Rodrigues, R., and Cirone, A. (2018). "MASW applications for road construction and maintenance." The Leading Edge, 37(10), 724-730.

Park, C., Richter, J., Rodrigues, R., and Cirone, A. (2018). “MASW applications for road construction and maintenance.” The Leading Edge, 37(10), 724-730.

Park, C.B., Miller, R.D., and Xia, J. (1998). “Imaging dispersion curves of surface waves on multi-channel record.” 68th Ann. Internat. Mtg. Soc. Expl. Geophys., Expanded Abstracts, p. 1377-1380.

Park, M. K., Park, S., Yi, M. J., Kim, C., Son, J. S., Kim, J. H., and Abraham, A. A. (2014). “Application of electrical resistivity tomography (ERT) technique to detect underground cavities in a karst area of South Korea.” Environmental Earth Sciences, 71(6), 2797-2806.

Park, S., Kim, C., Son, J. S., Yi, M. J., and Kim, J. H. (2009). “Detection of cavities in a karst area by means of a 3D electrical resistivity technique.” Exploration Geophysics, 40(1), 27-32.

Parker Jr, E. H., and Hawman, R. B. (2012). “Multi-channel Analysis of Surface Waves (MASW) in karst terrain, southwest Georgia: Implications for detecting anomalous features and fracture zones.” Journal of Environmental and Engineering Geophysics, 17(3), 129-150.

Parker, E. H., Jr., and Hawman, R. B. (2012). “Multi-channel Analysis of Surface Waves (MASW) in karst terrain, southwest Georgia: Implications for detecting anomalous features and fracture zones.” Journal of Environmental and Engineering Geophysics, 17(3), 129-150.

Parolai, S., Picozzi, M., Richwalski, S.M., and Milkereit, C. (2005). “Joint inversion of phase velocity dispersion and h/v ratio curves from seismic noise recordings using a genetic algorithm, considering higher modes.” Geophysical Research Letters, 32, L01303.

Pazzi, V., Di Filippo, M., Di Nezza, M., Carlà, T., Bardi, F., Marini, F., Fontanelli, K., Intrieri, E. and Fanti, R. (2018). “Integrated geophysical survey in a sinkhole-prone area: Microgravity, electrical resistivity tomographies, and seismic noise measurements to delimit its extension.” Engineering Geology, 243, 282-293.

Pegah, E., and Liu, H. (2016). “Application of near-surface seismic refraction tomography and multichannel analysis of surface waves for geotechnical site characterizations: A case study.” Engineering Geology, 208, 100-113.

Pei, D., Louie, J.N., and Pullammanappallil, S.K. (2007). “Application of simulated annealing inversion on high-frequency fundamental-mode Rayleigh wave dispersion curves.” Geophysics, 72(5), R77-R85.

Pei, H. F., Teng, J., Yin, J. H., and Chen, R. (2014). “A review of previous studies on the applications of optical fiber sensors in geotechnical health monitoring.” Measurement, 58, 207-214.

Pepe, P., V. Martimucci and M. Parise (2015). Geological and geophysical techniques for the identification of subterranean cavities. Engineering Geology for Society and Territory-Volume 5, Springer: 483-487.

Pérez-Flores, M. A., Antonio-Carpio, R. G., Gómez-Treviño, E., Ferguson, I., and Méndez-Delgado, S. (2012). “Imaging of 3D electromagnetic data at low-induction numbers.” Geophysics, 77(4), WB47-WB57.

Pérez-Santisteban, I., García-Mayordomo, J., Martín, A. M., and Carbó, A. (2011). “Comparison among SASW, ReMi and PS-logging techniques: Application to a railway embankment.” Journal of applied geophysics, 73(1), 59-64.

Peterie, S. L., R. D. Miller and J. Ivanov (2014). "Seismology and its applications in Kansas." Kansas: Kansas Geological Survey.

Pin, F. G., and Ketelle, R. H. (1983). Conductivity mapping of underground flow channels and moisture anomalies in carbonate terrain using electromagnetic methods. Report No. ORNL/TM-8866, Oak Ridge National Lab, Tennessee.

Plessix, R.-E. (2006). A review of the adjoint-state method for computing the gradient of a functional with geophysical applications. *Geophysical Journal International*, *167*(2), 495–503.

Pratt, R. G., Shin, C., & Hick, G. J. (1998). Gauss–Newton and full Newton methods in frequency–space seismic waveform inversion. *Geophysical Journal International*, *133*(2), 341–362.

Prins, C., K. Thuro and M. Krautblatter (2019). The Effectiveness of an Inverse Wenner-Schlumberger Array for Geoelectrical Karst Reconnaissance, on the Swabian Alb High Plain, New Line Wendlingen–Ulm, Southwestern Germany. IAEG/AEG Annual Meeting Proceedings, San Francisco, California, 2018-Volume 3, Springer.

Qian, Z., Jiang, Z., and Guan, Y. (2018). "Study on the Processes of Water and Grout Seepage in Porous Media Using Resistivity Method." ASTM Geotechnical Testing Journal, 42(5), 1359-1369.

Redpath, B. B. (1973). Seismic refraction exploration for engineering site investigations. No. EERL-TR-E-73-4. Army Engineer Waterways Experiment Station, Livermore, Calif.(USA). Explosive Excavation Research Lab.

Reed, J.W., Hourihan, D.T., and Thornton, G.J. (1998). "Compaction Grouting to Reduce Seismic Risk and Collapse Potential for Freeway Storm Drain System." Proc. Geot. Earthquake Engrg. and Soil Dyn. III, 666-677.

Reninger, P. A., Martelet, G., Lasseur, E., Beccaletto, L., Deparis, J., Perrin, J., and Chen, Y. (2014). “Geological environment of karst within chalk using airborne time domain electromagnetic data cross-interpreted with boreholes.” Journal of Applied Geophysics, 106, 173-186.

Reynolds, J. M. (2011). An introduction to applied and environmental geophysics, John Wiley and Sons.

Roberts, R.L., Hinze, W.J., and Leap, D.I. (1990). “Application of the gravity method to the investigation of a landfill in glaciated midcontinent, U.S.A.: a case history.” In: Geotechnical and Environmental Geophysics, vol. 2: Environmental and Groundwater, Ward, S.H. (ed.), Society of Exploration Geophysicists, Tulsa, Oklahoma, 253–259.

Rodriguez, V., F. Gutiérrez, A. Green, D. Carbonel, H. Horstmeyer and C. Schmelzbach (2014). "Characterizing sagging and collapse sinkholes in a mantled karst by means of ground penetrating radar (GPR)." Environmental and engineering geoscience 20(2): 109-132.

Romdhane, A., G. Grandjean, R. Brossier, F. Réjiba, S. Operto and J. Virieux (2011). "Shallow-structure characterization by 2D elastic full-waveform inversion." Geophysics 76(3): R81-R93.

Roth, M. J. S., and Nyquist, J. (2003). “Evaluation of Multi-Electrode Earth Resistivity Testing in Karst.” Geotechnical Testing Journal, 26(2), 167-178.

Roth, M. J. S., Mackey, J. R., Mackey, C., and Nyquist, J. E. (2002). “A case study of the reliability of multielectrode earth resistivity testing for geotechnical investigations in karst terrains.” Engineering Geology, 65(2-3), 225-232.

Rucker, D. F., Loke, M. H., Levitt, M. T., and Noonan, G. E. (2010). “Electrical-resistivity characterization of an industrial site using long electrodes.” Geophysics, 75(4), WA95-WA104.

Russell, M., Geraci, J., and Murray, D. (2008). "Compaction Grouting to Mitigate Liquefaction for a New Medical Retail Building." Proceedings Geotechnical Earthquake Engineering and Soil Dynamics IV, pp. 1-10.

Rybakov, M., Goldshmidt, V., Fleischer, L., and Rotstein, Y. (2001). “Cave detection and 4-D monitoring: a microgravity case history near the Dead Sea.” The Leading Edge, 20(8), 896-900.

Saarenketo, T., and Scullion, T. (2000). “Road evaluation with ground penetrating radar.” Journal of Applied Geophysics, 43(2-4), 119-138.

Saliba, R., Hudyma, N., and Prakash, B. (2008). “Subgrade Evaluation and Repair of a Roadway Depression Caused by a Deep Seated Sinkhole.” In Sinkholes and the Engineering and Environmental Impacts of Karst, 593-601.

Samouëlian, A., I. Cousin, A. Tabbagh, A. Bruand and G. Richard (2005). "Electrical resistivity survey in soil science: a review." Soil and Tillage research 83(2): 173-193.

Samyn, K., F. Mathieu, A. Bitri, A. Nachbaur and L. Closset (2014). "Integrated geophysical approach in assessing karst presence and sinkhole susceptibility along flood-protection dykes of the Loire River, Orléans, France." Engineering geology 183: 170-184.

Santamarina, J.C. and Fratta, D. (2005). Discrete signals and inverse problems: an introduction for engineers and scientists. John Wiley and Sons Ltd, West Sussex, England.

Santos, F. A., Triantafilis, J., Bruzgulis, K. E., and Roe, J. A. E. (2010). “Inversion of multiconfiguration electromagnetic (DUALEM-421) profiling data using a one-dimensional laterally constrained algorithm.” Vadose Zone Journal, 9(1), 117-125.

Schmertmann, J., Baker, W., Gupta, R., and Kessler, K. (1986). "CPT/DMT QC of ground modification at a power plant." ASCE GSP Geotechnical Special Publication (GSP) 6, pp. 985-1001.

Schmidt, W. (2005). Geological and Geotechnical Investigation Procedures For Evaluation of the Causes of subsidence Damage In Florida. Florida Geological Survey Special Publication No. 57.

Schrott, L. and O. Sass (2008). "Application of field geophysics in geomorphology: advances and limitations exemplified by case studies." Geomorphology 93(1-2): 55-73.

Schwarzbach, C., Börner, R. U., and Spitzer, K. (2005). “Two-dimensional inversion of direct current resistivity data using a parallel, multi-objective genetic algorithm.” Geophysical Journal International, 162(3), 685-695.

SESAME Project (2004). Guidelines for the implementation of the H/V spectral ratio technique on ambient vibrations measurements, processing and interpretation. http://sesame-fp5.obs.ujf-grenoble.fr/Papers/HV_User_Guidelines.pdf

Sevil, J., F. Gutiérrez, M. Zarroca, G. Desir, D. Carbonel, J. Guerrero, R. Linares, C. Roqué and I. Fabregat (2017). "Sinkhole investigation in an urban area by trenching in combination with GPR, ERT and high-precision leveling. Mantled evaporite karst of Zaragoza city, NE Spain." Engineering geology 231: 9-20.

Shamet, R. M., A. Perez and B. H. Nam (2017b). Sinkhole Risk Evaluation: Detection of Raveled Soils in Central Florida's Karst Geology Using CPT. Geo-Risk 2017: 257-266.

Shamet, R. M., K. Gray and B. H. Nam (2017a). Sinkhole Risk Evaluation by a Subsurface Cone Penetration Test. Geotechnical Frontiers 2017: 469-479.

Sheehan, J. R., Doll, W. E., Watson, D. B., and Mandell, W. A. (2005). "Application of seismic refraction tomography to karst cavities." US Geological Survey Karst Interest Group Proceedings, Rapid City, South Dakota, 29-38.

Shen, M., Juang, C. H., and Chen, Q. (2019). "Mitigation of liquefaction hazard by dynamic compaction—a random field perspective." Canadian Geotechnical Journal, 56(12), 1803-1815.

Siegel, T. and Cargill, P. (2005). Use of the Cone Penetration Test for Geotechnical Site Characterization in Clay-Mantled Karst. Sinkholes and the Engineering and Environmental Impacts of Karst: 331-335.

Siegel, T. C., and Belgeri, J. J. (1996). "The importance of a model in foundation design over deeply-weathered, pinnacled, carbonate bedrock." In International Journal of Rock Mechanics and Mining Sciences and Geomechanics Abstracts, 2(33), 86A.

Siegel, T. C., Belgeri, J. J., and Terry, W. M. (1999). "Compaction grouting verse cap grouting for sinkhole remediation in east Tennessee." In: Beck BF, Pettit AJ, Herring JG (eds) Hydrogeology and engineering geology of sinkholes and Karst. A.A. Balkema, Rotterdam, pp 157–163.

Siegel, T. C., Caskey, J. M., and Huckaba, D. A. (2005). "Combination of ground improvement techniques for support of shallow foundations in karst." In Innovations in Grouting and Soil Improvement, 1-8.

Silva, O. L., Bezerra, F. H., Maia, R. P., and Cazarin, C. L. (2017). "Karst landforms revealed at various scales using LiDAR and UAV in semi-arid Brazil: Consideration on karstification processes and methodological constraints." Geomorphology, 295, 611-630.

Simons, M. and P. Rosen (2007). "Interferometric synthetic aperture radar geodesy."

Slichter, L. B. (1933). "The interpretation of the resistivity prospecting method for horizontal structures." Physics, 4(9), 307-322.

Smith, T. J. (1997). "Sinkhole damage investigations for the insurance industry in west-central Florida." In The engineering geology and hydrogeology of karst terranes, 299-304.

Socco, L.V. and Boiero, D. (2008). "Improved Monte Carlo inversion of surface wave data." Geophysical Prospecting, 56, 357-371.

Solymar, Z.V. (1984). "Compaction of Alluvial Sands by Deep Blasting." Canadian Geotechnical Journal, 21, pp. 305-321.

Sørensen, K. I., and Auken, E. (2004). “SkyTEM-A new high-resolution helicopter transient electromagnetic system.” Exploration Geophysics, 35(3), 191-199.

Sowers, G. (1996). Building on Sinkholes. ASCE Press, New York.

Steeples, D. W. and R. D. Miller (1988). Seismic reflection methods applied to engineering, environmental, and ground-water problems. Symposium on the Application of Geophysics to Engineering and Environmental Problems 1988, Society of Exploration Geophysicists.

Steeples, D. W., Knapp, R. W., and McElwee, C. D. (1986). “Seismic reflection investigations of sinkholes beneath Interstate Highway 70 in Kansas.” Geophysics, 51(2), 295-301.

Stewart, M. T. (1982). “Evaluation of electromagnetic methods for rapid mapping of salt-water interfaces in coastal aquifers.” Groundwater, 20(5), 538-545.

Stow, D. A. V. (2005). Sedimentary Rocks in the Field: A Color Guide. Academic Press.

Strauss, J., Dahncke, D., and Nonamaker, F. (2004). "Compaction Grouting to Mitigate Settlement Beneath Approach Fills, California State Route 73 at Laguna Canyon Road." Proceedings Geotechnical Engineering for Transportation Projects, 1876-1883.

Styles, P., McGrath, R., Thomas, E., and Cassidy, N.J. (2005). “The use of microgravity for cavity characterization in karstic terrains.” Quart. J. Eng. Geol. Hydrogeol., 38(2), 155-169.

Suh, J., and Choi, Y. (2017). “Mapping hazardous mining-induced sinkhole subsidence using unmanned aerial vehicle (drone) photogrammetry.” Environmental Earth Sciences, 76(4), 144.

Šumanovac, F. and M. Weisser (2001). "Evaluation of resistivity and seismic methods for hydrogeological mapping in karst terrains." Journal of Applied Geophysics 47(1): 13-28.

Tanaka, S. and Sasaki, C. (1989). "Representative Construction Work in Sandy Ground For the Improvement of Liquefaction at the Noshiro Thermal Power Station." Journal of the Japanese Society of Soil Mechanics and Foundation Engineering, 37(3), pp. 86-90.

Tarantola, A. (1984). “Inversion of seismic reflection data in the acoustic approximation.” Geophysics, 49, 1259-1256.

Tarantola, A. (1984). Inversion of seismic reflection data in the acoustic approximation. *GEOPHYSICS*, *49*(8), 1259–1266.

Tarantola, A. (2005). *Inverse Problem Theory and Methods for Model Parameter Estimation*. Society for Industrial and Applied Mathematics.

Tarquinio, F. S., and Pearlman, S. L. (2001). “Pin piles in karst topography.” Proceedings of the Sinkholes and the Engineering and Environmental Impacts of Karst, 8th Multidisciplinary Conference.

Taylor, L., M. Brown, T. Sadek and J. Howe (2018). Assessment of karst hazard using cone penetration testing. Engineering in Chalk: Proceedings of the Chalk 2018 Conference, ICE Publishing.

Telford, W.M., Geldart, L.P, and Sheriff, R.E. (1990). Applied Geophysics, 2nd Ed., Cambridge University Press, Cambridge, England, 792 pp.

Tharp, T. M. (2003). Cover-collapse sinkhole formation and soil plasticity. Sinkholes and the engineering and environmental impacts of karst: 110-123.

Tihansky, A. B. (1999). "Sinkholes, west-central Florida." Land subsidence in the United States: US geological survey circular 1182: 121-140.

Tihansky, A. B. and L. A. Knochenmus (2001). "Karst features and hydrogeology in west-central Florida—a field perspective." US Geological Survey Karst Interest Group Proceedings. US Geological Survey Water-Resources Investigations Report: 01-4011.

Tillmann, A., and Stocker, T. (2000). “A new approach for the joint inversion of seismic and geoelectric data.” Proceedings of 63rd EAGE Conference and Technical Exhibition, Eur. Assoc. of Geosci. and Eng., Amsterdam.

Tønnesen, J.F. (1995). “Gravity measurements applied to the mapping of sediment thickness and bedrock morphology in the city of Trondheim, Norway.” J. Appl. Geophys., 34(2), 166.

Torrese, P. (2020). “Investigating karst aquifers: Using pseudo 3-D electrical resistivity tomography to identify major karst features.” Journal of Hydrology, 580, 124257.

Tran, K. T., M. McVay, M. Faraone and D. Horhota (2013). "Sinkhole detection using 2D full seismic waveform tomographySinkhole detection by FWI." Geophysics 78(5): R175-R183.

Tran, K. T., McVay, M., Mirzanejad, M., and Wasman, S. (2019). “Detection of Void in Karst Terrain with 3D Full Waveform Tomography.” Proceedings Geo-Congress 2019, pp. 367-375.

Triantafilis, J., and Monteiro Santos, F.A. (2013). “Electromagnetic conductivity imaging (EMCI) of soil using a DUALEM-421 and inversion modeling software (EM4Soil).” Geoderma 211–212, 28–38

Triantafilis, J., Wong, V., Monteiro Santos, F. A., Page, D., and Wege, R. (2012). “Modeling the electrical conductivity of hydrogeological strata using joint-inversion of loop-loop electromagnetic data.” Geophysics, 77(4), WB99-WB107.

Tuckwell, G., Grossey, T., Owen, S., and Stearns, P. (2008). “The use of microgravity to detect small distributed voids and low-density ground.” Quart. J. Eng. Geol. Hydrogeol., 41(3), 371-380.

Tzanis, A., (2010). “matGPR Release 2: A freeware MATLAB® package for the analysis & interpretation of common and single offset GPR data.” FastTimes, 15 (1), 17 – 43.

U.S. Army Corps of Engineers (2012). Conceptual Site Models. EM 200-1-12, Washington, D.C.

U.S. Army Corps of Engineers (2017). Grouting Technology. EM 1110-2-3506, Washington, D.C.

Utsi, E. C. (2017). Ground penetrating radar: theory and practice. Butterworth-Heinemann.

Valois, R., C. Camerlynck, A. Dhemaied, R. Guerin, G. Hovhannissian, V. Plagnes, F. Rejiba and H. Robain (2011). "Assessment of doline geometry using geophysics on the Quercy plateau karst (South France)." Earth surface processes and landforms 36(9): 1183-1192.

Van den Berghe, N., Poggiagliolmi, E., and Watts, G. (1986). “Offset-dependent seismic amplitudes from karst limestone in northern Belgium.” First Break, 4(5), 9-27.

Van der Pol, C. (1951) “Dynamic testing of road constructions.” J. Appl. Chem., 1, 281-290.

Van Schoor, M. (2002). “Detection of sinkholes using 2D electrical resistivity imaging.” Journal of Applied Geophysics, 50(4), 393-399.

van Schoor, M. (2002). “Detection of sinkholes using 2D electrical resistivity imaging.” Journal of Applied Geophysics, 50(4), 393-399.

Varnavina, A. V., Khamzin, A. K., Kidanu, S. T., and Anderson, N. L. (2019). “Geophysical site assessment in karst terrain: A case study from southwestern Missouri.” Journal of Applied Geophysics, 170, 103838.

Vaughan, C. J. (1986). “Ground-penetrating radar surveys used in archaeological investigations.” Geophysics, 51(3), 595-604.

Veni, G., H. DuChene, N. C. Crawford, C. G. Groves, G. N. Huppert, E. H. Kastning, R. Olson and B. J. Wheeler (2001). "Living with Karst: A Fragile Foundation: AGI Environmental Awareness Series 4." American Geological Institute, Alexandria, VA.

Virieux, J. (1984). SH-wave propagation in heterogeneous media; velocity-stress finite-difference method. *Geophysics*, *49*(11), 1933–1942.

Virieux, J. and S. Operto (2009). "An overview of full-waveform inversion in exploration geophysics." Geophysics 74(6): WCC1-WCC26.

Virieux, J., & Operto, S. (2009). An overview of full-waveform inversion in exploration geophysics. *Geophysics*, *74*(6), WCC1–WCC26.

Virieux, J., Asnaashari, A., Brossier, R., Métivier, L., Ribodetti, A., and Zhou, W. (2017). “An introduction to full waveform inversion.” In Encyclopedia of exploration geophysics, Society of Exploration Geophysicists, pp. R1-1.

Virieux, J., Asnaashari, A., Brossier, R., Métivier, L., Ribodetti, A., and Zhou, W. (2017). “An introduction to full waveform inversion.” In Encyclopedia of exploration geophysics, Society of Exploration Geophysicists, pp. R1-1.

Virieux, J., Asnaashari, A., Brossier, R., Métivier, L., Ribodetti, A., & Zhou, W. (2017). An introduction to full waveform inversion. In *Encyclopedia of Exploration Geophysics* (pp. R1-1-R1-40). Society of Exploration Geophysicists.

Vitale, A., Di Massa, D., Fedi, M., and Florio, G. (2018). “A method for inversion of 1D vertical soundings of gravity anomalies.” Geophysics, 83(2), G15-G23.

Vozoff, K., and Jupp, D.L.B. (1975). “Joint Inversion of geophysical data.” Geophys. J., 42, 977–991.

Vozoff, K., and Jupp, D.L.B. (1975). “Joint Inversion of geophysical data.” Geophys. J., 42, 977– 991.

Waltham, A. and P. Fookes (2003). "Engineering classification of karst ground conditions." Quarterly Journal of Engineering Geology and Hydrogeology 36(2): 101-118.

Waltham, T., A. C. Waltham, F. G. Bell and M. G. Culshaw (2005b). Sinkholes and subsidence: karst and cavernous rocks in engineering and construction, Springer Science and Business Media.

Waltham, T., F. G. Bell and M. G. Culshaw (2005a). "Prevention and remediation of sinkholes." Sinkholes and Subsidence: Karst and Cavernous Rocks in Engineering and Construction: 227-243.

Wang, C.-Y., Rui, F., Zhengsheng, Y., and Xingjue, S. (1986). “Gravity anomaly and density structure of the San Andreas fault zone.” Pure Appl. Geophys., 124(1), 127-140.

Wang, Y., Anderson, N., and Torgashov, E. (2019). “Condition Assessment of Building Foundation in Karst Terrain Using both Electrical Resistivity Tomography and Multi-channel Analysis Surface Wave Techniques.” Geotechnical and Geological Engineering, 1-17.

Wang, Y., Dong, L., Liu, Y., & Yang, J. (2016). 2D frequency-domain elastic full-waveform inversion using the block-diagonal pseudo-Hessian approximation. *Geophysics*, *81*(5), R247–R259.

Warner, J. (2008). Grouting in Karst—Time for New Thinking. Sinkholes and the Engineering and Environmental Impacts of Karst: 660-669.

Wathelet, M., Jongmans, D., and Ohrnberger, M. (2004). “Surface-wave inversion using a direct search algorithm and its application to ambient vibration measurements.” Near Surface Geophys., 2, 211–221.

Weary, D. J. (2015). "The cost of karst subsidence and sinkhole collapse in the United States compared with other natural hazards."

Weary, D. J. and D. H. Doctor (2014). Karst in the United States: A digital map compilation and database, US Department of the Interior, US Geological Survey.

Wenjin, L., and Jiajian, X. (1990). “Effectiveness of the high-precision gravity method in detecting sinkholes in Taian Railway Station of Shangdong province.” In: Geotechnical and Environmental Geophysics, Vol. 3: Geotechnical, Ward, S.H. (ed.), Society of Exploration Geophysicists, Tulsa, Oklahoma, pp. 169–174.

White, D. J. (1989). “Two-dimensional seismic refraction tomography.” Geophysical Journal International, 97(2), 223-245.

Whitelaw, J.L., Mickus, K., Whitelaw, M.J., and Nave, J. (2008). “High-resolution gravity study of the Gray Fossil Site.” Geophysics, 73(2), B25-B32.

Wightman, W.E., Jalinoos, F., Sirles, P., and Hanna, K. (2003) “Application of Geophysical Methods to Highway Related Problems.” Federal Highway Administration, Central Federal Lands Highway Division, Lakewood, CO.

Williams, P. (2003) Dolines. In: Gunn J (ed) Encyclopedia of caves and karst science. Taylor and Francis Group.

Witten, A. J. and Calvert, G. (1999). "Characterizing the distribution of near-surface solution channels using electromagnetic induction and ground penetrating radar." Journal of Environmental and Engineering Geophysics 4(1): 35-43.

Wolters, R. (ed.) (1973). Proc. Symp. on Sink-Holes and Subsidence Engineering – Geological Problems Related to Soluble Rocks. International Association of Engineering Geology, Hanover, Germany.

Wood, C. M., Cox, B. R., Green, R. A., Wotherspoon, L. M., Bradley, B. A., and Cubrinovski, M. (2017). “Vs-Based Evaluation of Select Liquefaction Case Histories from the 2010–2011 Canterbury Earthquake Sequence.” Journal of Geotechnical and Geoenvironmental Engineering, 143(9), 04017066.

Woods, C. (2014). "Karst-Related Sinkholes: Dynamic Compaction as an Effective Remediation Option." Geo-Strata, 18(6), 50-54.

Wust-Bloch, G. H. and M. Joswig (2006). "Pre-collapse identification of sinkholes in unconsolidated media at Dead Sea area by ‘nanoseismic monitoring’(graphical jackknife location of weak sources by few, low-SNR records)." Geophysical Journal International 167(3): 1220-1232.

Xeidakis, G., A. Torok, S. Skias and B. Kleb (2004). "Engineering geological problems associated with karst terrains: their investigation. monitoring, and mitigation and design of engineering structures on karst terrains." Bulletin of the geological Society of Greece 36(4): 1932-1941.

Xia, J., Miller, R. D., and Ivanov, J. (2007). “Sensitivity of high-frequency Rayleigh-wave data revisited.” In SEG Technical Program Expanded Abstracts 2007, 1142-1146.

Xia, J., Miller, R.D., and Park, C.B., (1999). “Estimation of near-surface shear-wave velocity by inversion of Rayleigh waves.” Geophysics, 64(3), 691-700.

Xia, J., Miller, R.D., and Park, C.B., (1999). “Estimation of near-surface shear-wave velocity by inversion of Rayleigh waves.” Geophysics, 64(3), 691-700.

Xie, X. Y., Chen, Y. F., and Zhou, B. (2016). "Data processing of backfill grouting detected by GPR in shield tunnel and research on equipment of GPR antenna." Proceedings 2016 16th International Conference on Ground Penetrating Radar (GPR), pp. 1-5.

Xing, Z., & Mazzotti, A. (2019). Two-grid full-waveform Rayleigh-wave inversion via a genetic algorithm — Part 1: Method and synthetic examples. *GEOPHYSICS*, *84*(5), R805–R814.

Yamanaka, H., and Ishida, H. (1996). “Application of generic algorithms to an inversion of surface wave dispersion data.” Bull. Earthq. Eng., 86, 436–444.

Yang, M. Z. and E. C. Drumm (2002). "Stability evaluation for the siting of municipal landfills in karst." Engineering Geology 65(2-3): 185-195.

Yang, P., Brossier, R., Métivier, L., & Virieux, J. (2016). A review on the systematic formulation of 3-D multiparameter full waveform inversion in viscoelastic medium. *Geophysical Journal International*, *207*(1), 129–149.

Yang, Q., & Malcolm, A. (2021). Frequency domain full-waveform inversion in a fluid-saturated poroelastic medium. *Geophysical Journal International*, *225*(1), 68–84.

Yang, Y., and Engquist, B. (2018). “Analysis of optimal transport and related misfit functions in full-waveform inversion.” Geophysics, 83(1), A7-A12.

Yong, A., Martin, A., Stokoe, K., and Diehl, J. (2013). ARRA-funded VS30 measurements using multi-technique approach at strong-motion stations in California and central-eastern United States. U.S. Geological Survey Open-File Report 2013–1102, 60 p. and data files.

Yoon, K., Vlad, I., Moghaddam, P., Mao, J., and Sheng, J. (2014). “An application of FWI to deep water Hernando NAZ streamer data in Gulf of Mexico.” SEG Technical Program Expanded Abstracts 2014, pp. 987-991.

Yu, Q. M., Zhou, H. L., Wang, Y. H., and Duan, R. X. (2016). "Quality monitoring of metro grouting behind segment using ground penetrating radar." Construction and Building Materials, 110, 189-200.

Yuan, Y. O., Simons, F. J., & Bozdağ, E. (2015). Multiscale adjoint waveform tomography for surface and body waves. *Geophysics*, *80*(5), R281–R302.

Yule, D.E., Sharp, M.K., and Butler, D.K. (1998). “Microgravity investigations of foundation conditions.” Geophysics, 63(1), 95-103.

Zhang, G.-x., F.-y. Jiang, C.-h. YU and F. GE (2009). "Monitoring sinkhole collapse by using optical fiber sensing technique of long gang central town, Shen Zhen City." Journal of Geological Hazards and Environment Preservation 20(4): 117-121.

Zhang, H., Maceira, M., Roux, P., and Thurber, C. (2014). "Joint Inversion of Body-Wave Arrival Times and Surface-Wave Dispersion for Three-Dimensional Seismic Structure Around SAFOD." Pure and Applied Geophysics, 171(11), 3013-3022.

Zhang, H., Maceira, M., Roux, P., and Thurber, C. (2014). “Joint Inversion of Body-Wave Arrival Times and Surface-Wave Dispersion for Three-Dimensional Seismic Structure Around SAFOD.” Pure and Applied Geophysics, 171(11), 3013-3022.

Zheng, L. N., Xie, Q., Hu, Y., Xu, F. F., and Ren, X. H. (2010). "Test study of electromagnetic CT for detecting grouting effect of Karst roadbed." (in Japanese), Hydrogeology and Engineering Geology, 6.

Zhou, J., Revil, A., Karaoulis, M., Hale, D., Doetsch, J., and Cuttler, S. (2014). “Image-guided inversion of electrical resistivity data.” Geophysical Journal International, 197(1), 292-309.

Zhou, W. (2007). “Drainage and flooding in karst terranes.” Environmental Geology, 51(6), 963-973.

Zhou, W. and B. F. Beck (2011). Engineering issues on karst. Karst management, Springer: 9-45.

Zhou, W. and M. Lei (2017). "Conceptual site models for sinkhole formation and remediation." Environmental Earth Sciences 76(24): 818.

Zhou, W., and Beck, B. F. (2008). “Management and mitigation of sinkholes on karst lands: an overview of practical applications.” Environmental Geology, 55(4), 837-851.

Zhou, W., Beck, B. and Stephenson, J. (2000). “Reliability of dipole-dipole electrical resistivity tomography for defining depth to bedrock in covered karst terranes.” Environmental Geology, 39, 760–766.

Zhu, J., Currens, J. C., and Dinger, J. S. (2011). “Challenges of using electrical resistivity method to locate karst conduits—a field case in the Inner Bluegrass Region, Kentucky.” Journal of Applied Geophysics, 75(3), 523-530.

Zhu, J., Taylor, T. P., Currens, J. C., and Crawford, M. M. (2014). “Improved Karst Sinkhole Mapping In Kentucky Using Lidar Techniques: A Pilot Study In Floyds Fork Watershed.” Journal of Cave and Karst Studies, 76(3).

Zisman, E. D., and Clarey, D. J. (2013). "Problems associated with the use of compaction grout for sinkhole remediation in west-central Florida." Proc. 13th Sinkhole Conference, NCKRI Symposium 2, 23-26.

Zisman, E. D., Wightman, M. J., and Taylor, C. (2005). “The effectiveness of GPR in sinkhole investigations.” In Sinkholes and the Engineering and Environmental Impacts of Karst, 608-616.